19960730 088

RAILGUN PLASMA ARMATURES

Final Report

Sponsor
US Army Strategic Defense Command
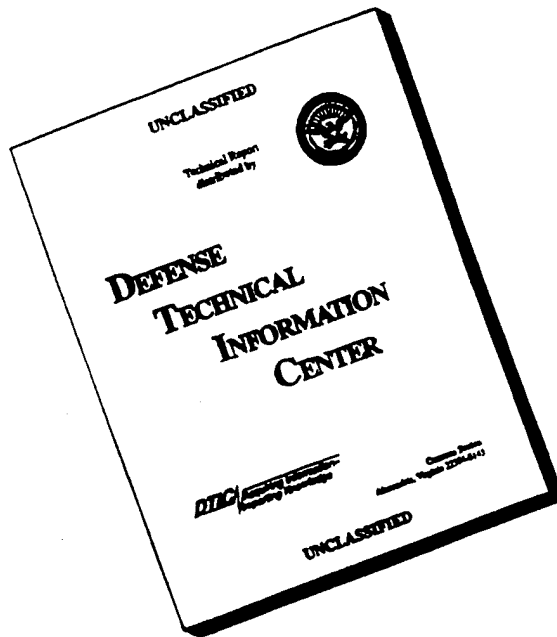Contract DASG 60-90-C-0015

April 1996

Authors

Dennis Keefer
Roger Crawford
Monty Smith
Jamie Taylor
Dmitri Kondrashov
Bruno Evans

University of Tennessee Space Institute
Center for Laser Applications
Tullahoma, Tennessee 37388-8897

DISCLAIMER NOTICE

THIS DOCUMENT IS BEST
QUALITY AVAILABLE. THE
COPY FURNISHED TO DTIC
CONTAINED A SIGNIFICANT
NUMBER OF PAGES WHICH DO
NOT REPRODUCE LEGIBLY.

TABLE OF CONTENTS

1. BACKGROUND

Railguns have the potential to accelerate macroparticles of gram and larger projectile masses to velocities higher than is possible with conventional chemical propellants or light gas guns. This was demonstrated by Rashleigh and Marshall in 1978[1] when they accelerated a gram sized projectile to a velocity of approximately 6 km/s. Numerous attempts to exceed this velocity have resulted in little success[2]. A major Strategic Defense Initiative (SDI) program was established to investigate the application of railgun technology to a very high velocity (10km/s or greater) launch system. Based on a large number of railgun experiments, it appears that there is some fundamental mechanism which severely limits acceleration at velocities greater than 5 km/s. Most experiments indicated that the plasma armature could break up into multiple armatures (secondaries) or restrike arcs could form.

As a result of these plasma armature problems UTSI and SAIC were awarded a contract in September 1986 to develop novel diagnostic techniques and improve models for plasma armatures in railguns, and to transfer the capabilities developed to other railgun facilities. UTSI was tasked to develop diagnostic techniques based on modern laser and high-speed optical spectroscopic instrumentation and analysis techniques. Both UTSI and SAIC developed models for the plasma armature. This contract, DASG-86-C-0121, was completed in August 1989 with a number of significant accomplishments[3]. A brief summary of these accomplishments is listed below. For detailed information see Reference 3 and the contract publications listed therein.

a) A railgun facility was constructed whose sole purpose was to provide advanced diagnostic techniques development and provide an understanding of the physics of railgun armatures[4].

b) Quartz fiberoptic probes were used successfully for the first time to obtain time-resolved spectral plasma emission directly from the bore of a railgun[5].

c) A comprehensive plasma radiation model for the plasma armature was developed to permit estimation of the plasma composition and plasma temperature from the time-resolved spectral measurements[A-19].

d) New deconvolution methods were developed for rail B-dot probes to provide better spatial resolution of the plasma current density and permit direct comparison with the optical emission[6].

e) A new phenomenological model of the plasma armature was developed, based on the optical measurements, which suggested that complex 3-D flow could lead to armature depletion at high velocity.

f) Hybrid armatures were proposed as a method to prevent armature depletion and primary separation.

g) A comprehensive experimental investigation of hybrid armatures established that the hybrid armature is running on plasma brushes and may have a trailing plasma armature attached. The hybrid armature performance and efficiency are comparable to plasma armatures[A-20].

h) A two-arc circuit model was developed which led to recognition that separation of the primary armature from the projectile was responsible for the failure of several experimental railguns to reach their predicted performance[7].

As a result of these accomplishments which expanded the understanding of performance limits in plasma armature railguns, UTSI proposed further experiments and modeling

1

developments to better understand the role of secondary arcs in performance degradation and the mechanisms responsible for separation of the primary arc.

2. INTRODUCTION

The detailed measurements obtained during the first contract were unprecedented in railgun experimentation, and have led to several important advances in understanding of the basic physical processes that govern the plasma armature. Based on these results a far more detailed picture has been developed for the dynamic interactions between the electromagnetic forces, the fluid mechanics, radiation transport and ablation that determine the characteristics of the plasma armature. This picture reveals that the armature is a complex three-dimensional magnetohydrodynamic (MHD) flow that continually exchanges mass, momentum and energy through boundary layer interactions with the gun bore.

This theoretical picture is far more complex than the simple models used to predict plasma armature railgun performance in the past. It offers clues to the reasons why railgun experiments have most often failed to achieve velocities significantly higher than 6km/s. Furthermore, this picture of the armature suggests ways in which these velocity limits may be overcome, and suggests some new directions for the development of hypervelocity railguns. A combined experimental and theoretical modeling effort must be focused on a systematic investigation of the phenomena which limit railgun velocity[A-13].

2.1 Technical Discussion

Observations of the time resolved emission from the plasma at the insulator surface disclosed a brief intense pulse of radiation which decreased to much smaller values during the peak values of plasma current density. Analysis of these signals and subsequent observations obtained at the rail surface revealed that insulator ablation products shield the insulator surface from the most intense radiation from the armature. Since this shielding is not observed at the rail surface, the conclusion is that the armature has considerably different boundary layer flows on the rail and insulator surfaces. Furthermore, the spectrum observed from both the rail surface and the insulator surface indicated the presence of significant concentrations of copper vapor. These results reveal that the armature flow must be strongly three-dimensional.

A consequence of the dissimilar characteristics of the rail and insulator boundary layer flows is that the plasma composition is not homogeneous. High resolution spectral measurements revealed considerably different concentrations of copper near the rail and insulator surfaces. Analysis of these spectra using our detailed plasma radiation model indicated a copper concentration of approximately 10% at the insulator surface and 50% or greater at the rail surface. Additional spectral measurements indicated that the copper concentration is not constant along the length of the armature at the rail surface but increases with distance from the projectile base.

These observations require further consideration of the consequences resulting from the dissimilar rail and insulator boundary layer flows. At the insulator, when the surface has been shielded from the intense radiation, a relatively cold and nonconducting boundary layer develops in which the hydrostatic pressure gradient in the plasma is not balanced by the electromagnetic JxB force. Since the pressure gradient is very large (tens of Kbar/m), a large mass flow develops in the boundary layer which removes material from the moving armature. The material lost from the armature must be replenished for the armature to remain intact. Some ablated insulator

2

material may be entrained into the armature near the base of the projectile, but material is most easily entrained through the rail boundary layer where the JxB forces extend all the way to the rail surface. Rail material is likely to be ejected into the boundary layer as molten droplets or dense vapor and can overcome the viscous drag to become entrained in the moving armature. This results in a three-dimensional flow where mass enters the armature through the rail interface and is lost from the armature along the insulator surface.

Although these observations are significant and suggest a mechanism which may limit velocity, they do not explain the occurrence of secondary arcs or arc restrike which has been observed in conjunction with the velocity limit. Although restrike and secondary arcs have been detected using B-dot probes, there is little information on the dynamics when current shifts from the primary to the secondary arc.

If mass loss from the armature is found to play a role in the promotion of restrike and velocity limits, then there are changes in the bore structure and in projectile design which could be investigated to overcome this limitation. The role of insulator ablation products on the fluid mechanical and radiative structure of the insulator boundary layer is important in determining the rate of mass loss along the insulator boundary. Large ablation rates will thicken and cool the boundary layer, leading to increased mass flow along the insulator, but much of the mass loss in the boundary layer may just be the ablation products. On the other hand, if ablation were reduced to zero, the boundary layer would be thinner and hotter and the mass loss would be reduced, but all of the mass loss would come from the armature. The details of this complicated interaction must be well understood.

If replenishment of the armature material from the rail surfaces becomes insufficient at high velocity, then new projectile designs could be used to supply the armature mass directly from the projectile.

2.2   Research Objectives and Approach

The primary objective was to develop a comprehensive understanding of restrike (secondary armature development), and the complex fluid mechanical, electromagnetic and radiative processes which govern the plasma armature at limiting velocities. This understanding can lead to new experimental design approaches to overcome the current railgun velocity limits. A second objective of this investigation was the evaluation of new projectile designs that can provide alternate sources of ablated material to protect insulator walls and replenish the armature mass.

A comprehensive experimental investigation of restrike phenomena and the effects of boundary layer flows was conducted at velocities near the current velocity limit. Hybrid armatures and innovative new projectile designs that which facilitated the replenishment of material into the plasma armature at high velocity were also investigated. Both of these studies utilized advanced optical and spectroscopic diagnostic techniques to characterize the plasma armatures and the interaction of the plasma with the advanced projectile designs.

The experimental investigations were integrated with the development of an analytical model designed to elucidate the effects of ablation and boundary layer flow. The model utilized a two-dimensional numerical magnetohydrodynamic (MHD) code together with separate boundary layer calculations to supply the required boundary conditions for the numerical code. The experimental investigation relied heavily on the advanced optical and spectroscopic diagnostic techniques developed at UTSI. Most of the experimental investigation was conducted at UTSI,

and required upgrade of the facility to permit experiments at higher velocity. Additional tests were conducted at the Westinghouse Thunderbolt railgun.

Basic studies of the armature and restrike physics were conducted at the UTSI facility. Diagnostic instrumentation and data analysis techniques developed at UTSI were applied at the Westinghouse facilities to validate experimental results at higher velocity in larger railguns. Scaling effects due to increased bore size were conducted on the Thunderbolt railgun which has a bore diameter nearly five times larger than the UTSI gun.

2.3   Research Tasks

a) *Upgrade of the UTSI Railgun*   The original UTSI railgun consisted of a two meter containment structure of which only one meter was used for electromagnetic acceleration. The other meter was used for the light gas gun injector. A separate injector was fabricated and the full two meters were used for a nominal 10mm round bore railgun. A NASA owned 240 kJ capacitor power supply, nearly identical to the current UTSI power supply, Was obtained on loan which doubled the stored energy to 480 kJ. The increased energy storage and increased barrel length permitted experiments to be performed at velocities where secondary arc formation limited performance. The additional meter of railgun was also be instrumented for B-dot probes and in-bore diagnostic probes which required additional high speed data acquisition channels. Conversion to a round-bore configuration facilitated projectile sealing and improved the information gained from laser transmission measurements, but it required fabrication of a honing machine to finish the bore after assembly. Barrel design and fabrication techniques were based on SNL and LLNL experience to minimize cost and schedule.

b) *Experimental Restrike Investigation*   Restrike had been identified as the phenomenon which limited railgun velocity. The way in which restrike is initiated is unknown, but from experiments performed with free-running arcs it appears to be closely associated with bore ablation. No experiments have been performed to characterize the bore gas conditions prior to restrike, or to study the dynamics of multiple arcs in railgun.

We will conduct an extensive study of restrike arcs using the optical and spectroscopic measurements to determine the composition and thermal state of the plasma during restrike. The arrays of emission probes and B-dot probes will be used to characterize the dynamics of multiple arcs. These experiments should offer considerable insight into the physical processes leading to restrike, and lead to new approaches for preventing its occurrence.

c) *Innovative Projectile Designs*   A number of previous studies have suggested that hybrid armatures having plasma brushes and a metallic core could reduce rail ablation and provide efficient acceleration to 6 km/s or greater. Few experiments have been performed with hybrids, and there has been no characterization of the plasma brushes. We will perform experiments to determine the evolution of the plasma brushes as material is ablated from the metallic armature and the plasma brushes thicken. It is not clear that the plasma will remain confined to the metallic armature region and may detach from the metal armature at some point. These experiments will be designed to characterize the plasma brushes and determine whether, and under what conditions, the plasma brushes detach from the metallic armature to form a normal plasma

4

armature. We will use our diagnostic instrumentation to determine whether a portion of the arc can be made to attach to the projectile, and the efficiency with which material can be injected or ablated into the plasma.

d) *Analytical Studies*   It is clear from the spectroscopic measurements obtained from both the rail and insulator that the boundary layers have considerably different composition and radiative characteristics. Optical shielding of the insulator surface results in a cooler boundary layer that reduces the electromagnetic force near the insulator surface and promotes mass loss from the armature. All of the current models of plasma armatures have neglected these effects. Current efforts to model the plasma armature using two-dimensional MHD numerical codes treat only the rail-to-rail and axial directions and will not provide insight into this important effect.

We will develop a two-dimensional MHD code, similar to the one we developed earlier for electrodeless arcs to study the coupling of the insulator boundary layer flow and the current distribution in the armature. This model will provide a basis for interpretation of our detailed spectroscopic measurements and insight into ways in which this mass loss mechanism can be controlled. The Atlanta office of SAIC, under the direction of Dr. Jad Batteh, has been developing detailed MHD boundary layer analyses to provide suitable rail boundary conditions that can be used for the two-dimensional MHD codes. We propose to enlist their considerable expertise in this area through a subcontract to develop similar boundary layer analyses which can provide suitable boundary conditions for the code to be developed at UTSI.

e) *Sandia National Laboratory Experiments*   The upgraded UTSI railgun will provide a facility to conduct experiments into the 5-6 km/s range where restrike limits velocity. Experiments at higher velocity will require a more advanced facility. The SNL railgun avoids the ablation induced restrike regime by injecting the projectile at velocities exceeding the current velocity limit, approximately 7-8 km/s. Currently, this gun has operated successfully on limited energy as part of a systematic development program to insure reliable fusing in the hydrogen driver gas. It is designed to operate at velocities of 12-15 km/s and will most likely provide the first opportunity to characterize plasma armatures at velocities in excess of 6 km/s.

The SNL railgun was originally designed to accept quartz optical fiber probe penetrations of the design developed for the UTSI gun, and can be instrumented with relative ease. We will transfer our diagnostic instrumentation and scientific and technical personnel to SNL and perform experiments there. We will supply one or more optical multichannel analyzers (OMA), a streak camera system, optical detectors and laboratory equipment required to perform optical calibrations. We have considerable experience in conducting this kind of off-site experimentation, and would require approximately two weeks on-site to perform the necessary system integration, calibration and data acquisition. Data acquired during the experiments would be returned to UTSI for reduction and analysis using our detailed radiation models.

f) *Thunderbolt Experiments*   There has been considerable speculation that large bore guns will not experience the same problems as smaller systems with regard to restrike and ablation limited performance. Currently, the Thunderbolt facility operated by Westinghouse at Milpitas, California offers the best opportunity to characterize high velocity plasma armatures in a larger bore railgun. Instrumentation of this gun will be

5

more difficult since no provisions were made for diagnostic penetrations in the original design. However if the gun structure can be modified to accept our quartz optical fibers, then we would propose to conduct off-site experiments, similar to those described in task f using the Thunderbolt railgun.

3. RAILGUN FACILITY, UPGRADES AND GUN CONFIGURATIONS

The importance of a dedicated railgun facility for instrumentation and diagnostic technique development was demonstrated during the first contract. In this investigation it was necessary to upgrade the performance capability of the UTSI railgun to allow armature performance diagnostics at velocities where arc restrike or secondary armature development limit performance. Following the experimental facility development philosophy from the initial investigation, maximum use of existing hardware, fabrication techniques and experience of previous researchers were utilized to upgrade the UTSI facility.

A total of 3.5 meters of gun containment structure had been obtained from the Lawrence Livermore National Laboratory but only 2.2 meters was used for the initial gun. Increased energy storage was needed to power the planned 2.4 meter railgun and provide velocity performance above 4 km/s. A 240 kJ capacitor discharge power supply was available from NASA Lewis Research Center for loan to this project. Thus a 2.4 meter, 10 mm diameter round bore railgun was designed for the total 480 kJ capacitor driven power supply.

To insure the correct current pulse length and to provide flexibility for the pulse shape, UTSI enlisted the support of IAP to design new inductors for the upgraded facility. Two, four sectored toroidal inductors were fabricated and provided 40 μH of inductance in each sector. Since the two power supplies had a total of eight modules, each module was connected to a separate inductor allowing flexible pulse shaping. The independent power supplies and inductors were very important for the augmented railgun to allow independent current pulses for primary and augmenting rails. The toroidal inductor also has the additional important feature of minimizing the external field which allowed the instrumentation and control systems to remain in the same room with the gun and power supplies.

The same single-stage light gas gun was used to preinject the projectiles into the railgun at nominal velocities of 1.0 km/s. The entire 3.5 meters of gun barrel was finished round and straight to a very high tolerance by a lapping machine. The ability to finish or recondition the bore before each shot was very important to experimental repeatability. The UTSI designed lapping machine provided a high quality bore from the light gas injector to the railgun muzzle. Procedures were developed for cleaning the bore after lapping to assure that there were no residues remaining in the bore. A final flush with acetone followed by vacuum drying produced a clean bore. A gun bore reconditioned by this system seldom produced secondary armatures, but a "dirty" barrel would almost assure development of a secondary armature. The facility diagnostics range and catch tank were expanded to improve muzzle velocity measurement and projectile diagnostics. The entire gun, range and catch tank were evacuated and filled to one-half atmosphere of helium for operational safety.

Four gun barrel configurations were developed for the investigations conducted under this contract. Each configuration will be briefly described below along with the rational for the configuration.

a) *Subscale Thunderbolt* Since the full-scale Thunderbolt railgun was too expensive to use for developing diagnostic instrumentation, the first UTSI bore was designed as an approximate

6

20% subscale of Thunderbolt. The Glidcop copper rails and Combat boron nitride insulators were designed to provide a strong, gas-tight bore. (Figure 1) Torlon tape was used between the rails and insulators for compliance and stress relief during structural clamping. The finish lapping of this bore configuration was difficult due to the low shear strength of the boron nitride. This high temperature ceramic has high compressive strength but lacked the surface hardness to resist mechanical erosion. A discussion of experimental results from this gun are presented in section 5.1.
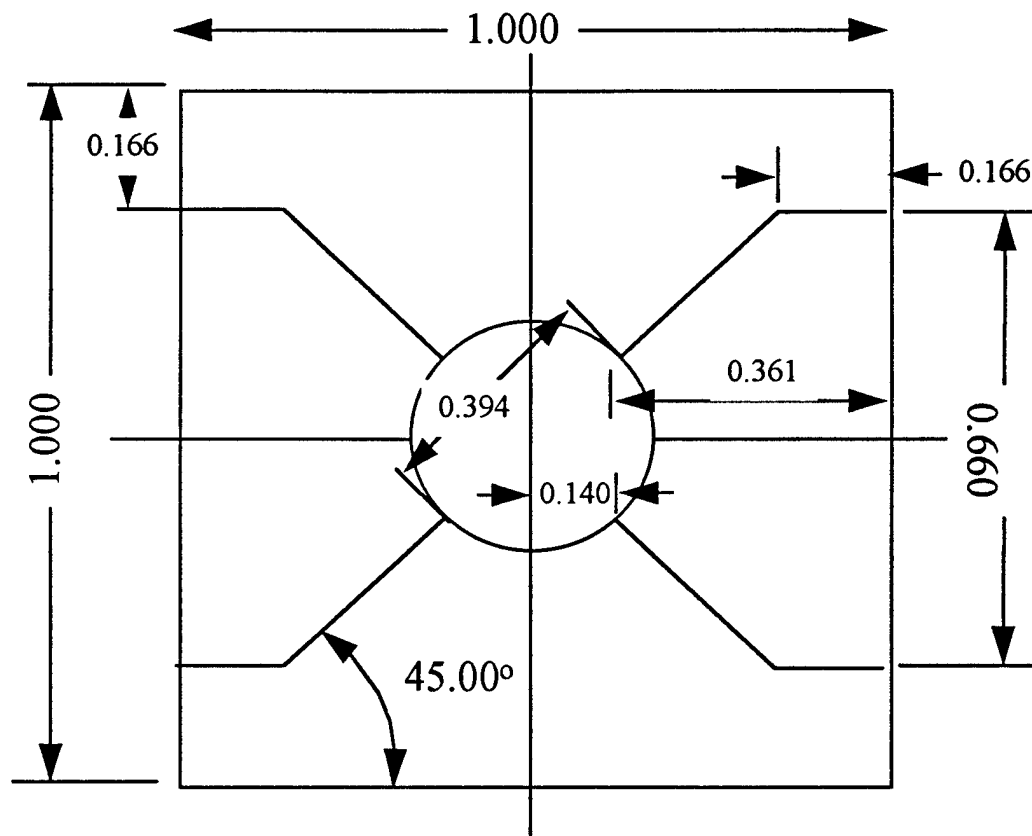

Fig. 1. Subscale Thunderbolt Bore Cross Section.

b) *Transaugmented Railgun* The poor performance obtained from the subscale Thunderbolt configuration influenced the decision to design an augmented railgun. The augmentation would provide increased performance without excessive bore currents and barrel erosion. The bore cross-section shown in Figure 2 provides a configuration that can be operated as a conventional railgun with the outer rails unpowered or as a separately augmented railgun with independent power supplies for the primary and augmenting sets of rails. The G-9 insulator material was selected because it produced less absorbing materials which provided good optical diagnostics through both insulator walls and rails. The design was also selected for ease of machining and assembly. The wide rails however produced a relatively low L' and M' inductance gradients. The transaugmented railgun configuration was found to be a excellent research tool because the driving magnetic field can be independently varied from the

armature current. This capability proved very valuable in developing and validating loss mechanisms for performance models.

c) *Muzzle Fed Railgun* The augmented configuration described above could also be assembled as a muzzle fed gun by connecting the inner and outer rails at the muzzle. This configuration feeds current from the breech along the outer rails and into the inner rails at the muzzle. This configuration was proposed by Cowan[8] to eliminate the velocity skin effect and suppress secondary arc formation. This configuration proved to be a very valuable aid in the understanding of the importance of 3-D electrodynamics. (See 5.4)

d) *High L' and M' Railgun* The final gun configuration of this investigation was a transaugmented railgun with both sets of rails designed for significant improvement in L' and M'. The bore cross-section is shown in Figure 3. The copper rails and G-9 insulators were selected for low cost fabrication as this configuration was more difficult to manufacture and assemble. Having two sets of augmented gun experiments on different inductance gradient configurations also provided valuable data for understanding the performance limitations of railguns.
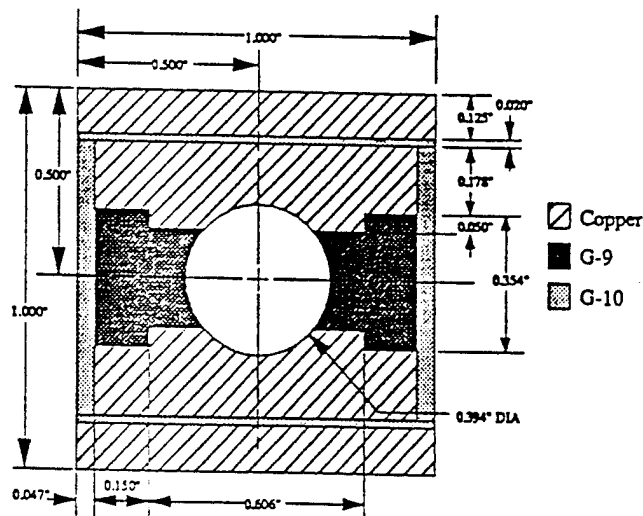

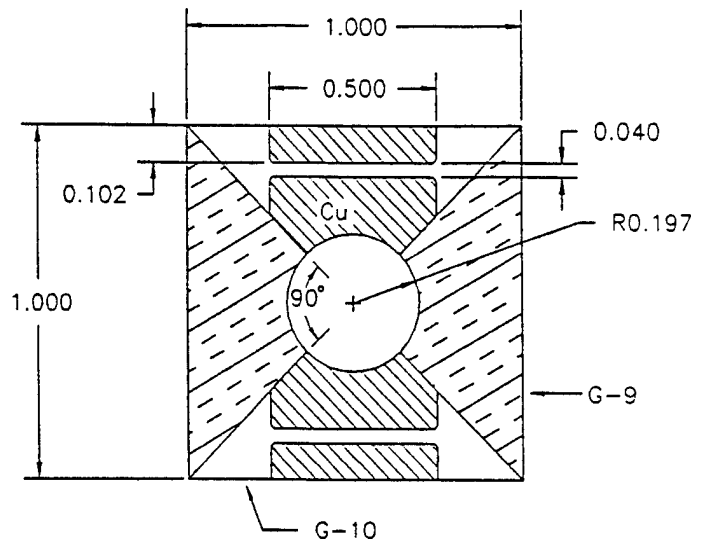Fig. 2. Transaugmented and Muzzle-fed Railgun Bore Cross Section.

Fig. 3. Cross section of the high inductance gradient railgun.
$L' = 0.425\ \mu H/m$, $M' = 0.35\ \mu H/m$.

4. INSTRUMENTATION AND DIAGNOSTIC TECHNIQUES

This investigation benefited from the instrumentation and diagnostic techniques developed on the first contract[3]. Primary diagnostic instrumentation consisted of a dense array of B-dot electromagnetic probes oriented to primarily sense rail current. Armature current and primary field probes were also used to analyze the axial variation of current and field density. Quartz optical fibers provided in-bore diagnostics where necessary to supplement the B-dot data. The railgun facility contained a complete set of conventional instrumentation for measuring electrical circuit parameters. Power supply, breech and muzzle voltages were measured and recorded with high frequency digitizers. Both primary and augmentation currents were measured with calibrated Rogowski coils and recorded with the high frequency data acquisition system. Two piezoelectric pressure transducers were located at the end of the light gas injector, just before the breech of the rails, to measure driving pressure and provide injection velocity. These pressure signals were used to initiate the data acquisition system and fire the power supplies. Muzzle velocity was measured by break wires in the first contract. An electromagnetic measurement system (MAVIS) was used for accurate projectile velocity determination in the upgraded facility. All data were acquired by LeCroy and DSP Technologies transient digitizers which were integrated with the required timing and signal conditioning units in a Camac crate under the control of a PC.

4.1 B-Dot Probes, Rail, Armature and Primary Field

The 2.4 meter railgun was instrumented with 23 B-dot probes equally spaced 100mm apart oriented to sense rail current. Three additional B-dot probes were located to measure primary armature current in a region of the gun where armature separation was likely to occur. Two more probes were located in the same region to measure the primary driving field. This total of 28 B-dot probes in 2.4 meters of railgun assured that the complete evolution of the armature would be measured during each experiment. The calibrated Rogowski coil was used to calibrate the B-dot probes. This required a careful set of experiments for the augmented railgun due to the influence of the augmenting current on the probes. The influence of the augmenting rail current was subtracted from the B-dot signals to obtain armature or rail current profile. Several reports by Smith and Evans documented the modeling and analysis techniques necessary to obtain true armature current distribution from the calibrated B-dot signals[A-15, A-17].

4.2 Position and Velocity from B-Dot Probe Signals

In railguns with limited B-dot probes it is desirable to be able to determine accurate armature position and velocity from a single probe. Smith and Evans developed a cross-correlation method to establish the armature position and velocity from a single B-dot probe[A-18]. This method was validated in the UTSI railgun where the dense B-dot array provided good position and velocity data for comparison. Numerous models and experimental emission measurements have demonstrated that the armature profile has a sharply rising leading edge immediately behind the projectile. This suggests a model of the leading edge of the armature current as a step function. With this approximation, the initial shape of the B-dot probe voltage pulse is the step function response of the probe, scaled by the velocity at which the armature is moving. This information can be used to determine both the time of passage and the velocity of the leading edge of the arc. A series of step function probe responses are calculated over a range of velocities. These generated curves are then compared with experimental data by means of a local area cross-correlation coefficient.

Results of the data analyzed with this method have been shown to provide accurate estimates for the time of passage of the arc. Velocity obtained with this technique differs somewhat from that obtained from the position versus time data. Of particular note is the fact that velocity estimates prior to total gun current maximum fall below those found by position data curve fit. This indicates that the step function model for the leading edge of the arc is not valid at these times. An improved leading edge current model derived from experimental B-dot probe data could provide an accurate one-probe velocity measurement.

4.3 In-Bore Fiber Optic Probes

The use of in-bore quartz fiber optic probes to obtain emission intensity and spectra provided valuable insight into the nonuniform and three-dimensional nature of plasma armatures. Extensive use of fiber optic probes was planned for the secondary armature investigation. However the lapped and cleaned bore of the UTSI railgun did not produce secondary or restrike arcs. We did see primary armature separation from the projectile near the muzzle, but the armature remained intact. Fiber optic probes were made for the LLNL and Thunderbolt railguns. However, the LLNL gun ceased operation before data could be obtained on armatures at high velocity. The optical probes were used in the Thunderbolt railgun, and the data obtained was similar to data from the UTSI gun. Boron nitride insulators did not provide a good environment for optical data due to the mechanical erosion of boron nitride powder into the bore. This material prevented most of the emission from reaching the insulator walls.

The experimental investigations conducted during this contract emphasized the augmented railgun configuration which is difficult to instrument for optical probes through the rail. The risk of shorting between the augmenting and primary rails at the optical penetrations was considered too large, and therefore rail emission data were not obtained. We still believe in the value of optical data for both emission intensity and spectral content, and we would recommend the technique for future investigations into primary armature separation.

4.4 MAVIS Electromagnetic Projectile Velocity Measurement

The accurate measurement of projectile muzzle velocity is essential for understanding the behavior of the plasma armature during launch. B-dot probes have traditionally been used to estimate projectile velocity. However our experimental data has shown that the primary armature can, and often does, separate from the projectile[A-7]. A MAVIS electromagnetic transducer velocity measurement system was fabricated based on a LLNL design, and it was located 80 cm from the muzzle in the flight range. MAVIS consists of a nonconducting tube which contains two coils mounted inside two permanent magnets separated by a sufficient distance to yield an accurate velocity measurement. A small aluminum foil on the nose of the projectile induces a current pulse in the coils when the projectile foil alters the magnetic field of the permanent magnet. As long as the projectile flies through the MAVIS tube a good velocity measurement is obtained. This rugged muzzle velocity system is recommended for all experimental programs where performance diagnostics depends on knowing the relative velocities of the armature and the projectile.

4.5 PIN Photodiode Armature Transition Measurement

Metal armatures provide for efficient railgun performance at lower velocities, however as metal armatures are pushed to higher performance levels they develop plasma brush arcs on the

10

sliding surfaces. This transition from sliding metal-to-metal contact to initiation of the plasma contacts is defined as armature transition. For improved barrel life it is desirable to delay armature transition to as high a velocity as possible. Thus in the UTSI solid armature experiments accurate measurement of transition was considered essential. The muzzle voltage signal provides a good measurement of transition by showing a jump in muzzle voltage. The transition muzzle voltage increase is often seen as two steps as the two contact surfaces transition. In the augmented railgun the muzzle voltage was influenced by the augmenting rail fields, making the armature transition difficult to evaluate.

Thus, we placed a PIN diode in the flight range, behind MAVIS, looking down the barrel. The initiation of transition arcs was detected by the PIN diode, and comparison of muzzle voltage signals in an unaugmented shot with the diode signals showed very good agreement. During the ring armature experiments[A-4] the PIN diode provided valuable transition data during the augmented shots. Solid and hybrid armature performance can not be analyzed properly without accurate transition measurement. Early transition of solid metal armatures nearly always results in loss of performance.

5. EXPERIMENTAL RESEARCH SUMMARY

During this contract UTSI conducted six major experimental investigations on three railgun barrel configurations. This section will present a brief summary of the experimental objectives, results and conclusions. More complete documentation in the form of published reports of the experimental results are presented in Appendix A.

5.1 Subscale Thunderbolt Experiments

The occurrence of secondary arcs in the Thunderbolt railgun experiments resulted in lower than predicted performance. It was found that the restrike arc referenced in many railgun experimental reports was in most cases a secondary arc which developed out of the primary arc. Increased diagnostic instrumentation density confirmed that the secondary arc develops off the rear of the primary armature. Early experiments with limited instrumentation did not resolve this evolution and the secondary arc was thought to be a restrike in the trailing gas from the primary arc. Once UTSI researchers recognized the importance of the secondary arc development on performance limits, a subscale Thunderbolt railgun was designed for the UTSI facility to investigate this effect.

This railgun has been described in section 3. The 2.4 meter long barrel and 10 mm bore diameter constructed with Glidcop copper rails and Combat boron nitride insulators provides a good 20% scale Thunderbolt configuration. The primary experimental objective was careful diagnostics of the secondary armature development using both B-dot and fiber optic probes. Five shots were conducted on this gun, and the results were of limited value due to the unique properties of the boron nitride insulators. For the first time the UTSI railgun produced secondary arcs which grew rapidly in strength and extinguished the primary arc. Performance was significantly reduced due to the secondary armature development. Optical data was not useful due to the erosion of boron nitride power from the insulator walls which significantly reduced the emission signal at the walls.

During reconditioning of the bore with the lapping machine it was found that the boron nitride was too soft and was removed much easier than the copper. This resulted in a bore that was not round. Projectile sealing could not be maintained along the insulator walls, and therefore

11

this configuration was unacceptable for the careful evaluation of the secondary arc development. The full scale Thunderbolt railgun with the boron nitride insulators produced similar results. A high temperature insulator must also have sufficient strength to resist mechanical erosion for successful application to railguns. This configuration was abandoned, and the decision was made to design a new research railgun for armature research.

5.2 Conventional Railgun Experiments (Low L')

A research railgun barrel was designed to provide a unique configuration for the investigation of armature and railgun performance in conventional, augmented and muzzle fed modes. Copper rails and G-9 insulators were chosen for ease of construction and good optical diagnostic properties. The bore cross-section was described in section 3. Careful experiments were performed to determine the self inductance of the primary rails and the mutual inductance of the augmenting rails[A-16]. Conventional railgun experiments were performed over a range of maximum currents to characterize the baseline performance of the gun. Data from these experiments was used to develop a performance model for the railgun and provide values for ablation drag and thermal effects (fusing kick)[A-11]. The performance model included the electromagnetic force (1/2 L'I*2), driving gas expansion, fusing pressure pulse and ablation drag.

Results of these experiments are presented in A-12 where both the conventional and augmented performance are compared. One gram lexan projectiles with aluminum fuses produced stable plasma armatures with no secondary arcs when the bore was lapped and cleaned between each shot. Thus the railgun performance was expected to follow the model since the known loss mechanisms were included. The conventional shots showed good agreement with the model for the first 60% of the acceleration, however near the end of the drive the armature slowed down. MAVIS velocity measurements correlated with the maximum inbore velocity of the armature. This data indicates that the primary armature is separating from the projectile while the electromagnetic driving force is still greater than the known losses. Primary armature separation results in a significant performance loss and can not be explained by any of the losses in the performance model.

Thus the conventional railgun experiments provided data for validation of a simple performance model, and they have identified a new performance problem. The railgun was then operated as an augmented railgun where the driving magnetic field can be varied independently from the armature current.

5.3 Transaugmented Railgun Investigation

Operation of the transaugmented railgun in the augmented mode requires selection of the power level for the augmenting rails and any time delays between primary and augmenting power supply triggering. Two primary rail current levels of 70 kA and 100 kA were selected for the augmented test series with augmenting currents of 30 kA to 140 kA. A complete summary of the experimental results are presented in A-12. Since the armature current was held constant for each of the augmented test series, the electrothermal and ablation effects modeled should not be influenced by the augmentation. The experimental results show, however that performance or efficiency are reduced as the augmenting current is increased. Less than 50% of the increased electromagnetic impulse was realized at the higher augmenting currents. Ablation drag and viscous losses can not explain the reduced performance.

The results of the transaugmented experiments are very significant since they show that the electromagnetic force model or one or more of the loss models are incorrect or missing.[A-13 and A-14] Further experiments with augmented railguns may help understand the electrodynamic interactions that occur in railgun structures, the MHD interactions that take place in plasma armatures, and the complex interactions between them.

5.4 Muzzle Fed Railgun Experiments

The UTSI 2.4 meter railgun was reconfigured so that current was fed from the breech to the muzzle along the outer rails and then returned to the armature along the inner rails. This configuration was first reported in the Soviet literature and was thought to prevent the restrike arc from forming. Experiments were performed on the UTSI muzzle fed gun with plasma armatures at peak currents of 70 and 100 kA. At a peak current of 100 kA the measured velocity increase was approximately 500 m/s, which is less than one-half of the velocity increase obtained in the conventional gun at the same current levels. This was unexpected since the muzzle fed railgun obtains its driving field from the outer rails with M' replacing L' in the force equation.[A-8]

B-dot probes showed that the armature was very compact, but separated from the projectile soon after fusing. Analysis of the B-dot records and the muzzle velocity from MAVIS measurements indicated that the projectile is accelerated by the fusing kick to exit velocity while the armature accelerates moderately through peak current. The armature velocity never reaches the measured projectile exit velocity. Thus we concluded that the armature separated from the projectile at fusing. There are no ablation or viscous loss mechanisms that can explain the performance of the muzzle fed railgun. We thus recognized that the electromagnetic force relation derived from two-dimensional theory is wrong. Three-dimensional electro-dynamic effects resulting in eddy currents were suspected as the primary loss mechanism, and a three-dimensional electromagnetics analysis of armature forces was initiated using the MEGA[A-5 and A-9] More detail on the three-dimensional electromagnetic time dependent analysis of railgun and moving armatures will be presented in section 6.4. The results of this analysis showed that the electromagnetic force on the armature was much less than predicted by the simple force model.

The muzzle fed railgun proved to be a very unacceptable configuration for improved performance, but the results forced the railgun community to recognize that three-dimensional electro-dynamic effects must be considered as one of the performance limiting mechanisms.[A-5]

5.5 High L' and M' Transaugmented Railgun Investigation

When the UTSI transaugmented railgun was designed the bore cross-section was selected for ease of fabrication and assembly. There was no attempt to maximize inductance gradients L' and M'. The use of the MEGA code at UTSI provided an opportunity to evaluate improved electromagnetic designs. Considering fabrication and assembly constraints, an improved barrel design was found which increased L' and M' approximately 50%. The bore cross-sections were presented in section 3.

A series of experiments were undertaken to determine whether the velocity performance of an augmented railgun scales linearly with the values of inductance gradient. The two bores used in these experiments had the same containment structure, bore materials, and bore preparation. The low inductance gradient (LIG) gun had calculated values of L' = 0.274 uH/m, M' = 0.249 uH/m and the high inductance gradient (HIG) gun had calculated values of L' = 0.425 uH/m, and M' = 0.350 uH/m. Experiments were conducted with nearly equal current levels in both guns

13

using a novel designed solid aluminum ring armatures. The measured velocities were used to determine if the calculated inductance ratio was consistent with the measured performance improvement ratio.[A-3 and A-4]

The nominal peak armature current was set to 70 kA for the experiments, and the peak augmentor current was varied from zero to 140 kA. The experimental conditions were held as similar as possible for both guns, but since the gun inductance was larger for the HIG railgun, the current pulse was somewhat longer. Also since the exit times for the projectiles were earlier in the HIG gun, the electromagnetic actions were different. Thus the acceleration rates during the drive near peak current were selected for comparison of the two configurations. The aluminum ring armatures have some unique operating characteristics which complicated the performance comparison and will be discussed in the next section. It was clear that the performance increase was of the same order as the increase in the calculated inductance gradient, and reaffirms the importance of careful electromagnetic design of the launcher structure. Because the influence of armature sliding friction appeared to be smaller in the experiments with large augmentation, the value of 1.45 is probably a reasonable experimental estimate of the self inductance ratio, and is only 6.5% less than the MEGA calculated value of 1.55. Once again, with solid as well as plasma armatures, the inability to accurately quantify drag forces makes it difficult to accurately determine electromagnetic force from acceleration determined from B-dot probes.

5.6 Solid and Transitioning Ring Armature Experiments

The continuing stability and performance problems associated with plasma armatures led to research on hybrid armatures. The performance benefits demonstrated with hybrid metal armatures during the first contract,[A-20] focused research efforts on solid metal armature configurations which can operate in a metal to metal contact mode to high velocity, thus reducing bore damage and providing high electromagnetic efficiency. A controlled transition to hybrid armature operation on plasma brushes may allow the solid to hybrid transition armature to consistently reach high velocity with better performance than plasma armatures. Thus UTSI initiated a solid armature investigation with both experimental and analytical techniques to understand solid to hybrid armature transition physics. A review of solid armature experimental data confirmed a consistent failure of metal to metal contact at relatively low velocity around one kilometer per second. Very limited metal to metal armature contact data exists for velocity above two kilometers per second.

A unique solid armature configuration was selected for this investigation based on three-dimensional electromagnetic analysis. The armature design requirements included minimizing velocity skin effects, maximizing useable action in the metal and improving loading or normal forces against the rail. A thin metal ring armature was selected for evaluation of transition and performance characteristics. Armature action at transition, velocity at transition and total electromagnetic efficiency were evaluated in a separately augmented (transaugmented) railgun, where the effects of velocity can be separated from action. A more complete understanding of armature transition velocity limits was the primary objective of this investigation. Performance evaluation of the ring armature in a hybrid mode was a secondary objective.

Details of the ring armature design are presented in reference A-4. The aluminum ring was 15 mm long for stability in the nominal 10 mm bore. The wall thickness of 1.0 mm was selected based on an action requirement of 100 kA for 2.0 ms which yields a final temperature of 80% melting temperature. A series of experiments were conducted with nominal peak armature current

14

of 70 kA and augmenting currents of 0, 75, 100 and 140 kA. Transition time was recorded using a PIN photodiode looking down the barrel to observe the plasma emission. Position and velocity was obtained from the B-dot probes in the gun structure. A complete summary of the experimental data is presented in reference A-4.

The ability to vary injection velocity, armature current and primary magnetic field independently has provided a new set of transition data which can be used to question existing transition models and develop new theories. The transition physics from this investigation was not independent of velocity. However, two independent velocity related effects were contained in the data set. Velocity increase resulting from increased augmentor current resulted in higher rail separation forces which certainly caused earlier transition due to loss of contact forces on the armature. Data from reference A-3 on high and low inductance gradient railgun configurations supports this conclusion. The second velocity related transition effect was observed in the low injection velocity shots. Below the velocity where combined friction and contact resistance produce a liquid metal contact boundary layer, significantly more electrical action can be deposited in the armature before transition. Thus the frictional losses at the armature interface must be included in the transition model. Velocity, normal force and current density all influence the nature of the liquid contact layer. Failure to maintain a thin liquid metal contact layer results in arcing and transition. The ring armature configuration has good potential for a high velocity solid-transitioning-hybrid armature, and future work should include inertial loading to assure high contact forces.

6. THEORETICAL RESEARCH SUMMARY

Theoretical analysis of experimental observations and basic railgun physics has been an integral part of this project since its inception. During the previous contract, this activity centered on spectroscopic and radiation transfer calculations to allow interpretation of the experimental data obtained from the in-bore optical measurements. Later, some signal processing analyses were carried out to improve the resolution of the experimental B-dot probe data which were obtained from the early square-bore railgun experiments. A performance model was developed which accounted for the formation of secondary arcs. During the current contract the theoretical analyses have focused on the fundamental electromagnetic and plasma flow processes which control and limit performance in electromagnetic launchers. Initially, the analyses were directed to performance models used to interpret the experimental results. Later theoretical analyses were directed toward detailed simulations of the transient electromagnetic interactions in the railgun armature and structure, and detailed simulations of the fluid flow in plasma and hybrid armatures. These detailed simulations, together with the extensive experiments carried out with the UTSI transaugmented railguns have led to a much more complete understanding of the performance limits observed in railgun experiments around the world.

6.1 Two-Dimensional MHD Simulations

Observations made on the Thunderbolt railgun and the subscale UTSI Thunderbolt railgun highlighted the critical importance of secondary arc formation and primary arc separation in limiting the velocity which could be obtained. This was confirmed by the two-arc performance model developed by UTSI.[A-14] A collaborative effort was undertaken with Dr. Robert Tipton at Lawrence Livermore National Laboratory to use the MHD computational code CALE to simulate the complex plasma flow in railgun plasma armatures. The objective of this effort was to provide

15

insight into the physical processes which lead to secondary arc formation and primary arc separation.

Two-dimensional simulations of the armature flow using CALE were obtained in the rail-to-rail plane. It was possible to simulate the primary separation that was observed if account was taken of the mass eroded from the projectile by frictional heating from the rails.[A-13] However, the development of secondary arcs was not observed in the simulations, and it was concluded that three-dimensional effects were likely responsible for this effect. At a workshop held at UTSI it was concluded that 3-dimensional simulations were too difficult to attempt, and that additional 2-dimensional simulations should be continued. However, we continued to believe that additional 2-dimensional simulations would be fruitless, and began 3-dimensional simulations of the electromagnetic interactions without including the plasma flow.

6.2 Three-Dimensional Electromagnetic Simulations

Comparison of railgun performance models with careful measurements made in the UTSI transaugmented railgun began to bring the fundamental assumptions used to determine railgun armature force into question. The force models based on inductance gradient as obtained from circuit analyses were inconsistent with a series of UTSI experiments in the transaugmented railgun made in which the armature current was held constant while the augmenting field was varied. It was suspected that neglect of velocity induced eddy currents was responsible for the breakdown of the models. We obtained the 3-dimensional finite-element electromagnetic code MEGA from the University of Bath, and began to analyze the transient behavior of the magnetic fields in the railgun structure during armature motion. These studies led to reduced predictions for the electromagnetic force in railguns which were presented in an award winning paper at the European Symposium on Electromagnetic Launch Technology at Celle, Germany in May 1993.[A-10] The effect of eddy current generation was found to be even more dramatic in the case of the muzzle-fed railgun configuration.[A-7] These studies showed that the simple models for force could be too large by as much as 50% and culminated in a Ph.D. Dissertation "The Electromagnetic Armature Force in Railguns" by Jaime Taylor.[A-2] The simulation studies with MEGA made it clear that realistic simulations of the plasma armature would require a full three-dimensional MHD simulation. No suitable three-dimensional codes existed, and so the development of a suitable MHD code was undertaken at UTSI.

6.3 Three-Dimensional Plasma Armature Simulations

Soon after the UTSI/LLNL simulations were completed, Dmitri Kondrashov became a Ph.D. student at UTSI. He had co-authored a paper simulating the railgun plasma armature in the insulator-to-insulator plane while in Russia at the High Temperature Institute (IVTAN) in Moscow. The basic three-dimensional Navier-Stokes fluid code from IVTAN became the basis for the UTSI MHD code named MAP3. A three-dimensional quasi-static Maxwell solver was developed to integrate with the fluid code, and the fluid code was modified to include radiation transport and surface ablation effects. The new electromagnetic solver was successfully benchmarked against the MEGA code for solid armature railgun test cases.

MAP3 was used to simulate the plasma armature flow in a 1 cm square-bore railgun. In contrast with earlier simulations, the simulation domain included the entire region from breech to projectile, eliminating the uncertainty in specifying boundary conditions at the rear of the armature. The results of this simulation were startling. The two-dimensional simulations had

16

predicted a recirculating flow along the axis of the railgun to the base of the projectile and then back along the rails. The MAP3 simulation showed a flow forward along the rails to the base of the projectile and then back along the axis of the railgun. Thus, the recirculating flow was in the complete opposite rotation sense from that predicted by the two-dimensional simulations. This effect was caused by the nature of the magnetic field diffusion into the rails. The field diffused faster at the corners of the rail and resulted in a current flow which was stronger near the insulator than along the axis. Because of the off-axis maximum of the J x B forces the plasma was forced forward near the insulators and flowed backward along the axis. The results of this simulation were presented at a second award winning paper at the Electromagnetic Launch Symposium at San Diego, California in 1993.[A-6] Subsequently, MAP3 was used to simulate the flow around a hybrid armature and predicted the strong crossflow components of flow which had been postulated on the basis of observations on recovered hybrid armatures [Ref. 8th EML Symposium Baltimore and IEEE Trans. Mag. Jan. 1997]. This research culminated in a Ph.D. Dissertation, "3-D MHD Plasma Armature Railgun Simulations" by Dmitri Kondrashov.[A-1]

Although the startling differences revealed in the MAP3 simulations of the plasma armature suggested a mechanism for the formation of secondary arcs, no secondary formation was observed in the simulation. The mechanism for formation of the secondary arc is the convective transport of high temperature, electrically conducting plasma to the rear of the armature by the rearward flow along the axis of the railgun. This conducting region at the rear of the armature can evolve into a secondary if ablated material from the rail and insulator becomes entrained between the front and rear of the expanding armature. The failure to observe this evolution in the initial simulations resulted from the lack of sufficient computer memory and speed to carry a computation a sufficient distance. Recently, the simulation has been run on a larger computer, and the full evolution of the single armature into separate primary and a secondary arcs was observed when the projectile reached a distance of 1m and velocity of approximately 2 km/s, consistent with observations in the UTSI square bore railgun [IEEE 23rd ICOPS, Boston, 1996].

Therefore, at the end of this investigation theoretical analyses and computer simulations, together with carefully controlled experiments, have enabled us to understand the physical processes responsible for several of the velocity limiting processes observed in railgun experiments: overestimation of electromagnetic force, secondary arc formation and primary arc separation.

7. Significant Results And Conclusions

At the start of this project, the goal for plasma armature railguns was to accelerate gram and larger sized projectiles to velocities of 10 km/s or greater. Experiments had shown that 1 gm projectile launches at velocities of 6 km/s were attainable in several experiments, with a few isolated experiments reporting 8 to 10 km/s. It was the purpose of this research investigation to understand the 6 km/s limit, and to find ways to overcome this limitation. Two phenomena had been observed which were associated with the velocity limit, restrike and secondary arcs, but their physical basis was poorly understood. Entrained ablation products from the rail and insulator were assumed to be associated with these phenomena, and measures had been proposed to decrease or eliminate ablation.

The results of this investigation have provided significant insight into the formation of secondary arcs and identified two other physical effects which also act to limit velocity: eddy current generation in the rails and separation of the primary arc from the projectile. Eddy current

generation is not only a velocity limiting mechanism, but it is also related to the *expectation* of attainable velocity. Previous calculations of the armature force attainable in a railgun were based on a simple formula which related force to the driving current and inductance gradient of the railgun structure. Careful theoretical analysis and three-dimensional simulations showed that this simple formula overestimated the armature force, and therefore led to overprediction of attainable velocity. Part of the force predicted by the simple formula was exerted on the rails instead of the armature, and part was unavailable because of energy dissipation in the rails due to eddy currents induced by the armature motion. These effects are significant (5-10%) in the case of simple railguns and become serious in the case of augmented (15-25%) railguns and disastrous for muzzle-fed railguns (40-60%).

Primary separation was observed in data obtained from the Thunderbolt railgun and the UTSI subscale Thunderbolt railgun. Comparison of projectile time and velocity at muzzle exit with armature position within the bore showed that the armature detached from the projectile and slowed prior to projectile launch. The projectile ceased to accelerate once this separation occurred. The best understanding of the physical mechanism for this separation came from the two-dimensional simulations using CALE. In these simulations, separation occurred only when material eroded from the projectile due to frictional contact with the rail was included in the simulation. This cold material formed a nonconducting buffer between the projectile and the primary arc. In these simulations the separation of the primary armature was very similar to the experimental observations.

Secondary arc formation was the most difficult phenomenon to understand. Secondary arcs were observed in almost all railgun experiments, particularly when higher velocities were reached. Secondary formation was attributed to the slowing down of the tail of the primary arc caused by the accumulation of mass ablated from the bore. This slowing resulted in an increase in the value of the local electric field which, in turn, resulted in an increase in current at the rear of the arc. In spite of its pervasive appearance in experiments, all attempts to induce secondary formation in the two-dimensional CALE simulations failed, regardless of the amount of ablation introduced. The explanation was finally found from three-dimensional simulations using the MAP3 code.

When it was finally possible to do three-dimensional simulations of the railgun plasma armature, the results were in sharp contrast with the earlier two-dimensional simulations. In the two-dimensional simulations the armature flow consisted of a recirculation of the flow along the axis toward the projectile and then backward along the rail. This flow was driven by the strong J x B forces along the axis and the viscous drag of the rail, together with the lower density near the axis as compared with the plasma near the rail. The primary armature in the three-dimensional simulations also had a recirculation, but in the *opposite* sense! This startling three-dimensional effect was caused by the finite diffusion of the magnetic field into the rail (the velocity skin effect). Since the field penetrated fastest at the outer corners of the rail, the current density maximized at a point between the axis and the insulator wall. The strong J x B forces accelerated the flow in this region toward the projectile and it flowed away from the projectile along the axis where the J x B force was smaller. The flow away from the projectile along the axis convected the highest temperature, and highest electrical conductivity, plasma toward the rear of the armature with little cooling to the bore surfaces. As a result, the current also migrated toward the rear of the armature where it evolved into a secondary arc decelerated by entrained ablation products liberated by the primary arc. The secondary arc, decelerated by accumulating mass between the

18

primary and secondary arcs, and by the attendant viscous drag, effectively reduces the inductance of the gun and severely limits the velocity which can be attained.

This picture of the plasma armature, together with numerous experimental observations, makes it unlikely that plasma armature railguns will achieve the velocities once expected. Some improvement in performance is likely to be possible through improved materials and shaping of the rails to reduce the flow along the axis. However, it is not possible to operate a hypervelocity plasma armature without replenishing armature material lost through viscous interaction with the bore, and the best source of material to replenish the bore is the projectile itself. This concept leads to the hybrid armature as a more likely means to reach velocities in excess of 10 km/s.

8. REFERENCES

1. S.C. Rashleigh and R.A. Marshall, "Electromagnetic Acceleration of Macroparticles to High Velocity," Jol. of Applied Physics, Vol. 49, pp. 2540-2542, April 1978.

2. R.S. Hawke, W.J. Nellis, G.H. Newman, J. Rego and A.R. Susoeff, "Summary of EM Launcher Experiments Performed at LLNL," IEEE Transactions on Magnetics, Vol. 22, No. 6, pp. 1510-1515, 1986.

3. D. Keefer, R. Crawford, A. Sedghinasab and L.M. Smith, "Experimental and Theoretical Studies of Arcs in Railgun Systems," Final Report, U.S. Army S.D.C. Contract DASG60-86-C-0121, October 1990.

4. D. Keefer and R. Crawford, "Optical Diagnostics of Railgun Plasma Armatures," IEEE Transactions on Magnetics, Vol. 25, No. 1, pp. 295-299, 1989.

5. A. Sedghinasab, D. Keefer and H. Crowder, "In-Bore Spectral Measurements in a Plasma Armature Railgun," IEEE Transactions on Plasma Science, Vol. 17, No. 3, pp. 360-364, 1989.

6. L.M. Smith and D. Keefer, "Railgun Armature Plasma-Current Density from Deconvolved B-Dot Probe Signals," IEEE Transactions on Plasma Science, Vol. 17, No. 3, pp. 501-506, 1989.

7. D. Keefer, "Arc Motion in Railgun Plasma Armatures," IEEE Transactions on Plasma Science, Vol. 17, No. 3, pp. 446-449, 1989.

8. M. Cowan, "Solid Armature Railgun Without the Velocity Skin Effect," IEEE Transactions on Magnetics, Vol. 29, No. 1, pp. 385-390, January 1993.

9. APPENDIX A.

Contract Publications

1. D. Kondrashov, "3-D MHD Plasma Armature Railgun Simulations," Ph.D. Dissertation, UTSI, May 1996.

2. J. Taylor, "The Electromagnetic Armature Force in Railguns," Ph.D. Dissertation, UTSI, May 1995.

3. D. Keefer, R. Crawford and J. Taylor, "Inductance Gradient Scaling Experiments in an Augmented Railgun," IEEE Transactions on Magnetics, Vol. 31, No. 1, pp. 326-331, January 1995.

4. R. Crawford, J. Taylor and D. Keefer, "Solid Ring Armature Experiments in a Transaugmented Railgun," IEEE Transactions on Magnetics, Vol. 31, No. 1, pp. 138-143, January 1995.

5. J. Taylor, R. Crawford and D. Keefer, "Muzzle-Fed Railgun Experiments with 3-D Electromagnetic Simulations," IEEE Transactions on Magnetics, Vol. 31, No. 1, pp. 360-365, January 1995.

6. D. Kondrashov and D. Keefer, "3-D Plasma Armature Railgun Simulations," IEEE Transactions on Magnetics, Vol. 31, No. 1, pp. 634-639, January 1995.

7. D. Keefer, R. Crawford and J. Taylor, "Plasma Armature Studies in Augmented and Muzzle-Fed Railguns," AIAA 93-3154, AIAA 24th Plasmadynamics and Lasers Conference, Orlando, Florida, July 1993.

8. D. Keefer, R. Crawford and J. Taylor, "Muzzle-Fed Railgun Experiments," Proceedings of 9th IEEE Pulsed Power Conference, Albuquerque, New Mexico, June 1993.

9. J. Taylor and D. Keefer, "Calculations of the Electromagnetic Force in Railguns," Proceedings of 9th IEEE Pulsed Power Conference, Albuquerque, New Mexico, June 1993.

10. D. Keefer, J. Taylor and R. Crawford, "The Electromagnetic Force in Railguns," Proceedings of the Fourth European Symposium on Electromagnetic Launch Technology Conference, Celle, Germany May 1993, Paper No. 1503.

11. J. Foster, "Development of a Computational Model of the Gasdynamic and Ablation Effects in Plasma Armature Railguns," UTSI M.S. Thesis, May 1993.

12. J. Taylor, R. Crawford and D. Keefer, "Experimental Comparisons of Conventional and Transaugmented Railguns," IEEE Transactions on Magnetics, Vol. 29, No. 1, pp. 523-529, January 1993.

13. R. Crawford, D. Keefer and R. Tipton, "Velocity Limiting Magnetohydrodynamic Effects in Railgun Plasma Armatures," IEEE Transactions on Magnetics, Vol. 29, No. 1, pp. 781-786, January 1993.

14. D. Keefer and R. Tipton, "The Role of Fluid Mechanics in Plasma Armature Railguns," AIAA 92-0084, 30th Aerospace Sciences Meeting, Reno, Nevada, 1992.

15. B. Evans and L.M. Smith, "Determining Railgun Plasma Current Distribution Using Jasson's Method to Deconvolve B-Dot Probe Signals," IEEE Transactions on Plasma Science, Vol. 20, No. 4, pp. 432-438, August 1992.

16. J. Taylor, "A Study of the UTSI Transaugmented and Classical Railgun," M.S. Thesis, UTSI, December 1991.

17. B. Evans, "Analysis of Magnetic Probe Signals to Determine the Plasma Armature Current Distribution," M.S. Thesis, UTSI, December 1991.

18. B. Evans and L.M. Smith, "Cross-Correlation-Based Method for Determining the Position and Velocity of a Railgun Plasma Armature from B-Dot Probe Signals," IEEE Transactions on Plasma Science, Vol. 19, No. 5, pp. 926-934, October 1991.

19. D. Keefer, A. Sedghinasab and R. Crawford, "Simultaneous In-Bore Rail and Insulator Spectra from a Railgun Plasma Armature," IEEE Transactions on Magnetics, Vol. 27, No. 1, pp. 217-219, January 1991.

20. R. Crawford, D. Keefer and A. Sedghinasab, "Railgun Hybrid Armatures, Experimental Results and Performance Characteristics," IEEE Transactions on Magnetics, Vol. 27, No. 1, pp. 240-244, January 1991.

3-D MHD Plasma Armature Railgun Simulations

A Dissertation Presented

for the Doctor of Philosophy Degree

The University of Tennessee, Knoxville

Dmitri A. Kondrashov

May 1996

ABSTRACT

The goal of a plasma armature railgun is to accelerate the projectile to hypervelocities (i.e., to velocities beyond 5 km/s). Despite extensive research, projectile velocities achieved in the plasma armature railgun experiments were under 6-8 km/s - unfortunately, far less than predicted theoretical values. Experimental and numerical studies did not bring a full understanding of the factors limiting performance of the plasma railgun. The numerical studies so far have been limited to 1-D and 2-D computer models. In this dissertation, it is demonstrated that these models inadequately predict the main physical features of railgun plasma flow. To understand the railgun physics, 3-D magnetohydrodynamic (MHD) modelling is necessary.

To perform a 3-D MHD time-dependent computer simulation of the plasma armature railgun, a new code MAP3 (MHD Arc Plasma) was developed at University of Tennessee Space Institute (UTSI). MAP3 uses an efficient numerical method to solve Maxwell's equations and Navier-Stokes equations to develop a complex time-dependent electromagnetic and velocity vector field distribution in the railgun. The importance of MAP3 numerical scheme that uses a staggered grid to solve Maxwell's equations, is demonstrated.

MAP3 provides the first qualitative and quantitative understanding of 3-D physical phenomena in the plasma armature railgun. The results of the 3-D computer simulation for 1-cm and 2-cm bore railguns with ablating walls, are presented.

A profound influence of the inherently 3-D nature of the railgun electromagnetic field on the plasma flow is demonstrated. A strong spatial nonuniformity of the electromagnetic force generates a flow of plasma towards the projectile near the rail and away from the projectile along the center of the bore. This plasma flow is exactly the opposite to flow

provided by the previous 2-D numerical models. A zone of high-shear flow near the rail surfaces can increase viscous losses, which are not accounted for in the usual performance estimates.

A direct simulation of the particular experiment is the logical step to develop this work further. A satisfactory qualitative agreement was demonstrated between numerically obtained B-dot signal (armature magnetic field) and typical experimental data. MAP3 can be used to study secondary arc formations. The 3-D flow has a tendency to elongate the plasma or arc armature, creating a current conducting tail. This process may play an important role in the formation of secondary arcs. MAP3 can be extended to analyze conditions believed to be accountable for the development of the secondary arcs and to provide reliable quantitative simulation. These conditions should include current that changes in time, and higher ablation rates.

THE ELECTROMAGNETIC ARMATURE FORCE IN RAILGUNS

A Dissertation

Presented for the

Doctor of Philosophy

Degree

The University of Tennessee, Knoxville

Jaime R. Taylor

May 1995

ABSTRACT

Plasma armature transaugmented and muzzle-fed railgun experiments were performed in the UTSI 2.4 m, 1 cm bore diameter railgun. These experiments were evaluated with a performance model that included the simple electromagnetic force equation for the particular railgun, viscous and ablation armature drag, and the compression of bore gas ahead of the projectile. This evaluation revealed that at least one of the force or drag models was incorrect. The simple electromagnetic force equations for a "real railgun", one with a finite rail thickness, were derived using the conservation of power at the breech. Strain energy due to the transverse component of current density in the rails and losses from eddy current generation from field diffusion and armature motion were neglected in this derivation.

Three-dimensional (3-D) electromagnetic simulations were performed on a generic square bore railgun configuration with the codes MEGA and MAP3 to determine the seriousness of the losses not included in the derivation. These simulations showed that only a fraction of the force predicted by the simple electromagnetic force model was exerted on the armature. For example, a force of 510 N was predicted for the muzzle-fed railgun at steady-state while a calculated armature force of -170 N was found from the 3-D simulation with a stationary armature. This showed that the simple electromagnetic force model could not be used to predict railgun performance for the muzzle-fed railgun.

-v-

A modification to the simple electromagnetic force equation is proposed,

$$F = \pm \frac{1}{2} \alpha \, L' I_1^2 + \beta \, M' I_1 I_2 \, ,$$

where the positive sign gives the force for the transaugmented railgun and the negative sign gives the force for the muzzle-fed railgun. The parameters α and β represent the fraction of force exerted on the armature from the inner and outer rails respectively. 3-D simulations are required to find values for α and β.

Evaluation of the transaugmented and muzzle-fed railgun experiments using the modified electromagnetic force equation in the performance model showed that one of the drag models was still in error. Further evaluation of the experiments, and published results of 3-D MHD simulations suggested two possibilities that could explain the further deficit in performance. The value of C_f (the viscous drag coefficient found from turbulent pipe flow) could be in error by an order of magnitude due to the increased velocity gradient at the rail surface produced by the $\mathbf{J} \times \mathbf{B}$ forces in the plasma armature. Another possibility is that material trapped in the "cold" region between the armature and projectile (which was not included in the performance model) reached a mass an order of magnitude greater than the mass of the armature itself.

INDUCTANCE GRADIENT SCALING EXPERIMENTS
IN AN AUGMENTED RAILGUN

Dennis Keefer, Roger Crawford, and Jaime Taylor
The University of Tennessee Space Institute
Center for Laser Applications
Tullahoma, Tennessee 37388-8897

ABSTRACT

A series of experiments were undertaken to determine whether the velocity performance of a separately augmented railgun scales linearly with the values of the inductance gradients. Two different railgun configurations which had the same containment, bore materials and bore preparation were used in these experiments. The low inductance gradient (LIG) gun had calculated values of $L' = 0.274$ μH/m, $M' = 0.249$ μH/m and the high inductance gradient gun (HIG) had calculated values of $L' = 0.425$ μH/m, $M' = 0.35$ μH/m. Experiments were conducted with nearly equal current levels in both guns using solid aluminum ring armatures. The measured velocities were used to determine whether the calculated inductance ratio was observed in performance. Frictional drag of the solid armatures complicated the data analysis but the increase in velocity performance was consistent with the calculated values of the inductance gradients.

INTRODUCTION

For the past several years the UTSI railgun research program has focused on understanding why plasma armature railguns have failed to achieve their expected velocity [1]. We have used a combined experimental and theoretical approach that has included: optical and electrical diagnostic measurements [2], 2-D and 3-D computational simulations of the plasma flow [3,4], 2-D and 3-D computational simulations of the electromagnetics [5,6], and quantitative experiments using a carefully prepared railgun which could be operated in conventional, separately augmented or muzzle-fed configurations [7,8].

Most of these quantitative experiments were performed in a 10-11 mm diameter round bore by 2.4 m long augmented railgun using both plasma and solid aluminum ring armatures. The results obtained with the conventional and augmented configurations led us to question the validity of simple, conventional methods for calculating the electromagnetic forces. Three-dimensional electromagnetic simulations of simple, square railgun configurations confirmed that the simple

1

force expressions based on inductance gradients overestimated the electromagnetic accelerating forces [5]. The railgun used in the experiments was designed for reliability and ease of assembly, but had relatively small values of self and mutual inductance gradients. A new railgun has been designed and fabricated with the same bore characteristics as the earlier railgun, but it has inductance gradients which are larger by approximately 50%. We have begun a series of experiments to compare the velocity performance of the new railgun with earlier experiments. Our goal is to determine whether the velocity performance scales linearly with inductance gradient as predicted by the simple electromagnetic force models. The results of our first experiments using the solid aluminum ring armatures will be described in this paper.

EXPERIMENTAL CONFIGURATION

The low inductance gradient (LIG) railgun used for our previous experiments consisted of a 10-11 mm diameter round bore railgun of 2.4 m length having copper rails and G-9 glass fiber reinforced melamine insulators. A second set of rails was included which could be connected at the muzzle to provide either a separately augmented [7] or a muzzle-fed [8] configuration. The rails were constructed from 2.54 cm wide copper bar stock for convenience of fabrication and assembly (Figure 1), but provided low values of self and mutual inductance gradients, 0.27 μH/m and 0.25 μH/m, respectively. The new high inductance gradient (HIG) railgun has the same bore diameter, length and materials, but the rails were fabricated from 1.27 cm wide bar stock to provide self and mutual induction gradients of 0.43 μH/m and 0.35 μH/m, respectively (Figure 2). For both railgun configurations, the values of the inductance gradients were determined from 2-D calculations using the finite element electromagnetic code, MEGA. Both railgun configurations were contained in G-10 material compressed in the same bolted aluminum V-block structure used by Hawke et al [1].

An integral 1 m long helium light gas gun was used to preaccelerate the projectiles into the railgun with approximately 825 m/s velocity. The ring armatures were right circular cylinders 15 mm in length with a mass of approximately 1.3 g. The cylindrical armatures were machined to a snug fit in the bore with a 1 mm wall thickness. A Lexan sabot was used to accelerate the armature and separate the driver gas from the ring (Figure 3). Two separate capacitor power supplies, each with 240 kJ energy storage capacity and separate inductors, were used to separately power the inner and outer rail pairs to provide either conventional railgun experiments or experiments using

2

a variable range of augmentation. A unique feature of these experiments was that the railgun and preaccelerator bore was lapped full length with an expandable iron lap and aluminum oxide compound before every experiment. After lapping, the bore was cleaned with kerosene and then flushed with filtered acetone and vacuum dried to provide a clean, uniform bore surface for every experiment. This procedure improved the quantitative comparison by eliminating uncertainties related to bore deterioration from previous shots.

Electrical diagnostic measurements consisted of rail and augmentor currents provided by integration of the digitized signals from Rogowski coils, and current transformers at the breech, muzzle and augmentor feed to measure the respective voltages. Rail B-dot probes spaced 100mm apart along the railgun were used to detect the time of passage of the projectile. Several additional B-dot probes were used to measure the primary component of the magnetic field (perpendicular to the axis and in the symmetry plane containing both insulators). A PIN photodiode placed in the flight range detected light emitted from the bore to determine the time of transition of the armature from solid to hybrid. A MAVIS magnetic transducer placed in the flight range recorded the time of passage of the armature to obtain an independent measure of muzzle velocity.

EXPERIMENTAL RESULTS

A similar series of experiments using the solid aluminum ring armatures were performed in both railguns. For all of the experiments discussed in this paper the nominal peak value of the armature current was set to 70 kA. The peak value of the augmentor current ranged from zero to 140 kA. The experimental conditions were kept as similar as possible for both railgun configurations, but since the gun inductance was larger for the new HIG railgun, the current pulse was somewhat longer. Also, since the velocities were generally higher in the HIG railgun, the exit times for the projectiles were earlier. There was no MAVIS data obtained for the HIG experiments, since a change in the configuration of the "duckbills" at the muzzle resulted in an asymmetric muzzle arc formation which deflected the projectile.

The currents for the conventional configuration (zero augmentor current) shots in the LIG and HIG railguns are shown in Figure 4. Note that the maximum current for the HIG gun is smaller and decays somewhat faster than for the LIG gun. This is due to the higher inductance and resistance of the HIG gun structure. The corresponding position-time data obtained from the rail B-dot probes for these conventional experiments are shown in Figure 5. The velocity

3

is greater in the HIG shot and the projectile exits the bore approximately 300 μs earlier. The corresponding velocity-time curves, obtained from a fourth order fit of the position-time data, are shown in Figure 6, together with the ideal velocity calculated from the simple force model,

$$F = \frac{1}{2} \left(L'I_1^2 + 2\alpha M'I_1I_2 \right) \tag{1}$$

where L' is the self inductance gradient, M' is the mutual inductance gradient, I_1 is the armature current and I_2 is the augmentor current. The factor α is a factor less than unity that accounts for a reduction in projectile force caused by the axial forces in the rails [5].

It is clear that the acceleration is greater for the HIG railgun, but the velocity profiles differ significantly from the predictions made using the simple force model of Equation 1. It appears that these differences are caused by the neglect of sliding friction. Three-dimensional MEGA calculations of the armature force for these conventional gun and armature configurations are smaller than the predictions of the simple model by less than 5%. Due to the open configuration of this armature design, it is impossible to develop any acceleration of the rings from a plasma armature. Furthermore, examination of the B-dot probe data and the photodiode data showed that no separate plasma armature formed during the LIG shots, although transition to a hybrid armature occurred after current maximum and prior to muzzle exit. Analysis of the B-dot probe data indicated that a trailing plasma armature formed prior to muzzle exit on the 100 kA and 140 kA augmented HIG experiments. Three-dimensional MEGA calculations were used to predict the signals that would be seen by the rail B-dot probes, and these indicated that the armature current was confined to a distance between 10 and 13 mm [9]. Therefore, it is probable that some of the differences between the experimental and theoretical velocity profiles can be attributed to sliding friction of the solid armature.

Some additional solid aluminum ring armature experiments were performed in the LIG railgun using a reduced entrance velocity. These experiments achieved less than half the momentum increase of the otherwise identical experiments. Crawford et al attributed this large difference in performance to a transition from dry friction to a lubricating liquid film [9].

The currents for the augmented LIG and HIG railguns with equal armature and augmentor peak currents (70 kA) are shown in Figure 7. The filled symbols are for the LIG experiment and the open symbols are for the HIG experiment. The diamonds represent the armature currents and the squares represent the augmentor currents. As in the conventional experiment, the currents

4

are smaller and decay faster in the HIG railgun. The corresponding velocity-time curves obtained from a fourth order fit of the B-dot position-time data are shown in Figure 8, together with the velocity predicted using Equation 1. The value of α used in Equation 1 to account for the axial forces which act on the rails of the railgun was chosen to be 0.85. The 0.85 fraction was a nominal value determined from 3-D MEGA simulations for an augmented square bore railgun configuration, and is consistent with values obtained by analysis of plasma armature experiments in the LIG railgun [10].

Comparison of the experimental and theoretical velocity in the LIG experiment clearly shows the influence of frictional drag. It appears that this armature did not transition to a lubricating liquid film until approximately 1 ms. After this transition the acceleration is similar to that predicted by Equation 1. Comparison of the experimental and theoretical velocity for the HIG experiment suggests an earlier transition to a lubricating film. The acceleration observed near the muzzle in the experiment is considerably larger than the prediction. This effect has often been observed in hybrid armatures and might be attributed to a loss of projectile mass.

DISCUSSION AND CONCLUSIONS

Our goal was to determine whether the velocity performance scaled linearly with inductance gradient. This can be done by relating the measured change in projectile momentum to the electromagnetic impulse calculated from the measured currents and Equation 1,

$$\Delta p = \frac{1}{2}L' \int_0^\tau I_1^2 dt + \alpha M' \int_0^\tau I_1 I_2 dt \tag{2}$$

where Δp is the measured change in momentum and τ is the time of muzzle exit. All frictional drag forces have been neglected in Equation 2. Using Equation 2, an experimental measure of the ratio of $L'H$ to $L'L$ is given by,

$$\frac{L'_H}{L'_L} = \frac{\Delta p_H}{\Delta p_L} \frac{A_L}{A_H} \tag{3}$$

where A is an effective action given by,

$$A = \int_0^\tau I_1^2 dt + 2\alpha \frac{M'}{L'} \int_0^\tau I_1 I_2 dt \ . \tag{4}$$

5

Application of this equation is straightforward in the case of the conventional railgun where I_2 is zero. For the augmented railgun cases, the MEGA calculated ratios of M'/L' and α were used to determine the effective action.

The performance results for both railguns are given in Table 1. Crawford et al provide details on the transition behavior of the circular armatures in a separate paper [9]. The table contains entries for the measured momentum increment, Δp and the effective action, A, defined by Equation 4. It also contains the measured ratio of the self inductance gradients as determined from Equation 3. For both the 100 kA and 140 kA augmented shots in the HIG railgun it appeared from the B-dot probes and the PIN photodiode that a plasma armature developed near the muzzle, so the data for these two experiments was analyzed only up to the time the armature transitioned from a hybrid to a plasma. The corresponding LIG data were truncated to the same times to provide a reasonable comparison.

The experimentally determined values of the self inductance ratio for the conventional and 70 kA augmented experiments were 1.98 and 2.23, respectively. These values significantly exceed the MEGA calculated ratio of 1.55. The experiments at 100 and 140 kA augmentation yield values of 1.45 and 1.44, respectively, and are somewhat lower than the MEGA values. In both of these latter experiments, the data were evaluated only over a portion of the total acceleration time.

Figures 6 and 8 may provide some explanation for the large values of the self inductance ratio observed in the conventional and 70 kA augmented shots. In both cases the observed velocity lags significantly behind the theoretical velocity in the LIG railgun. This suggests that the frictional drag of the armature is greater in the LIG railgun early in the acceleration profile. Since the influence of drag was not considered in deriving Equation 3, dissimilar drag forces can result in uncertainty in the determination of the inductance gradient ratio. Since the bore and projectile conditions were the same in the HIG and LIG railguns, the apparent reduction of frictional drag seen in the HIG railgun may have been the result of increased rail displacement. The reduced width and increased inductance gradient in the HIG railgun combine to increase the pressure on the rail by a factor of 3, and the G-10 backing may have allowed enough additional rail separation to reduce the frictional drag. In the higher augmentation cases, any dissimilarities in frictional drag are less significant because the larger electromagnetic forces dominate. Also, the stronger separation forces may have acted to reduce friction in the LIG railgun for the large augmentation experiments.

On the basis of the results of this limited set of experiments, it was not possible to determine whether the velocity performance scales linearly with inductance gradient as predicted by the simple electromagnetic force models. However, it was clear that the performance increase was of the same order as the increase in the calculated inductance gradient, and reaffirms the importance of careful electromagnetic design of the launcher structure. Because the influence of sliding friction appeared to be smaller in the experiments with large augmentation, the value of 1.45 is probably a reasonable experimental estimate of the self inductance gradient ratio, and is only 6.5% less than the MEGA calculated value of 1.55. Once again, with solid as well as plasma armatures, the inability to accurately quantify drag forces makes it difficult to determine electrical force parameters from from B-dot position-time records.

REFERENCES

1. R. Hawke, W. Nellis, G. Neuman, J. Rego, and A. Susoeff, "Summary of EM Launcher Experiments Performed at LLNL," 3rd Symposium on EM Launch Technology, Austin, Texas, April 1986.

2. D. Keefer, A. Sedghinasab, and R. Crawford, "Simultaneous In-Bore Rail and Insulator Spectra from a Railgun Plasma Armature," *IEEE Trans. Mag.*, Vol. 27, No. 1, pp. 217-219, January 1991.

3. R. Crawford, D. Keefer, and R. Tipton, "Velocity Limiting Magnetohydrodynamic Effects in Railgun Plasma Armatures," *IEEE Trans. Mag.*, Vol. 29, No. 1, pp. 781-786, January 1993.

4. D. Kondrashov and D. Keefer, "3-D Plasma Armature Simulations," 7th Symposium on EM Launch Technology, San Diego California, March 1994.

5. J. Taylor and D. Keefer, "Calculations of the Electromagnetic Force in Railguns," Proc. 9th IEEE Pulsed Power Conf., Albuquerque, New Mexico, June 21-23, 1993.

6. D. Keefer, R. Crawford, and J. Taylor, "Plasma Armature Studies in Augmented and Muzzle Fed Railguns," AIAA 93-3154, AIAA 24th Plasmadynamics and Lasers Conference, Orlando, Florida, July 6-9, 1993.

7. J. Taylor, R. Crawford, and D. Keefer, "Experimental Comparisons of Conventional and Transaugmented Railguns," *IEEE Trans. Mag.*, Vol. 29, No. 1, pp. 523-529, January 1993.

8. D. Keefer, R. Crawford, and J. Taylor, "Muzzle-Fed Railgun Experiments," Proc. 9th IEEE Pulsed Power Conf., Albuquerque, New Mexico, June 21-23, 1993.

9. R. Crawford, J. Taylor, and D. Keefer, "Solid Ring Armature Experiments in a Transaugmented Railgun," 7th Symposium on EM Launch Technology, San Diego California, March 1994.

10. J. Wise, "An Application of a Parameter Fitting Model to the University of Tennessee Space Institute Transaugmented Railgun," Master's Thesis, University of Tennessee Space Institute, December 1993.

TABLE 1. Performance results from conventional and augmented experiments in the LIG and HIG railguns.

Shot No.	I_1 kA	I_2 kA	m g	Δp kg - m/s	A 10^6A^2s	$\dfrac{L_H'}{L_L'}$
11993-H	72	0	1.14	0.98	5.46	
72393-L	74	0	1.18	0.65	7.15	1.98
112393-H	72	72	1.22	2.30	10.82	
72893-L	74	75	1.22	1.51	15.84	2.23
12393-H	68	102	1.19	1.59	8.23	
42993-L	71	106	1.28	1.20	8.98	1.45
121393-H	68	135	1.20	0.89	6.31	
6493-L	68	138	1.22	0.68	6.93	1.44
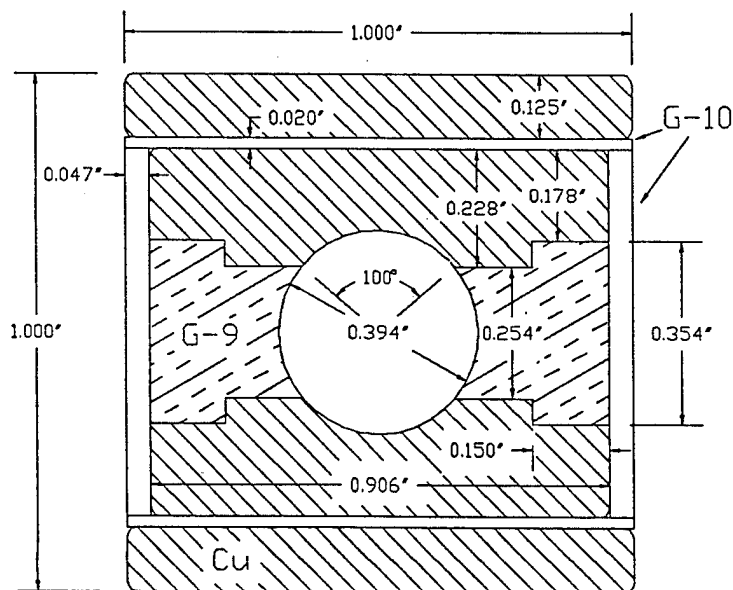
Figure 1. Cross section of the low inductance gradient railgun.
$L' = 0.274$ μH/m, $M' = 0.249$ μH/m.

9
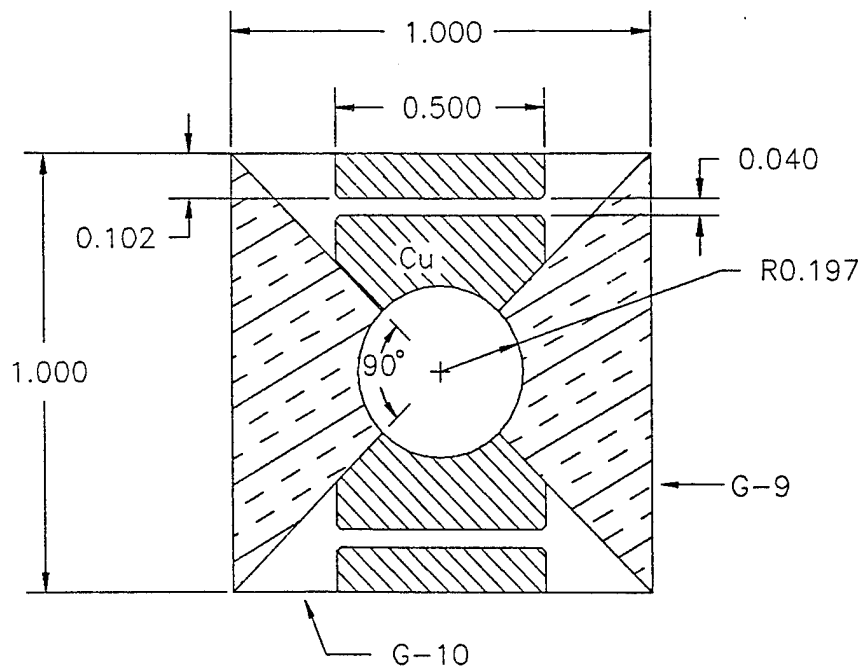
Figure 2. Cross section of the high inductance gradient railgun.
$L' = 0.425~\mu\text{H/m}$, $M' = 0.35~\mu\text{H/m}$.
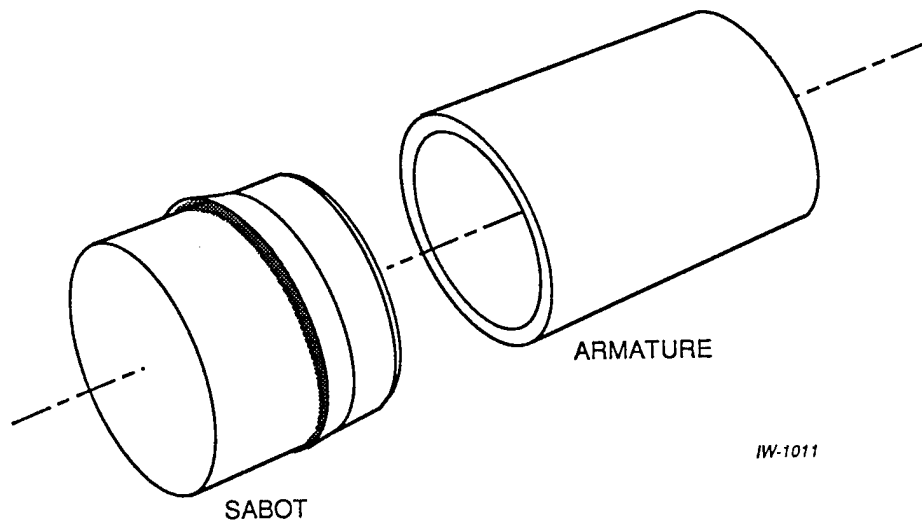
Figure 3. Sketch of the ring armature and sabot.

10
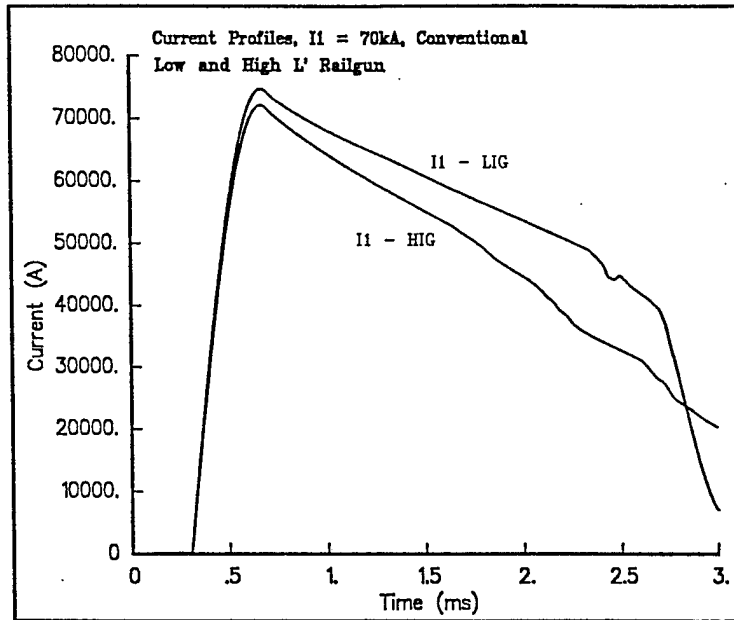
Figure 4. Current profiles for conventional railgun experiments
in the LIG and HIG railguns.
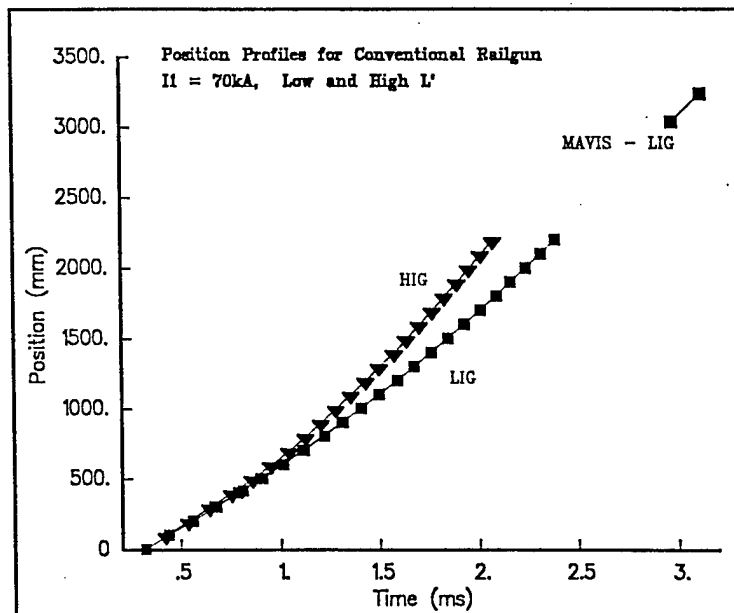
Figure 5. Position-time data for conventional railgun experiments
in the LIG and HIG railguns. Obtained from rail B-dot probes.

11
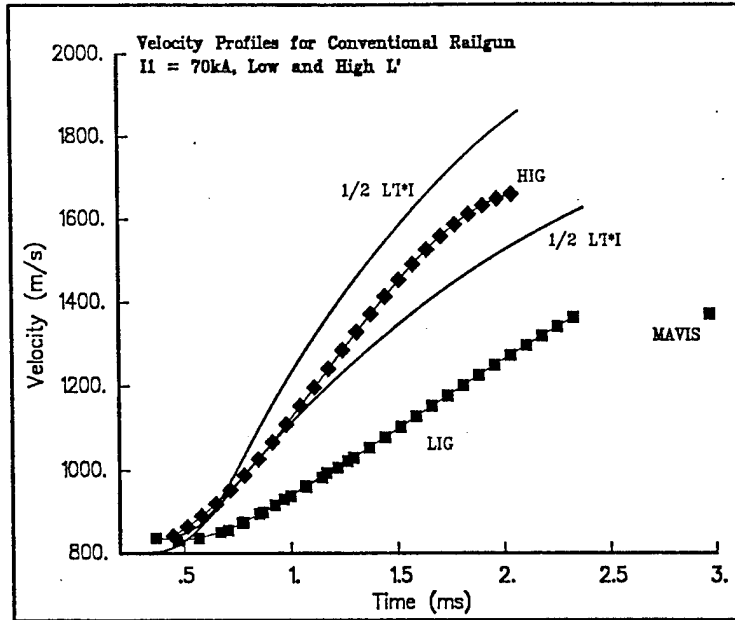
Figure 6. Velocity-time curves for the conventional LIG and HIG railgun experiments obtained from fitting of the position-time data and from Equation 1.
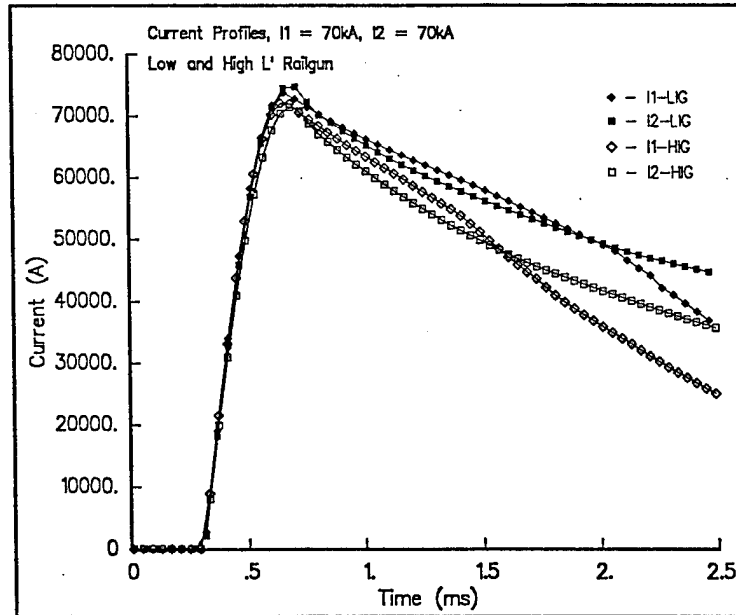
Figure 7. Current profiles for augmented railgun experiments in the LIG and HIG railguns. Closed symbols are for LIG and open symbols are for HIG. The diamonds are the armature currents and the squares are the augmentor currents.

12

Velocity Profiles for Transaugmented Railgun
I1 = 70kA, I2 = 70kA, Low and High L'
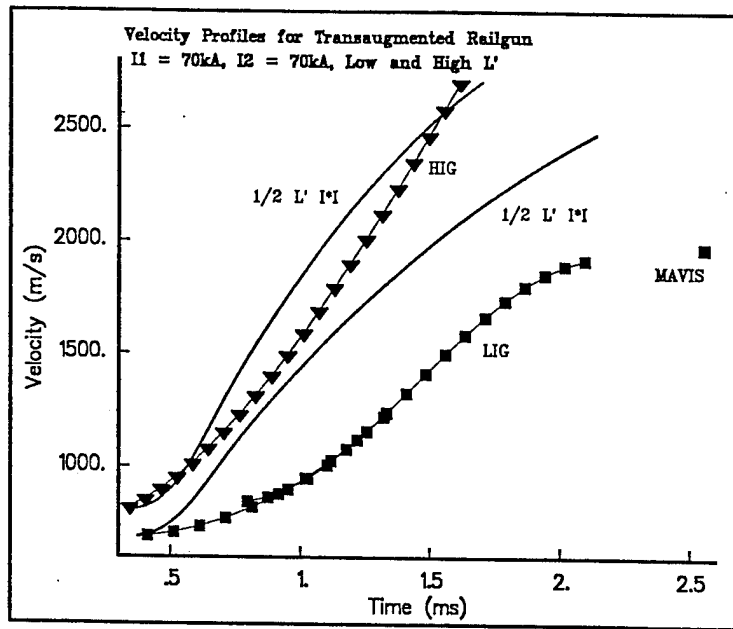
Figure 8. Velocity-time curves for the augmented LIG and HIG railgun
experiments obtained from fitting of the position-time data and from Equation 1.

13

Solid Ring Armature Experiments in a Transaugmented Railgun

Roger Crawford, Jaime Taylor and Dennis Keefer

Center for Laser Applications
University of Tennessee Space Institute
Tullahoma, TN 37388

Abstract - The UTSI 2.4 m long, 11 mm diameter, transaugmented (separately augmented) railgun was used to accelerate solid aluminum ring armatures to velocities up to 3 km/s. The armature consisted of a 15 mm long aluminum tube with a tapered nose and wall thickness of 1 mm. The 1.2 to 1.3 gm armatures were tested in a series of both conventional and augmented experiments to evaluate performance, transition velocity and transition action. Precise transition location was determined by correlation of muzzle voltage and the armature light emission measured by a PIN diode looking down the muzzle. The electromagnetic forces in this armature were determined using the MEGA 3-D finite element code. The ring armature produces a magnetic squeeze in the insulator plane which, because of the high compliance of the thin ring, loads the ring against the rails to increase the contact force. Augmentation increases the contact force and increases the transition velocity. This armature configuration may have application in all velocity ranges since it appears to operate as a true hybrid after transition with no plasma armature formation.

I. INTRODUCTION

A continuing research program at the University of Tennessee Space Institute has contributed significantly to the understanding of railgun operational physics. Advanced diagnostics instrumentation techniques have been applied to further understanding of both plasma and hybrid armatures in both conventional and augmented railguns. The continuing stability and performance problems associated with plasma armatures lead to research on hybrid armatures. The performance benefits demonstrated with hybrid metal armatures focused research efforts on solid metal armature configurations which can operate in a metal to metal contact mode to high velocity thus reducing bore damage and providing high electromagnetic efficiency. A controlled transition to hybrid armature operation on plasma brushes may allow the solid to hybrid transition armature to consistently reach high velocity with better performance than plasma armatures. Thus, UTSI initiated a solid armature investigation with both experimental and analytical techniques to understand solid to hybrid armature transition physics.

II. OBJECTIVES

An extensive review of solid armature experimental data shows a consistent failure of metal to metal contact at relatively low velocity around one kilometers/second. Very limited metal to metal armature data exists above two kilometers/second. A unique solid armature configuration was selected for the UTSI investigation based on three-dimensional electromagnetic analysis. The armature design requirements included minimizing velocity skin effects, maximizing useable action in the metal, and improving loading (normal) forces against the rail. A thin metal ring armature was selected for an investigation of transition. Armature action at transition, velocity at transition and total electromagnetic efficiency were evaluated in a separately augmented (transaugmented) railgun, where the effects of velocity can be separated from action. A more complete understanding of armature transition velocity was the primary objective of this investigation. Performance evaluation of the ring armature in a hybrid mode was a secondary objective.

III. RING ARMATURE DESIGN

The design requirements for a solid metal armature are listed below:

- Low voltage sliding contact
- Low total armature mass
- Maximum electrical action at transition (high transition velocity)
- Compatibility of armature with launch package/sabot
- Efficient operation as a hybrid after transition

Each of the design requirements will be discussed briefly and the design approach outlined. Low voltage sliding contact requires a high conductivity armature material in high pressure sliding contact with the rail. Copper and aluminum are candidate materials. The minimum armature mass supports selection of aluminum or aluminum-copper combinations. Maximum electrical action is obtained with a combination of high electrical conductivity and high energy capacity to melt. In this study we evaluated only aluminum armatures operating on copper rails. Since molten aluminum wets copper these armatures leave significant aluminum films on the rails. Attempts to optimize materials were not included in this investigation.

Compatibility of the metal armature with a launch package sabot must be considered. The ring armature can

be split into two cylinders which will separate with the projectile sabot. Thus, the ring armature configuration satisfies the design requirements and should operate as a thin plasma brush hybrid after transition.

The physical dimensions were determined by a minimum length criterion for stability in the bore and by a minimum wall thickness determined from material allowable electrical action. Criteria from Reference 5 were used to determine the minimum armature cross-sectional area for the expected electrical action.

$$A = \left[\int_{t1}^{t2} \frac{I^2(t) \; dt}{g_1}\right]^{1/2}$$

where $g_1 = 27 \times 10^{15} \; A^2 - s/m^4$ for aluminum.

An average current of 100 kA for a duration of $2 \times 10^{-3} s$ was used to calculate minimum action area for the aluminum ring armature. Substituting into the expression for A yields: $A = 0.27 \; cm^2$. The ring armature length was set at 15 mm with a 4 mm nose taper and an 11 mm cylindrical section. A one millimeter wall thickness yields a cross-section area of 0.22 cm² for the cylindrical section which would be in contact with the rails. Since the UTSI railgun is a capacitor-inductor driven gun, a 100 kA peak current shot will have an average current below 90 kA for a 2 ms pulse. Thus, the 0.22 cm² area for a 1.0 mm wall thickness will assure the armature action remains below the limit set by g_1, which is an 80% melt temperature value.

Figure 1 shows the dimensions of the aluminum ring armatures used in this investigation. The UTSI railgun barrel is lapped before each shot to insure high bore quality. Thus, the outer diameter of the armature was increased approximately 0.025 mm each shot to assure a slight interference fit. The armature wall thickness was maintained at 1.0 mm. A 10 mm long polycarbonate pusher and light gas gun was used to accelerate the ring armature into the railgun at velocities from 500 to 900 m/s.
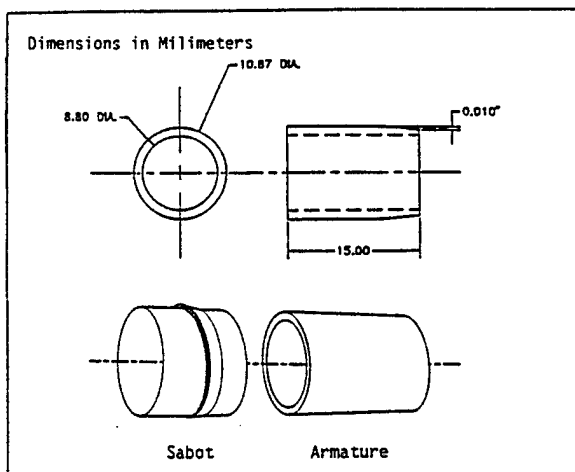
Figure 1. Ring Armature Design.

The three-dimensional finite element electrodynamics code MEGA was used to evaluate the ring armature [6]. Interaction between the ring armature current distribution and the rail plus armature magnetic fields produce compressive forces on the insulator facing portion of the ring. The compliant ring structure allows the compressive forces to be reacted by rail normal force. If the gun structure was rigid, increased rail currents would result in higher armature/rail contact forces. See Figure 2 for the force vector distribution near the rear of the armature. Since any separation of the rails due to electromagnetic forces will reduce the armature/rail normal force, inertial loading of a split ring armature may be required to assure good sliding contact. For the 70 kA armature currents the rail/armature electromagnetic reaction force is approximately 20 Newtons.
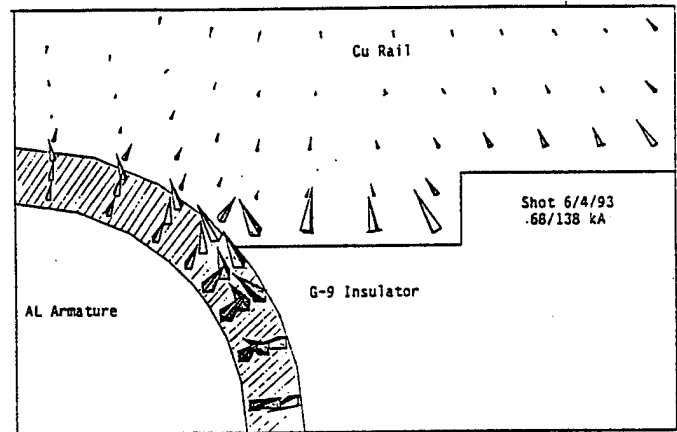

Figure 2. Electromagnetic Armature/Rail Contact Forces.

IV. EXPERIMENTAL INVESTIGATION

The ring aluminum armature experimental investigation was conducted at the UTSI railgun facility. The augmented railgun can be operated in either a conventional or augmented mode utilizing separate power supplies. The 2.4 m long railgun with a nominal 10 mm bore diameter is connected to a 1.1 m single stage helium gas injector. The design features copper rails and G-9 insulators supported by a G-10 substructure. For a more complete description of the railgun facility including diagnostic instrumentation see References 1 and 7.

Projectile velocity and armature current distribution were determined from thirty B-dot probe signals measuring both changing rail current and rate of change of the primary driving field (Z-axis). These probes are located 100 mm apart and provide accurate armature position data from which velocity was determined. Injection velocity into the railgun was measured by two high response pressure transducers located at the exit of the helium accelerator. A MAVIS electromagnetic transducer located in the flight range was used to provide accurate muzzle velocity measurement and confirm B-dot derived velocity [8].

Since determination of armature transition position and velocity was an important new requirement, a PIN diode was located in the flight range, behind MAVIS, looking down the barrel. The light emission from the transition arcs can be compared with the muzzle voltage record to determine armature transition. This is an important diagnostic because the muzzle voltage on augmented shots contains strong induced voltages from the transient augmenting field. Figure 3 shows the correlation between a PIN diode signal and muzzle voltage for a conventional shot. Note the intermittent 20 volt jumps in muzzle voltage corresponding to the initial rise in emitted light from the bore. This initial transition signal is associated with arcing on one rail surface, and as the emission signal increases another 20 volt intermittent jump in muzzle voltage occurs corresponding to a second arcing contact. Some dynamic solid armature contact is noted for most of the hybrid plasma brush mode. Both muzzle voltage records and PIN diode signals were used to determine transition in all experiments where data was acquired.
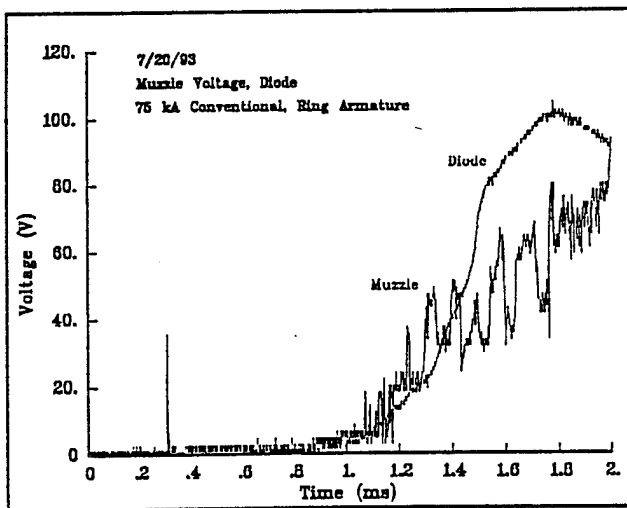
Figure 3. Transition Data Example.

A nine shot test matrix was completed in this investigation. Three conventional and four augmented experiments were conducted at high injection velocity (734 to 882 m/s) with nominal peak bore currents of 70 kA (68-76). Peak augmenting currents ranged from 75 to 140 kA on the four augmented shots. These seven experiments produced muzzle velocities from 1,368 to 2,994 m/s which provided transition velocities of 1,030 m/s to 1,575 m/s. The last two experiments were conducted at reduced injection velocity (570 and 590 m/s) to evaluate the influence on transition position and action. Table I below contains the significant performance data from the nine shots.

Table I.   Ring Armature Performance Data

Shot Date	Arm I 1(kA) Peak	Aug I2 (kA) Peak	Mass (gm)	Entr Vel (km/s)	Muzz Vel (km/s)	Delta V Exp (km/s)	Delta V Elect (km/s)	Efficient Exp/Elec %
7/20/93	76	0	1.18	0.882	1.471	0.589	0.886	66
7/23/93	74	0	1.18	0.798	1.368	0.570	0.830	69
7/28/93	74	75	1.22	0.734	1.969	1.235	1.782	69
4/29/93*	71	106	1.28	0.851	2.354	1.503	1.364	110
6/ 4/93	68	138	1.22	0.807	2.994	2.187	1.979	110
6/ 9/93	71	140	1.30	0.770	2.650	1.880	1.961	96
9/17/93	75	0	1.35	0.825	1.382	0.557	0.735	76
9/30/93	74	0	1.35	0.570	0.822	0.303	1.070	28
10/ 6/93	74	0	1.44	0.590	0.931	0.341	0.919	37

*Augmentor Power Supply - Crowbar Failure - Ringing Current

Since all shots have a nominal armature current of 70 kA peak current, the muzzle velocity differences result primarily from augmentor current level and injection velocity differences. Armature drag is the only loss mechanism proposed for these experiments other than electromagnetic losses which would reduce the effective values of L' and M'.

The theoretical incremental velocity increase (electromagnetic) was determined from the following force expression integrated over the time of electromagnetic acceleration.

$$FORCE = \frac{1}{2} L' I_1^2 + \alpha M' I_1 I_2$$

The following values of L', M' and α were determined from two and three dimensional MEGA analysis [9]. The correction factor α accounts for the axial force lost in the rails.

$$L' = 0.274 \, \mu \, H/m \qquad M' = 0.249 \, \mu \, H/m \qquad \alpha = 0.85$$

The efficiency variation from the nine experiments demonstrated reasonable repeatability on the duplicate experiments. The higher efficiencies obtained at the 100 kA - 140 kA augmentor currents have not been completely explained, but may result from α dependence on velocity or friction force reduction at higher velocity.

The last two shots at low injection velocity exhibited a significant loss in efficiency which can only be the result of much higher armature drag. The significance of these two low performance experiments will be discussed in the next section.

V. TRANSITION RESULTS

Transition data was obtained on eight of the nine ring armature shots. The 4/29/93 augmented shot experienced a failure of the augmentor power supply crowbar switch which produced a ringing augmentor current and obscured transition on the muzzle voltage record. These

eight shots represent four different sets of test conditions. In the cases where two or three repeat data sets were obtained the transition results were repeatable with a mean deviation of approximately 10%.

Before presenting and discussing the transition data, the experimental results from high velocity shot 6/4/93 will be reviewed. This shot had a peak armature current of 68 kA as shown in Figure 4. Position-time data for the rail and Z-axis B-dot probes is presented in Figure 5 along with the MAVIS record. Curve fitting and differentiating the B-dot position-time data yields a velocity-time record, Figure 6. The predicted velocity calculated from the experimental current records and L', M', α from section IV is also shown on Figure 6. The experimental velocity deficit early in the drive and higher acceleration in the later part of the drive were typical for this set of experiments. Reference 7 attempts to explain this difference in theoretical and experimental acceleration.

Figure 6.   6/4/93 Experimental and Theoretical Velocity-Time.

The muzzle voltage record shows the initial transition at approximately 1.0 ms followed by both side plasma brushes by 1.2 ms and muzzle exit at 1.66 ms (Figure 7). PIN diode data was not obtained for this shot. Rail B-dot data for seven probes near the muzzle shows the compact nature of armature current (Figure 8). Details of the B-dot 19 record is compared with a MEGA B-dot simulation of 1.0 and 1.5 cm long ring armatures in Figure 9. The correlation between the experimental B-dot 19 curve and the 1.5 cm armature calculations supports the conclusion that the entire armature is carrying current as a true hybrid after transition. Data from shot 6/4/93 supports the potential of the ring armature design for good high velocity transition and operation.

Figure 4.   6/4/93 Current-Time Data.
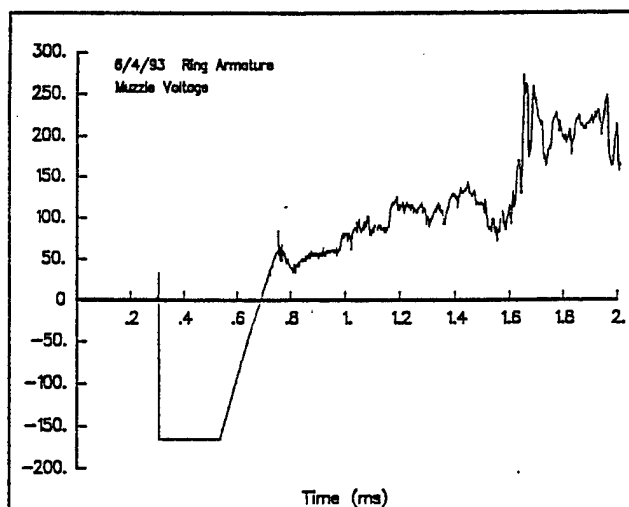
Figure 7.   6/4/93 Muzzle Voltage Data.

Figure 5.   6/4/93 Position-Time B-Dot Data.
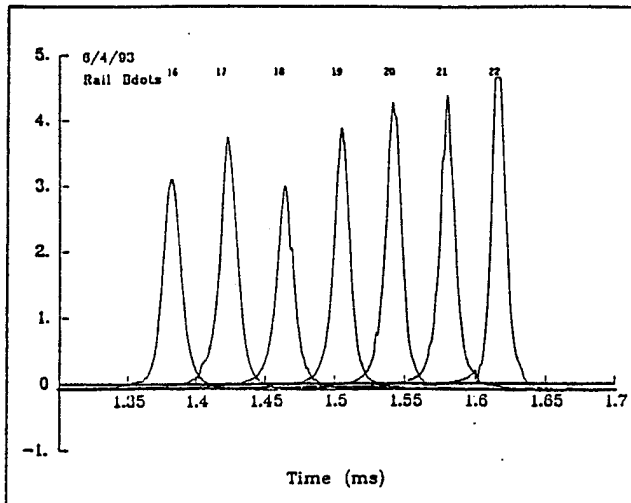
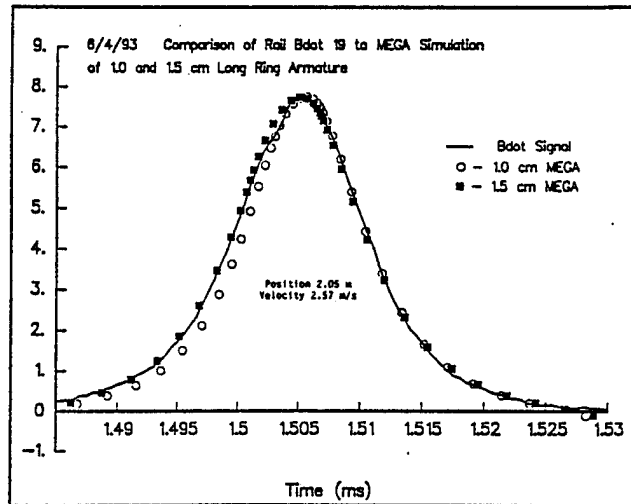Figure 8. 6/4/93 B-Dot Data Near Muzzle.

Figure 9. 6/4/93 B-Dot 19 Data-MEGA Calculations.

Table II presents the transition data for the eight experiments. The initial goal was to obtain transition at increasing velocity using augmentation so that armature current could be held constant.

Table II.   Ring Armature Transition Data

Shot Date	Peak (kA) I1/I2	Entr Vel (km/s)	Muzz Vel (km/s)	Trans Vel (km/s)	Trans Posit (m)	Trans Time (ms)	Trans Curr (kA)	Trans Action $(A^2 \cdot s)$
7/20/93	76/0	0.882	1.471	1.038	0.777	1.15	67	3.50E6
7/23/93	74/0	0.798	1.368	1.048	0.947	1.35	62	4.12E6
7/28/93	74/75	0.734	1.969	1.279	0.908	1.37	60	4.12E6
4/29/93	71/106	0.851	2.354	*	*	*	*	*
6/ 4/93	68/138	0.807	2.994	1.575	0.735	0.98	62	2.21E6
6/ 9/93	71/140	0.770	2.650	1.454	0.715	0.93	65	2.14E6
9/17/93	75/0	0.825	1.382	1.030	0.799	1.17	65	3.48E6
9/30/93	74/0	0.570	0.822	0.711	1.426	2.67	52	8.29E6
10/ 6/93	74/0	0.590	0.931	0.823	1.372	2.38	54	7.39E6

*Transition Not Measured/Observed

For an approximately constant injection velocity and armature current the muzzle velocity and transition velocity both increased with augmentor current. The transition position and time of transition did not show consistent trends except for the highest velocity shots which transitioned earlier in both position and time. There was also a 50 percent reduction in transition action at the highest velocities.

The lack of clear velocity influence on transition and previous work [10] which indicated that transition was independent of velocity lead to the last two experiments in Table II. Injection velocity was reduced by increasing the mass of the sabot. The results of shot 9/30/93 were so significant that a repeat shot 10/6/93 was conducted for confirmation. The injection velocities of 570 to 590 m/s and armature current of 74 kA produced very poor acceleration and efficiency (Table I). Transition velocities were very low while transition time, position and action were significantly increased. Clearly the reduced injection velocity shots experienced a large increase in drag losses as shown in Figure 10. The velocity-time records for the two low injection velocity shots are compared with shot 9/17/93, all at nominal 74 kA. The very low efficiency confirms high drag forces over most of the acceleration. Only the difference between dry sliding friction and liquid film drag could explain the large performance loss of the lower injection velocity shots. Thus, high velocity solid contact requires a very thin molten armature layer to promote low voltage contact and modest viscous drag.
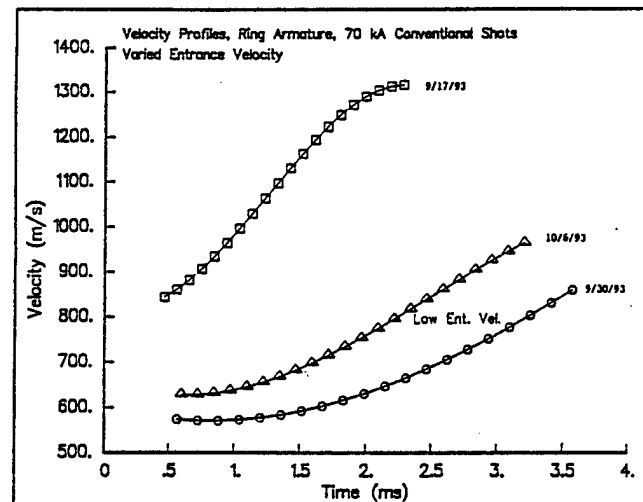

Figure 10.   High and Low Injection Velocity Comparison.

This thin molten layer makes the solid armature efficient and results in transition when the layer can not be maintained. Failure to maintain sufficient normal contact force would remove the frictional energy necessary to provide a liquid contact layer resulting in transition.

VI. CONCLUSIONS

The value of the separately augmented railgun as a research tool has been reconfirmed. The ability to vary injection velocity, armature current and primary magnetic field independently has provided a new set of transition data which can be used to question existing transition models and develop new theories. The transition physics from this investigation was not independent of velocity. However, two independent velocity related effects were contained in the data set. Velocity increase caused by increased augmentor current resulted in higher rail separation forces which certainly caused earlier transition. Data from Reference 7 on high and low L' gun configurations supports this conclusion. The second velocity related transition effect was noted in the low injection velocity shots. Below the velocity where combined friction and contact resistance produce a liquid contact boundary layer, significantly more electrical action can be deposited in the armature before transition. Thus, the nature of frictional loss at the armature interface must be included in the transition model.

Solid armature transition is a complex process that occurs in the thin (the order of roughness height) high velocity contact layer where both friction (viscous) and electrical resistance cause large energy dissipation and material phase change. At relative velocities above 700 m/s aluminum armatures are running on a very thin molten film, which is clearly observed on the copper rails. Velocity, normal force and current density all influence the nature of the liquid contact layer. Failure to maintain a thin contact layer results in arcing and transition.

The one solid armature experimental variable that could not be controlled in this investigation was armature-rail normal force. High contact forces have been demonstrated as essential to maintain low voltage contact and increase transition velocity [10]. The ring armatures in this investigation had only a small interference pre-load and modest electromagnetic normal force. At high augmentor current levels rail separation forces would have significantly reduced armature contact forces and may have dominated transition.

The ring armature configuration has good potential for a high velocity solid-transitioning-hybrid armature because the thin ring reduces the velocity skin effect due to temperature dependent conductivity and improved magnetic field penetration. Future work with the ring armature concept should include inertial loading to assure high rail contact forces. Also, new materials with composite conductivity, energy capacity and strength properties should be considered for improving transition velocity.

REFERENCES

[1] J. Taylor, R. Crawford and D. Keefer, "Experimental Comparison of Conventional and Trans-Augmented Railguns," *IEEE Trans. on Magnetics*, Vol. 29, No. 1, pp. 523-529, January 1993.

[2] R. Crawford, D. Keefer and A. Sedghinasab, "Railgun Hybrid Armatures, Experimental Results and Performance Characteristics," *IEEE Trans. on Magnetics*, Vol. 27, No. 1, pp. 240-244, January 1991.

[3] M. Cowan, "Solid-Armature Railguns Without the Velocity-Skin Effect," *IEEE Trans. on Magnetics*, Vol. 29, No. 1, pp. 385-390, January 1993.

[4] N. Colon, L. Tran, K. Luu, L. Paul, D. Chang and D. Sink, "High Transition Velocities for Solid Armatures in the 10-mm MTR Railgun," *IEEE Trans. on Magnetics*, Vol. 29, No. 1, pp. 775-780, January 1993.

[5] J. Garner, A. Zielinski and K.A. Jamison, "Design and Testing of a Mass-Stabilized Projectile for Small Caliber Electromagnetic Launcher," *IEEE Trans. on Magnetics*, Vol. 25, No. 1, pp. 197-202, January 1989.

[6] D. Rodger and P.J. Leonard, "Modelling the Electromagnetic Performance of Moving Railgun Launches Using Finite Elements," *IEEE Trans. on Magnetics*, Vol. 29, No. 1, pp. 496-498, January 1993.

[7] D. Keefer, R. Crawford and J. Taylor, "Effect of the Inductance Gradients in a Transaugmented Railgun," 7th EMC Symposium, April 1994, San Diego, CA.

[8] J.V. Parker, "Magnetic-Probe Diagnostics for Railgun Plasma Armatures," *IEEE Trans. on Plasma Science*, Vol. 17, No. 3, pp. 487-500, June 1989.

[9] J. Taylor and D. Keefer, "Calculations of the Electromagnetic Force in Railguns," Proceedings of the Ninth IEEE Pulsed Power Conference, June 1993, Albuquerque, NM.

[10] J. Barber and A. Challita, "Velocity Effects on Metal Armature Contact Transition," *IEEE Trans. on Magnetics*, Vol. 29, No. 1, pp. 733-738, January 1993.

MUZZLE-FED RAILGUN EXPERIMENTS
WITH 3-D ELECTROMAGNETIC SIMULATIONS

Jaime Taylor, Roger Crawford, and Dennis Keefer
University of Tennessee Space Institute
Center for Laser Applications
Tullahoma, TN 37388-8897
USA

ABSTRACT

The UTSI 2.4 m transaugmented railgun was reconfigured so that current was fed from the breech to the muzzle along the outer rails and then returned to the armature along the inner rails. Experiments were performed using plasma armatures at peak currents of 70 and 100 kA. At a peak current of 100 kA the measured increase in projectile velocity was approximately 500 m/s; less than half of that obtained from a conventional configuration in the same railgun, and considerably less than predicted for the muzzle-fed configuration. B-dot probes showed that the armature was very compact, but separated from the projectile soon after fusing. Three-dimensional (3-D) finite element electromagnetic simulations on the UTSI railgun structure showed that the electromagnetic force on the armature was much less than predicted by the simple force model. The reduction in force was due primarily to axial forces exerted in the rails.

INTRODUCTION

The muzzle-fed configuration, reportedly first operated in the former Soviet Union, is a railgun in which the current is fed into the breech to the muzzle, then returned to the armature via the muzzle. Figure 1 shows a circuit diagram for the muzzle-fed configuration. The driving force in a muzzle-fed railgun is supplied by the augmenting rail behind the armature. In front of the armature the field produced by the inner rails is mostly cancelled, depending on the coupling between the augmenting and inner rails, by the field produced by the augmenting rails. Extending the circuit analysis used to predict the driving force in augmented railguns to the muzzle-fed configuration, the electromagnetic force for the muzzle-fed case was obtained as,

$$F = \frac{1}{2}M'I^2 + \frac{1}{2}\left(M' - L'\right)I^2 \ . \tag{1}$$

Written in this form it is easy to see that as the rails become more coupled and the value of M' approaches that of L', Equation 1 approaches the force equation for a conventional railgun,

$1/2L'I^2$, with M' replacing L'. The first expression in Equation 1 is the force due to the magnetic field produced by the augmenting rail behind the armature and the second expression demonstrates the field cancellation in front of the armature.

In this configuration the armature moves into regions of the rail where the field has already diffused. Cowan suggested that this would eliminate the high current densities produced at the rear of solid armatures by the velocity skin effect [1]. Our further speculation was that for plasma armatures the impedance path for secondaries would increase in this configuration, and this might delay or prevent their formation.

Muzzle-fed railgun experiments were performed at UTSI with the same bore conditions as used for the UTSI transaugmented railgun experiments [2,3]. Results of these experiments will be presented. 3-D electromagnetic simulations were performed using MEGA, a finite element code, developed at the University of Bath [4]. These simulations, performed on the UTSI railgun structure (Figure 2), were used to help analyze the experiments and explain the decidedly poor performance of the muzzle-fed railgun.

UTSI RAILGUN FACILITY

The UTSI 2.4 m long, 1.0 cm round bore, transaugmented railgun was converted to a muzzle feed configuration. A 1.1 m single stage helium gas injector provided pre-acceleration of projectiles into the railgun with a velocity of approximately 1 km/s. The rails were powered by two 240 kJ capacitor discharge power supplies each of which were connected through separate, four sectored, toroidal inductors. The Lexan projectiles of 1 gm mass utilized lip seals and were initiated with an aluminum foil fuse.

Twenty-three B-dot probes, located 100 mm apart, measured changing rail current and were used to obtain accurate armature positions. A MAVIS electromagnetic transducer, placed in the enclosed flight range, was used to provide an accurate time-of-flight measurement of projectile velocity. Consistent bore quality was assured for each experiment by lapping the entire railgun from the light gas gun to the muzzle before each shot using an expandable iron lap. After lapping, acetone was circulated through the bore and dried under vacuum to remove all traces of lapping compound and hydrocarbon residue. This procedure was found to eliminate secondary arcs and provide repeatable performance of our gun. Details associated with the structure, instrumentation and experimental procedure of our railgun can be found in References 2 and 3.

2

Values of L', the self inductance per unit length, and M', the mutual inductance per unit length, were needed for performance evaluations. These values were obtained from a 2-D calculation using the MEGA code for the cross section of our gun (Figure 2) at a frequency of 10 kHz. The value of 0.274 μH/m was obtained for L' and a value of 0.249 μH/m was obtained for M'.

EXPERIMENTAL INVESTIGATION

Four experiments were performed on the muzzle-fed railgun, one at a peak current of 70 kA and three at a peak current of 100 kA. The experimental results are given in Table 1, together with results for similar experiments in the conventional configuration for comparison. The increase in velocity for the 100 kA muzzle-fed experiments achieved less than 50% of the expected change in velocity calculated from Equation 1. This was even more significant than it appears, since most of the acceleration seen in the experiment could be accounted for by thermal forces exerted during the fusing transient. Since the initial experimental results differed so much from prediction, three experiments were performed at 100 kA to establish repeatability.

The B-dot signals indicated a compact well-formed plasma armature with no evidence of secondary formation. Figure 3 shows the armature velocity obtained from the B-dot probes, together with the exit velocity obtained from MAVIS, notice the severe primary separation. Results for a similar experiment in the conventional railgun configuration are also shown in Figure 3 for comparison. The armature velocity scarcely exceeds the initial velocity. It is likely that most of the increase in projectile velocity is due to the electrothermal "kick" which accompanies the fusing transient.

Equation 1 can be rearranged in the form $1/2 L'_{\text{eff}} I^2$ where L'_{eff} has the value, obtained from L' and M', of 0.224 μH/m. This is 82% of the value of L'. From the simple electromagnetic force models the force for the muzzle-fed shots should have been 82% of that for the conventional shots. However, as can be seen in Table 1 and Figure 3, the change in velocity measured for the muzzle-fed configuration was less than half of that measured for the conventional case. There were no secondary arcs or other anomolous effects observed in the armature, so where did the excess force go? We conducted some 3-D electrodynamic simulations using MEGA to help formulate an answer to this question.

3-D ELECTROMAGNETIC SIMULATIONS

The 3-D finite element code MEGA was used to simulate the UTSI muzzle-fed railgun. Previously, simulations were performed on a generic square bore railgun to provide initial insight. Details of the generic simulations can be found in References 5 and 6.

The simulation model consisted of the UTSI railgun cross section, a 0.5 cm long solid armature, and a rail section of 5.5 cm. At the ends of the rails a tangent magnetic flux boundary condition was used. This condition basically assumed the B field had reached its 2-D limit at 2.0 cm from the armature. The fields do not actually reach this limit until nearly 3 times that distance from the armature. Simulations with longer rail lengths were performed and it was found this approximation affected the armature force by less than 2%.

A Helmholtz step input current with an amplitude of 100 kA was used along with an armature velocity of 1000 m/s. Copper was used for both the rails and the armature. Once quasi-steady-state was reached (i.e. the field had diffused through the armature), the armature force should have been very similar to that of a plasma armature.

Using MEGA, the axial component of the $\mathbf{J}\mathbf{x}\mathbf{B}$ force was integrated over the armature and then over the total computational domain. Figure 4 shows the axial force in the armature and the total axial force for an armature velocity of 1 km/s, together with the force predicted by Equation 1. The field diffused into the structure reaching a quasi-steady-state in approximately 800 μs. Note that the effective value of L' decreased in time as the fields diffuse into the structure. This was opposite the effect observed for the conventional railgun [5]. The force exerted on the armature was 59% of the force predicted by Equation 1 evaluated at early time (i.e. a time corresponding to the values of L' and M' used in experimental performance evaluation).

The difference in the axial force on the armature and Equation 1 resulted from force exerted in the rails, 72% of which was found behind or above the armature. The magnetic field produced by the current in the outer rail diffused into the inner rail prior to the arrival of the armature. A large eddy current formed in the rail behind the armature (Figure 5), and the transverse component of this current interacted with the magnetic field from the outer rail to produce the large axial rail force. Figure 5 is in the plane of symmetry between the insulators. The shaded region represents the curvature of the round bore.

4

A simulation with the actual experimental current profile was performed to determine if dI/dt played a significant role in the armature force. The results of this simulation can be seen in Figure 6 along with the velocity predicted by Equation 1 and 60% of Equation 1. The factor of 60% comes from the armature force at quasi-steady-state being 60% of that predicted by Equation 1. The MEGA simulation with the experimental current profile compares well with the modification of Equation 1.

It should be pointed out that these electromagnetic velocity predictions do not take into consideration the fusing transient, viscous drag, etc. At the current level which the muzzle-fed railgun shots were performed, the fusing transient was quite significant and could have accounted for all the projectile acceleration. The effects of primary separation were not taken into consideration and could possibly explain the remaining discrepancy between predicted velocity and experimental velocity.

Figure 7 shows the force distribution in the armature and the rails for the muzzle-fed case. In front of the armature the axial force was negative due to the fact that the B generated by the outer rails in front of the armature does not entirely cancel out the B generated by the inner rail there (Figure 1). In a conventional railgun there is a negative axial force in front of the armature due to the self field of the armature and a velocity induced eddy current flowing ahead of the armature. For the conventional case, the negative axial force is quite small and limited to a small fraction of the armature. In the muzzle-fed case, nearly half the armature experiences a negative axial force. The significant difference in force distribution in the armature between the conventional and muzzle-fed case might have played a role in the fluid flow in the armature and contributed to early primary separation.

It was suggested by Cowan [1] that the muzzle-fed configuration could reduce the velocity skin effect. Looking back at the generic square bore railgun simulations [5,6], the current distribution for the muzzle-fed configuration with an armature velocity of 1 km/s was more uniform than for the conventional case (Figure 8). The peak current density in the armature of the muzzle-fed case was approximately half that seen in the conventional case, and appeared in the rear of the armature for both cases. For the generic model used in this simulation, one would have to approximately double the total current in the muzzle-fed case to achieve the same driving force as in the conventional case, thus eliminating any advantages gained.

5

SUMMARY

Plasma armature experiments in a muzzle-fed railgun have shown significantly poorer performance than a conventional railgun with the same bore structure. The 3-D MEGA simulations for the muzzle-fed railgun have shown that the simple force model overestimates the armature force by nearly a factor of two. A significant fraction of the available force predicted by Equation 1 acts to produce an axial force in the rails. By identifying the inadequacy of the simple force model, we have accounted for a large fraction of the velocity deficit that might otherwise have been attributed to fluid mechanical drag effects. The explanation for the remaining experimental velocity deficit is most likely associated with primary separation. The muzzle-fed configuration has been found to be of no practical interest for electromagnetic launchers. However, as with the transaugmented railgun, it has turned out to be a valuable research tool.

ACKNOWLEDGEMENT

REFERENCES

[1] M. Cowan, "Solid-Armature Railguns without the Velocity Skin Effect," *IEEE Trans. on Magn.*, Vol. 29, No. 1, pp. 385-390, January 1993.

[2] J. Taylor, R. Crawford, and D. Keefer, "Experimental Comparison of Conventional and Trans-Augmented Railguns," *IEEE Trans. on Magn.*, Vol. 29, No. 1, pp. 523-529, January 1993.

[3] D. Keefer, J. Taylor, and R. Crawford, "The Electromagnetic Force in Railguns," in *Proceedings of the Fourth European Symposium on Electromagnetic Launch Technology Conference*, May 2-6, 1993, Celle, Germany, Paper No. 1503.

[4] D. Rodger and P. J. Leonard, "Modelling the Electromagnetic Performance of Moving Railgun Launchers Using Finite Elements," *IEEE Trans. Magn.*, Vol. 29, No. 1, pp. 496-498, January 1993.

[5] J. Taylor and D. Keefer, "Calculations of the Electromagnetic Force in Railguns," *Proceedings of the Ninth IEEE Pulsed Power Conference*, June 21-23, 1993, Albuquerque, New Mexico.

[6] J. Taylor and D. Keefer, "Muzzle-Fed Railgun Experiments," *Proceedings of the Ninth IEEE Pulsed Power Conference*, June 21-23, 1993, Albuquerque, New Mexico.

Table 1. Summary of UTSI 2.4 m muzzle-fed railgun experiments.

Shot	Type	Peak Rail Current (kA)	Mass of projectile (gm)	Muzzle Velocity (km/s)	Δ v_E Measured (km/s)	$\dfrac{\Delta\ v_E}{\Delta\ v_{electromagnetic}}$ (%)
8/16/91	Conven	67	.980	1.669	.630	116
10/24/91	Conven	105	.979	2.258	1.162	101
6/17/91	Conven	106	.984	2.476	1.365	115
11/20/92*	Conven	109	1.06	2.008	.988	79
11/11/92	Muz Fed	70	1.03	1.292	.279	67
11/18/92	Muz Fed	106	1.05	1.470	.457	48
12/14/92✿	Muz Fed	106	1.06	1.350	<.400	<41
1/27/93	Muz Fed	108	1.06	1.496	.429	41

* Secondary developed
✿ Entrance velocity could not be determined from data. Nominal entrance velocity for this railgun has been 1.0 ± 0.05 (km/s), there was nothing to suggest this was not a nominal shot.

MUZZLE-FED CIRCUIT
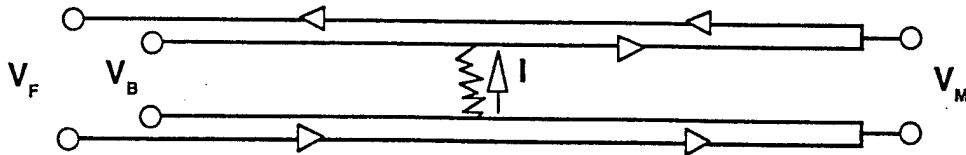
Figure 1. Muzzle-fed circuit diagram.
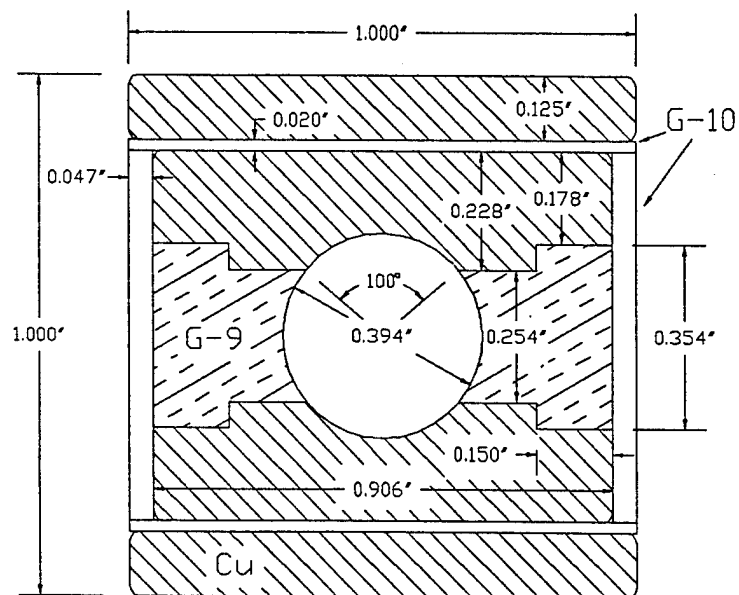
Figure 2. Muzzle-fed railgun bore cross section.
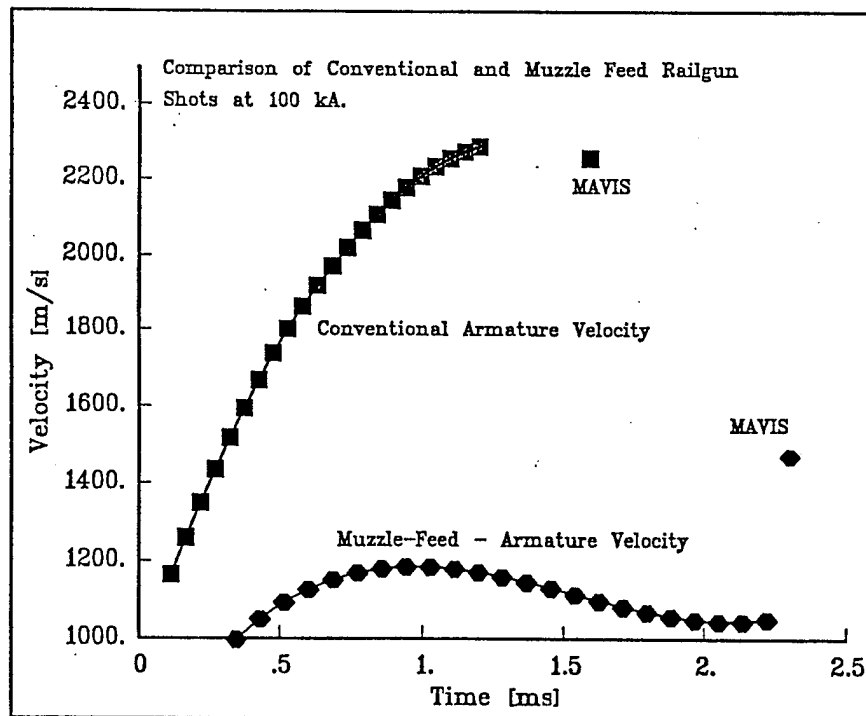
Figure 3. Comparison of conventional and muzzle-fed railgun shots
with 100 kA peak current.
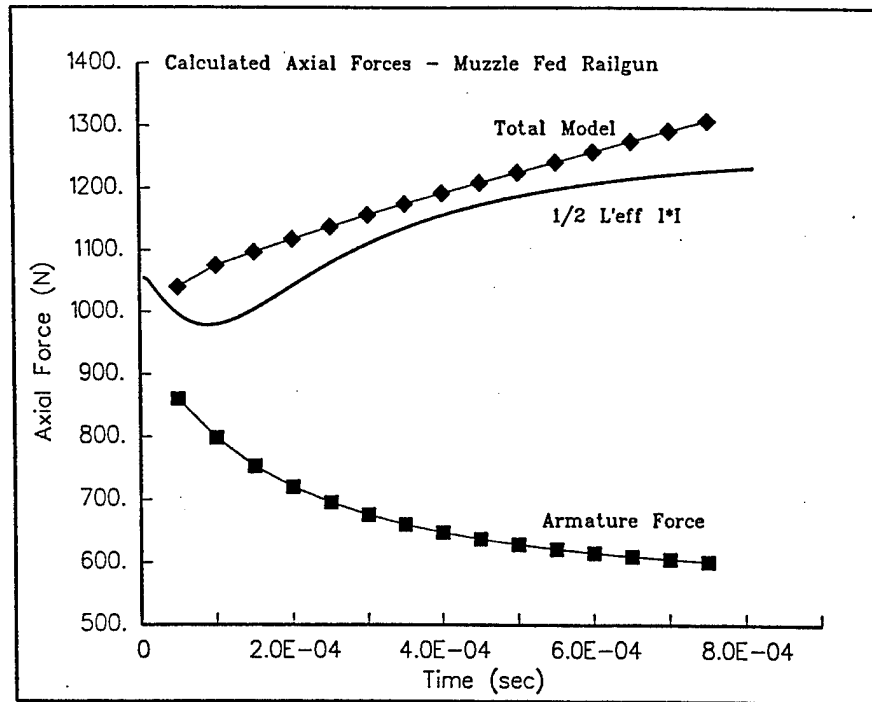
9

Figure 4. Armature and total axial forces for the muzzle-fed railgun at an armature velocity of 1 km/s using 3-D MEGA simulations of the UTSI railgun structure.
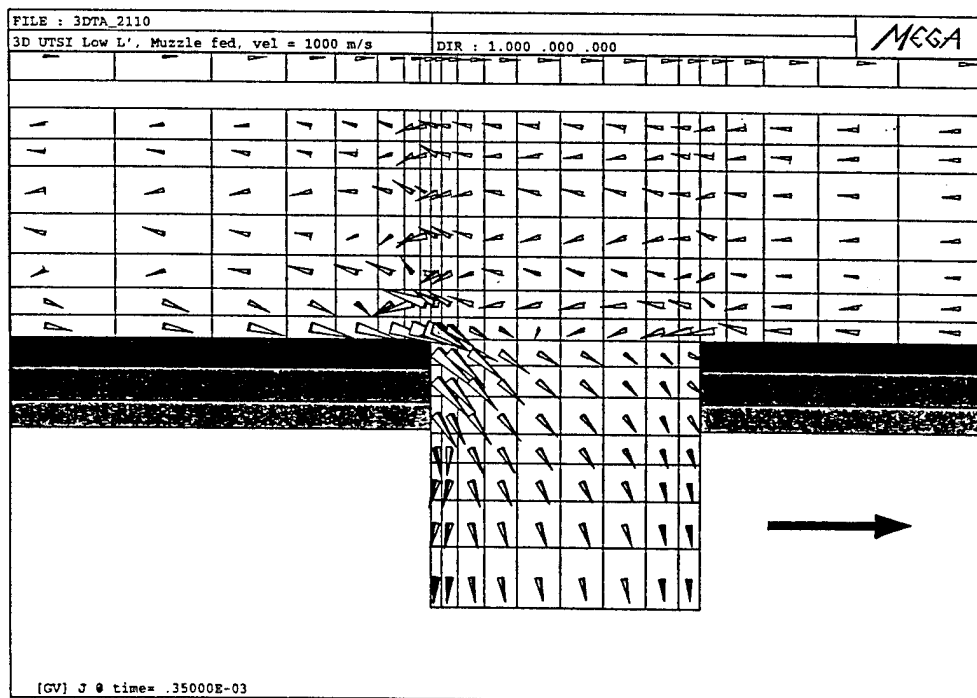
Figure 5. Vector plot of J for an armature velocity of 1 km/s at time 350 μs for UTSI railgun structure. The center plane, between insulators, is shown.
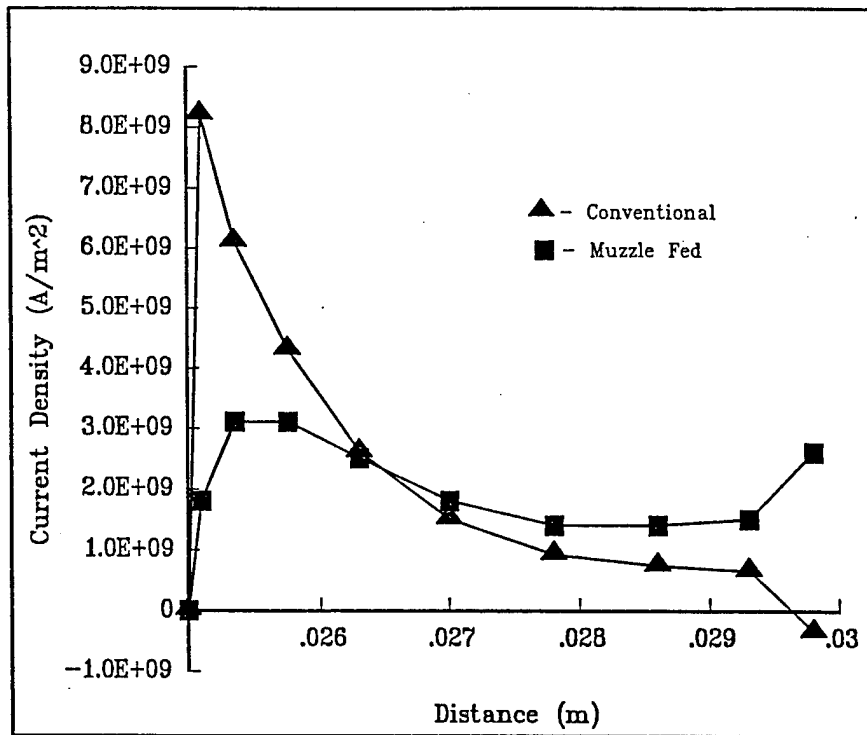
10
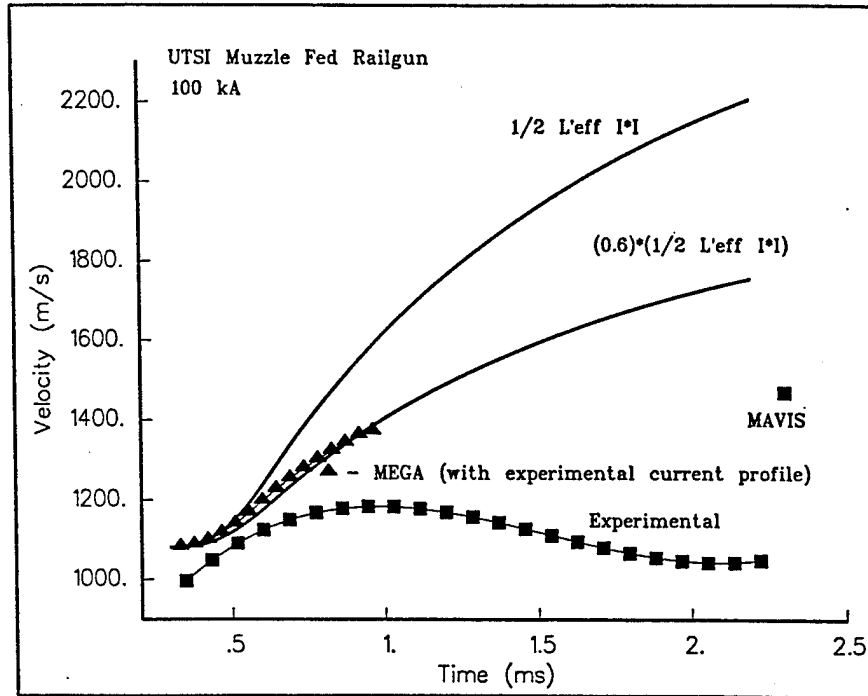
Figure 6. Comparison of experimental velocity with that predicted
by the inductance gradients and MEGA.
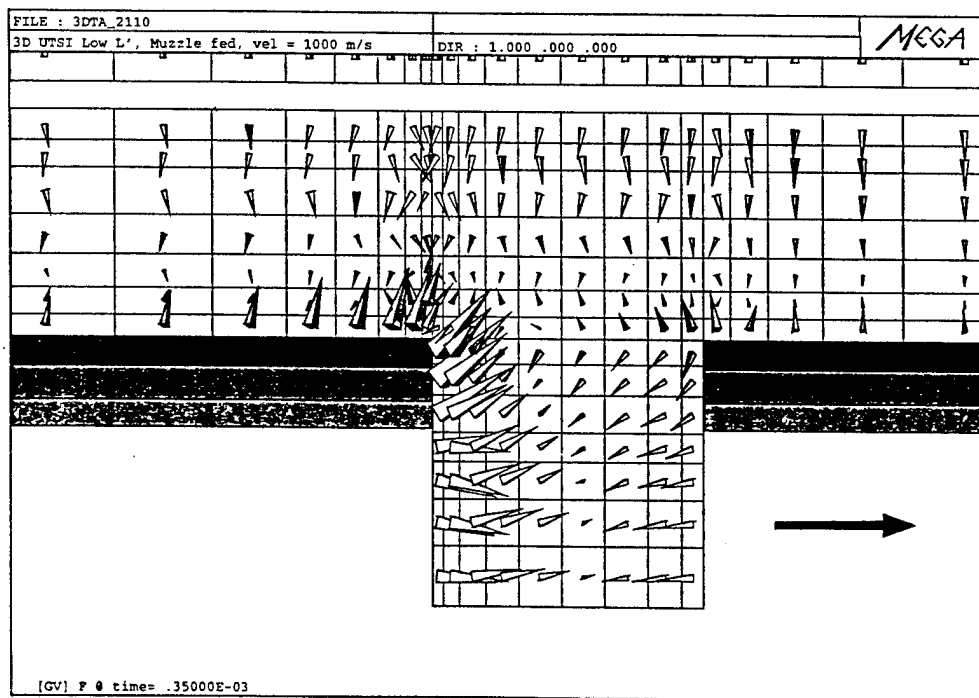
Figure 7. Vector plot of F for an armature velocity of 1 km/s at time 350 μs
for UTSI railgun structure. The center plane, between insulators, is shown.

11

Figure 8. Current distribution in armature for conventional and muzzle-fed railguns 0.2 mm below rail and armature interface.

3-D Plasma Armature Railgun Simulations

Dmitri Kondrashov and Dennis Keefer
Center for Laser Applications
University of Tennessee Space Institute
Tullahoma, Tennessee 37388-8897
USA

Abstract—A three-dimensional Navier-Stokes code developed at the High Temperature Institute in Moscow (IVTAN) has been extended to provide a simulation for the railgun plasma armature. This code was previously used with an approximate electromagnetic model to provide a two-dimensional simulation of a railgun plasma armature flow in the plane containing the insulators. A new three-dimensional electromagnetic solver has been incorporated into the code to permit full 3-D nonsteady MHD simulations of the plasma armature flow in a railgun. The finite-difference equations for magnetic vector potential and electric potential are solved using the ICCG method. The new electromagnetic solver was validated using 3-D solutions obtained from the finite element electromagnetic code MEGA. A full bore, 3-D simulation of a plasma armature reveals flow patterns significantly different than those of rail or insulator plane 2-D simulations. In particular, the maximum J × B force occurs off-axis and results in a plasma flow away from the projectile along the axis of symmetry. A zone of high shear flow forms near the rail surfaces which increases the viscous losses. Zones of low current, nearly stagnant flow form near the base of the projectile, consistent with experimental observations of a buffer between the armature and the projectile.

INTRODUCTION

Considerable progress has been made during the past few years in the MHD modelling of plasma armature railguns. A comprehensive overview of the evolution of MHD codes for plasma armatures is given by Batteh and Thornhill [1]. The broad range of 1-D models and more recent 2-D rail-to-rail [2]-[4] and insulator-to-insulator [5] models have provided considerable insight into the physical mechanisms associated with the performance of railguns. However, several important phenomena which are inherently three-dimensional cannot be fully understood in 1-D or 2-D simulations. A matter of particular

interest is the 3-D plasma flow which results from nonuniform electromagnetic forces and the ablation of both rail and insulator. Experimental results from a hybrid armature study at UTSI provided evidence for such 3-D armature flows [6]. The dynamics of this three-dimensional plasma motion is important in understanding the observed mechanisms of primary separation and secondary arc formation which are associated with loss of performance.

Another important issue is the 3-D nature of the electromagnetic fields in the railgun. The results of computer simulations [7] indicate that 3-D electromagnetic effects in a railgun with a solid armature significantly influence the value of the axial armature force, depending on the railgun configuration. With a plasma armature the spatial nonuniformity of J × B and J · E plays an important role in the dynamics of plasma motion. In order to analyze the corresponding effects, a full 3-D MHD code is required. A new 3-D MHD code has been developed to address these issues. The code includes a 3-D, transient Navier-Stokes code, and a 3-D, transient electromagnetic code. A first simulation of a railgun plasma armature using this code is presented in this paper.

3-D PLASMA ARMATURE MODEL

A 3-D time-dependent MHD code was developed at the University of Tennessee Space Institute (UTSI) based on a 3-D time-dependent Navier-Stokes code developed at the High Temperature Institute (IVTAN), Moscow and a 3-D time-dependent electrodynamic code developed at UTSI.

The plasma is described as a fluid with the mass density ρ, velocity,

$$\mathbf{v} = (v_1, v_2, v_3) \ ,$$

internal energy per unit volume e, pressure p, viscosity μ, and total thermal conductivity k_{tot} which includes radiation thermal conductivity. The equations describing plasma motion in the Navier-Stokes code including the MHD terms are:

$$\frac{\partial \rho}{\partial t} + \nabla \cdot \rho \mathbf{v} = 0 \ ;$$

$$\frac{\partial \rho \mathbf{v}}{\partial t} + \nabla \cdot U_{ij} = \mathbf{J} \times \mathbf{B} + \nabla \cdot \tau_{ij} - \nabla p \ ;$$

$$\frac{\partial}{\partial t}\left(\rho e + \frac{\rho v^2}{2}\right) + \nabla \cdot \left(\rho \mathbf{v} \left(\frac{v^2}{2} + \frac{p}{\rho} + e\right)\right)$$
$$= \nabla \cdot (\mathbf{v} \cdot \tau_{ij}) + \nabla \cdot k_{tot} \nabla T + \mathbf{J} \cdot \mathbf{E} \qquad (1)$$

$$\tau_{ij} = \mu \left(\frac{\partial v_i}{\partial x_j} + \frac{\partial v_j}{\partial x_i} \right) - \frac{2}{3} \mu \nabla \cdot \mathbf{v} \; ;$$

$$U_{ij} = \rho \mathbf{v}_i \mathbf{v}_j \; .$$

The pressure and temperature are found from equations of state:

$$P = f_P(\rho, e)$$

$$T = f_T(\rho, e) \; .$$

The equations of state and transport properties μ, k_{tot}, and electrical conductivity, σ, are those for a 10% copper-90% hydrogen plasma [9] at temperatures in the range 5000 K to 60000 K and at pressures in the range 1 to 7000 atm. The thermal diffusion equation was not solved in the rail. Thus the electric conductivity and other properties of the rail remained constant throughout the calculations.

The distinguishing features of the IVTAN Navier-Stokes code are calculation of convective terms using Godunov's procedure or the Riemann problem, and applying a finite-difference method to solve terms with viscosity. The Navier-Stokes code has been benchmarked against problems of laminar compressible gas flow [8]. The fluid dynamic and electrodynamic equations are coupled through the electromagnetic force and dissipated power terms in the plasma motion equations, and through the values of conductivity and velocity in the electromagnetic equations.

The electromagnetic solver solves Maxwell's equations in the MHD approximation:

$$\frac{\partial \mathbf{B}}{\partial t} = -\nabla \times \mathbf{E} \; ;$$

$$\nabla \times \mathbf{B} = \mu_0 \mathbf{J} \; ; \qquad (2)$$

$$\mathbf{J} = \sigma(\mathbf{E} + \mathbf{v} \times \mathbf{B}) \; .$$

The magnetic vector potential $\mathbf{A}$ and electric scalar potential φ are introduced to insure that the divergence of $\mathbf{B}$ is zero:

$$\mathbf{B} = \nabla \times \mathbf{A} \; , \qquad \mathbf{E} = -\nabla \varphi - \frac{\partial \mathbf{A}}{\partial t} \; .$$

The resulting equations for φ and $\mathbf{A}$ are:

$$-\nabla^2 \mathbf{A} = \sigma \mu_0 \left(-\frac{\partial \mathbf{A}}{\partial t} - \nabla \varphi + \mathbf{v} \times \nabla \times \mathbf{A} \right) \; ; \qquad (3)$$

and

$$\nabla \cdot \sigma \left(\nabla \varphi + \frac{\partial \mathbf{A}}{\partial t} - \mathbf{v} \times \nabla \times \mathbf{A} \right) = 0 \; . \qquad (4)$$

In deriving (3) the Coulomb gauge $\nabla \cdot \mathbf{A} = 0$ was used.

Equation (4) represents conservation of current:

$$\nabla \cdot \mathbf{J} = 0 \; .$$

The corresponding finite-difference equations are solved by ICCG (incomplete Cholesky conjugate gradients method) which provides an efficient solution for (3) and (4) with nonuniform conductivity that varies from very high (rail-like) to very low (essentially zero) values. The electromagnetic solver was benchmarked against the 3-D finite-element electromagnetic code MEGA [10], using a simple square bore, copper rail, copper armature problem.

NUMERICAL GRID AND SIMULATION PARAMETERS

A 60 cm long, 2 cm square bore railgun has been simulated. The computations are performed in one quarter of the railgun cross section due to the symmetry assumptions. A uniform grid with 260 points in the axial direction and 10 × 10 points in the cross section is used in the Navier-Stokes code. The chosen sizes of uniform grid spacing will resolve with sufficient accuracy the diffusion of magnetic field into the armature and the rail. The entire region from the breech to the projectile is simulated, so the problem of specifying boundary conditions at the armature trailing edge is avoided. The base of the projectile is the right hand boundary, and as it moves, new grid points are added into the computational domain. The 260 × 25 × 15 grid for the electromagnetic solver matches the gasdynamical grid inside the bore but is extended outside the bore to an air boundary with nonuniform spacing.

The algorithm for the electromagnetic solver allows the region of computation to move as the armature moves to save computational resources. During the run, the value of current passing into the rail and through the armature structure is kept constant and equal to the initial value $I_0 = 120$ kA (total gun current is equal to 240 kA). The total mass of the projectile m_{pr} is taken to be equal to $4g$.

INITIAL AND BOUNDARY CONDITIONS

The problem was initiated by first allowing the projectile to accelerate from rest at $x = 3$ cm to a velocity of 355 m/s through expansion of a cold nonconducting gas compressed at $p = 100$ atm using only the Navier-Stokes code. This simulated the condition of using a light gas gun injector and made it unnecessary to assume boundary conditions at the rear of the armature. When the projectile reached the initiation velocity at $x = 11$ cm the temperature in an axial region near the base of the projectile was increased to $T_0 = 10,000$ K to make the plasma conducting, simulating the action of a fuse. The desired increase of the temperature was achieved by changing the density at constant pressure in the armature region. The initial length of the plasma armature was chosen to be 4 cm to avoid nonphysical behavior, e.g. excessive heating, after starting the whole code. At this point the simulation continued,

solving both the Navier-Stokes code and the electrodynamics code.

In the Navier-Stokes code a no-slip condition on the solid surfaces is used to determine viscous momentum flux on the boundary. The radiation absorbing condition is specified for heat flux on the rail, insulator, projectile, and breech surfaces, i.e. the normal component of energy flux, $q_n = \sigma T^4$. Also, on the rail and insulator surfaces ablation is allowed, so the corresponding convective fluxes of mass, momentum and energy are used as boundary values for interior calculations.

The projectile velocity, $\mathbf{V}_{pr}$, is determined from Newton's law:

$$m_{pr}\frac{d\mathbf{V}_{pr}}{dt} = \int p dS \ ,$$

where the pressure integral is taken over the base of the projectile. The side of the cell adjacent to the projectile is expanding with velocity $\mathbf{V}_{pr}$ and, when necessary, new grid points are added into the computational domain. The Riemann problem algorithm for the moving boundary is used for the calculation of convective fluxes at the base of the projectile. On the symmetry boundaries, corresponding symmetry conditions are imposed.

In the electromagnetic solver a separate set of boundary conditions is needed for (3) and (4). For the magnetic vector potential a current source condition is imposed at the breech, a tangent flux condition ($B_n = 0$) is imposed at the outer boundaries and a normal flux condition ($B_\tau = 0$) is specified on the rail-to rail symmetry plane.

The scalar potential, (4), requires a "no-current" condition $J_n = 0$ on the interfaces between conducting and nonconducting regions, a "ground value" of zero on the insulator-insulator symmetry plane, and the current source condition given by (5) at the breech:

$$\int \mathbf{J} dS = \mathbf{I}_0 \ . \tag{5}$$

ABLATION MODEL

The main goal in simulating ablation was to observe the 3D flow which results from the incoming mass from both rail and insulator. Attention is paid to the dynamics of the flow rather than the details of the surface process. A relatively simple physical model has been chosen to simulate the ablation rate from the surface. It follows generally from [6].

It is assumed that the ablation occurs through melting of the surface at melting temperature T_m of the material. The ablation mass flow rate m is proportional to radiative heat flux and is given as:

$$m = \frac{\sigma T^4}{H} \ ,$$

where H is the heat of fusion of the material.

The material properties have been taken from [11]. The computed fluxes of mass, energy, and momentum due to the ablation appear as boundary values for the correspondent fluxes in the continuity, momentum, and energy equations.

RESULTS AND DISCUSSION

The state of the simulation at $238\ \mu s$ after fusing is presented. The projectile has reached the velocity $\mathbf{V}_{pr} = 780\ \text{m/s}$, is located at $x \approx 25\ \text{cm}$ and the length of the armature is approximately 11 cm. The plasma velocity vectors in the projectile reference frame and current density contour line plots are superimposed and are shown on seven different surfaces. They represent two insulator-to-insulator and two rail-to-rail planes, including the central planes in both directions. The results are also shown on three transverse plane cuts through the railgun bore - near the rear, middle and front of the armature where the transverse velocity vectors are presented. The relative position of these surfaces is shown in Fig. 1.

Let us first examine the rail-to-rail, A-R and 8-R planes, Figs. 2 and 3, respectively. We notice two nonsymmetric circulation patterns of a different intensity; the small one, in the corner between rail and projectile in the A-R plane, is the same one which is observed in many 2-D rail-to-rail calculations [4]-[6]. It is caused mainly by rail ablation where the ablated material which is entering the domain with the negative rail velocity is carried away from the projectile. However, the second circulation pattern is much stronger, and it causes the appearance of a flow with negative velocity on the central insulator-to-insulator plane (see A-I, Fig. 4). At the T-91 (Fig. 5) and T-119 (Fig. 6) plane we see two very well-defined parts of this circulation.
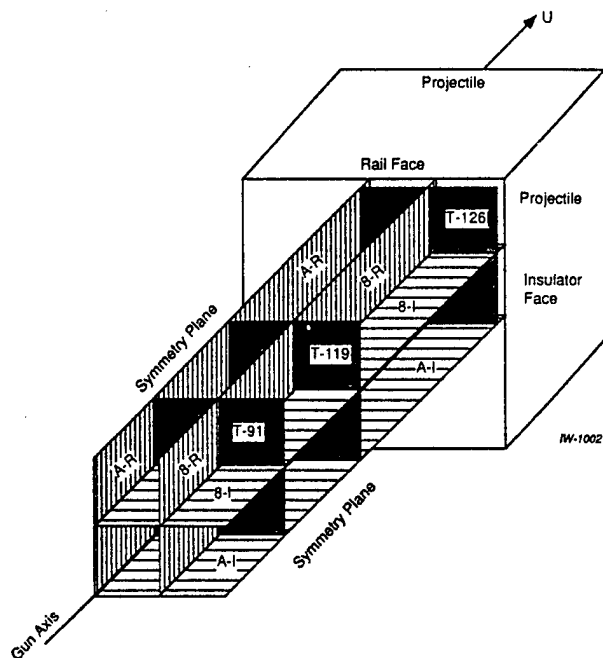

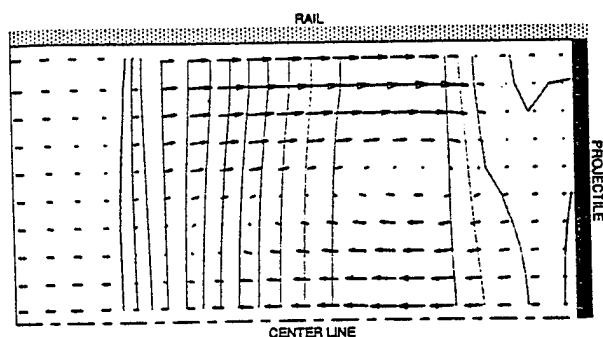Fig. 1. Positions and identification of the diagnostic planes.

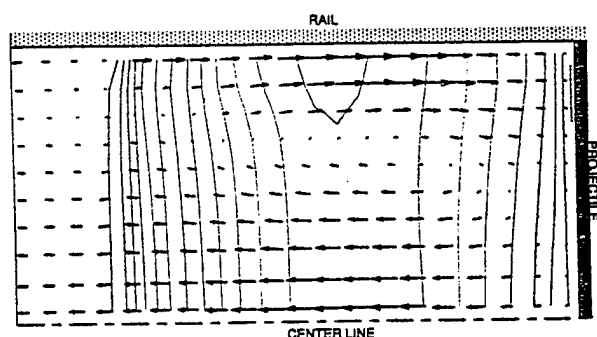Fig. 2. Velocity vectors and contours for the magnitude of the current density on plane A-R.

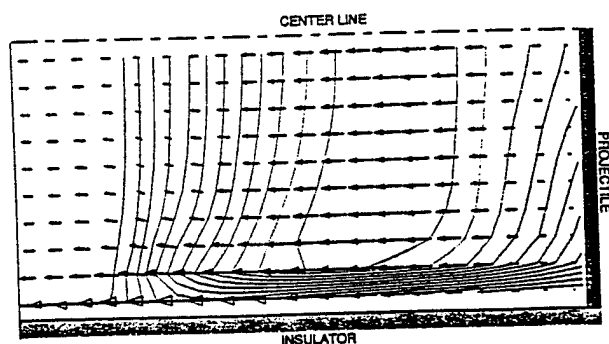Fig. 3. Velocity vectors and contours for the magnitude of the current density on plane 8-R.

Fig. 4. Velocity vectors and contours for the magnitude of the current density on plane A-I.
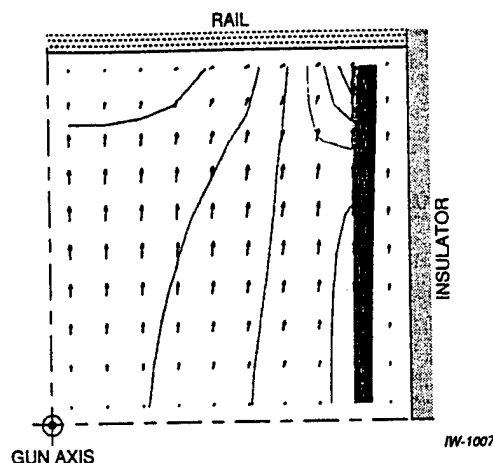
Fig. 5. Velocity vectors and contours for the magnitude of the current density on the transverse plane T-91.
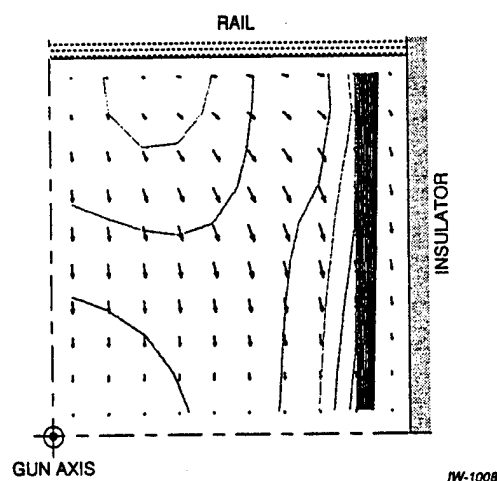
Fig. 6. Velocity vectors and contours for the magnitude of the current density on the transverse plane T-119.

An explanation of this phenomena lies in the fact that the rate of magnetic field diffusion into the rail at the corner between the rail and the insulator is much faster than that in the center of the bore. This is indicated on the contour plot of the magnetic field shown in Fig. 7. As a consequence, the current, which flows where the magnetic field has been diffused, is concentrated off the center line in a region near the corner, as we observe on A-I, 8-I (Fig. 8) and T-91 planes. That, in turn, causes the electromagnetic force to be very nonuniform across the bore and its maximum is shifted away from the center to a point between the center and the wall. As a result, acceleration of the plasma takes place mostly near the rail in the 8-I plane.

The accelerated plasma reaches the projectile with a relative positive velocity near the insulator-rail corner (see 8-R plane), where it turns diagonally toward the center line (see T-126, Fig. 9), and moves away from the
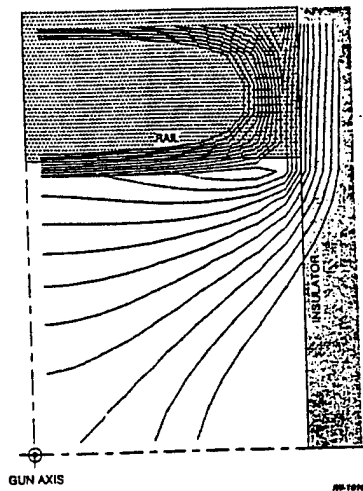
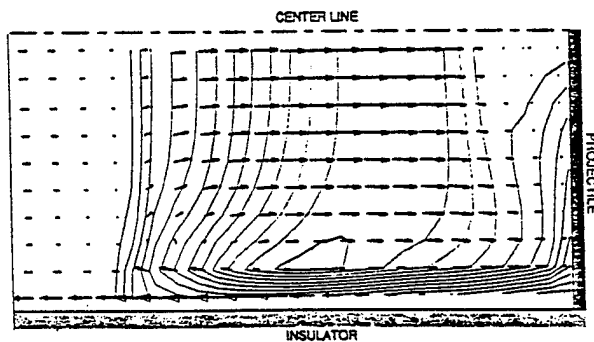Fig. 7. Contour plot of the magnitude of the magnetic field at the transverse plane T-91.

Fig. 8. Velocity vectors and contours for the magnitude of the current density on plane 8-I.
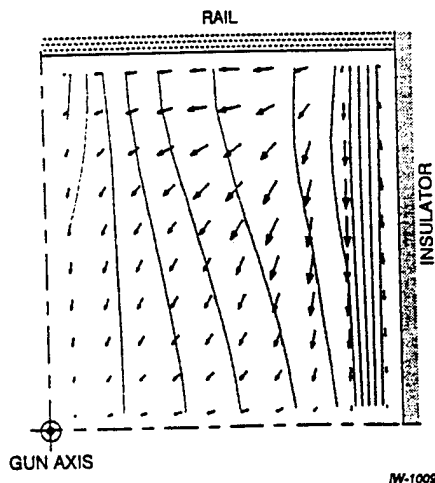

Fig. 9. Velocity vectors and contours for the magnitude of the current density on the transverse plane T-126.

projectile because the electromagnetic force is not sufficient to balance the pressure gradient in the armature on the A-I plane. Simultaneously, a stagnation zone exists on the A-R plane near the rail.

Near the insulator, a relatively cold nonconducting layer has been formed due to ablation, where the force is much smaller than in the center. This explains the high negative velocities of the plasma and ablative products near the insulator in the A-I and 8-I planes as well as drift of the plasma toward the insulator on the projectile surface. As one can see on the 8-I plane, some part of the plasma near the insulator is circulated back through the armature by the small circulation at the rear.

The existence of the main circulation which pushes the plasma forward near the rail surface increases the viscous drag on the rail, and may be an additional source of losses in the railgun. Also, the hot material which moves away from the projectile on the central A-I plane is a potential source for elongation of the armature and the development of secondaries. Some evidence of this can be seen on the A-R plane where current contour lines are curved toward the breech along the center line of the bore.

CONCLUSIONS

This first simulation of a railgun plasma armature has progressed only a relatively short distance down the bore at this time. However, the qualitative plasma flow observed from this 3-D simulation is different in significant ways from those observed in either rail-to-rail or insulator-to-insulator 2-D simulations. In particular, the effects of current diffusion into the rail leads to a current distribution that peaks between the axis and the insulator. This current distribution, in turn, leads to larger velocity gradients and viscous losses at the rail. It also creates a vortex structure which carries hot armature materials away from the armature along the axis, elongating the current distribution in the armature. This effect could be a precurser of secondary arc formation. Although only a limited portion of the available results was presented here, other variables, such as temperature, pressure and electrical conductivity appear to be reasonable. These results should be interpreted as a preliminary attempt at a qualitative understanding of the complex flows in the plasma armature. Much additional work will be required to provide reliable, quantitative simulations.

REFERENCES

[1] J. Batteh and L. D. Thornhill, "A perspective on the modelling of plasma armatures," AIAA 24th Plasmadynamics and Lasers Conference, July 1993.

[2] R. Crawford, D. Keefer, and R. Tipton, "Velocity limiting magnetohydrodynamic effects in plasma armatures," 6th Symposium on EML.

[3] M. A. Huerta and G. S. Boynton, "2D heat conducting simulation of plasma armatures," *IEEE Transactions on Magnetics*, 27, 261 (1991).

[4] M. N. Frese, "The internal structure and dynamics of the railgun," *IEEE Transactions on Magnetics*,

Vol. 25, No. 1, pp. 233-239.

[5] V. N. Zatelepin and D. A. Kondrashov, "Decay of current armature at magnetic propulsion," 30th Symposium on Engineering Aspects of MHD, July 1992.

[6] R. Crawford, D. Keefer and A. Sedghinasab, "Railgun hybrid armatures, experimental results and performance characteristics," *IEEE Transactions on Magnetics*, Vol. 27, No. 1, pp. 240-244, 1991.

[7] D. Keefer, R. Crawford, and J. Taylor, "Plasma armatures studies in augmented and muzzle fed railguns," AIAA 24th Plasmadynamics and Lasers Conference, July 1993.

[8] V. N. Zatelepin and D. A. Kondrashov, "An explicit-implicit scheme for integrating unsteady 3D Navier-Stokes equations," *High Temperature*, Vol. 30, No. 4, p. 752-760, July-August 1992.

[9] R. Marshall, "The properties of copper and hydrogen plasmas," September 1986.

[10] D. Rodger, "Finite-element method for calculating 3-D electromagnetic field distributions," *IEEE Proceedings*, Vol. 130, No. 5, 1983. .

[11] R. A. Meger et al, "NRL experimental and theoretical research of plasma armatures in railgun," AIAA 24th Plasma Dynamics and Lasers Conference, July 1993.

PLASMA ARMATURE STUDIES IN AUGMENTED

AND MUZZLE FED RAILGUNS

by

Dennis Keefer, Ph.D., Roger Crawford, Ph.D., and Jaime Taylor
University of Tennessee Space Institute
Center for Laser Applications
Tullahoma, Tennessee 37388-8897

ABSTRACT

A 2.4 m long, 1 cm diameter round bore railgun was developed and operated at UTSI to investigate the performance of trans-augmented and muzzle fed plasma armature railguns. The railgun was designed with copper rails and G-9 insulators, and incorporated a single augmenting turn which could be converted to muzzle feed. The barrel contained an array of B-dot probes spaced 10 cm apart to provide good resolution of the plasma armature current distribution and velocity. A MAVIS electromagnetic transducer was used to provide accurate measurements of the muzzle velocity. Gun bore lapping and cleaning provided a high quality gun bore for each shot and repeatable multi-shot data.

A carefully planned set of experiments was conducted on the UTSI railgun operated in the conventional, augmented and muzzle fed configurations. Both primary and augmenting rails were operated at peak currents of 70 to 140 kA. The enhanced performance provided by augmentation was found to be significantly less than predicted by theory, even though the railgun operated without the formation of secondary armatures. These results indicated that at least one of the accepted railgun force or drag models was wrong. The muzzle-fed railgun, first operated in the former Soviet Union, provided very poor performance results in the UTSI experiments. Most acceleration was provided by electrothermal forces during fusing. A three-dimensional electrodynamics code MEGA was used to evaluate both the augmented and muzzle-fed results. The experiments and the MEGA calculations have identified the role of eddy currents and forces in the rails, in the reduction of armature forces, and have shown that the muzzle fed configuration is of no practical interest for electromagnetic launchers.

I. INTRODUCTION

To examine the effects of augmentation UTSI constructed a 2.4 m trans-augmented railgun designed to function in either conventional or augmented mode. The design was such as to allow easy conversion to a muzzle fed railgun. The purpose of the trans-augmented railgun experiments was to gain an improved understanding of the effects of increasing the magnetic flux and, therefore, the force on the armature while still operating with essentially the same power dissipation in the bore [1].

The muzzle fed experiments were done to understand the effects associated with feeding the current to the armature from the muzzle instead of the breech. The original philosophy was that the muzzle fed railgun would increase the impedance path for secondaries by reducing the velocity skin effect, and would reduce rail separation forces.

This paper summarizes three series of experiments, two on the transaugmented and one on the muzzle fed, in a carefully prepared railgun for which secondary arcs did not typically form. A performance model was constructed which included all the known fluid mechanical drag effects and electrothermal acceleration. This model was used to estimate the performance losses so that experimental data could be compared with ideal electromagnetic performance. For the transaugmented case the electromagnetic force was modeled with the usual [1]

$$F = \frac{1}{2} L' I_1^2 + M' I_1 I_2 \ .$$

With the typical energy arguments and circuit analysis models used to obtain Equation (1) the electromagnetic force

for the muzzle fed railgun was obtained as

$$F = M' I_1^2 - \frac{1}{2} L' I_1^2 .$$

Comparison of the experimentally observed velocity with the performance model suggested that the electromagnetic forces had been overestimated. We have performed a series of 3-dimensional (3-D) electromagnetic simulations for all three configurations with moving armatures using MEGA [2]. The axial force on the armature, calculated by taking the integral of $J \times B$ over the armature, was compared with the force calculated by Equations 1 and 2 for each configuration.

II. UTSI RAILGUN FACILITY

A. The UTSI Augmented and Muzzle Fed Railgun

The UTSI railgun was constructed with a 2.4 m long barrel and a 1.0 cm bore diameter. A 1.1 m single stage helium gas injector provided pre-acceleration of projectiles into the railgun with a velocity of approximately 1 km/s. The design featured copper rails and G-9 insulators supported by a G-10 substructure as shown in Fig. 1 [3]. The configuration of the G-10 backing and aluminum anvils were the same as used in Refs. [3,4]. Two separate 240 kJ capacitor banks and two separated four sectored toroidal inductors were used to provide independent current sources for the inner and augmenting rails.

For the muzzle fed railgun the current was provide by the capacitor and inductor attached to the breech of the augmenting rails. The current path was from the breech of the augmenting rails to the muzzle, where the inner rails joined the augmenting rails. Lexan projectiles of approximately 1 gm mass with flexible lip seals and an aluminum foil fuse were used for all shots.

B. Instrumentation and Experimental Procedure

Twenty-three B-dot probes located 100 mm apart measured changing rail current and were used to obtain accurate armature positions [5]. Two pressure transducers were located 95 and 55 mm before the breech end of the rails. These were used to initiate the timing of the data acquisition system and power supplies, to measure the entrance velocity of the projectile into the rails and to measure the initial pressure of the gas in the bore. A MAVIS electromagnetic transducer, placed in the enclosed flight range, was used to provide accurate muzzle velocity measurements [6].

To maintain consistent bore quality for conventional, augmented and muzzle fed experiments, before each shot the bore was lapped from the breech of the light gas gun to the muzzle using a rotating, expandable iron lap. After lapping, acetone was circulated through the bore to remove all traces of lapping compound and hydrocarbons. The bore was dried under vacuum and then backfilled with one-half atmosphere of helium. A bore scope was used to check for foreign materials or incomplete lapping, and was used after each shot to determine the degree of bore damage.

Values of L', the self inductance per unit length, and M', the mutual inductance per unit length, were needed for performance evaluations. These values were calculated using the 2-D cross section of our gun, Figure 1, at 10,000 Hz with MEGA. The value of 0.274 μH/m was obtained for L' and a value of 0.249 μH/m was obtained for M'.

III. EXPERIMENTAL INVESTIGATION

A. Transaugmented Railgun

Two series of experiments were performed for the transaugmented case, one using a nominal peak armature current of 70 kA and the second using a nominal peak current of 100 kA. For each series the armature power dissipated in the bore remained the same, while the peak augmenting current ranged from 0 to 140 kA, with an
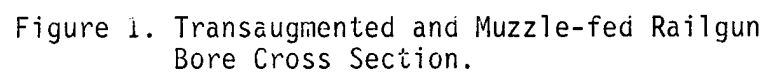
Figure 1. Transaugmented and Muzzle-fed Railgun
Bore Cross Section.

augmenting current of 0 kA referring to a conventional railgun shot. This gave a factor of three range of total armature force for the 70 kA series and a factor of two range for total armature force for the 100 kA series. Conventional shots at higher currents were performed to compare with the augmenting shots at the higher levels of electromagnetic impulse.

The results of these experiments are given in Table 1. The measured increase in projectile momentum was plotted as a function of the total electromagnetic impulse in Figure 2. The total electromagnetic impulse was defined as the integral of the force given by Equation 1 taken over the time the projectile was in the barrel.

It can be seen in Figure 2 that with increasing electromagnetic impulse the efficiency decreases. At the low values of electromagnetic impulse, the greater than 100% of predicted momentum change may be attributed to continuing gasdynamic expansion of the accelerator gas and the electrothermal acceleration. Primary separation was also observed for all shots performed on the UTSI railgun. MAVIS measured the projectile velocity 80 cm after muzzle exit while the B-dot probes gave the armature position versus time, thus after differentiation, armature velocity. Figure 3 shows a 70 kA baseline conventional shot for which the armature velocity peaks then decreases implying primary separation. A detailed interpretation of this data is given in Refs. [1,7].

B. Muzzle Fed Railgun

For the muzzle fed case one 70 kA peak current and three 100 kA peak current shots were performed. The results, shown in Table 1, were quite unexpected, which deemed it necessary to check for repeatability in performance for at least one current level. The experiment was repeatable and the B-dot signals showed a compact armature without a secondary. What cannot be seen from the B-dot probes but is seen in Figures 3 and 4 , 70 kA and 100 kA peak currents respectively, was that the projectile apparently separated from the armature just after fusing. The projectile velocity for the muzzle fed shots considerably exceeded the peak armature velocity implying early primary separation.

Equation 2 can be rearranged in the form $1/2 \, L'_{eff} \, I^2$ where L'_{eff} has the value, obtained from L' and M', of 0.224 μH/m. This is 82% of the value of L' which from the simple model of the electromagnetic force says the force for the muzzle fed railgun should have been 82% of that for the conventional. However as can be seen in Table 1, and Figures 3 and 4, the change in velocity measured for the muzzle fed case is well below half that measured for the conventional case. Where did the excess force go?

IV. COMPARISON WITH THE PERFORMANCE MODEL

A railgun performance model was constructed which include the electrothermal acceleration, and the various fluid mechanical drag mechanisms. This model included the accelerating effects of the continued expansion of the helium accelerating gas and the electrothermal acceleration due to the vaporization and heating of the aluminum foil fuse. It also included the drag effects due to compression, acceleration and viscous drag of the residual bore gas ahead of the projectile, the vicious drag of the plasma armature and ablation drag. The details of this model have been given in Refs. [1,8,9].

Values of parameters used to model electrothermal expansion and ablation drag were obtained from the conventional baseline shots of 70 kA and 100 kA. Inclusion of the accelerating gasdynamics and electrothermal effects removed the greater than 100% momentum efficiency observed at the lowest values of electromagnetic momentum. The inclusion of various drag effects improved the prediction at higher values of electromagnetic momentum, but there was still a significant deficit in performance, as shown in Figure 5.

For the muzzle fed shots again the same parameters obtained for the conventional shots were used. The model predictions were basically the same as predictions made by Equation 2 alone. The model included the electrothermal expansion which increased the value predicted by the model, however the model quit calculating at the point the projectile would have theoretically exited the bore. Values for Table 1 were obtained by evaluation of Equation 2 over the time the projectile was actually in the bore, which was considerably longer than predicted in the model. Figure 6 shows a comparison of the experimental velocity increase with that predicted by the model for a 100 kA muzzle fed shot.

For a given series of transaugmented experiments with fixed armature current the ablation rate remains essentially constant as the augmentation is increased. Therefore, the electrothermal acceleration and the ablation drag

Table 1. Summary of UTSI 2.4 m Railgun Experiments

Shot	Peak Rail Current (kA)	Peak Augmented Rail Current (kA)	Mass of projectile (gm)	Muzzle Velocity (km/s)	Δv_E Measured (km/s)	$\dfrac{\Delta v_E}{\Delta v_{electromagnetic}}$ (%)

Conventional

Shot	Peak Rail Current (kA)	Peak Augmented Rail Current (kA)	Mass of projectile (gm)	Muzzle Velocity (km/s)	Δv_E Measured (km/s)	%
8/16/91	67	0	.980	1.669	.630	116
10/24/91	105	0	.979	2.258	1.162	101
6/17/91	106	0	.984	2.476	1.365	115
11/20/92*	109	0	1.06	2.008	.988	79
9/19/91	120	0	.992	2.379	1.299	84
9/6/91	134	0	.994	2.655	1.602	85
7/30/91	138	0	.996	2.493	1.469	73

Augmented

Shot	Peak Rail Current (kA)	Peak Augmented Rail Current (kA)	Mass of projectile (gm)	Muzzle Velocity (km/s)	Δv_E Measured (km/s)	%
9/25/91	68	30	.980	1.966	.886	99
1/14/92	67	71	.985	2.333	1.203	87
1/10/92	64	103	.994	2.36	1.305	78
1/16/92*	65	138	1.008	2.418	1.366	66
4/15/92	65	140	1.008	2.788	1.692	87
1/17/92	104	49	.992	2.620	1.539	76
10/29/91	105	107	.995	3.085	1.990	72
6/28/91	104	108	.968	3.046	1.950	63
7/10/91	102	142	.969	3.135	2.055	60

Muzzle-Feed

Shot	Peak Rail Current (kA)	Peak Augmented Rail Current (kA)	Mass of projectile (gm)	Muzzle Velocity (km/s)	Δv_E Measured (km/s)	%
11/11/92	70		1.03	1.292	.279	67
11/18/92	106		1.05	1.470	.457	48
12/14/92✿	106		1.06	1.350	<.400	<41
1/27/93	108		1.06	1.496	.429	41

* Secondary developed

✿ Entrance velocity could not be determined from data. Nominal entrance velocity for this railgun has been 1.0 ± 0.05 (km/s), there was nothing to suggest this was not a nominal shot.

L' = 0.274 (μH/m)

M' = 0.249 (μH/m)

Values of L' and M' obtained from 2D MEGA calculations with frequency = 10,000 Hz.
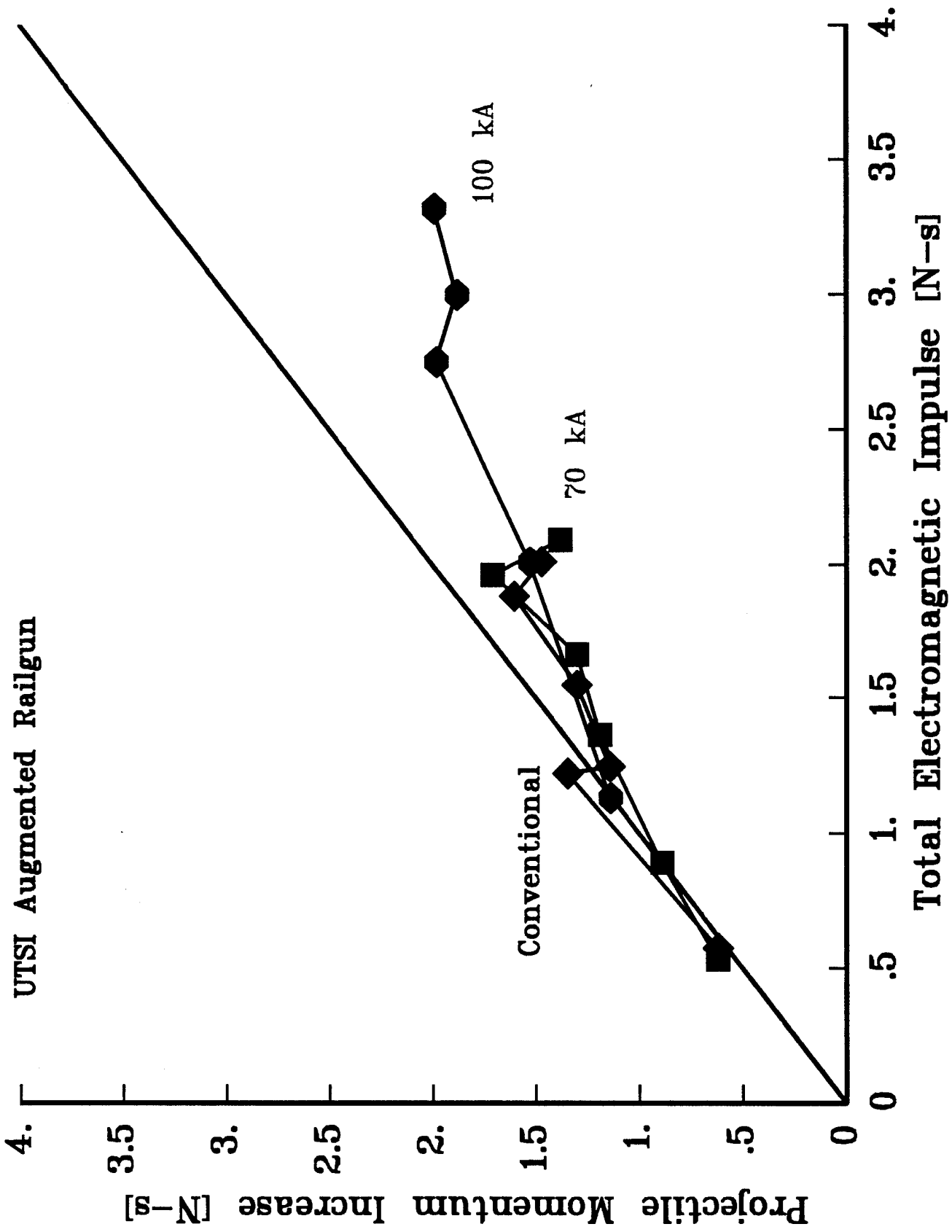
Figure 2. Comparison of increased projectile momentum with electromagnetic impulse for conventional and
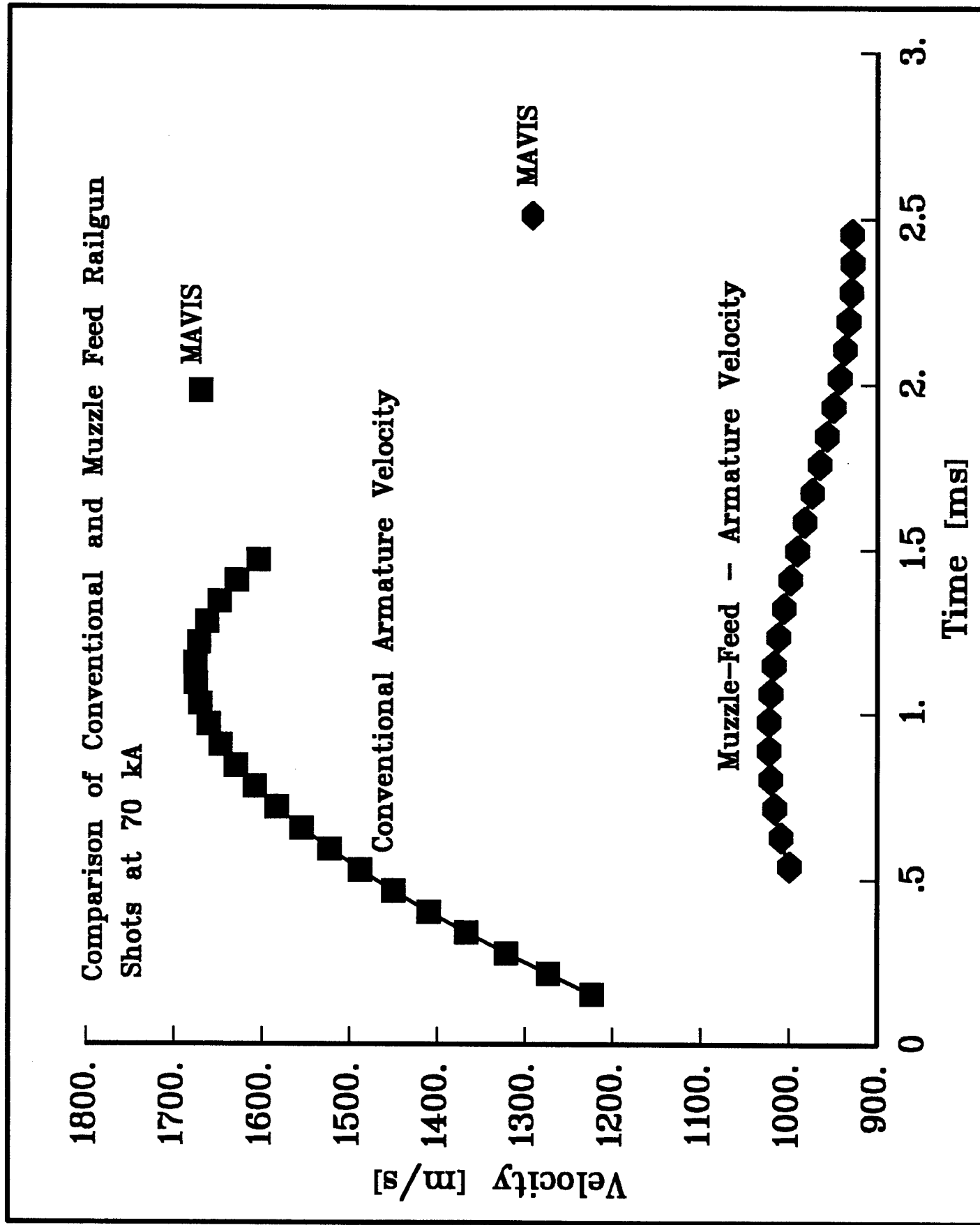
Figure 3. Comparison of conventional and muzzle feed railgun shots at 70 kA.

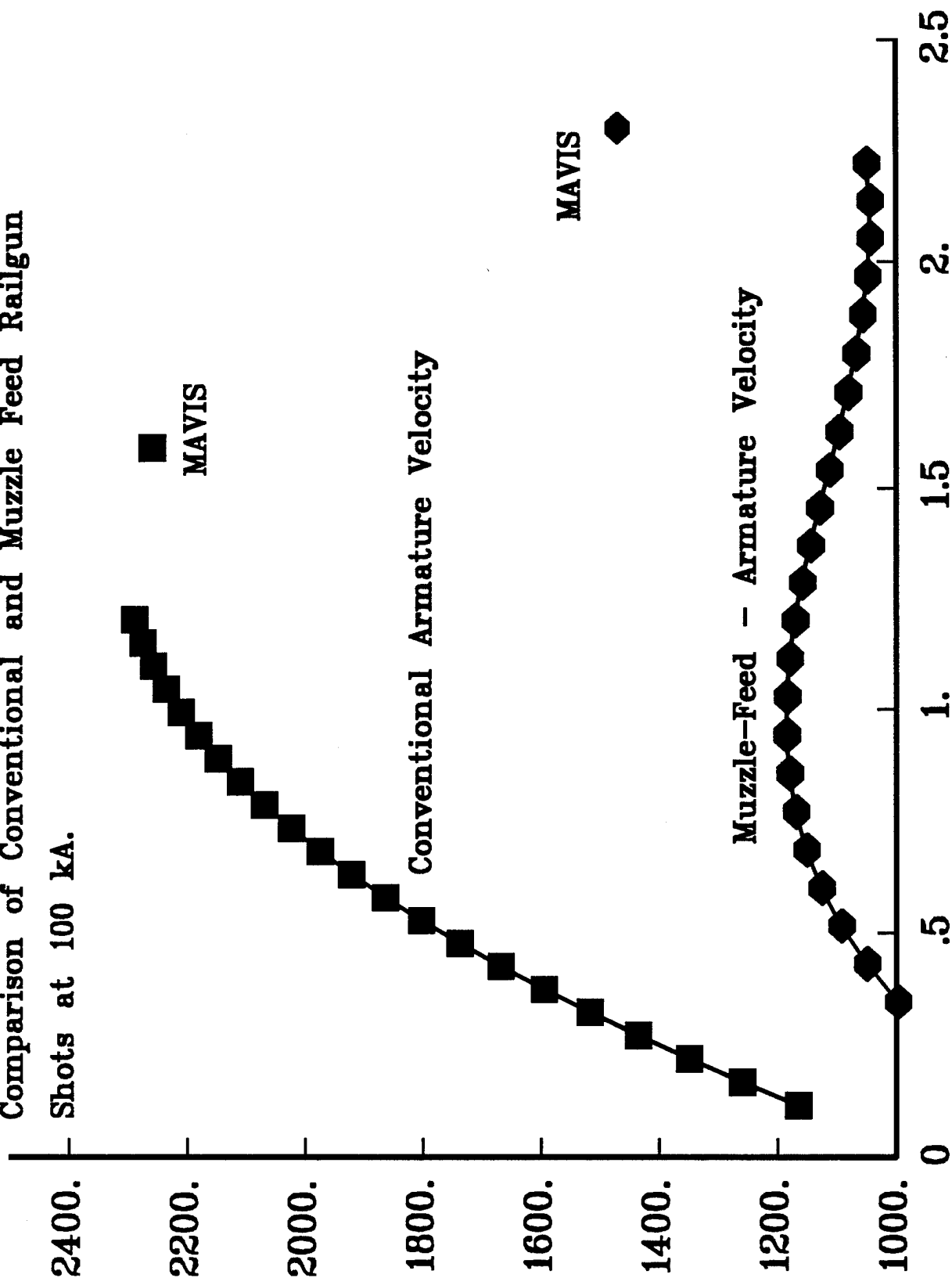Comparison of Conventional and Muzzle Feed Railgun
Shots at 100 kA.

MAVIS

Conventional Armature Velocity

MAVIS
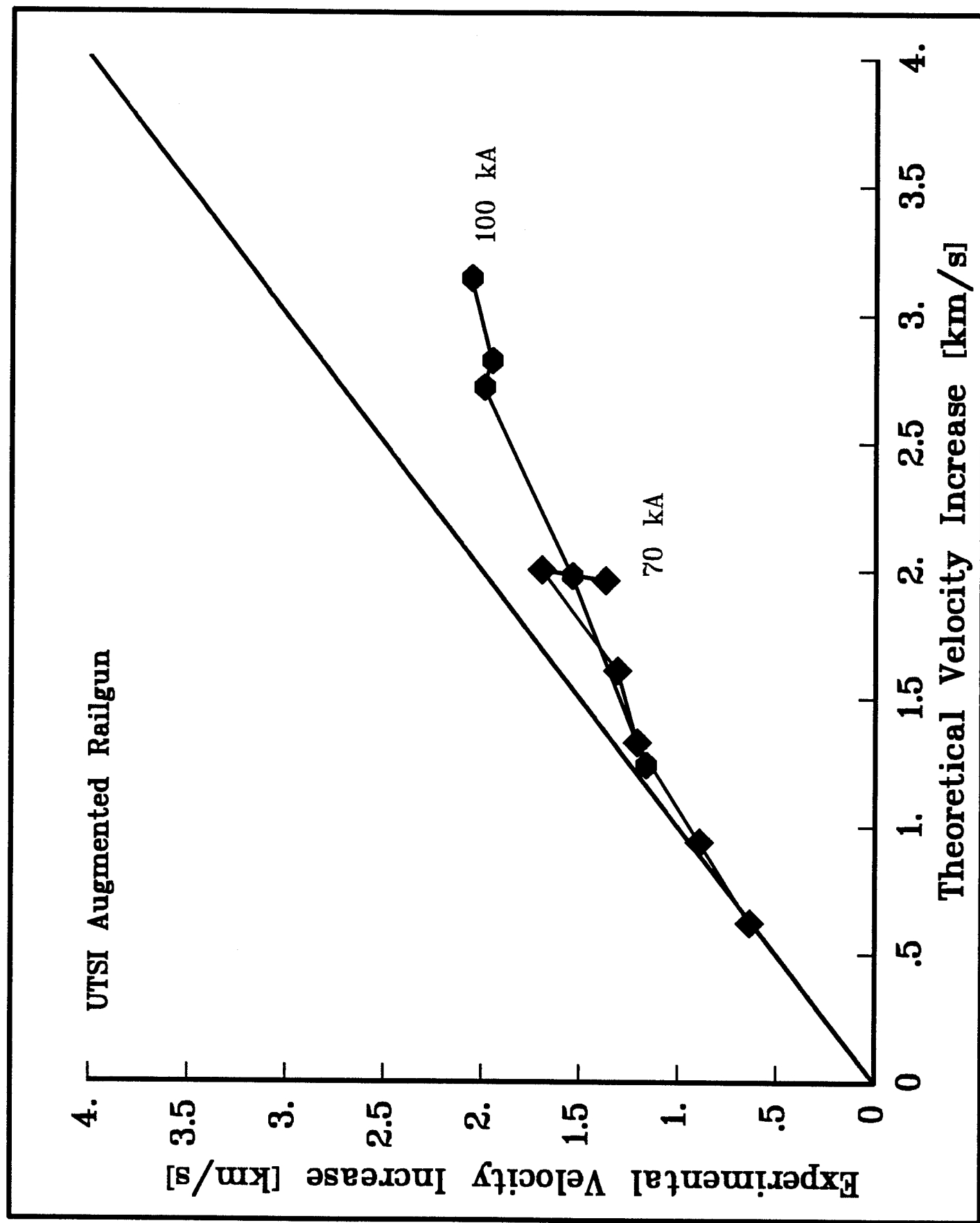
Muzzle-Feed – Armature Velocity

Velocity [m/s]

Time [ms]

Figure 5. Comparison between experimentally observed velocity increase and performance model predictions for augmented railgun.
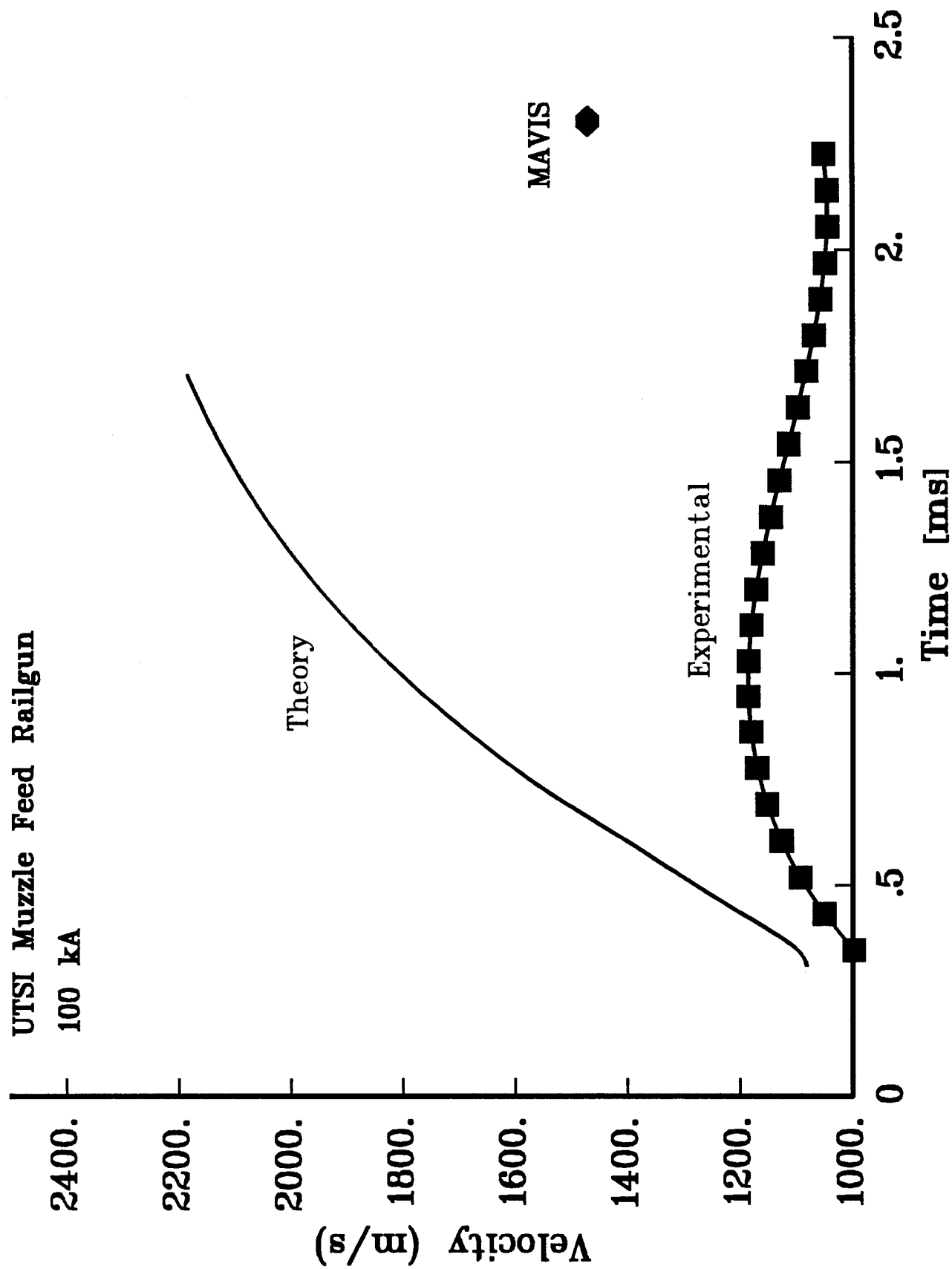
Figure 6. Comparison of railgun model with the experimental velocity for 100 kA muzzle fed

is also essentially constant. The predicted increase in velocity with increasing augmentation is essentially due only to the increased electromagnetic force provided by the augmented turn, less the increased viscous drag due to the higher velocity. Since the observed increase in velocity was less than predicted, we suspected that the electromagnetic force model was inaccurate. For the muzzle fed experiments, again these statements are true except that now the viscous drag should be less with the lower velocities. To further investigate the force model, we employed 3-dimensional simulations using MEGA.

It should also be noted that effects due to primary separation are not well understood at this point and were not included in the model.

V. 3-D ELECTROMAGNETIC SIMULATIONS

The widely used simple railgun electromagnetic force model, $1/2\, L'\, I^2$, can be derived in several ways. The most common is to use conservation of energy, where it is assumed that there are no losses due to eddy currents and that all of the electromagnetic force appears in the moveable armature. Neither of these assumptions are correct for a railgun which has a moving armature and a structure excited by a transient current pulse. Eddy currents are generated both by the transient pulse and the moving armature, and these eddy currents reduce the energy available to do work on the armature. Furthermore, some of the available energy acts to produce a force on the rails and is not available to the armature. Both these effects reduce the electromagnetic force below that predicted by the simple force model of Equation 1 and 2.

These effects are largely 3-D in nature, and to acquire some insight into these processes we used the 3-D, electromagnetic code, MEGA, to perform simulations on a simple railgun model. This simple model was used, rather than the exact geometry used in the experiments, since modeling the complex rail cross section required more computer memory than was available on our IBM RISC 6000 workstation.

The simulation model consisted of a 1 cm square bore with a 0.5 cm long solid armature. Both rail and armature were assumed to be copper, as was the augmenting turn. In order to separate the effects of the transient current pulse and the armature motion, simulations were performed using a Helmholtz step function with an amplitude of 100 kA for the input current. Calculations for both the augmented and muzzle fed railguns used the same current input for both the armature and for the augmenting turn. The inductance gradients L' and M' are inherently 2-D parameters in which it is assumed that the self and mutual inductance are linear functions of railgun length. In order to compare the results of the 3-D simulations with the simple force model, values of L' and M' were calculated as a function of time for this same current input using a 2-D MEGA calculation on the cross section of the rails.

For the simulation parameters chosen, the diffusion of the magnetic field into the copper structure is essentially complete in approximately 300 μs. During this time the values of L' and M' will be changing as the current penetrates deeper into the structure.

A simulation for a 2-D railgun with infinitely wide rails was performed to compare with the 3-D case. Figure 7 shows the current distribution for a 2-D MEGA simulation with an armature velocity of 2 km/s at a time of 300 μs. In the 2-D case the B field is trapped in the bore and diffuses from the back of the armature to the front, and from the inside of the rails to the outside. The effects of eddy current generation due to armature motion remain in the rails at the rear of the armature due to the lack of field diffusion in the rails. In Figure 8 the current distribution for a 3-D MEGA simulation with an armature velocity of 2 km/s at a time of 300 μs is shown. For the 3-D simulation the B field wraps around the armature and rails allowing the field to diffuse from all directions. This accounts for the eddy current generation, due to armature motion, ahead of the armature and for the circulating current in the rails above the armature. These two cases produce significantly different current distributions and thus different force distributions in the armature.

For the conventional railgun simulation in 3-D the total axial force, axial force on the armature and the force predicted from the simple force model are shown in Figure 9. The total axial force is obtained by integrating the axial component of $\mathbf{J} \times \mathbf{B}$ over the whole structure consisting of both armature and rails. The armature force is obtained by integrating the axial component of $\mathbf{J} \times \mathbf{B}$ over the armature volume. After 300 μs the 2 km/s armature force is approximately 8% smaller than that predicted by the simple force model. Note that the force predicted by the simple model at a frequency of 10 kHz (25 μs), the typical practice is to use the high frequency value of L' for performance evaluation, is almost the same as the armature force after the field has diffused.

The forces for the transaugmented case are shown in Figure 10. After 300 μs the 2 km/s armature force is
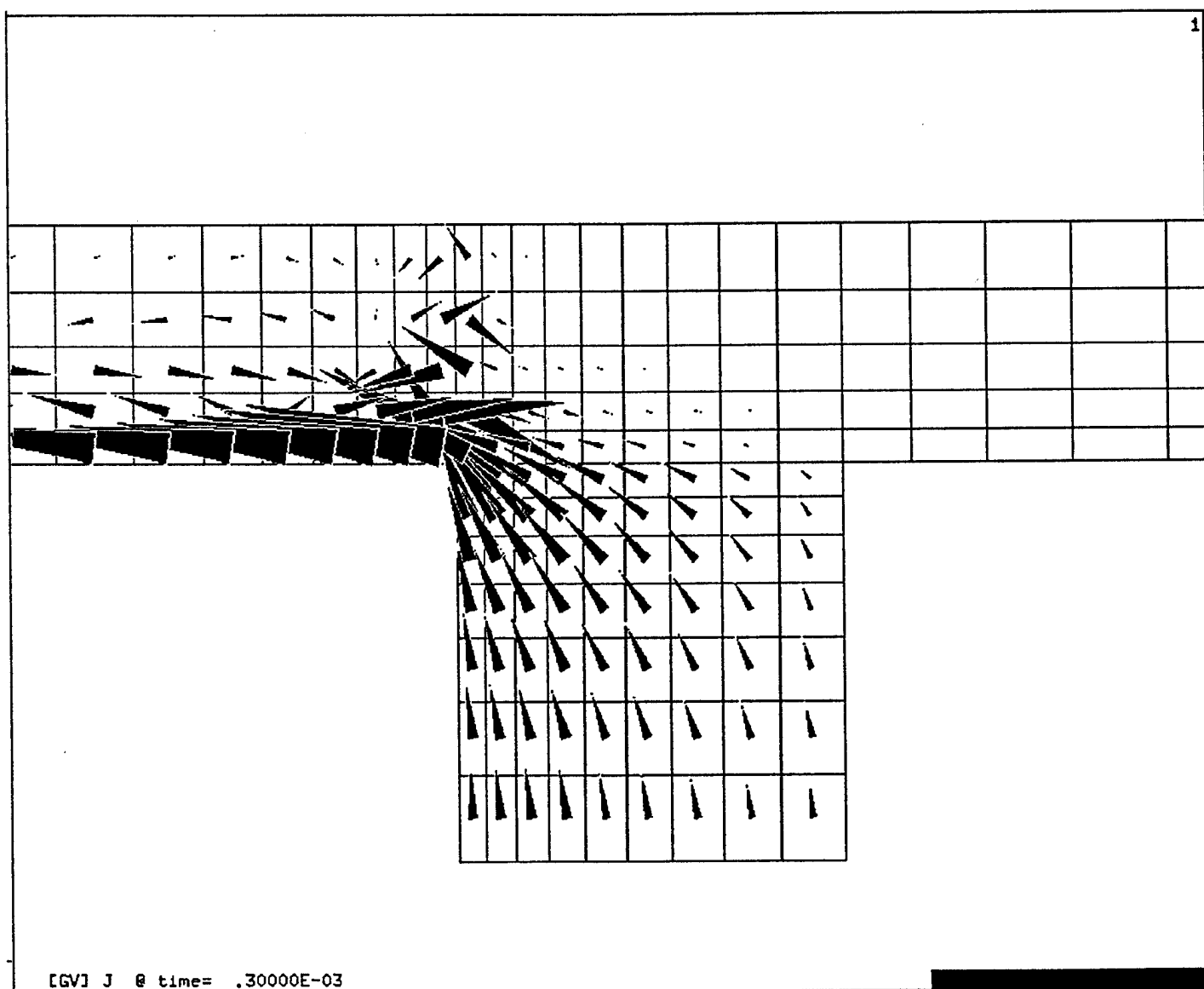
[GV] J @ time= .30000E-03

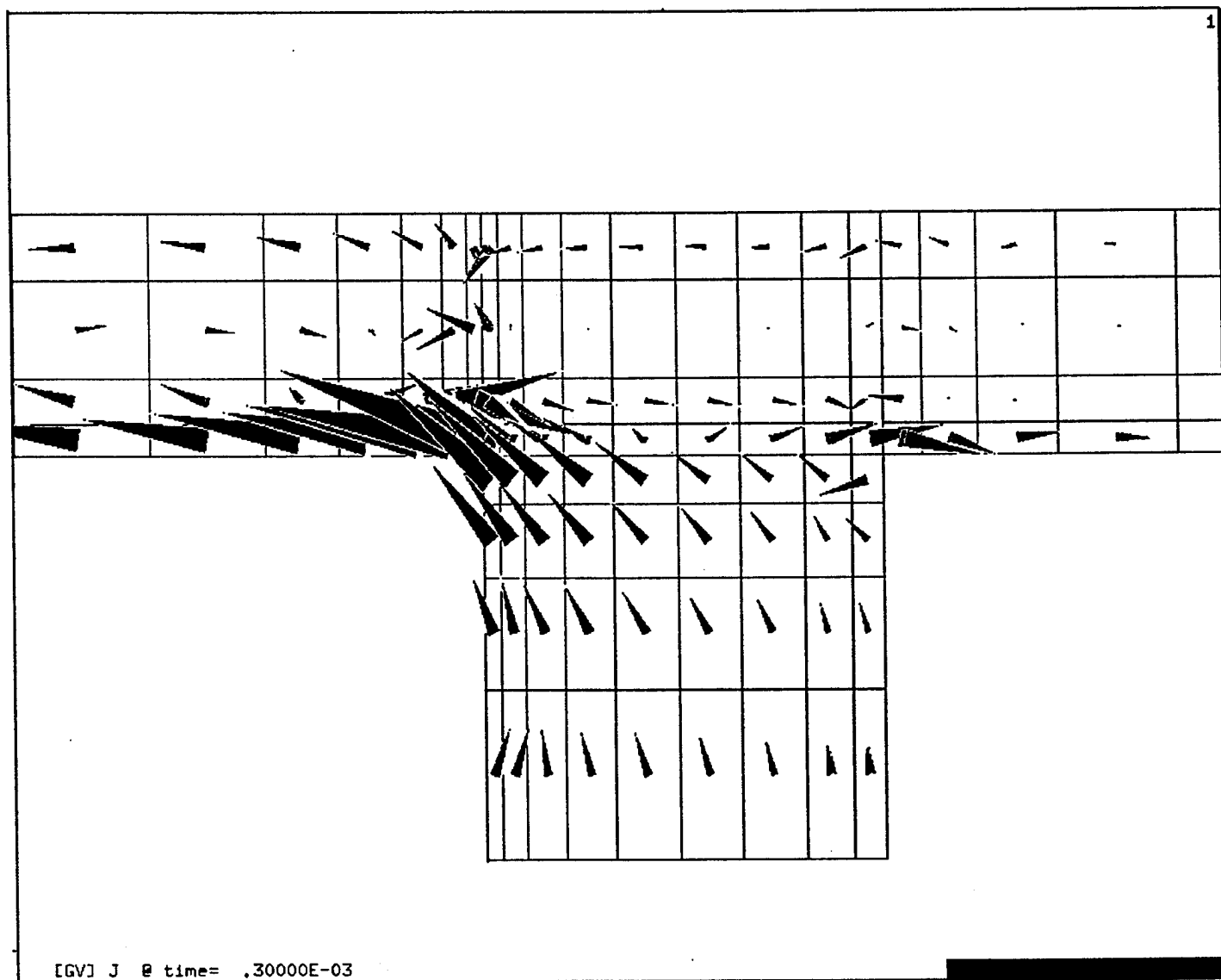Figure 7. Current density for an armature velocity of 2 km/s at a time of 300 μs using a 2-D MEGA simulation.

Figure 8. Current density for an armature velocity of 2 km/s at a time of 300 μs
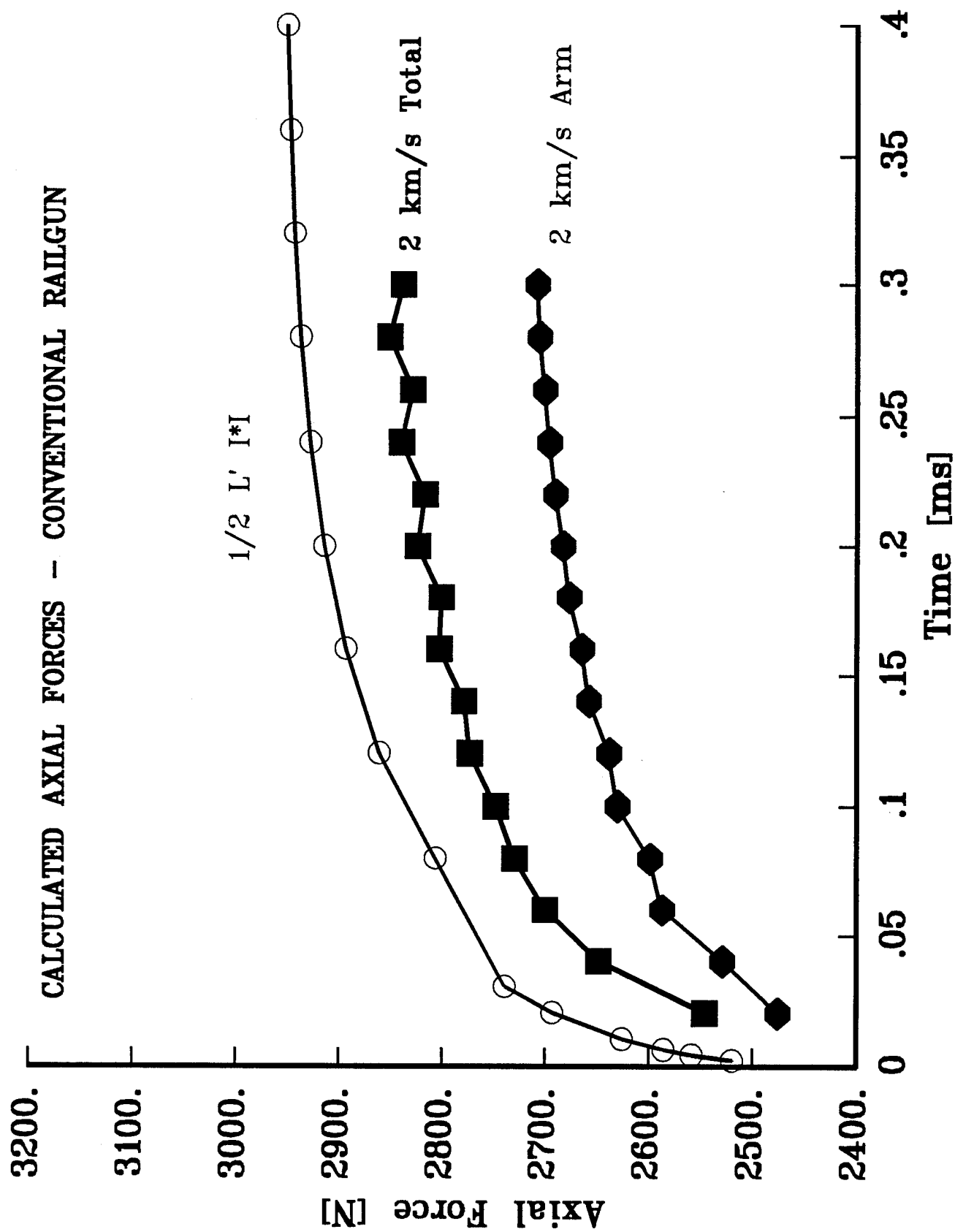using a 3-D MEGA simulation.

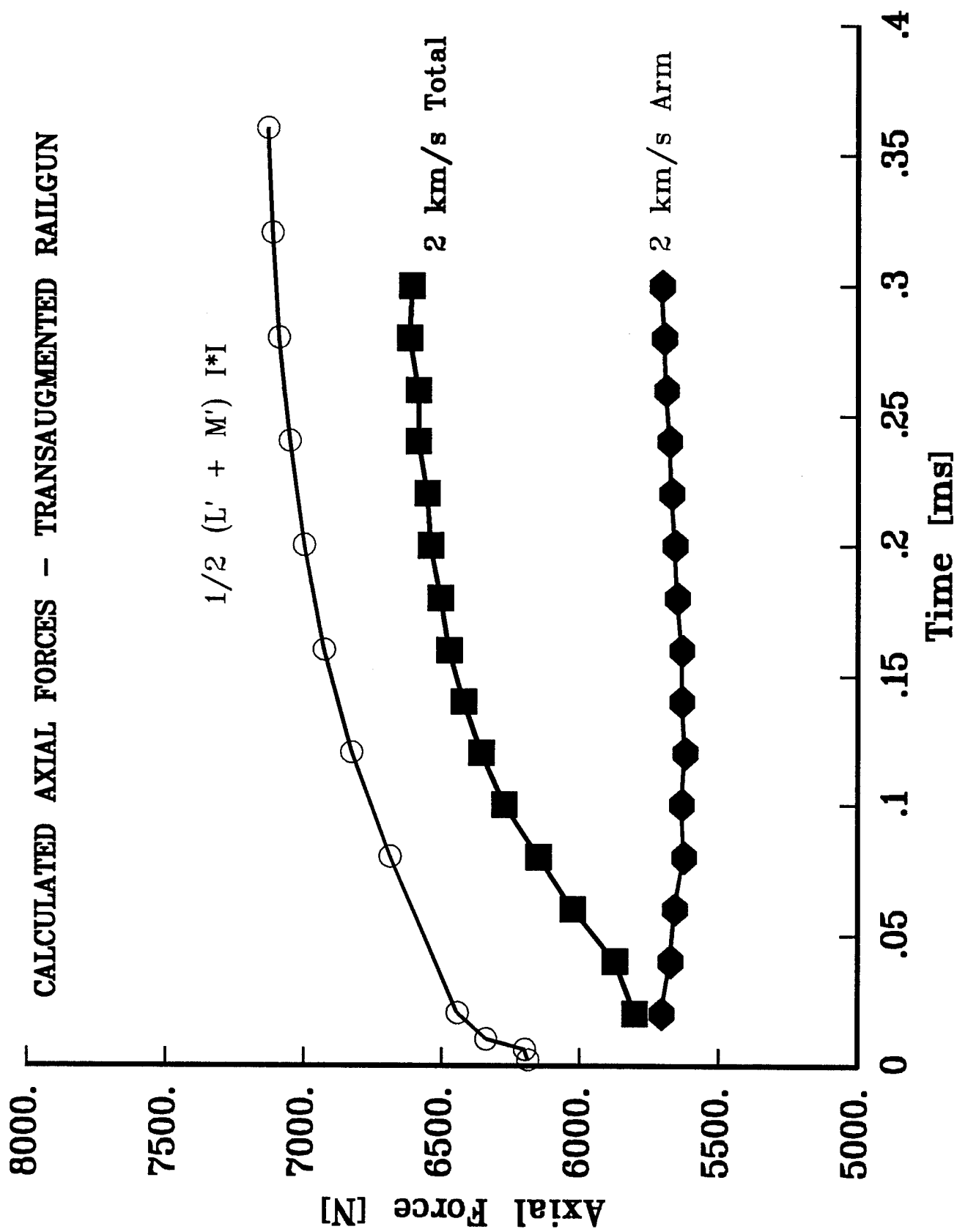Figure 9. Armature and total railgun axial forces for the conventional railgun when aperture closing of

Figure 10. Armature and total railgun axial forces for the augmented railgun at an armature velocity of 2 km/s using 3-D MEGA simulations.

19% smaller than that predicted from the simple force model. Comparing the simple model at 10,000 kHz to the value of the armature force at 300 μs there is still approximately a 10% deficit.

In Figure 11 the forces for the muzzle fed case are seen. For this case one cannot find a preferred frequency to pick his value of L' and M'. Once quasi-steady state has been reached the armature force is only 62% of that predicted by the simple force model.

VI. CONCLUSIONS

3-D simulations using MEGA show that the simple force model overestimates the true armature force. This is significant for the transaugmented case and critical in the muzzle fed case. The missing force is found to be in the rails themselves. More force is exerted in the rails for the augmented and muzzle fed cases due to the augmenting current having had time to diffuse into the interior of the rail prior to the arrival of the armature, and the transverse component of rail current interacts with this larger magnetic field. This acts to reduce the effectiveness of the augmenting rails. For the case of the muzzle fed railgun this was more critical since all accelerating force is provided by the augmented rail.

These facts help but do not fully explain the UTSI railgun experiments. The further key might lie in effects associated with primary separation, which are not yet fully understood. For the muzzle fed experiments MAVIS was a crucial piece of instrumentation. Had it not been for MAVIS the exit velocity of the projectile could not have been determined, thus determining primary separation would not have been so straightforward.

With the UTSI performance model a constant mass was used for the armature, based on the length of the armature measured by the B-dot probes, and armature temperature and composition determined from spectroscopic measurements made on the plasma armature [1]. This is okay as long as there is no mass trapped between the armature and projectile. Once primary separation occurs the armature could start acting as a MHD pump, pumping material into the region between the armature and projectile. This material would not show up on the B-dot traces if it were neutral. The viscous drag associated with this material would be proportional to its mass and could account for the further loss in performance.

The trans-augmented and muzzle fed railgun have turned out to be valuable research tools. The trans-augmenting railgun allows one to vary the applied electromagnetic force without changing the power dissipated in the bore. The muzzle fed railgun has allowed us to quantify the effectiveness of the augmenting rail in a more sensitive way than with the transaugmented railgun.

More importantly the muzzle fed railgun could help us to gain insight into primary separation. Primary separation took place on all UTSI railgun shots limiting acceleration of the projectile at the end of each shot. Primary separation was much more serious for the muzzle fed experiments. Careful bore preparation before each shot has left the electromagnetic current and force distributions as the major difference between conventional and muzzle fed shots. These differences could play a significant role in the fluid dynamics of the armature and contribute to primary separation.

RECOMMENDATIONS

Differences between the muzzle fed, conventional and trans-augmented cases should help to answer questions as to what causes primary separation. MEGA should give initial insight into this question by examining the differences in $\mathbf{J} \times \mathbf{B}$ force distributions over the armature for the conventional, transaugmented and muzzle fed cases. As shown by MEGA calculations 2-D simulations cannot duplicate the force distributions seen in the 3-D conventional railgun. Even more significant is the fact that the muzzle fed electromagnetic force distributions cannot be modeled in 2-D. The electromagnetic force distributions were the only difference in the conventional, transaugmented and muzzle fed experiments. To gain real insight into the problem of primary separation a 3-D MHD code will have to be developed.

Future plans for the UTSI railgun are to use a new cross section design that will have increased values for both L' and M'. The bore itself will be identical to the bore we are currently using. By varying the electromagnetics while keeping bore conditions constant we hope to gain understanding into the physics that limits railgun performance.
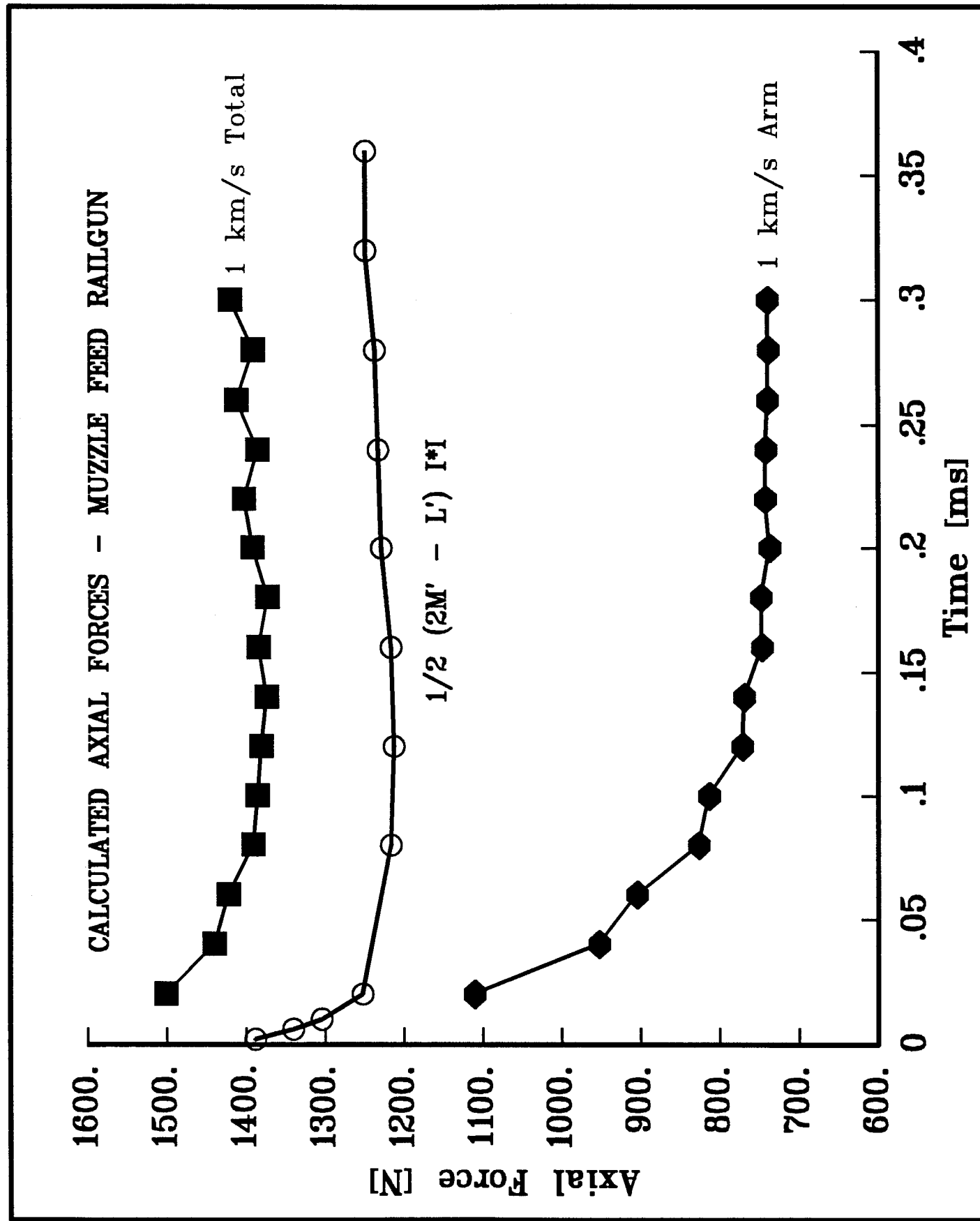
Figure 11. Armature and total railgun axial forces for the muzzle fed railgun at an armature velocity of 1 km/s using 3-D MEGA simulations.

ACKNOWLEDGMENT

BIBLIOGRAPHY

[1]   J. Taylor, R. Crawford, and D. Keefer, "Experimental Comparison of Conventional and Trans-augmented Railguns," *IEEE Trans. on Magn.*, Vol. 29, No. 1, pp. 523-529, Jan. 1993.

[2]   D. Rodger and P. J. Leonard, "Modelling the Electromagnetic Performance of Moving Railgun Launchers Using Finite Elements," *IEEE Trans. Mag.*, Vol. 29, No. 1, pp. 496-498, Jan. 1993.

[3]   John Foster, "Development of a Computational Model of the Gasdynamic and Ablation Effects in Plasma Armature Railguns, UTSI Thesis, May 1993.

[4]   D. Keefer and R. Crawford, "Optical Diagnostics of Railgun Plasma Armatures," *IEEE Trans. on Magnetics*, Vol. 25, No. 1, Jan. 1989.

[5]   J. V. Parker, "Magnetic-Probe Diagnostics for Railgun Plasma Armatures," *IEEE Trans. on Plasma Science*, Vol. 17, No. 3, pp. 487-500, June 1989.

[6]   Allen R. Susoeff, Personal Document With Sketches of Magnetic Induction Device, Nuclear Explosives Engineering Div., Lawrence Livermore Laboratory, October 17, 1990.

[7]   D. Keefer, J. Taylor, and R. Crawford, "The Electromagnetic Force in Railguns,"

[8]   G. E. Rolader and J. H. Batteh, "Effect of in-Bore Gas on Railgun Performance," *IEEE Trans. on Magn.*, Vol. 27, No. 1, Jan. 1991.

[9]   J. V. Parker, W. M. Parsons, C. E. Cummings and W. E. Fox, "Performance Loss Due to Wall Ablation in Plasma Armature Railguns," Conference Title: AIAA 18th Fluid Dynamics and Plasma Dynamics and Lasers Conference, pp. 1-9, July 1985.

MUZZLE-FED RAILGUN EXPERIMENTS

Dennis Keefer, Roger Crawford, and Jaime Taylor
University of Tennessee Space Institute
Center for Laser Applications
Tullahoma, TN 37388-8897

Abstract

The UTSI 2.4 m transaugmented railgun was reconfigured so that current was fed from the breech to the muzzle along the outer rails and then returned to the armature along the inner rails. Experiments were performed using plasma armatures at peak currents of 70 and 100 kA. At a peak current of 100 kA the measured increase in projectile velocity was approximately 500 m/s; less than half of that obtained from a conventional configuration in the same railgun, and considerably less than predicted for the muzzle fed configuration. B-dot probes showed that the armature was very compact, but separated from the projectile soon after fusing. Three-dimensional (3-D) finite element electromagnetic simulations showed that the electromagnetic force on the armature was much less than predicted by the simple force model. The reduction in force was due primarily to axial forces exerted in the rails.

I. Introduction

The muzzle fed configuration, reportedly first operated in the former Soviet Union, is a railgun in which the current is fed into the breech to the muzzle, then returned to the armature via the muzzle. Figure 1 shows a circuit diagram for the muzzle fed configuration. The driving force in a muzzle fed railgun is supplied by the augmenting rail behind the armature. In front
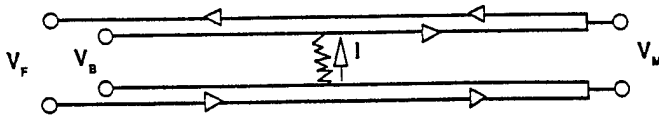
MUZZLE-FED CIRCUIT

Figure 1. Muzzle fed circuit diagram.

of the armature the field produced by the inner rails is mostly cancelled, depending on the coupling between the augmenting and inner rails, by the field produced by the augmenting rails. Extending the circuit analysis used to predict the driving force in augmented railguns to the muzzle fed configuration, the electromagnetic force for the muzzle fed case was obtained as,

$$F = \frac{1}{2} M' I^2 + \frac{1}{2} (M' - L') I^2 \ . \tag{1}$$

Written in this form it is easy to see that as the rails become more coupled and the value of M' approaches that of L', Equation 1 approaches the force equation for a conventional railgun, $1/2 L' I^2$, with M' replacing L'. The first expression in Equation 1 is the force due to the magnetic field produced by the augmenting rail behind the armature and the second expression demonstrates the field cancellation in front of the armature.

In this configuration the armature moves into regions of the rail where the field has already diffused. Cowan suggested that this would eliminate the high current densities produced at the rear of solid armatures by the velocity skin effect [1]. Our further speculation was that for plasma armatures the impedance path for secondaries would increase in this configuration, and this might delay or prevent their formation.

Muzzle fed railgun experiments were performed at UTSI with the same bore conditions as used for the UTSI transaugmented railgun experiments [2,3]. Results of these experiments will be presented. 3-D electromagnetic simulations were performed using MEGA, a finite element code, developed at the University of Bath [4]. These simulations were used to help analyze the experiments and explain the decidedly poor performance of the UTSI muzzle fed railgun.

II. UTSI Railgun Facility

The UTSI 2.4 m long, 1.0 cm round bore, transaugmented railgun was converted to a muzzle feed configuration. A 1.1 m single stage helium gas injector provided pre-acceleration of projectiles into the railgun with a velocity of approximately 1 km/s. The rails were powered by two 240 kJ capacitor discharge power supplies each of which were connected through separate, four sectored, toroidal inductors. The Lexan projectiles of 1 gm mass utilized lip seals and were initiated with an aluminum foil fuse.

Twenty-three B-dot probes, located 100 mm apart, measured changing rail current and were used to obtain accurate armature positions. A MAVIS electromagnetic transducer, placed in the enclosed flight range, was used to provide an accurate time-of-flight measurement of projectile velocity. Consistent bore quality was assured for each experiment by lapping the entire railgun from the light gas gun to the muzzle before each shot using an expandable iron lap. After lapping, acetone was circulated through the bore and dried under vacuum to remove all traces of lapping compound and hydrocarbon residue. This procedure was found to eliminate secondary arcs and provide repeatable performance of our gun. Details associated with the structure, instrumentation and experimental procedure of our railgun can be found in References 2 and 3.

Values of L', the self inductance per unit length, and M', the mutual inductance per unit length, were needed for performance evaluations. These values were obtained from a 2-D calculation using the MEGA code for the cross section of our gun [2,3] at a frequency of 10 kHz. The value of 0.274 μH/m was obtained for L' and a value of 0.249 μH/m was obtained for M'.

III. Experimental Investigation

Four experiments were performed on the muzzle fed railgun, one at a peak current of 70 kA and three at a peak current of 100 kA. The experimental results are given in Table 1, together with results for similar experiments in the conventional configuration for comparison. The increase in velocity for the 100 kA muzzle fed experiments achieved less than 50% of the expected change in velocity calculated from Equation 1. This was even more significant than it appears, since most of the acceleration seen in the experiment could be accounted for by thermal forces exerted during the fusing transient. Since the initial experimental results differed so much from prediction, three experiments were performed at 100 kA to establish repeatability.

Table 1. Summary of UTSI 2.4 m Muzzle Fed Railgun Experiments.

Shot	Type	Peak Rail Current (kA)	Mass of projectile (gm)	Muzzle Velocity (km/s)	Δv_E Measured (km/s)	$\frac{\Delta v_E}{\Delta v_{electromagnetic}}$ (%)
08/16/91	Conven	67	.980	1.669	.630	116
10/24/91	Conven	105	.979	2.258	1.162	101
06/17/91	Conven	106	.984	2.476	1.365	115
11/20/92*	Conven	109	1.06	2.008	.988	79
11/11/92	Muz Fed	70	1.03	1.292	.279	67
11/18/92	Muz Fed	106	1.05	1.470	.457	48
12/14/92ᵃ	Muz Fed	106	1.06	1.350	<.400	<41
01/27/93	Muz Fed	108	1.06	1.496	.429	41

* Secondary developed

ᵃ Entrance velocity could not be determined from data. Nominal entrance velocity for this railgun has been 1.0 ± 0.05 (km/s), there was nothing to suggest this was not a nominal shot.

The B-dot signals indicated a compact well-formed plasma armature with no evidence of secondary formation. Figure 2 shows the armature velocity obtained from the B-dot probes, together with the exit velocity obtained from MAVIS, notice the severe primary separation. Results for a similar experiment in the conventional railgun configuration are also shown in Figure 2 for comparison. The armature velocity scarcely exceeds the initial velocity. It is likely that most of the increase in projectile velocity is due to the electrothermal "kick" which accompanies the fusing transient.
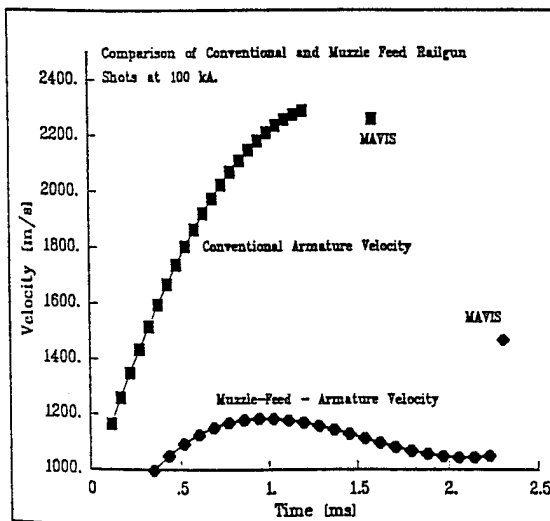
Equation 1 can be rearranged in the form $1/2 L'_{eff} I^2$ where L'_{eff} has the value, obtained from L' and M', of 0.224 μH/m. This is 82% of the value of L'. From the simple electromagnetic force models the force for the muzzle fed shots should have been 82% of that for the conventional shots. However, as can be seen in Table 1 and Figure 2, the change in velocity measured for the muzzle fed configuration was less than half of that measured for the conventional case. There were no secondary arcs or other anomolous effects observed, so where did the excess force go? We conducted some 3-D electrodynamic simulations using MEGA to help formulate an answer to this question.

IV. 3-D Electromagnetic Simulations

The 3-D finite element code MEGA was used to simulate a generic muzzle fed railgun in order to provide some insight into these experimental results. A simple generic railgun model was used, rather than the exact geometry used in the experiments, since modelling the complex rail cross section required more memory than was available on our IBM RISC 6000 workstation.

The simulation model consisted of a 1 cm square bore railgun with a 0.5 cm long solid armature. The rail width was 1 cm and the rail thickness was 3 mm. The separation of inner and augmenting rail was 1.5 mm. Copper was assumed for both rails and armature. A Helmholtz step function input current with an amplitude of 100 kA was used for both fixed armatures and constant velocity moving armatures. Details of the simulation can be found in Reference 5, presented in these proceedings.

Using MEGA, the axial component of the JxB force was integrated just over the armature and also over the total computational domain. Figure 3 shows the axial force in the armature and the total axial force for an armature velocity of 1 km/s, together with the force predicted by Equation 1. The field diffused into the structure reaching a steady state in approximately 300 μs. Note that the effective value of L' decreases in time as the fields diffuse into the structure. This is opposite the effect observed for the conventional railgun. The MEGA simulations predict that the total axial force exerted on the structure (rails plus armature) at 300 μs are 13% greater than predicted by Equation 1. However, the force exerted on the armature is only 53% of the total force and 59% of the force predicted by Equation 1.

Figure 2. Comparison of conventional and muzzle fed railgun shots with 100 kA peak current.
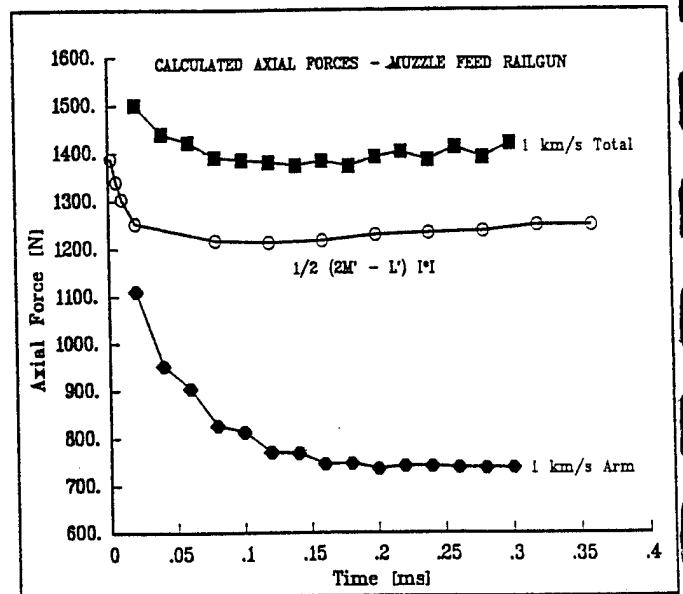

Figure 3. Armature and total axial forces for the muzzle fed railgun at an armature velocity of 1 km/s using 3-D MEGA simulations.

The difference in the axial force on the armature and Equation 1 results from force exerted in the rails, 82% of which is found behind or above the armature. The magnetic field produced by the current in the outer rail diffuses into the inner rail prior to the arrival of the armature. A large eddy current forms in the rail behind the armature, and the transverse component of this current interacts with the magnetic field from the outer rail to produce the large axial rail force (Figure 4). Figure 4 is in the plane of symmetry between the insulators.
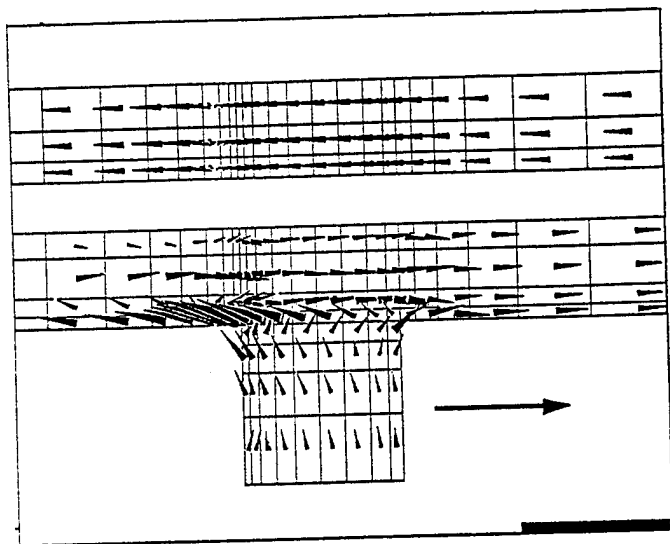
Figure 4. Current density for an armature velocity of 1 km/s at time of 300 μs using a 3-D MEGA simulation.

It was suggested by Cowan [1] that the muzzle fed configuration could reduce the velocity skin effect. The current distribution for the muzzle fed configuration with an armature velocity of 1 km/s, as calculated with MEGA, was more uniform than for the conventional case (Figure 5). The peak current density in the armature of the muzzle fed case was approximately half that seen in the conventional case, and appeared in the rear of the armature for both cases. For the generic model used in our simulations, one would have to approximately double the total current in the muzzle fed case to achieve the same driving force as in the conventional case, thus eliminating any advantages gained.
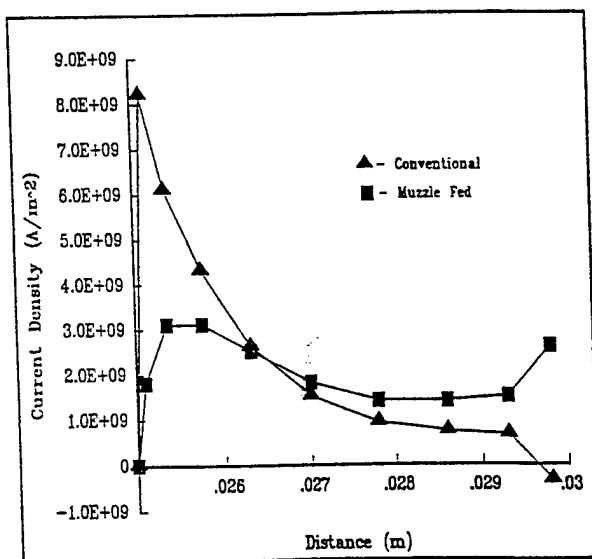
Figure 5. Current distribution in armature for conventional and muzzle fed railguns 0.2 mm below rail and armature interface.

V. Summary

Plasma armature experiments in a muzzle fed railgun have shown significantly poorer performance than a conventional railgun. The 3-D MEGA simulations for the muzzle fed railgun have shown that the simple force model overestimates the armature force by a factor of approximately two. A significant fraction of the available force predicted by Equation 1 acts to produce an axial force in the rails. By identifying the inadequacy of the simple force model, we have accounted for a large fraction of the velocity deficit that might otherwise have been attributed to fluid mechanical drag effects. The muzzle fed configuration has been found to be of no practical interest for electromagnetic launchers. However, as with the transaugmented railgun, it has turned out to be a valuable research tool.

References

[1] M. Cowan, "Solid-Armature Railguns without the Velocity Skin Effect," IEEE Trans. on Magn., Vol. 29, No. 1, pp. 385-390, January 1993.

[2] J. Taylor, R. Crawford and D. Keefer, "Experimental Comparison of Conventional and Trans-Augmented Railguns," IEEE Trans. on Magn., Vol. 29, No. 1, pp. 523-529, January 1993.

[3] D. Keefer, J. Taylor and R. Crawford, "The Electromagnetic Force in Railguns," in Proceedings of the Fourth European Symposium on Electromagnetic Launch Technology Conference, May 2-6, 1993, Celle, Germany, Paper No. 1503.

[4] D. Rodger and P. J. Leonard, "Modelling the Electromagnetic Performance of Moving Railgun Launchers Using Finite Elements," IEEE Trans. Magn., Vol. 29, No. 1, pp. 496-498, January 1993.

[5] J. Taylor and D. Keefer, "Calculations of the Electromagnetic Force in Railguns," Proceedings of the Ninth IEEE Pulsed Power Conference, June 21-23, 1993, Albuquerque, New Mexico.

CALCULATIONS OF THE ELECTROMAGNETIC FORCE
IN RAILGUNS

Jaime Taylor and Dennis Keefer
University of Tennessee Space Institute
Center for Laser Applications
Tullahoma, TN 37388-8897

Abstract

Recent experiments in the UTSI 2.4 m railgun have led us to reexamine the electromagnetic force in railguns. The 3-dimensional (3-D) finite element code MEGA, developed at the University of Bath, was used to simulate the transient electromagnetic field in conventional, transaugmented and muzzle fed railgun configurations. These time-dependent simulations used a step input of current together with armature velocities of 0, 1 and 2 km/s. The force available to the armature was found to be less than predicted by the inductance gradient of the railgun. The missing force on the armature was primarily due to forces exerted in the rails.

I. Introduction

Failure of the UTSI transaugmented [1], muzzle fed [2] and conventional railgun experiments to agree with the standard railgun models have led us to reexamine the electromagnetic force in railguns. Rashleigh and Marshall reported the force exerted on the armature and projectile of a conventional railgun to be,

$$F = \frac{1}{2}L'I^2, \tag{1}$$

where L' is the self inductance per unit length of the rails and I is the driving current [3]. The most common way to obtain Equation 1 is through conservation of energy for a conservative system where it is assumed that there are no eddy currents and that all of the mechanical work done by the system results from the armature motion. The electromagnetic force on the armature of a transaugmented railgun obtained in this same manner is,

$$F = \frac{1}{2}L'I_1^2 + M'I_1 I_2, \tag{2}$$

where M' is the mutual inductance per unit length of the rails. The electromagnetic force on the armature of a muzzle fed railgun is similarly,

$$F = \frac{1}{2}(2M' - L')I^2. \tag{3}$$

Equations 1, 2 and 3 will be referred to as the simple force model (SFM).

There are three important assumptions in the derivation of the SFM: The system is conservative, the mutual and self inductances of the railgun circuits are proportional to the length of the circuit and all the mechanical work is done by the armature. The first is violated because eddy currents are generated both by the transient current pulses used in railguns and by the relative motion of the rails and the armature. These eddy currents violate the assumption of a conservative system and reduce the magnetic energy available to do mechanical work. The second is violated because the induction of the circuit changes with time due to diffusion of the magnetic fields into the railgun structure and changes in the magnetic field near the armature caused by velocity induced eddy currents in the rails. The third is incorrect since some of the axial force in a railgun is exerted directly in the rails producing strain energy in the structure rather than force on the armature.

The railgun is a 3-D device, and 2-D analyses of the magnetic fields do not accurately predict the eddy currents that exist in the 3-D structure. We have used the 3-D finite element code MEGA, developed at the University of Bath [4], to analyze conventional, transaugmented and muzzle fed railgun configurations. These simulations provide insight into the complicated transient magnetic field structure and provide an estimate for the magnitude of the available armature force.

II. 3-D Electromagnetic Simulations

A simple generic railgun model was used for these simulations, rather than the exact geometry used in the UTSI experiments, since modeling the complex rail cross section required more memory than was available on our IBM RISC 6000 workstation.

The generic model, shown in Figure 1, consisted of a 1 cm square bore railgun with a 0.5 cm long solid armature. The width of the inner and augmenting rails were the same and equal to the armature width. The rails were 3 mm thick with a 1.5 mm gap between the inner and augmenting rails. Both the rails and armature were assumed to be copper, as was the augmenting turn. Fixed and constant armature velocity simulations of 1 and 2 km/s were performed. A Helmholtz step function input current of 100 kA was used for all simulations. By using a step input, instead of a typical current pulse, a quasi-steady-state was reached after a period of time and made it possible to separate the transient effects from the effects of the armature motion.
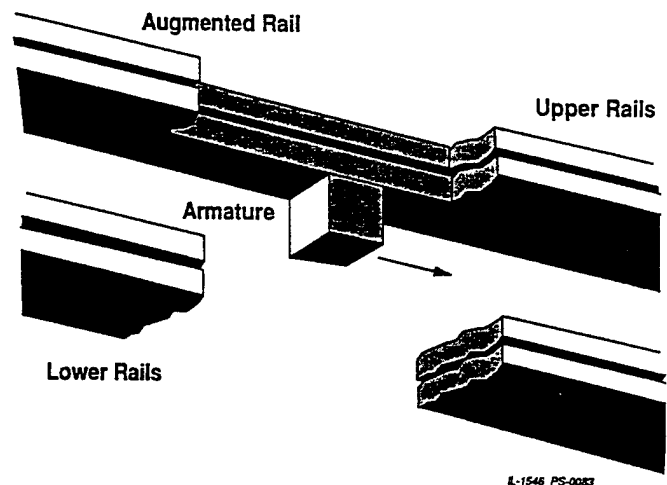

Figure 1. Sketch showing the section through the generic railgun used for presentation of graphical results from MEGA simulations.

Calculations for the transaugmented and muzzle fed railgun used the same current input for both the armature and for the augmenting turn. The "inductance gradients" L' and M', are inherently 2-D parameters in which it is assumed that the self and mutual inductance are linear functions of railgun length. In order to compare the results of the 3-D simulation with the SFM, values of L' and M' were calculated as a function of time for this same current input using a 2-D MEGA calculation. For the 3-D cases, the axial force

$$F_z = \int \mathbf{J} \times \mathbf{B} \cdot \hat{z} dV, \qquad (4)$$

was integrated over both the armature region and the total computational domain to obtain the driving force on the armature (F_a) and the total force (F_t) in the axial direction. The difference between the two was the axial force exerted in the rails.

For the 3-D case there was no way to explicitly check MEGA's accuracy. The muzzle fed case offered the most unexpected results and was checked for grid dependencies over grids which doubled in node spacing in the xy-plane (cross section of the railgun) and along the z-axis (direction of armature acceleration). By doubling the node spacing in the xy-plane F_a changed by approximately 1.5% indicating little grid dependence in this plane. The node spacing was doubled three times in the z-direction to create four separate grids. The armature force was sensitive to the spacing in the z-direction but appeared to approach a limiting value with smaller grid spacing.

There was a slight time step dependence of the value obtained for the forces. For the simulation parameters chosen, the diffusion of the field into the copper structure was essentially complete in approximately 300 μsec. The time step and interval were both set to obtain maximum resolution during the transient part of the problem.

A 2-D railgun, one with infinitely wide rails, was also simulated and compared with the 3-D conventional case.

III. Results

Figure 2 shows the current distribution at 300 μsec for the 2-D railgun with an armature velocity of 2 km/s. The current concentrated at the rear of the armature and there was no current in the rails ahead of the armature. Figure 3, shown in the plane of symmetry between the insulators (see Figure 1), shows
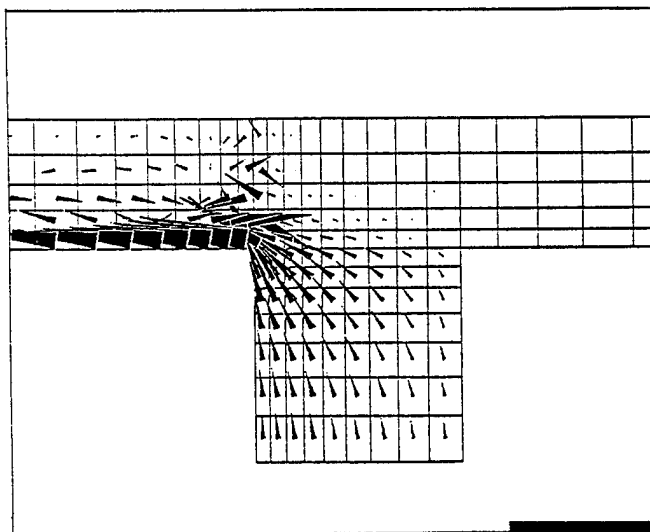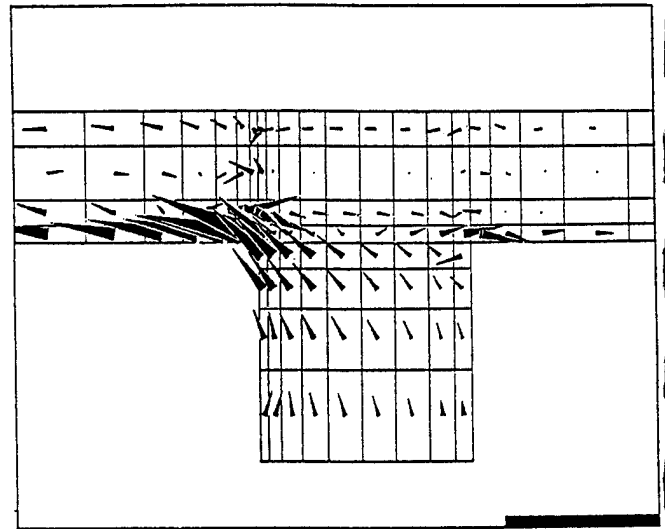

Figure 3. Current density for an armature velocity of 2 km/s at a time of 300 μs using a 3-D MEGA simulation.

the current distribution at 300 μsec for the 3-D conventional railgun with an armature velocity of 2 km/s. Eddy currents were generated in front of the armature for this case, since in 3-D the B-field can wrap around the armature and penetrate into the region ahead of it. In the 2-D case the B-field in front of the armature between the rails was zero.

Table 1 lists the armature force, the total force and the force calculated from the SFM at 300 μsec for the conventional, transaugmented and muzzle fed railguns. Figure 4 shows the axial force in the armature and the total axial force for an armature velocity of 2 km/s, together with the force predicted by the SFM. For the conventional case it is seen that the total force was in relative agreement with the SFM. The armature force for the stationary armature case was less than that for the case with a moving armature. This is due to the velocity skin effect which limits penetration of the magnetic fields into the rails near the armature and reduces the fraction of the total force which is exerted on the rails.

Figure 2. Current density for an armature velocity of 2 km/s at a time of 300 μs using a 2-D MEGA simulation.
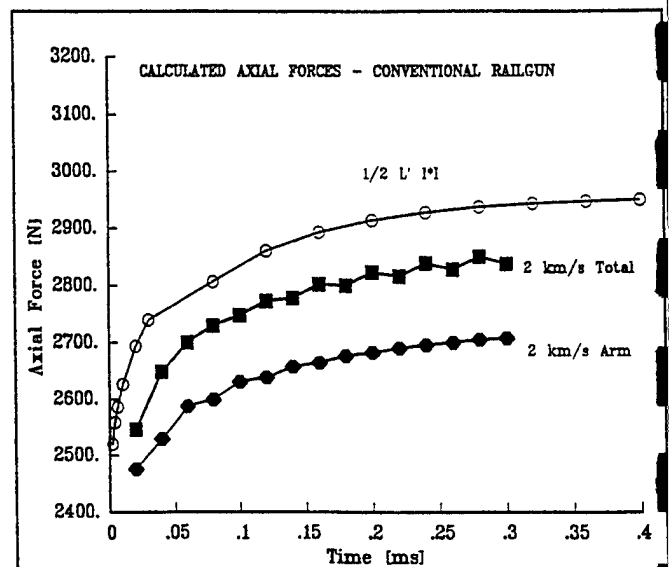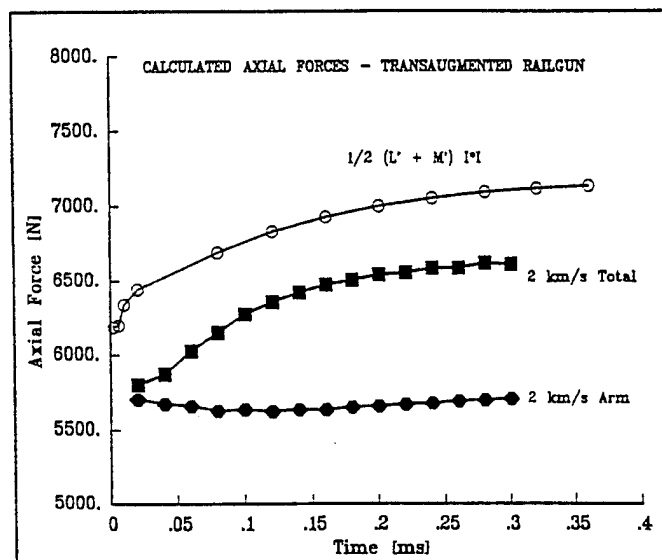

Figure 4. Armature and total axial forces for the conventional railgun at an armature velocity of 2 km/s using a 3-D MEGA simulation.

Table 1. The Armature, Total and Simple Model Forces at 300 μsec.

	ARMATURE	F_a	F_t	SFM
CONVENTIONAL	Stationary	2500	2907	2938
	2 km/s	2708	2838	
TRANS-AUGMENTED	Stationary	5564	7080	7098
	2 km/s	5704	6608	
MUZZLE FED	Stationary	581	1323	1243
	1 km/s	738	1418	

For the transaugmented case with an armature velocity of 2 km/s, once quasi-steady-state had been reached, the SFM overestimated the armature force by 19%. If one were to use the high frequency limit values for L' and M', the typical practice for performance evaluation, then the armature force would be overestimated by 10%. Figure 5 shows the forces for the 2 km/s case as a function of time. The armature force remains relatively constant in time while the total force increases as the B-field penetrates into the structure [5].

Figure 5. Armature and total axial forces for the augmented railgun at an armature velocity of 2 km/s using a 3-D MEGA simulation.

Figure 6 shows the axial force in the armature and the total axial force for an armature velocity of 1 km/s, together with the force predicted by Equation 3. For the muzzle fed case the armature force was only 59% of that predicted by the SFM for an armature velocity of 1 km/s, once quasi-steady-state had been reached. Unlike the transaugmented case this prediction becomes worse when taking the high frequency values of the inductance gradients. This shows a significant breakdown of the SFM used to calculate the armature force. Details of the experimental results for the muzzle fed railgun are described in another paper in these proceedings [2].
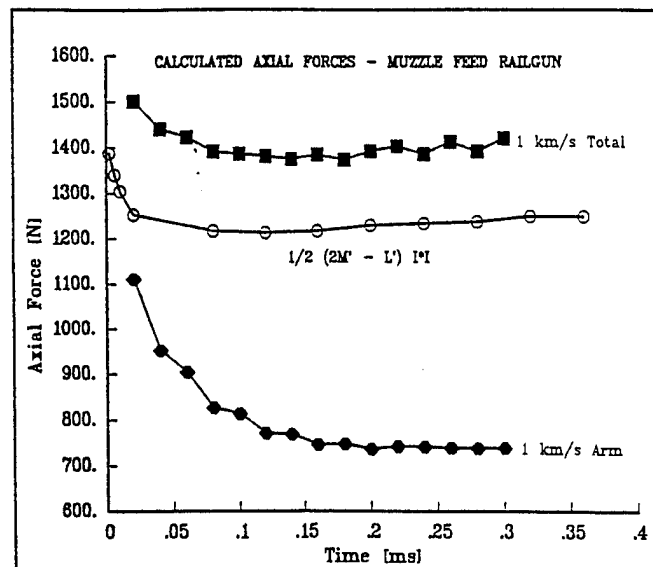

Figure 6. Armature and total axial forces for the muzzle fed railgun at an armature velocity of 1 km/s using 3-D MEGA simulations.

IV. Conclusions

3-D simulations using MEGA show that the SFM overestimates the true armature force. The difference was larger for the transaugmented case than the conventional case because a larger fraction of the available force was exerted in the rail. This occurs because the field from the augmenting rail has had time to diffuse into the interior of the rail prior to arrival of the armature. The SFM overestimates the armature force for the muzzle fed railgun by nearly a factor of two.

Acknowledgement

References

[1] J. Taylor, R. Crawford and D. Keefer, "Experimental Comparison of Conventional and Trans-Augmented Railguns," IEEE Trans. on Mag., Vol. 29, No. 1, pp. 523-529, January 1993.

[2] D. Keefer, Roger Crawford and Jaime Taylor, "Muzzle-Fed Railgun Experiments," Proceedings of the Ninth IEEE Pulsed Power Conference, June 21-23, 1993, Albuquerque, New Mexico.

[3] S. C. Rashleigh and R. A. Marshall, "Electromagnetic Acceleration of Macroparticles to High Velocity," J. Appl. Phys., Vol. 49, pp. 2540-2542, April 1978.

[4] D. Rodger and P. J. Leonard, "Modelling the Electromagnetic Performance of Moving Railgun Launchers Using Finite Elements," IEEE Trans. Mag., Vol. 29, No. 1, pp. 496-498, January 1993.

[5] D. Keefer, J. Taylor and R. Crawford, "The Electromagnetic Force in Railguns," Proceedings of the Fourth European Symposium on Electromagnetic Launch Technology Conference, May 2-6, 1993, Celle, Germany, Paper No. 1503.

559

The Electromagnetic Force in Railguns

Dennis Keefer, Jaime Taylor and Roger Crawford
The University of Tennessee Space Institute
B. H. Goethert Parkway
Tullahoma, TN 37355

Abstract

A 2.4 m long, 1 cm diameter railgun was constructed to permit careful experimental comparison of the performance obtained with plasma armatures in both conventional and transaugmented railgun configurations. A performance model was developed which included the effects of electrothermal acceleration, compression of the bore gases ahead of the projectile, viscous and ablation drag. The electromagnetic forces were modeled as $1/2L'I_1^2 + M'I_1I_2$. Comparison of the experimental result revealed that at least one of the force or drag models was incorrect. Subsequent examination of the electromagnetic forces using the three-dimensional electromagnetic code MEGA indicates that the electromagnetic force is less than that predicted using the simple circuit model.

Introduction

In the seminal experiments of Rashleigh and Marshall [1] in 1978, railguns achieved a velocity of 5.9 km/s. Since that time, the velocity performance of railguns has been predicted using the circuit model value of $1/2L'I^2$ for the electromagnetic force. Hawke [2] conducted a series of experiments in a 5.2 m long railgun and showed a significant departure from the predicted velocity in the range of 4 km/s. High velocity railgun experiments using plasma armatures have largely failed to achieve their predicted velocity, and for the most part have not exceeded the nominal 6 km/s achieved in 1978. Parker [3,4] attributed this discrepancy to armature fluid effects, primarily ablation drag and the resulting secondary arc formation, and suggested the use of ablation resistant materials for the rails and insulator. However, conventional railguns utilizing ablation resistant bore materials have generally failed to exceed the nominal 6 km/s barrier.

The transaugmented railgun is an ideal experimental configuration to investigate the forces in a railgun, since it permits a decoupling of the total electromagnetic force and the power dissipated in the armature. In most ablation drag models the rate of mass ablation is assumed to be proportional to the electrical power dissipated in the armature. The additional magnetic field provided by augmentation makes it possible to vary the total electromagnetic force at a constant dissipated armature power.

We have conducted two series of experiments in a carefully prepared railgun in which no secondary arcs formed and the armature currents were essentially constant. It was possible to vary the total electromagnetic force by as much as a factor of three using an independently powered augmenting turn [5]. A detailed performance model was constructed which includes all the known fluid mechanical drag effects, electrothermal acceleration and the usual model for the electromagnetic force [5],

$$F = 1/2L'I_1^2 + M'I_1I_2 . \qquad (1)$$

Comparison of the experimentally observed velocity with the performance model suggested that the electromagnetic forces had been overestimated. We have performed a series of 3-dimensional electromagnetic simulations of both conventional and augmented railgun configurations with moving armatures using MEGA [6]. These simulations show that the electromagnetic force on the armature is reduced below that predicted by the simple circuit model in Equation 1.

Transaugmented Railgun Experiments

The UTSI transaugmented railgun was designed to function as either a conventional or augmented railgun with a 2.4 m long barrel and a 1.0 cm bore diameter. A 1.1 meter single stage helium gas injector provided pre-acceleration of projectiles into the railgun with a velocity of approximately 1 km/s. The design featured copper rails and G-9 insulators supported by a G-10 substructure [5]. The armature and augmentor circuits were powered by separate 240 kJ capacitor discharge power supplies connected through separate four-sectored, toroidal inductors. Lexan projectiles of approximately 1 gm mass with flexible lip seals and an aluminum foil fuse were used to initiate the plasma armatures.

Twenty-three B-dot probes located 100 mm apart measured changing rail current and were used to obtain accurate armature positions. Two z-axis (oriented to measure the primary magnetic field component) and three armature B-dots were also installed. Two pressure transducers were located 95 and 55 mm before the breech end of the rails. These were used to initiate the timing for the data acquisition system and power supplies, to measure the entrance velocity of the projectile as it entered the rails and to measure the pressure of the gas in the bore. A MAVIS electromagnetic transducer, placed in the enclosed flight range, was used to provide accurate muzzle velocity measurements [7].

Consistent bore quality for both conventional and augmented shots was maintained by lapping the entire railgun from the light gas gun to the muzzle using a rotating, expandable iron lap before each shot. After lapping, acetone was circulated through the bore and then dried under vacuum to remove all traces of lapping compound and hydrocarbon residue. This procedure was found to eliminate the secondary arcs which are often observed when using plasma armatures.

Two series of experiments were performed, one using a nominal peak armature current of 70 kA and the second using a nominal peak current of 100 kA. Since the muzzle voltage was essentially the same at either current, this resulted in an increase of the dissipated armature power of approximately 43% with the higher peak current, independent of the degree of augmentation. In the absence of augmentation the self armature force was greater by a factor of approximately two at the higher current. The augmenting current ranged from zero to 140 kA giving a factor of three range of total armature force for the 70 kA series and a factor of two range of total armature force for the 100 kA series.

The results of these experiments are given in Table 1. The measured increase in projectile momentum is plotted as a function of the total electromagnetic impulse in Figure 1. The total electromagnetic impulse is defined as the integral of the force given by Equation 1 over the time the projectile is in the barrel. A straight line representing equality of impulse and momentum is also plotted for comparison. At the lowest range of values, some of the measured values of momentum increase exceed that expected from the electromagnetic force, even though no drag mechanisms are included. At low values of electromagnetic impulse, the greater than predicted momentum change may be attributed to continuing gasdynamic expan-
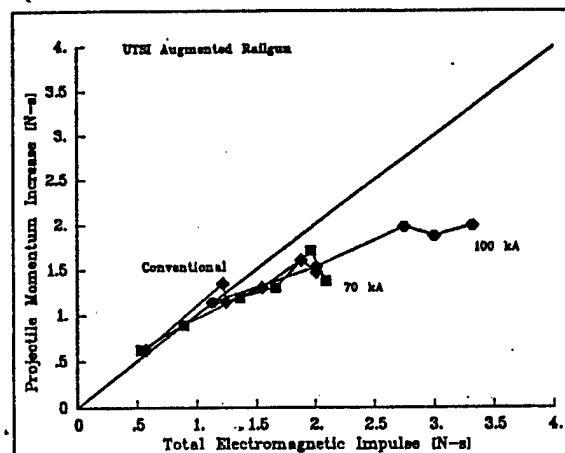

Figure 1: Comparison of increased projectile momentum with electromagnetic impulse for conventional and augmented railgun experiments.

sion of the accelerator gas and the electrothermal acceleration produced during the fusing transient and by expansion of ablation products heated by the armature.

At the higher values of electromagnetic impulse, the measured values of momentum increase are less than that predicted from the electromagnetic impulse. It is important to note that this deficit in measured performance occurs in the absence of secondary arcs, and that it occurs gradually without the characteristic sudden onset at higher velocities as observed by Hawke [2]. However, primary separation, where a space develops between the primary plasma armature and the base of the projectile, was observed near the muzzle in nearly all of our experiments. The loss of acceleration due to this effect is not well understood [8], and was not included in our performance model. These data represent a wide range in the degree of augmentation, but the data tend to fall along a single curve. The measured increase in momentum appears to depend only on the electromagnetic impulse, regardless of the degree of augmentation used in generating the electromagnetic force.

Table 1. Summary of UTSI 2.4 m Railgun Experiments

Shot	Peak Rail Current (kA)	Peak Augmented Rail Current (kA)	Mass of projectile (gm)	Muzzle Velocity (km/s)	$\Delta\ v_E$ Measured (km/s)	$\dfrac{\Delta\ v_E}{\Delta\ v_{electromagnetic}}$ (%)
Conventional						
8/16	67	0	.980	1.669	.630	116
10/24	105	0	.979	2.258	1.162	101
6/17	106	0	.984	2.476	1.365	115
11/20*	109	0	1.06	2.008	.988	79
9/19	120	0	.992	2.379	1.299	84
9/6	134	0	.994	2.655	1.602	85
7/30	138	0	.996	2.493	1.469	73
Augmented						
9/25	68	30	.980	1.966	.886	99
1/14	67	71	.985	2.333	1.203	87
1/10	64	103	.994	2.36	1.305	78
1/16*	65	138	1.008	2.418	1.366	66
4/15	65	140	1.008	2.788	1.692	87
1/17	104	49	.992	2.620	1.539	76
10/29	105	107	.995	3.085	1.990	72
6/28	104	108	.968	3.046	1.950	63
7/10	102	142	.969	3.135	2.055	60

* Secondary developed

3

Comparison with
The Performance Model

Direct comparison of the increase of projectile momentum and the electromagnetic impulse does not include the effects of electrothermal acceleration or the various fluid mechanical drag mechanisms which act to decrease velocity. A railgun performance model was constructed which included these effects to more carefully evaluate the experimental results. This model included the accelerating effects of the continued expansion of the helium accelerating gas and the electrothermal acceleration due to the vaporization and heating of the aluminum foil fuse. It also included the drag effects due to compression, acceleration and viscous drag of the residual bore gas ahead of the projectile, the viscous drag of the plasma armature and ablation drag. The details of this model have been given by Taylor et al [5].

Inclusion of the accelerating gasdynamic and electrothermal effects removed the greater than 100% momentum efficiency observed at the lowest values of electromagnetic momentum. The inclusion of the various drag effects improved the prediction at higher values of electromagnetic momentum, but there was still a significant deficit in performance, as shown in Figure 2. For a given series of experiments with fixed armature current the ablation rate remains essentially constant as the augmentation is increased.
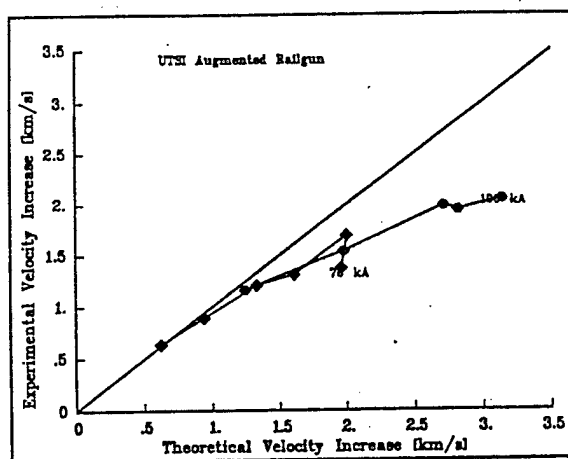

Figure 2: Comparison between experimentally observed velocity increase and performance model predictions for augmented railgun.

Therefore, the electrothermal acceleration and the ablation drag is also essentially constant. The predicted increase in velocity with increasing augmentation is essentially due only to the increased electromagnetic force provided by the augmented turn, less the increased viscous drag due to the higher velocity. Therefore, since the observed increase in velocity with increasing augmentation was less than predicted, we suspected that the electromagnetic force model was inaccurate. To further investigate the force model, we employed 3-dimensional simulations using MEGA.

3-Dimensional Electromagnetic
Simulations

The widely used simple railgun electromagnetic force model, $1/2L'I^2$, can be derived in several ways. The most common is to use conservation of energy, where it is assumed that there are no losses due to eddy currents and that all of the electromagnetic force appears in the moveable armature. Neither of these assumptions are correct for a railgun which has a moving armature and a structure excited by a transient current pulse. Eddy currents are generated both by the transient pulse and the moving armature, and these eddy currents reduce the energy available to do work on the armature. Furthermore, some of the available energy acts to produce a force on the rails and is not available to the armature. Both these effects reduce the electromagnetic force below that predicted by the simple force model of Equation 1.

These effects are largely three-dimensional in nature, and to acquire some insight into these processes we used the 3-dimensional, finite element code, MEGA, to perform simulations on a simple railgun model. This simple model was used, rather than the exact geometry used in the experiments, since modeling the complex rail cross section required more computer memory than was available on our IBM RISC 6000 workstation.

The simulation railgun model consisted of a 1 cm square bore railgun with a 0.5 cm long solid armature. Both rail and armature were assumed to be copper, as was the augmenting turn. In order to separate the effects of the transient current pulse and the armature motion, simulations were performed using a Helmholz step function with an amplitude of 100 kA for the input current. Both fixed armature and constant velocity moving armature calculations were performed using this same input current. Calculations for the augmented railgun used the same current input for both the armature and for the augmenting turn. The inductance gradients L' and M' are inherently two-

dimensional parameters in which it is assumed that the self and mutual inductance are linear functions of railgun length. In order to compare the results of the 3-D simulation with the simple force model, values of L' and M' were calculated as a function of time for this same current input using a 2-dimensional MEGA calculation.

For the simulation parameters chosen, the diffusion of the magnetic field into the copper structure is essentially complete in approximately 300 μs. During this time the values of L' and M' will be changing as the current penetrates deeper into the structure. This field diffusion results in eddy current formation which, in the three-dimensional case, results in current flow ahead of the armature. Graphical results of our 3-dimensional MEGA simulations will be shown in the plane of symmetry between the insulators, as shown in Figure 3.

Figure 4a: Current density for a stationary armature at a time of 300 μs using a 2-D MEGA simulation.

Figure 3: Sketch showing the section through the railgun used for presentation of graphical results from MEGA simulations.

There are significant differences between the 2- and 3-dimensional simulations as shown in Figure 4. Current density distributions are shown at 300 μs after the fields have diffused into the structure for the case of the stationary armature (4a and 4b) and for the moving armature at a velocity of 2 km/s (4c and 4d). For the 3-D fixed armature case (4b) the currents are more uniform in the armature and there are currents extending forward of the armature in the rails. Much
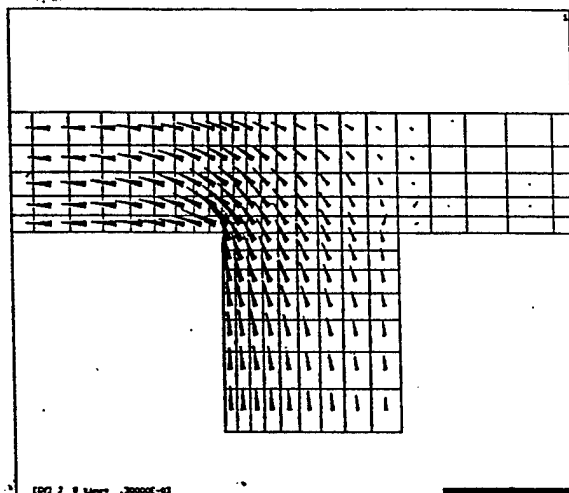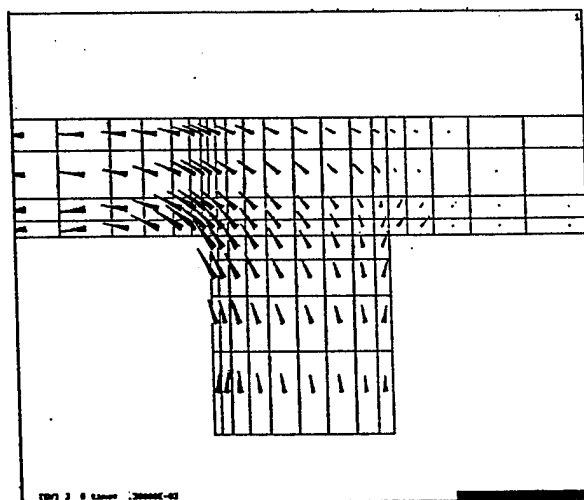

Figure 4b: Current density for a stationary armature at a time of 300 μs using a 3-D MEGA simulation.
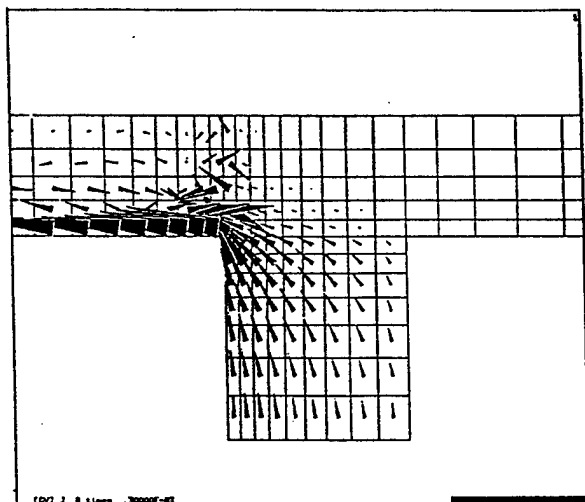
5

Figure 4c: Current density for an armature velocity of 2 km/s at a time of 300 μs using a 2-D MEGA simulation.

larger differences are observed for the case of an armature moving at a velocity of 2 km/s as shown in 4c and 4d. There is a strong eddy current flow in the rail ahead of the armature in the 3-D simulation (4d), where none appears in the 2-D simulation (4c). The motion of the rails through the field gradient near the armature also induces eddy currents in the rails. The velocity induced eddy current is observed in the rail just at the armature position (4d). This effect is much more pronounced in the 3-D simulation and extends well ahead of the armature. In the 2-D simulation this effect is concentrated near the rear sliding interface.

The forces obtained from the three-dimensional conventional railgun simulation are shown in Figure 5. The total axial force is obtained by integrating the axial component of $J \times B$ over the whole structure consisting of both armature and rails. Some of the axial force is located in the rails and some is located in the armature. The true armature force is obtained by the integration of the axial component of $J \times B$ only over the armature volume. These forces are shown as a function of time, together with the force predicted from the simple force model, in Figure 6. The simple force model shows increasing total force with time as the field diffuses into the structure, and the armature
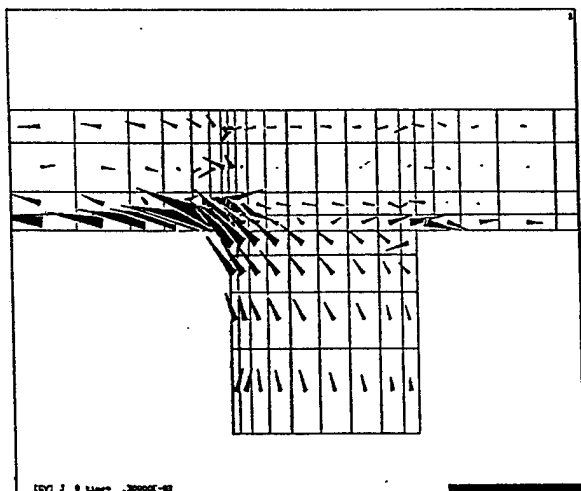

Figure 4d: Current density for an armature velocity of 2 km/s at a time of 300 μs using a 3-D MEGA simulation.
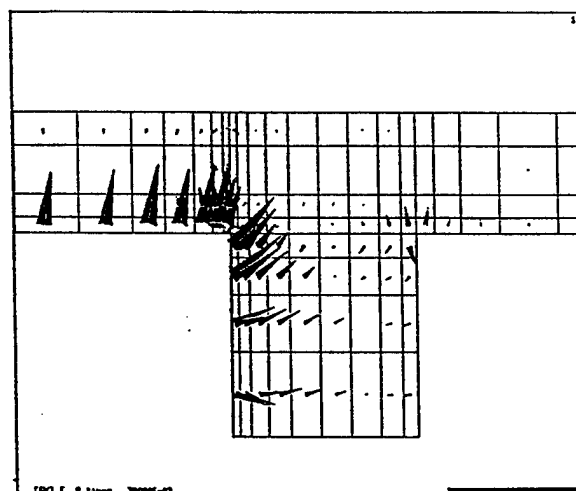

Figure 5: Rail and armature forces for the conventional railgun at an armature velocity of 2 km/s and a time of 300 μs using a 3-D MEGA simulation.
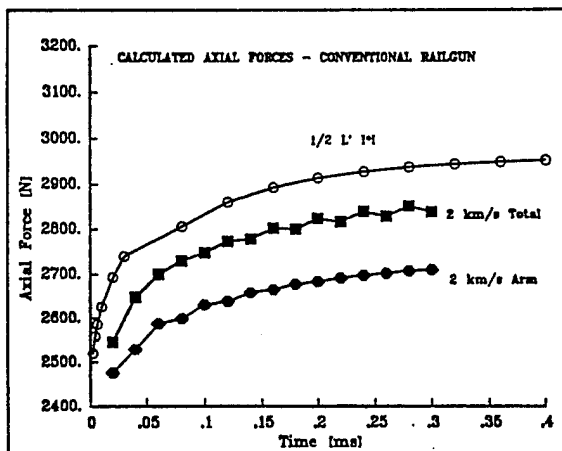
6

Figure 6: Armature and total railgun axial forces for the conventional railgun at an armature velocity of 2 km/s using 3-D MEGA simulations.

Figure 7: Current density for the augmented railgun at an armature velocity of 2 km/s and a time of 300 μs using a 3-D MEGA simulation.

forces increase in a similar manner. After 300 μs the 2 km/s armature force is approximately 8% smaller than that predicted by the simple force model. It is interesting to note that the force predicted by the simple model at a frequency of 10 kHz (25 μs) is almost exactly the same as the armature force after the field has fully diffused (300 μs).

Current density distributions are shown in Figure 7 for the transaugmented railgun at a time of 300 μs and a velocity of 2 km/s. The augmenting current has completely diffused into the rail and is essentially uniform. Armature current is concentrated near the rear interface, and strong eddy currents are induced in the rail near and ahead of the armature position. The forces for this case are shown in Figure 8. The outer rail is lightly loaded, but the inner rail experiences very large separation forces behind the armature, and there are significant axial components of the forces in the inner rail. After 300 μs the 2 km/s armature force is 19% smaller than that predicted from the simple force model.

Results and Conclusions

Three-dimensional simulations using MEGA show that the simple force model given by Equation 1 overestimates the true armature force. The difference
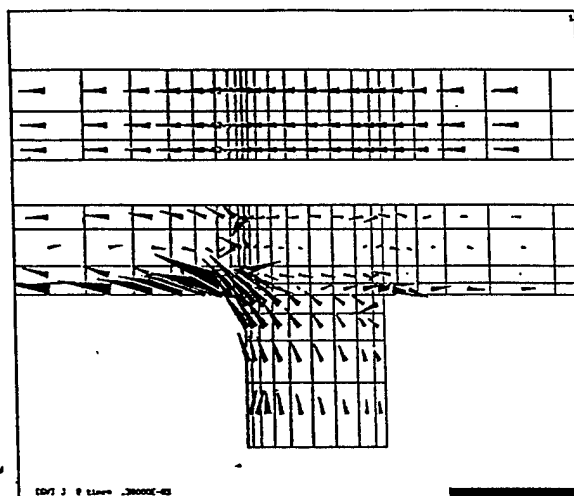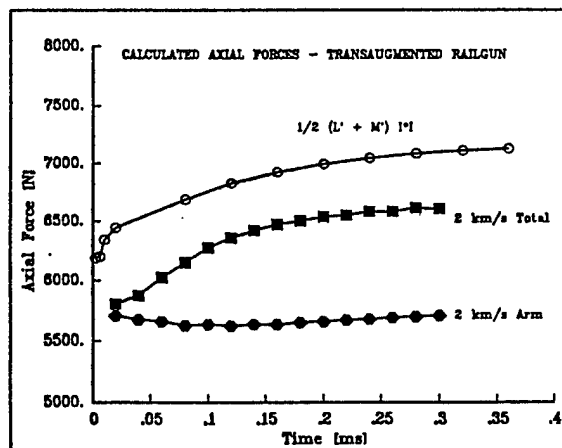

Figure 8: Armature and total railgun axial forces for the augmented railgun at an armature velocity of 2 km/s using 3-D MEGA simulations.

7

is larger for the transaugmented railgun because a larger fraction of the available force is exerted in the rail, rather than the armature. The reason that a larger portion of the force appears in the rail is that the magnetic field due to the augmenting current has had time to diffuse into the interior of the rail prior to the arrival of the armature, and the transverse component of the rail current interacts with this larger magnetic field. For the case of the augmented railgun the overestimation of the armature force was substantial, 19% for the simulation case of equal currents in the armature and in the single augmenting turn.

These MEGA simulations were carried out using a different geometry than the experiments. The experiments were conducted in a round bore railgun with plasma armatures. The experimental railgun had a relatively small L' value of 0.274 μH, because of the use of rather wide rails. The simulation railgun was a square bore configuration with a solid armature and rails only the width of the bore. The simulation railgun had a calculated L' of 0.518 μH, considerably larger than the experiment. Because of these differences, direct comparison of the results cannot be made. However, in the two experiments using approximately equal 100 kA currents in the armature and augmentor, the observed velocity was approximately 76% of the predictions based on our performance model. The corresponding MEGA calculation with an armature velocity of 2 km/s shows that the armature forces are approximately 90% of the value predicted based on the 10 kHz values of L' and M'. The lower velocity observed in the experiments is partially accounted for by the losses associated with primary separation, which was not included in the performance model.

The MEGA simulations also show that, for a conventional railgun, the inductance gradient, L' and the armature force increase with time as the fields diffuse into the conducting structure of the railgun. This means that the use of a single value for L' tends to overestimate the force during the early part of the acceleration. There can be a substantial electrothermal acceleration force due to fusing and to the heating and expansion of ablation products, particularly at early times. This electrothermal force is often neglected in railgun performance models and can partially explain why comparisons of measured performance with predictions based on Equation 1 are in generally better agreement at low velocity and then diverge at higher velocity.

Although we have shown that the simple electromagnetic force model overestimates the true armature force, this is not the sole reason that experiments have failed to achieve their expected velocity. Plasma armatures exhibit two characteristics which severely limit velocity: primary separation and secondary formation. Ablation is thought to play an important role in secondary formation, but the mechanisms responsible for primary separation are not clear. The MHD flows which exist in the plasma armature are very complex and strongly three-dimensional [8]. These flows have been simulated using 2-dimensional MHD codes, but secondary formation was not observed. Primary separation could be observed in the simulations when material was injected into the base flow region. It is clear that 3-dimensional MHD simulations are needed to provide further insight into the mechanisms which control primary separation and secondary formation in plasma armatures.

References

1. S. C. Rashleigh and R. A. Marshall, "Electromagnetic Acceleration of Macroparticles to High Velocity," *J. Appl. Phys.*, Vol. 49, pp. 2540-2542, April 1978.

2. R. S. Hawke, W. J. Nellis, G. H. Newman, J. Rego and A. R. Susoeff, "Summary of EM Launcher Experiments Performed at LLNL," *IEEE Trans. Mag.*, MAG-22(6), pp. 1510-1515, 1986.

3. J. V. Parker, W. M. Parsons, C. E. Cummings and W. E. Fox, "Performance Loss Due to Wall Ablation in Plasma Armature Railguns," Conference Title: AIAA 18th Fluid Dynamics and Plasmadynamics and Lasers Conference, pp. 1-9, July 1985.

4. J. V. Parker, "Why Plasma Armature Railguns Don't Work (and What Can Be Done About It)," *IEEE Trans. Mag.*, Vol. 25, No. 1, pp. 418-424, Jan. 1989.

5. J. Taylor, R. Crawford and D. Keefer, "Experimental Comparisons of Conventional and Trans-Augmented Railguns," *IEEE Trans. Mag.*, Vol. 29, No. 1, pp. 523-528, 1993.

6. D. Rodger and P. J. Leonard, "Modelling the Electromagnetic Performance of Moving Railgun Launchers Using Finite Elements," *IEEE Trans. Mag.*, Vol. 29, No. 1, pp. 496-498, 1993.

7. Allen R. Susoeff, Personal Document With Sketches of Magnetic Induction Device, Nuclear Explosives Engineering Div., Lawrence Livermore Laboratory, October 17, 1990.

8. R. Crawford, D. Keefer, and R. Tipton, "Velocity Limiting Magnetohydrodynamic Effects in Railgun Plasma Armatures," *IEEE Trans. Mag.*, Vol. 29, No. 1, pp. 781-786, 1993.

DEVELOPMENT OF A COMPUTATIONAL MODEL OF THE GAS DYNAMIC AND ABLATION EFFECTS IN PLASMA ARMATURE RAILGUNS

A Thesis

Presented for the

Master of Science

Aerospace Engineering

The University of Tennessee, Knoxville

John K. Foster

May 1993

Abstract

Railgun performance has not reached the expected level as originally indicated by electromagnetic theory. That is, projectile exit velocities do not approach the extremely high velocities that ideal analysis indicated   Various researchers re-examined railgun theory, and attempted to determine ways of improving railgun performance.

Research at the University of Tennessee Space Institute has been conducted to explore the causes of that decrease in performance. Ablation in the railgun bore has been identified as a factor in the reduction of peak expected performance. However, some experimental data indicated that some ablation effects, primarily the electrothermal interaction of the expanding ablated material and the driving gas, actually increased performance under certain conditions.

The purpose of this thesis is to describe the effort undertaken to identify some of the effects that ablation imposes on the performance of railguns, and to describe the computer model created to simulate these effects. This computer model included routines which accounted for the gas dynamics of the injector's driving gas through use of the (1)time-dependent method of characteristics, (2) the electromagnetic forces occurring within the electric arc armature, (3) the rate of ablation of material from the wall, and (4) the electrothermal interaction between each of these. A description is made of each routine's impact on the simulation, and each routine's importance to the calculation procedure is identified.

This effort concluded that the electrothermal interaction which occurred in each shot caused the driving potential of the injector light gas to increase, thereby increasing the force attributable to the light gas. This increase in force caused the railgun to produce velocities higher than were expected.

iii

Experimental Comparison of Conventional and Trans-Augmented Railguns

J. Taylor, R. Crawford, and D. Keefer

Center for Laser Applications, University of Tennessee Space Institute, Tullahoma, Tennessee 37388

Abstract–A 2.4 m long, 1 cm diameter round bore railgun was constructed at UTSI to perform careful experiments which compared the performance of conventional and trans-augmented plasma armature railguns. The gun was constructed with copper rails and G-9 insulators and had a single augmenting turn. Two separate 240 kJ capacitor banks and inductors were used to provide current independently to the armature and to the augmenting turn. The barrel was fitted with an array of B-dot probes spaced 10 cm apart to provide good resolution of the plasma armature characteristics. A MAVIS electromagnetic transducer was used to provide accurate measurements of the muzzle velocity. The gun bore was lapped full length from the light gas injector to the muzzle between each shot to provide a uniform, high quality bore surface for each experiment. Conventional railgun experiments were performed over a range of currents to characterize the base performance of the railgun and to provide data for the development of ablation drag and thermal propulsive models. Experiments were then performed for a range of (separately powered) augmentation currents but with railgun currents equal to those used in the conventional experiments. The enhanced performance provided by augmentation was found to be significantly less than predicted by theory, even though the railgun operated without the formation of secondary armatures or restrikes.

I. INTRODUCTION

In the years since J. V. Parker's paper "Why Plasma Armature Railguns Don't Work, and What Can Be Done About It" [1] much of the active research on plasma armature railguns has been directed toward the control of bore ablation. Parker suggested several possible methods to control ablation, one being the use of augmentation. Augmentation increases the magnetic flux in the bore of a railgun, thus increasing the accelerating force on the armature, without increasing the operating current. Operation at lower current in the plasma armature reduces the power dissipated in the bore, thus reducing ablation.

To examine the effects of augmentation we constructed a 2.4 meter trans-augmented railgun with two 240 kJ capacitor banks, one for the conventional railgun rails (inner rails) and one for the augmented set of rails (outer rails). Conventional (no augmentation current) railgun experiments were performed to establish baseline performance and to determine parameter values for a performance model. The augmenter was then powered over a range of currents while keeping

the armature current pulse nearly the same as in the baseline experiments. The purpose of these experiments was to gain an improved understanding of the effects of increasing the magnetic flux and, therefore, the force on the armature while still operating with essentially the same armature power.

II. EXPERIMENTAL RESULTS

A. The UTSI Augmented Railgun

The UTSI trans-augmented railgun was designed to function as either a conventional or augmented railgun with a 2.4 m long barrel and a 1.0 cm bore diameter. A 1.1 meter single stage helium gas injector provided pre-acceleration of projectiles into the railgun with a velocity of approximately 1 km/s. The design featured copper rails and G-9 insulators supported by a G-10 substructure as shown in Fig. 1. The configuration of the G-10 backing and aluminum anvils were the same as used in Ref. 2. Two separate 240 kJ capacitor banks and two separate four sectored, toroidal inductors were used to provide separate currents to the inner rails and the augmenting rails. Lexan projectiles of approximately 1 gm mass with flexible lip seals and an aluminum foil fuse were used for all shots.
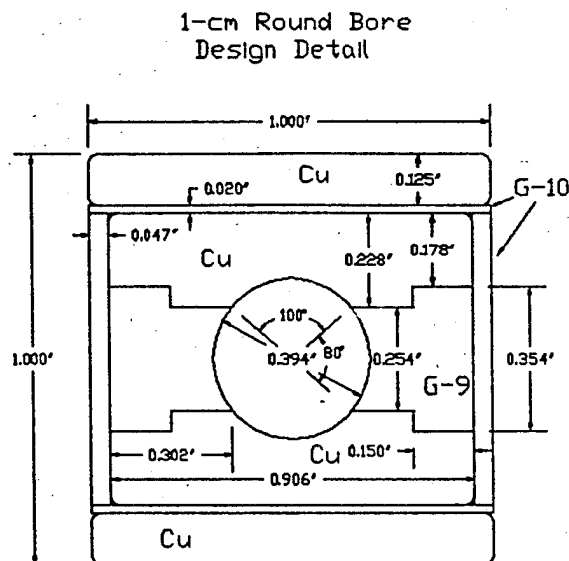

Fig. 1. Cross section for the UTSI 2.4 m trans-augmented railgun.

B. Instrumentation and Experimental Procedure

Twenty-three B-dot probes located 100 mm apart measured changing rail current and were used to obtain accurate armature positions [2]. Two pressure transducers were located 95 and 55 mm before the breech end of the rails. These were used to initiate the timing for the data acquisition system and power supplies, to measure the entrance velocity of the projectile into the rails and to measure the initial pressure of the gas in the bore. A MAVIS electromagnetic transducer, placed in the enclosed flight range, was used to provide accurate muzzle velocity measurements [3].

Consistent bore quality for both conventional and augmented shots was maintained by lapping the railgun from the breech of the light gas gun to the muzzle before each shot using a rotating, expandable iron lap. After lapping, acetone was circulated through the bore to remove all traces of lapping compound and hydrocarbons. The bore was dried under vacuum and then back-filled with one-half atmosphere of helium prior to each shot. A bore scope was used before each shot to check for foreign materials or incomplete lapping, and was used after each shot to determine the degree of bore damage.

Values for L', the self inductance per unit length, and M'_{12}, the mutual inductance per unit length, were needed for performance evaluations. These values were measured at approximately 200 kHz (high frequency limit) directly on the UTSI railgun. The value of 0.289 $\mu H/m$ was obtained for L' and a value of 0.218 $\mu H/m$ was obtained for M'_{12}.

C. Experimental Results

Table 1 gives a summary of the experiments performed on the UTSI trans-augmented railgun. The table is grouped into three sections, a nominal 100 kA inner rail current series and a nominal 70 kA inner rail current series in order of increasing augmentation, and three additional unaugmented shots listed separately. The measured increase in velocity from the pressure transducers to the muzzle exit is tabulated together with a calculated momentum efficiency. The momentum efficiency is defined as the measured increase in projectile momentum divided by the total electromagnetic impulse,

$$\eta = \frac{m_p(V_M - V_0)}{\frac{1}{2}L' \int_0^{tm} I_1^2 dt + M'_{12} \int_0^{tm} I_1 I_2 dt} \quad , \quad (1)$$

where m_p is the projectile mass, V_M is the measured muzzle velocity, V_0 is the measured injection velocity, L' is the high-frequency self inductance gradient of the inner rails, M'_{12} is the high-frequency mutual inductance gradient, I_1 is the inner rail current, I_2 is the outer rail current and the limits of integration are from the time the power supplies are triggered until the time of muzzle exit.

TABLE I
SUMMARY OF UTSI 2.4 m RAILGUN EXPERIMENTS

Shot	Peak Rail Current (MA) @ time (ms)	Peak Augmented Rail Current (MA) @ time (ms)	mass of projectile (gm)	Muzzle Velocity (km/s)	Δv_t Measured (km/s)	$\frac{\Delta v_t}{\Delta v_{electromagnetic}}$ (%)
919	.120 @ .359	0	.992	2.379	1.299	74.3
906	.134 @ .361	0	.994	2.655	1.602	81.5
730	.138 @ .368	0	.996	2.493	1.469	67.5
617	.106 @ .353	0	.984	2.476	1.365	112
1024	.105 @ .368	0	.979	2.258	1.162	93.5
117	.104 @ .368	.049 @ .388	.992	2.620	1.539	78.4
1029	.105 @ .368	.107 @ .388	.995	3.085	1.990	75.8
628	.104 @ .353	.108 @ .269	.968	3.045	1.950	68.8
710	.102 @ .355	.142 @ .270	.969	3.135	2.055	62.9
816	.067 @ .370	0	.980	1.669	.630	110
925	.068 @ .368	.030 @ .353	.980	1.966	.886	98.7
114	.067 @ .374	.071 @ .389	.985	2.333	1.203	93.0
110	.064 @ .368	.103 @ .388	.994	2.360	1.305	86.4
116	.065 @ .365	.138 @ .396	1.008	2.418	1.366	72.8

Fig. 2 shows the measured projectile momentum increase plotted as a function of the total electromagnetic impulse for two series of augmented experiments, one with a nominal 70 kA inner rail current and one with a nominal 100 kA inner rail current. In both series the performance decreases with increasing impulse.

An attempt was made to isolate the effectiveness of just the augmenting field. The projectile momentum increase (due only to the augmenting field) was determined by

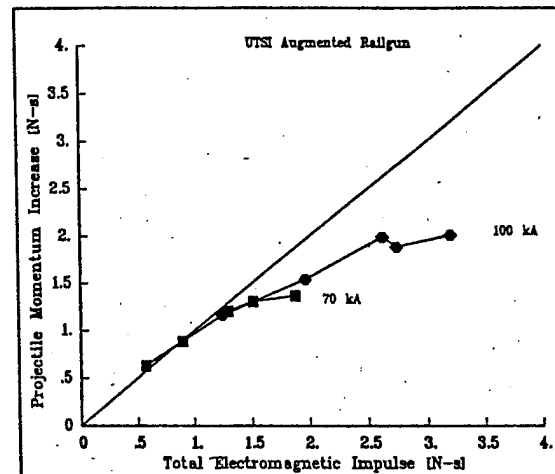$$\Delta p_a = m_a(V_{ma} - V_{oa}) - m_c(V_{mc} - V_{oc}) \quad (2)$$

Fig. 2. Experimental momentum increase versus electromagnetic impulse for augmented shots.

where subscript a refers to the augmented shot and subscript c refers to the conventional shot with similar inner rail current. The increase in electromagnetic impulse (due only to the augmentation) was determined by,

$$\frac{1}{2}L' \int_0^{tma} I_{1a}^2 dt + M_{12}' \int_0^{tma} I_{1a} I_{2a} dt - \frac{1}{2}L' \int_0^{tmc} I_{1c}^2 dt .$$

(3)

The measured increase in projectile momentum due to augmentation is plotted as a function of the increase in electromagnetic impulse due to augmentation in Fig. 3. Here too, the performance decreases with increasing electromagnetic impulse.

The increase in projectile momentum is plotted as a function of total electromagnetic impulse for all the shots in Table 1, both augmented and conventional, in Fig. 4.

Certain general observations can be made concerning armature configuration and the effectiveness of augmentation on the basis of this series of experiments:

1. No secondary arcs or restrike was observed for any of the experiments reported in Table 1. We believe this was a result of the extreme care taken to prepare the barrel prior to each shot. In general, the observed armature length was somewhat shorter for the augmented shots, and the filamentary erosion tracks on the copper rails were less pronounced.

2. It can be seen from Table 1 or Fig. 2 that, for both the 100 kA series and the 70 kA series, the efficiency decreased as the level of augmentation increased. The efficiencies that were greater than
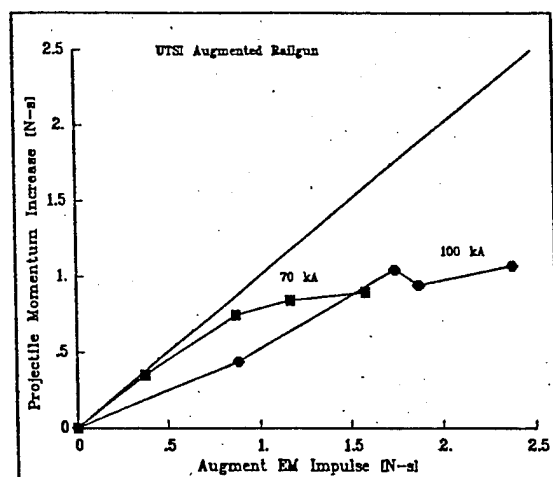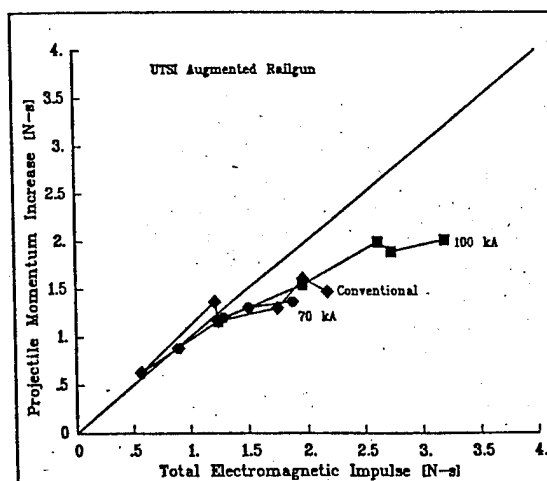

Fig. 4. Experimental momentum increase versus electromagnetic impulse.

100% are due to the fact that not all of the projectile acceleration is a result of electromagnetic forces. Some of the acceleration comes from continued expansion of the injector gas and electrothermal propulsion due to vaporization of the aluminum fuse and electrothermal heating of the bore gases throughout the drive.

3. Similar current profiles were used on the inner rails for both augmented and conventional shots, so the armature power dissipated in the bore and the quantity of material ablated from the bore is also similar. Ablation and viscous drag increase with velocity and could be somewhat larger for the augmented experiments, but the analysis in Section III shows that these effects are small for our experimental conditions. Therefore, it is reasonable to assume that most of the additional impulse supplied by the augmenting turn would result in increased projectile momentum. Fig. 3 clearly shows that this assumption is incorrect, and that less than 50% of this increased electromagnetic impulse is realized in increased projectile momentum at the higher augmenting currents.

4. Fig. 4 shows that the increase in momentum correlates very well with total electromagnetic impulse, regardless of how the electromagnetic impulse is supplied. For example, in the region near 2 N-s impulse, unaugmented shots and shots with both 70 kA and 100 kA inner rail currents all produce approximately the same increase in projectile momentum.

In the next section we will develop a performance model which includes the effects of ablation and armature related fluid drag, the drag due to the acceleration of the initial bore gas, and the acceleration produced by continued injector gas expansion and electrother-

Fig. 3. Momentum increase due only to the augmenting rails.

mal acceleration due to the fusing transient. This model will be used to further analyze the results of these experiments.

### III. THEORETICAL INTERPRETATION

No secondary arcs were observed during this series of experiments and, therefore, a relatively simple performance model for the augmented railgun can be constructed. The experimental data from the conventional shots can be used to evaluate the model parameters which determine ablation and viscous drag and the acceleration caused by electrothermal and gas expansion effects. The model can then be used to predict the performance of the augmented shots using the parameters determined from the conventional shots.

A. Forces on the Projectile and Armature

A summary of the forces acting on the projectile and armature can be seen in Fig. 5. The primary driving force is the electromagnetic force where J is the current density in the armature and B is the magnetic field in the bore. Acceleration forces produced by electrothermal heating may be generated throughout the drive of the armature, but it is predominant during the time in which the fuse vaporizes to form the plasma armature. The armature experiences viscous and armature ablation drag which are described in papers by Parker [1,4]. There are also retarding forces due to acceleration of the initial bore gas ahead of the projectile [5], and projectile friction.

B. Electromagnetic Forces

The correct value of the electromagnetic force acting on the armature is obtained by integration of the axial component of the integral of the $J \times B$ force
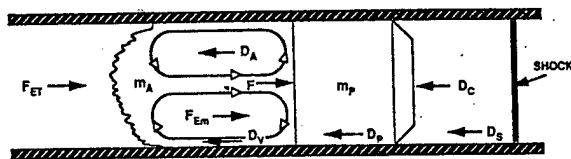
F_{Em} - Electromagnetic Force $\int_{Armature} JxB \cdot \hat{k} \, dV$

F_{ET} - Pressure of Trailing Bore Gases - Electrothermal Heating

D_V - Armature Viscous Drag

D_A - Armature Ablation Drag

F - Net Armature Force = $F_{ET} + F_{Em} - D_V - D_A - m_A \frac{dV}{dt}$

D_P - Projectile Friction

D_C - Force Due to Bore Gas Compression

D_S - Viscous Drag of Bore Gas

Acceleration = $\frac{1}{m_P} (F - D_P - D_C - D_S)$

Fig. 5. Railgun projectile forces.

over the total current distribution within the bore. However, the 3-dimensional distribution of both current density and the magnetic induction is unknown. For this reason, energy arguments or idealized 2-dimensional or filament models are commonly used to determine the total armature force. These models all result in a total axial armature force given by,

$$F = \frac{1}{2}L'I_1^2 + M'_{12}I_1I_2 \quad . \qquad (4)$$

Since the value of L' and M'_{12} can vary by as much as 20% with frequency (because of the depth of field diffusion into rails) an appropriate value of L' must be chosen. Consistent with accepted practice, the high frequency limit of L' and M'_{12} was used in the development of our performance model.

There is also a question as to whether eddy current generation due to the moving armature and diffusing fields could play a significant role in the reduction of the electromagnetic force. In the $J \times B$ relationship the influence of eddy currents would show up as a reduction, or redistribution of B, but in the ideal force given by (5) they are neglected. Three-dimensional effects could also be a source of error since the ideal relationship assumes that all of the $J \times B$ force is in the axial direction [6,7].

C. Fluid Mechanical Effects

Rolader and Batteh [5] have analyzed the effects of bore gas compression in front of the projectile. There are three drag forces associated with this compression. The first arises because the velocity of the shock wave is greater then that of the projectile, which causes the mass of the compressed gas to increase. The second is due to the acceleration of this gas, and the third is due to the viscous drag of the gas. The armature also experiences viscous and ablation drag. The ablation drag is due to stationary bore material being ablated and then accelerated up to the armature velocity. The amount of material ablated is assumed to be proportional to the electrical power dissipated in the bore. A value for the viscous drag coefficient, $C_d = 0.003$, was taken from Parker's free arc experiments, and the ablation constant was obtained by fitting to our data for a conventional railgun experiment [1,5].

The helium expansion from the light gas gun continues to accelerate the projectile throughout the drive, as does the electrothermal heating of gases in the bore. Light gas gun experiments were performed to determine a decay constant for the helium expansion in the gun. This same decay constant, β, was used with an empirical formula to model the pressure due to electrothermal expansion of gas in the bore,

$$p = [p_0 + (\gamma t)^\eta] e^{-\beta t} \qquad (5)$$

where p is the total pressure of gas on the projectile, p_0 is the initial pressure of helium, and γ and η are

Velocity Limiting Magnetohydrodynamic Effects in Railgun Plasma Armatures

Roger Crawford and Dennis Keefer

Center for Laser Applications, University of Tennessee Space Institute, Tullahoma, Tennessee 37388

Robert Tipton

Lawrence Livermore National Laboratory, Livermore, California 94550

Abstract–The results of a four year theoretical and experimental research program in railgun armature physics at UTSI will be reviewed with an emphasis on understanding how the MHD flowfield and electromagnetic interactions limit the velocity in plasma and hybrid armature railguns. Our understanding of the three-dimensional plasma armature flowfield has been developed through a combination of highly instrumented railgun experiments, secondary arc performance models and two-dimensional MHD calculations. These two-dimensional calculations are only qualitative in nature, but they provide insight into the complex armature flow and indicate that the formation of secondary armatures, ablation drag and primary armature separation are interrelated. Experimental evidence suggests that three-dimensional MHD flow effects are very important in controlling these phenomena. A complete understanding of these complex armature effects will require the development of detailed three-dimensional MHD codes validated by highly instrumented and diagnosed railgun experiments.

I. INTRODUCTION

Why are railguns limited to velocities of about 6 km/s? The elusive promise for hypervelocity railguns has been unfulfilled for more than a decade. Numerous railguns have been constructed whose predicted velocity was greater than 6 km/s. Few have actually exceeded 6 km/s, and none have reached their predicted performance. It is essential to understand what it is that limits performance if velocities above 6 km/s are ever to be reliably obtained. Currently accepted theories attribute this failure to ablation drag, secondary arcs and primary armature separation. Optical and B-dot diagnostic measurements have led to new physical and computational models which provide considerable insight into the magnetohydrodynamic velocity limiting mechanisms. This paper will address "all" the velocity limiting mechanisms, not just secondary armatures and ablation drag. Although secondary armatures reduce electromagnetic drive, experiments have shown that elimination of secondaries does not assure theoretical performance. The real velocity limiting mechanism is primary armature separation from the projectile. Careful examination of B-dot records and projectile muzzle velocity from numerous railgun experiments shows that in many cases the primary armature stops driving and separates from the projectile late in the launch. This means that the net drag forces on the armature are greater than the electromagnetic thrust forces. New experiments and theoretical analyses are needed to identify, separate and quantify the MHD and EM loss mechanisms and to identify new strategies which will achieve higher velocities.

II. PHYSICAL MODEL OF THE RAILGUN PLASMA ARMATURE

All hypervelocity railguns are driven by plasma armatures or hybrid/plasma armatures. Often, it has been tacitly assumed that a plasma armature was just like a solid armature, but with negligible mass and higher resistance. Acceleration of a projectile by a plasma differs in almost every respect from a solid armature. In a plasma armature all the electromagnetic force is transmitted to the projectile by fluid pressure. This pressure is generated and sustained by the electromagnetic forces in a dynamic, flowing plasma which is dominated by thermal radiation, viscous and magnetohydrodynamic (MHD) forces. Diagnostic measurements and computer simulations have provided some understanding of these complex armature flows.

Quartz optical fibers were used to obtain direct optical measurements of the plasma emission from within the bore of a railgun. These measurements in combination with in-bore pressure measurement, rail current B-dot probes and armature current B-dot probes have led to the development of improved physical understanding of the plasma armature [1]. When the emission from the plasma was observed simultaneously through both the rail and the insulator surfaces, the emission at the rail surface follows the current, but the emission at the insulator surface decreases soon after the current begins to rise. The decrease in emission is caused by absorption of radiation in the vapor which is ablated from the insulator surface by the intense radiation from the plasma interior. However there is a striking similarity in the spectral features, which suggests that strong three-dimensional mixing occurs within the plasma armature which quickly transports rail material to the insulator surfaces. These diagnostic measurements led to a new physical model for the plasma armature which modifies and extends the ablation model proposed earlier by Parker [2] and the fluid mechanics model proposed by Keefer and Tipton [3].

The projectile is accelerated by fluid pressure in the plasma which is sustained within the plasma and near the rail surface by the Lorentz ($\mathbf{J} \times \mathbf{B}$) body force. Near the insulator surface vapor shielding from ablation reduces the plasma temperature and, therefore, the electrical conductivity of the plasma. Thus, the current density is reduced near the insulator and the $\mathbf{J} \times \mathbf{B}$ force can no longer balance the high pressure at the base of the projectile. This results in a leakage of material from the armature along the insulator surfaces which fills the bore behind the armature and increases the bore pressure behind the armature. This lost armature material must be replaced to prevent depletion of the armature mass. Most of the replacement material must be obtained from the rail surface where the $\mathbf{J} \times \mathbf{B}$ force is strong enough to accelerate ablated material into the armature. This process is accompanied by ablation drag which establishes a strong recirculation cell in the plasma armature.

Experimental results from a hybrid armature investigation at UTSI provided graphic evidence of the three-dimensional armature flow [4]. The ablated flow patterns on the recovered hybrid armatures clearly show the flow of plasma from the rail surface around the hybrid to the insulator surface which results in a stagnation streamline along the insulator facing surface of the armature. The expansion of the nonconducting material escaping along the insulator surface leads to a current distribution on the rail which has an airfoil shape. An attempt to represent this complex three-dimensional armature flow is shown in Fig. 1. This complex 3-D MHD flow in the armature must be considered if the velocity limiting mechanisms are to be understood and controlled.

Experimental attempts to control ablation and momentum drag with ceramic insulators have resulted in poor performance due to the development of long armatures. These results are consistent with increased armature leakage along the cold insulator boundary because there are no ablated products to slow the leakage flow. An increased loss of armature mass must be replaced by rail ablated products resulting in higher momentum drag. Thus the 3-D fluid mechanics of the plasma armature defeats the low ablation railgun, because the rail will always be required to provide the armature mass lost.

III. FLUID DYNAMIC FORCES, THRUST AND DRAG

Two primary sets of forces (fluid dynamic and electromagnetic) are acting in the railgun and determine the limiting velocity. In this section the fluid dynamic and thermodynamic forces will be evaluated for their relative influence on limiting velocity. Viscous drag, momentum drag, and gasdynamic pressure all significantly influence projectile acceleration.

Viscous drag losses occur as armature viscous drag, cold buffer gas viscous drag, projectile friction and viscous drag on the bore gas ahead of the projectile. The armature drag depends on length, density, velocity and viscosity of the armature. Most current models estimate viscous armature drag from simple hypersonic boundary layer models where

$$F(\text{viscous drag}) = C_f \rho V^2 \pi r l \quad .$$

The drag coefficient C_f is determined from turbulent compressible boundary theory and has values of 0.001
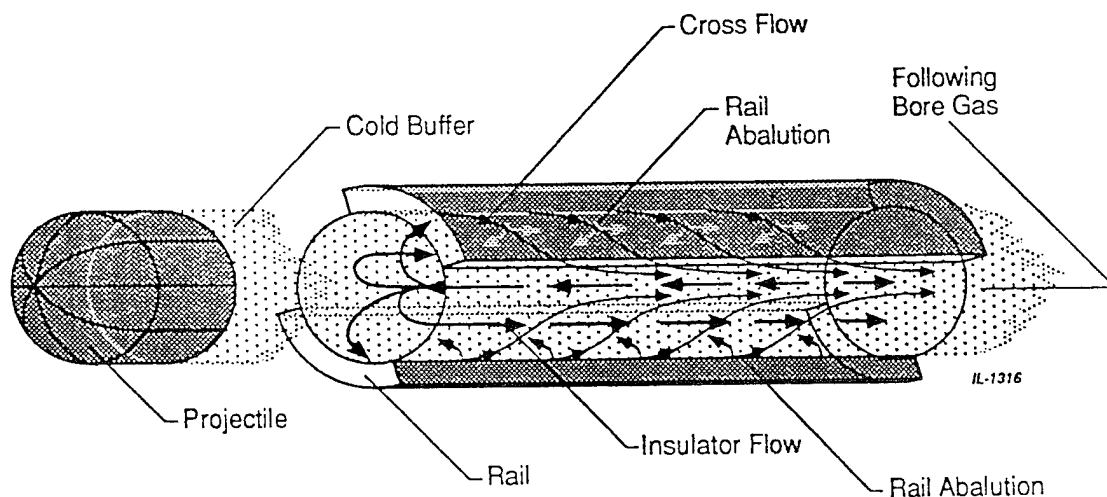

Fig. 1. 3-D plasma armature flow.

to 0.003. This analysis for armature drag is very approximate and neglects several effects including the three-dimensional flowfield. The composition of the armature is not well defined and thus the viscosity of the armature material near the wall is an unknown. The MHD boundary layer on the rail contains a thin layer where the current is conducted by small moving arc filaments. Viscous drag has not been well characterized for the MHD boundary layer. Since the plasma density is low due to the high plasma temperature, this drag term has been assumed to be small. However the viscous armature losses should not be neglected since they increase with velocity squared and the value of C_f has not been experimentally validated.

Diagnostic measurements and observation of recovered projectiles indicate that a nonconducting "buffer" gas layer forms between the current carrying arc and the projectile. This buffer gas drag has been neglected in most performance models because the size of this nonconducting region behind the projectile is difficult to measure. But since the density is much higher in this high pressure region, the viscous drag in the cold buffer gas could easily be as large as the armature drag. When primary armature separation occurs the buffer region drag will significantly increase, which may help explain the rapid loss in acceleration at primary armature separation. Accurate measurement of projectile position by optical techniques and simultaneous measurement of armature position by optical current probes are required for resolution of the cold buffer region size.
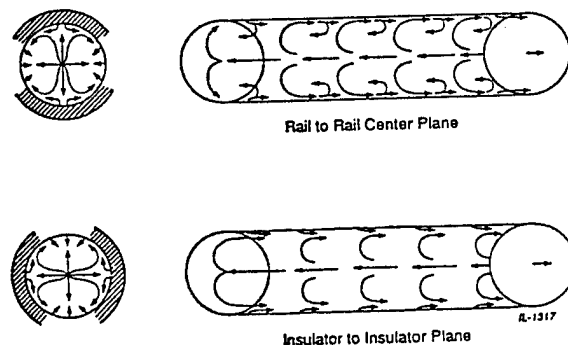
Projectile viscous drag has been considered insignificant in most railgun models based on extensive experience from two-stage light gas gun data. Except for the case where solid metal armatures are considered, the projectile is supported in a plastic bore rider. At velocities above 1 km/s the frictional energy release is sufficient to vaporize the plastic which provides a complex Couette boundary layer flow. Two-stage light gas gun experiments show velocity loss of 2% or less. Although projectile drag may be small it is not insignificant, and the projectile and bore material vaporized by the friction is released into the base region of the projectile. This accumulation increases the mass in the buffer gas layer and may influence the primary armature separation. Thus the projectile friction may indirectly play a significant role in limiting velocity.

The bore gas ahead of the projectile contributes to the drag (pressure) forces on the projectile. The combined viscous and momentum drag of the in-bore gas on a high velocity shot at atmospheric pressure has been analyzed by Rolader and Batteh [5], and the losses are significant when velocity exceeds sonic velocity in the bore gas. Thus it is essential to consider all of these "small" viscous loss mechanisms as their combined effects are largest at the limiting velocity.

Momentum drag (ablation drag) has been identified and generally accepted as the primary loss mechanism in plasma armatures by many railgun performance modelers [2]. A large amount of material may be removed from the bore by radiation, convection and arc root erosion. This mass, if incorporated into the armature, would produce large momentum drag resulting in a significant performance loss. The rail surface is damaged by arc root current transfer and radiation heating. In addition there are strong three-dimensional flows from the rail surface to the insulator surface caused by the nonuniform electromagnetic forces near the insulator walls. This strong flowfield, which is of the same order as projectile velocity, causes significant convective heat transfer which can remove ablated products from the bore surface. In most railgun experiments the observed armature size is relatively constant, 6 to 10 bore diameters. Thus the armature is not accumulating mass, and up to primary armature separation the buffer region does not appear to accumulate mass. Momentum drag results from the acceleration of the ablated mass by the armature in a process that continuously exchanges mass in the armature. Fig. 2 illustrates the processing of material by the armature. Ablated products that leave the armature with higher exit velocity than entrance velocity cause momentum drag and reduce driving pressure on the projectile. The following equation for driving pressure contains the viscous forces, momentum drag force, armature acceleration drag, electromagnetic acceleration force and bore pressure behind the armature.

$$P_{base}A = \int_{vol} \mathbf{J} \times \mathbf{B} \cdot \mathbf{k} dv + P_{bore}A$$
$$- \int_{sur.\ arm} F_{viscous} ds - M_{arm} \frac{dV}{dt}$$
$$- \int_{sur.\ arm} \dot{m}V \cdot ds$$

Rail to Rail Center Plane

Insulator to Insulator Plane

NOTE: Velocity in Projectile Frame

Fig. 2. Armature material processing.

The integrals are taken over the volume and surface of the bore in the region of the armature. Bore pressure (P_{bore}) from gasdynamics behind the armature acts as an accelerating force on the armature. M_{arm} is the mass of the armature and buffer gas behind the projectile. The surface integral of $\dot{m}V \cdot ds$ yields the momentum drag of fluid processed by the armature.

Due to the complex flowfield around the plasma armature, momentum drag is impossible to measure directly, and is equally difficult to model, requiring a full 3-D MHD code. Careful experiments with calibrated instrumentation will be required to evaluate the magnitude of the ablation drag relative to all other loss mechanisms. Results from a UTSI investigation of augmented railgun performance indicate that the ablation drag model does not explain the performance efficiency losses with increasing augmentation [6]. Since the ablation drag term has the form,

$$F(\text{ablation drag}) = \alpha IV$$

where α is the ablation constant, I is the armature current and V is the armature voltage, an increase in armature power should correlate with ablation drag. In the cases where armature current profile was held constant and the augmenting current increased, the predicted performance with constant ablation was not obtained. Reference [6] contains a summary of the augmented experiments and performance model estimates of the losses.

Gasdynamic pressure, other than electromagnetic pressure, has often been ignored in railgun performance analysis. There are three gasdynamic pressure components acting on the armature and projectile, and their influence is significant. Failure to correctly account for all the pressure contributions to the net driving force leads to errors in evaluating the electromagnetic performance. The first pressure force is the remaining light gas gun driving pressure which acts on the rear of the armature. An estimate of the acceleration resulting from residual gas gun drive can be obtained from a cold shot without electromagnetic drive. The gas gun drive during a hot shot will be larger due to the thermal energy transferred to the driving gas which increases pressure and the speed of sound.

The second pressure force is associated with the fusing transient and armature formation in a process similar to an explosion. Pressure transducers just upstream of the fusing location record the passage of a strong shock wave. Fig. 3 shows the pressure transducer record of the pressure transient. Taylor, et al [5] modeled the fusing pressure pulse for a series of UTSI railgun experiments to provide the correct acceleration profile during the initial electromagnetic drive. The empirical pressure pulse is also shown in Fig. 3 along with the empirical equation. Failure to account for these two pressure forces will yield electromagnetic efficiencies greater than unity for the first portion of
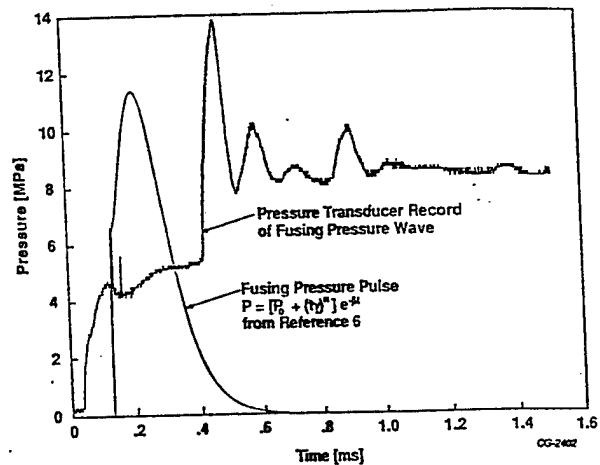

Fig. 3. Pressure transient from armature fusing.

the acceleration, and will bias the evaluation of overall efficiency.

The third pressure effect is associated with the release of ablated gasses into the bore behind the armature. This traveling source of "warm" gas which leaks around and out of the armature pressurizes the region between the armature and the cold driving gas and contributes to the acceleration. A detailed gasdynamic model of this pressure term is being developed at UTSI, and the magnitude of this effect has not been estimated. All three pressure forces are important and should not be neglected in analyzing railgun performance. Also, the bore pressure ahead of the projectile must be included in the drag forces.

IV. COMPUTATIONAL ANALYSIS OF ARMATURE MHD AND EM EFFECTS

This complex armature flow is difficult to analyze with computational models. Theoretical analysis has progressed from simple zero dimensional models to rather sophisticated two-dimensional MHD codes, but none of these can predict the complex behavior revealed by the diagnostic measurements. No models have been developed which describe either the three-dimensional armature flow or the associated three-dimensional, time dependent electromagnetic field. This complex electrodynamic field generates eddy currents in the gun structure which can alter the force acting on the armature. Recent experiments suggest that this effect is significant, and detailed simulations are needed to estimate its magnitude and to explore methods to minimize its reduction of the armature force.

Initial performance analysis of railguns was based simply on the total mechanical work done by a circuit with a changing inductance. This simple model leads

to a total force on the projectile given by, $F = 1/2L'I^2$ where L' is the inductance gradient of the gun and I is the armature current. Detailed simulations of the two-dimensional armature flow with time dependent currents, radiation transfer and ablation showed the primary separation which had been observed in numerous experiments, but failed to predict the observed reduction in velocity [3]. However, in all these models it was assumed that the total force acting on the armature was given by the equation above. Only 3-D models can utilize the $\mathbf{J} \times \mathbf{B} \cdot \mathbf{k}$ form of electromagnetic force.

The plasma flow in a railgun armature clearly has important three-dimensional features. Most current hydrocodes which include MHD and plasma radiation transfer can only calculate two spatial dimensions. However, simulations using these two-dimensional codes can provide vital insight into the physical mechanisms which control the formation and evolution of secondary arcs and the separation of the primary arc from the projectile. The CALE code developed at LLNL was recently used to simulate the evolution of a railgun armature. Conditions for the simulation were similar to those used in a recent HELEOS experiment.

The detailed plasma flow is shown in Fig. 4. The transverse (rail-to-rail) current density contours are plotted in the upper half of each figure, and the plasma velocity vectors are plotted in the lower half. During the rising part of the current pulse, a nonconducting buffer of compressed gas accumulates at the base of the projectile. Recovered projectiles from plasma railguns rarely show any evidence of base ablation. It is this buffer which protects the projectile base from ablation. After passing through current maximum, the electromagnetic pressure decreases and this volume of compressed gas begins to expand, moving the projectile away from the armature. The armature then begins to pump residual bore material forward into the region of decreasing pressure, slowing the primary arc and increasing the separation. The base pressure is now too small to provide any significant acceleration to the projectile and its maximum velocity is reached. The two-dimensional CALE simulations produced this separation only when material was added to the computational domain at the juncture of the projectile base and the rail. This suggests that vapor eroded from the projectile by frictional heating is responsible for the buffer formation and primary separation [3].

V. SUMMARY AND RECOMMENDATIONS

The principal need for a railgun model is to aid in understanding how the processes represented by the electromagnetic equations and fluid mechanical equations interact to produce the driving force on the projectile. The railgun is an inherently three-dimensional device. These three mutually orthogonal directions
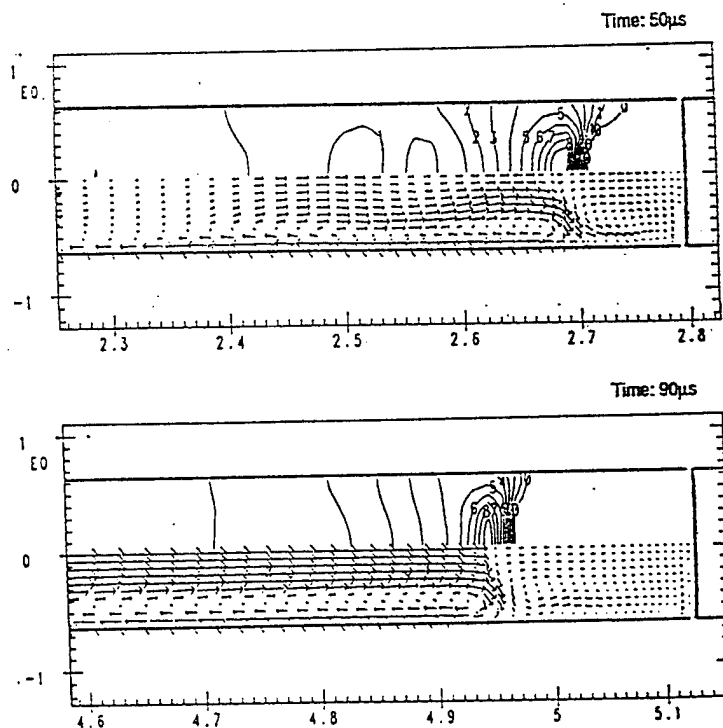

Fig. 4. 2-D CALE simulation of primary separation
(Rail-to-rail current density, top and velocity vectors, bottom).

are defined by the current, the magnetic field and the acceleration. Although two-dimensional simulations have provided valuable insight into physical mechanisms, it is not possible to adequately describe either the MHD flow or the electromagnetic field by using simulations in fewer than three dimensions.

Two-dimensional simulations of the complex MHD armature flow have provided valuable insights into the physical mechanisms responsible for the separation of the primary arc from the projectile. However, the two-dimensional simulations have not been able to positively identify the mechanisms that initiate secondary arc formation. It is very likely that secondary formation is directly linked to the complex three-dimensional flow from the rail to the insulator caused by the reduction of $J \times B$ forces near the insulator surface. This effect is also responsible for a loss of material from the armature which requires replenishment from either the bore surfaces or the projectile. Furthermore, previous 2-D MHD simulations have not included fluid viscosity, so it has not been possible to estimate the magnitude of the viscous drag produced by the complex armature flow or the increasing mass of the buffer layer.

The physical models and computer simulations described in this paper provide understanding and a rational approach to solving the railgun velocity limits. In order to achieve higher velocities there must be changes in the structure and operation of railguns and their projectiles. Three-dimensional simulations for both the electromagnetic field and the armature flow will provide a basis on which new strategies are developed to overcome the drag forces and electrodynamic loss mechanisms that now limit the velocity in railguns. These strategies are likely to include laminated rail components, stiff, low-friction projectiles, hybrid armatures and advanced, augmented and distributed energy barrel designs. Careful and detailed theoretical analysis will enable a thoughtful and effective implementation of these and other strategies which will result in much higher velocities.

REFERENCES

[1] D. Keefer, A. Sedghinasab and R. Crawford, "Simultaneous in-bore rail and insulator spectra from a railgun plasma armature," *IEEE Transactions on Magnetics*, vol. 27, no. 1, pp. 217-219, 1991.

[2] J. Parker, "Why plasma armature railguns don't work (and what can be done about it)," *IEEE Transactions on Magnetics*, vol. 25, no. 1, pp. 418-424, 1989.

[3] D. Keefer and R. Tipton, "The role of fluid mechanics in plasma armature railguns," AIAA 92-0084, 30th Aerospace Sci. Mtg., Reno, NV, 1992.

[4] R. Crawford, D. Keefer and A. Sedghinasab, "Railgun hybrid armatures, experimental results and performance characteristics," *IEEE Transactions on Magnetics*, vol. 27, no. 1, pp. 240-244, 1991.

[5] G. Rolader and J. Batteh, "Effect of in-bore gas on railgun performance," *IEEE Transactions on Magnetics*, vol. 27, no. 1, pp. 120-125, 1991.

[6] J. Taylor, R. Crawford and D. Keefer, "Experimental comparison of conventional and trans-augmented railguns," This Publication.

The Role of Fluid Mechanics
in Plasma Armature Railguns

Dennis Keefer
The University of Tennessee Space Institute
Tullahoma, Tennessee 37388

Robert Tipton
Lawrence Livermore National Laboratory
Livermore, California 94550

30th Aerospace Sciences
Meeting & Exhibit
January 6-9, 1992 / Reno, NV

THE ROLE OF FLUID MECHANICS IN PLASMA ARMATURE RAILGUNS

Dennis Keefer*
The University of Tennessee Space Institute
Tullahoma, Tennessee 37388
and
Robert Tipton**
Lawrence Livermore National Laboratory
Livermore, California 94550

Abstract

Experimental railgun velocities have generally been limited to approximately 6 km/s. This velocity limit is usually accompanied by the evolution of the plasma armature into two separate arc structures and a separation of the armature from the projectile. A three-dimensional physical model for the plasma armature is proposed which is based on experimental observations. A railgun performance model named TWOARC, consistent with this physical model, was developed to correlate railgun experiments in which secondary arcs occurred. Predictions of this model are compared with arc trajectories observed in experiments in 12 mm and 56 mm diameter railguns. The CALE two-dimensional MHD code was used to simulate the complex flow in a railgun plasma armature. The simulations exhibit the observed behavior of plasma armatures and provide some insight into the complex armature flow.

I. Introduction

Why have railguns been limited to velocities of about 6 km/s? The elusive promise for hypervelocity railguns has been unfulfilled for more than a decade. Marshall [1] reported a series of experiments in 1978 in which a railgun powered by a homopolar generator achieved several shots with velocities near 6 km/s. Since that time, numerous railguns have been constructed whose predicted velocity was greater than 6 km/s. Few have actually exceeded 6 km/s, and none have reached their predicted performance. Various drag mechanisms have been proposed to explain these results, including bore ablation, secondary arcs and viscosity [2]. All these mechanisms depend upon the complex MHD flow in the plasma arcs driving the projectiles. It is essential to understand what it is that

---

* B. H. Goethert Professor of Engineering Science and Mechanics, Member AIAA
** Staff Scientist

limits performance if velocities above 6 km/s are ever to be reliably obtained. Diagnostic measurements at The University of Tennessee Space Institute (UTSI) have led to physical and computational models which provide considerable insight into the complex armature flows. These models now provide a rational basis on which to propose solutions which can overcome present velocity limits.

II. Physical Model of a Plasma Armature

Solid metal armatures can be used for railguns which operate below 2 km/s, but all hypervelocity railguns are driven by plasma armatures. Often, it has been tacitly assumed that a plasma armature was just like a solid armature, but with negligible mass and higher resistance. Acceleration of a projectile by a plasma differs in almost every respect from a solid armature. In a solid armature the electromagnetic force developed in the metal is transmitted directly to the projectile, but in a plasma armature all the electromagnetic force is transmitted to the projectile by fluid pressure. This pressure is generated and sustained by the electromagnetic forces in a dynamic, flowing plasma which is dominated by thermal radiation and electromagnetic forces. The resulting flow is strongly three-dimensional and contains complex recirculation cells. Optical and magnetic diagnostic measurements and two-dimensional computer simulations have provided some understanding of these complex plasma armatures.

Several years ago, UTSI succeeded in using quartz optical fibers to obtain direct optical measurements of the plasma emission from within the bore of a railgun [3,4]. These measurements led to the development of a physical model for the plasma armature which has now been incorporated into two computational models. Three key measurements are shown in Figs. 1-3. In Fig. 1 the emission from the plasma is shown as a function of time as observed simultaneously through both the rail and the insulator surfaces in a 1 cm square
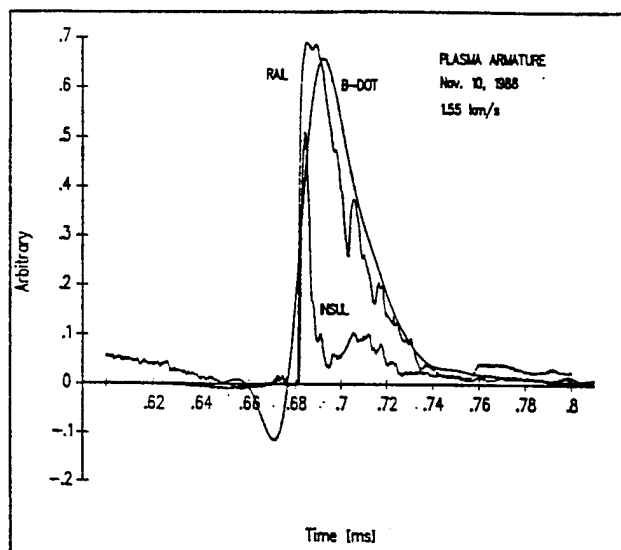
Figure 1. Measured optical emission at the rail and insulator surfaces compared with the arc current.

bore railgun. The current measured by a rail B-dot probe is also shown for comparison. The emission at the rail surface follows the current, but the emission at the insulator surface decreases soon after the current begins to rise and decreases to a minimum near the current maximum. The decrease in emission results from shielding of the insulator surface by vapor which is ablated from the insulator surface by intense thermal radiation from the interior of the plasma.

Figure 2 shows the spectra obtained simultaneously from the rail and insulator for a one microsecond exposure at a point in the armature near the maximum
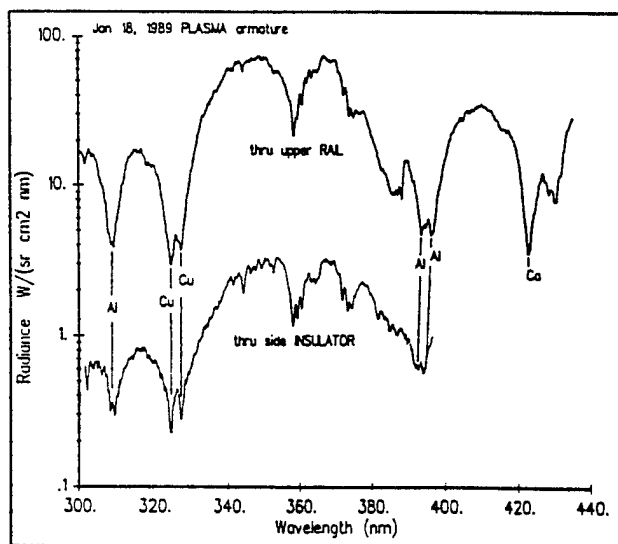
Figure 2. Simultaneous emission spectra measured at rail and insulator surfaces. One microsecond exposure.

value of current density. There is a considerable difference in the intensity of the emission from the rail and insulator surfaces because of the vapor shielding, but there is a striking similarity in the spectral features. This result suggests that strong mixing occurs within the plasma armature which quickly transports rail material (copper) to the insulator surfaces. Detailed plasma radiation transport models were developed at UTSI to analyze these spectra [4]. A comparison between this model and an experimental spectrum obtained from measurements we made at the Thunderbolt facility is shown in Fig. 3. The radiation transport model provides reasonable estimations for plasma composition and temperature.
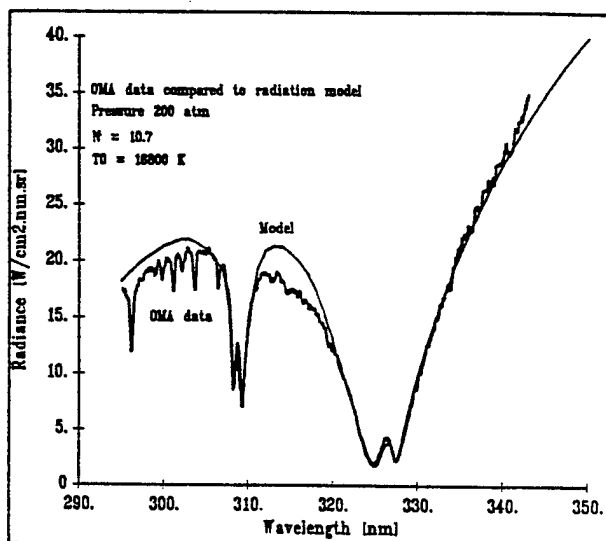

Figure 3. Comparison of measured spectra and plasma radiation model. The armature temperature estimate is 16,800 K and the armature composition estimate is 27.5% Cu and 2.5% Al.

These diagnostic measurements have led us to propose a physical model for the plasma armature which modifies and extends the ablation model proposed earlier by Parker [2]. The projectile is accelerated by fluid pressure in the plasma which is sustained within the plasma and near the rail surface by the Lorentz (J x B) body force. Near the insulator surface vapor shielding reduces the plasma temperature and, therefore, the electrical conductivity of the plasma. Thus, the current density is reduced near the insulator and the J x B force can no longer balance the high pressure developed at the base of the projectile. This results in a cross flow from the rail to the insulator and a leakage of material from the armature along the insulator surfaces which fills the bore behind the armature. This lost armature material must be replaced to prevent depletion of the arma-

ture mass. The replacement material will be obtained primarily from the rail surface where the J x B force is strong enough to accelerate ablated material into the armature. This process is accompanied by ablation drag which establishes a strong recirculation cell in the plasma armature. The expansion of the nonconducting material escaping along the insulator surface leads to a current distribution on the rail which has an "airfoil" shape. An attempt to represent this complex three-dimensional armature flow is shown in Fig. 4.
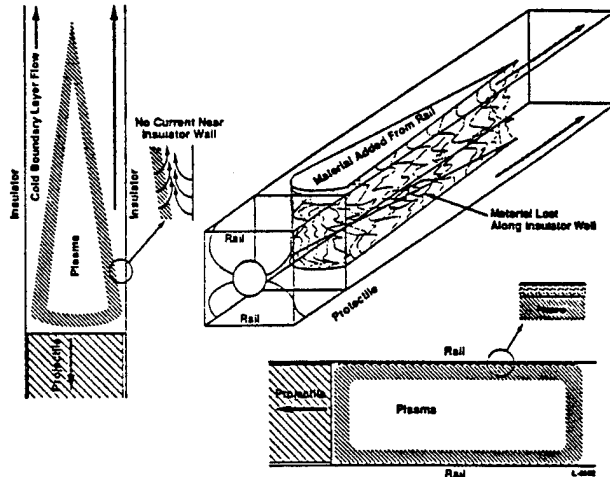
Figure 4. Schematic representation of the three-dimensional armature flow.

III. TWOARC Railgun Performance Model

The phenomenon of "restrike" or secondary arcs has long been associated with degraded velocity performance [5]. We have constructed a computational railgun performance model called TWOARC which includes the effects of a secondary arc. The railgun model is consistent with the physical model for the plasma armature described above, and accounts for the dynamic interactions of a railgun circuit carrying two arcs. The electromagnetic force on each of the two arcs was determined from a two-dimensional railgun model. The circuit model includes the time and distance dependent rail resistances and the velocity and distance dependent rail inductances as shown schematically in Fig. 5. The position of the arcs and projectile in the railgun is determined by the electromagnetic, inertial, pressure, viscous and ablation drag forces as shown schematically in Fig. 6. An important feature of the model is that the material ablated from the bore does not accumulate in the primary arc (nearest the projectile) but is trapped between the two arcs and accelerated by the secondary arc. Approximate physical
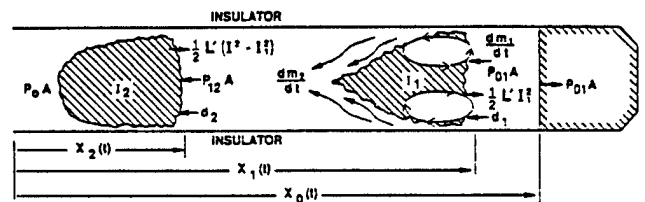
Two Arc Railgun Circuit Model
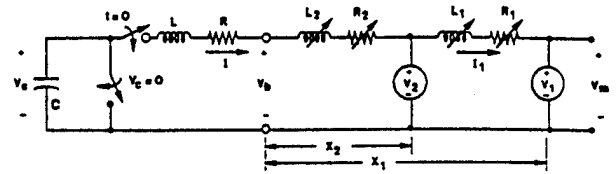
$$L_1(t) = L'[X_1(t) - X_2(t)]$$
$$L_2(t) = L'[X_2(t)]$$

$$\left[\frac{1}{C}\int_0^t I(\tau)\,d\tau - V_0\right] + \left[L\frac{dI}{dt} + IR\right] + \left[L_2\frac{dI}{dt} + I\frac{dL_2}{dt}\right] + IR_2 + [V_2(I - I_1)] = 0$$

$$\left[L_1\frac{dI_1}{dt} + I_1\frac{dL_1}{dt}\right] + I_1 R_1 + [V_1(I_1)] - [V_2(I - I_1)] = 0$$

Figure 5. Circuit schematic and equations for the UTSI TWOARC code.

Two Arc Railgun Armature Model

$$m_1\frac{dv_1}{dt} - \frac{1}{2}L'I_1^2 - d_1 - A(P_{12} - P_{01}) - \frac{dm_1}{dt}v_1$$

$$m_2\frac{dv_2}{dt} - \frac{1}{2}L'(I^2 - I_1^2) - d_2 + A(P_0 - P_{12}) - \frac{dm_2}{dt}v_2$$

Figure 6. Schematic of the physical model and force equations for the UTSI TWOARC code.

models are used to describe ablation, armature resistance and separation of the armatures and the projectile. Unknown parameters in these models were determined by correlations with experimental data from 12 mm railgun experiments performed at Lawrence Livermore National Laboratory (LLNL) and the 56 mm diameter Thunderbolt railgun. Because of the approximate nature of the physical models and the uncertainty in the parameters, such as the ablation coefficient armature resistance and the viscous coefficient, the model is not predictive but is useful for the correlation and interpretation of experimental results.

A correlation between the model predictions and B-dot probe data from the 12 mm diameter, 5.2 m long LLNL railgun [5] is shown in Fig. 7. The armature divided into primary and secondary arcs soon after the pulse began. These arcs continued to separate as the secondary arc dissipated its electromagnetic force to accelerate the ablated material released by the primary arc. The primary arc continued to accelerate the projectile until well after current maximum, but then the primary arc separated from the projectile.
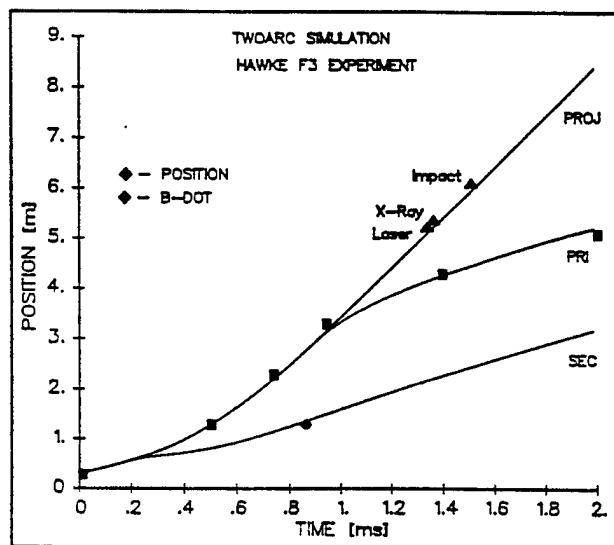

Figure 7. Comparison of the TWOARC simulation with B-dot and other position data from the 12 mm LLNL railgun.
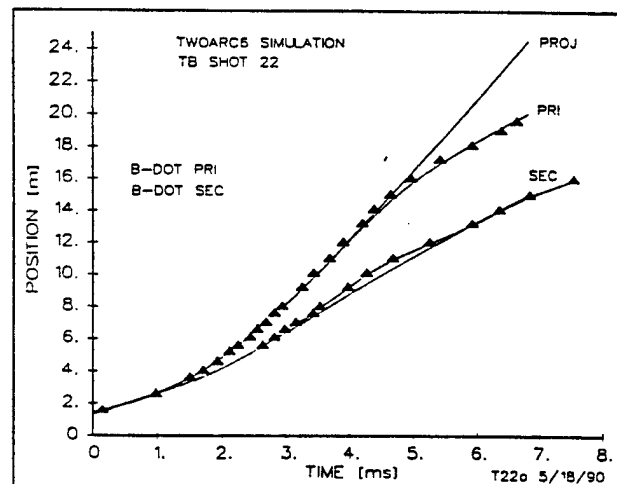
Figure 8. Comparison of the TWOARC simulation with B-dot position data from the 56 mm THUNDER-BOLT railgun.

This separation of the primary arc from the projectile effectively uncoupled the Lorentz forces from the projectile and no further acceleration took place. Figure 8 shows a similar behavior for the 56 mm diameter, 20 m long Thunderbolt railgun. In this experiment the large number of closely spaced B-dot probes more clearly defined the trajectory of the two arcs.

Examination of the detailed information available from TWOARC reveals that prior to primary separation, approximately 80% of the available electromagnetic impulse was converted into projectile momentum. However, when primary separation occurred almost none of the available electromagnetic impulse was converted to projectile acceleration. Instead, the primary arc apparently dissipated its electromagnetic force by pumping residual bore material forward into the increasing volume between the primary arc and the projectile.

The TWOARC simulations clearly show that while performance is degraded by parasitic secondary arcs, it is primary separation which prevents further acceleration and imposes the observed velocity limit. Insight into the dynamic plasma mechanisms which lead to secondary formation and primary separation has been enhanced through simulations of the plasma armature using the two-dimensional CALE magneto-hydrodynamic code.

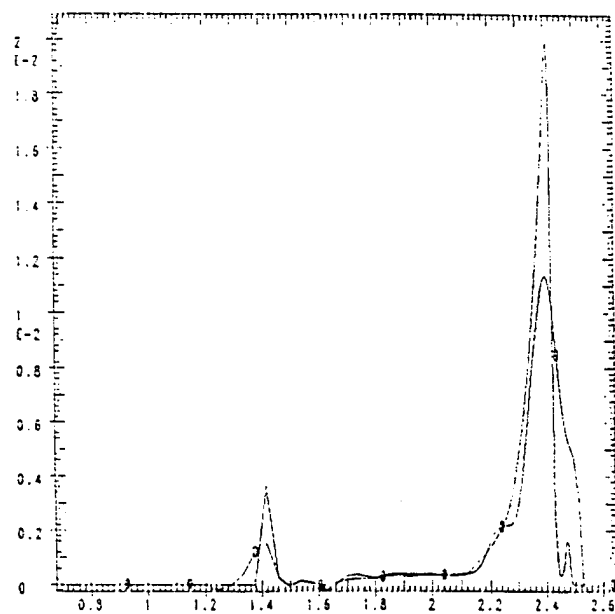## IV. Two-Dimensional Plasma Armature Simulations

The plasma flow in a railgun armature clearly has important three-dimensional features. Most current hydrocodes which include MHD and plasma radiation transfer can only handle two dimensions. However, simulations using these two-dimensional codes can provide vital insight into the physical mechanisms which control the formation and evolution of secondary arcs and the separation of the primary arc from the projectile. The CALE code developed at LLNL was used to simulate the evolution of a railgun armature. The CALE code is an arbitrary Lagrangian-Eulerian MHD code which includes magnetic diffusion and radiation transfer, but neglects fluid viscosity. The simulations used a mixed computational domain in which the fluid mechanics were simulated in an axisymmetric cylindrical domain while the magnetic field solutions were obtained in a plane which included the rails. Conditions for the simulation were similar to those used in a recent HELEOS experiment [6] and include the time dependence of the current pulse driving the railgun. The simulations show that the secondary arc does not "restrike" suddenly in the empty bore, but evolves slowly from the tail of the primary arc as shown in Fig. 9.
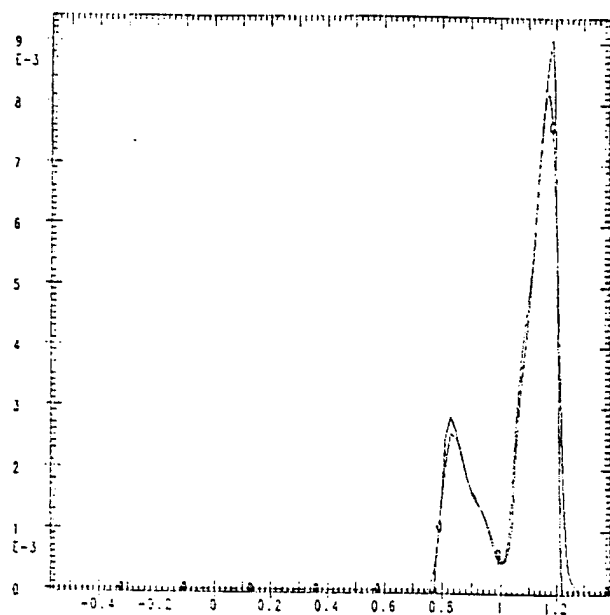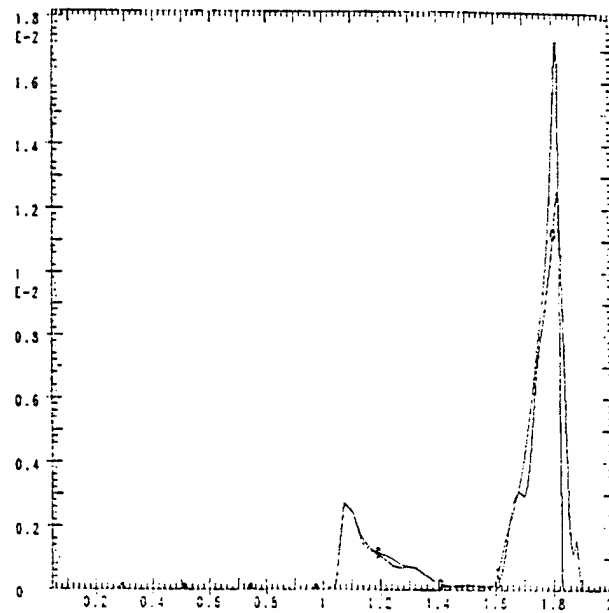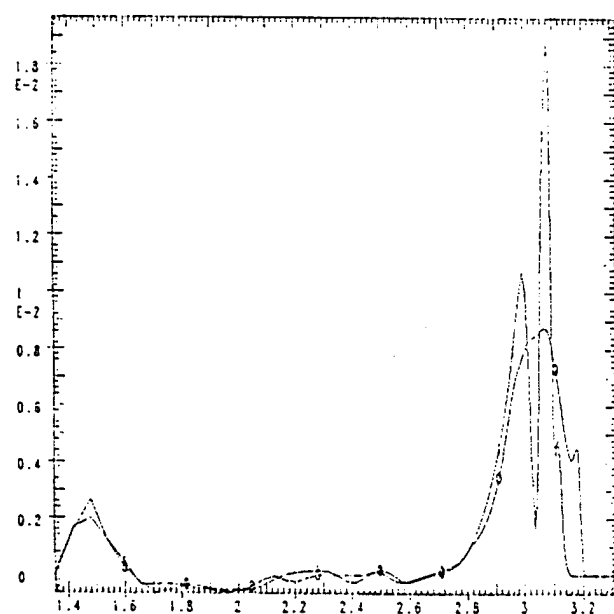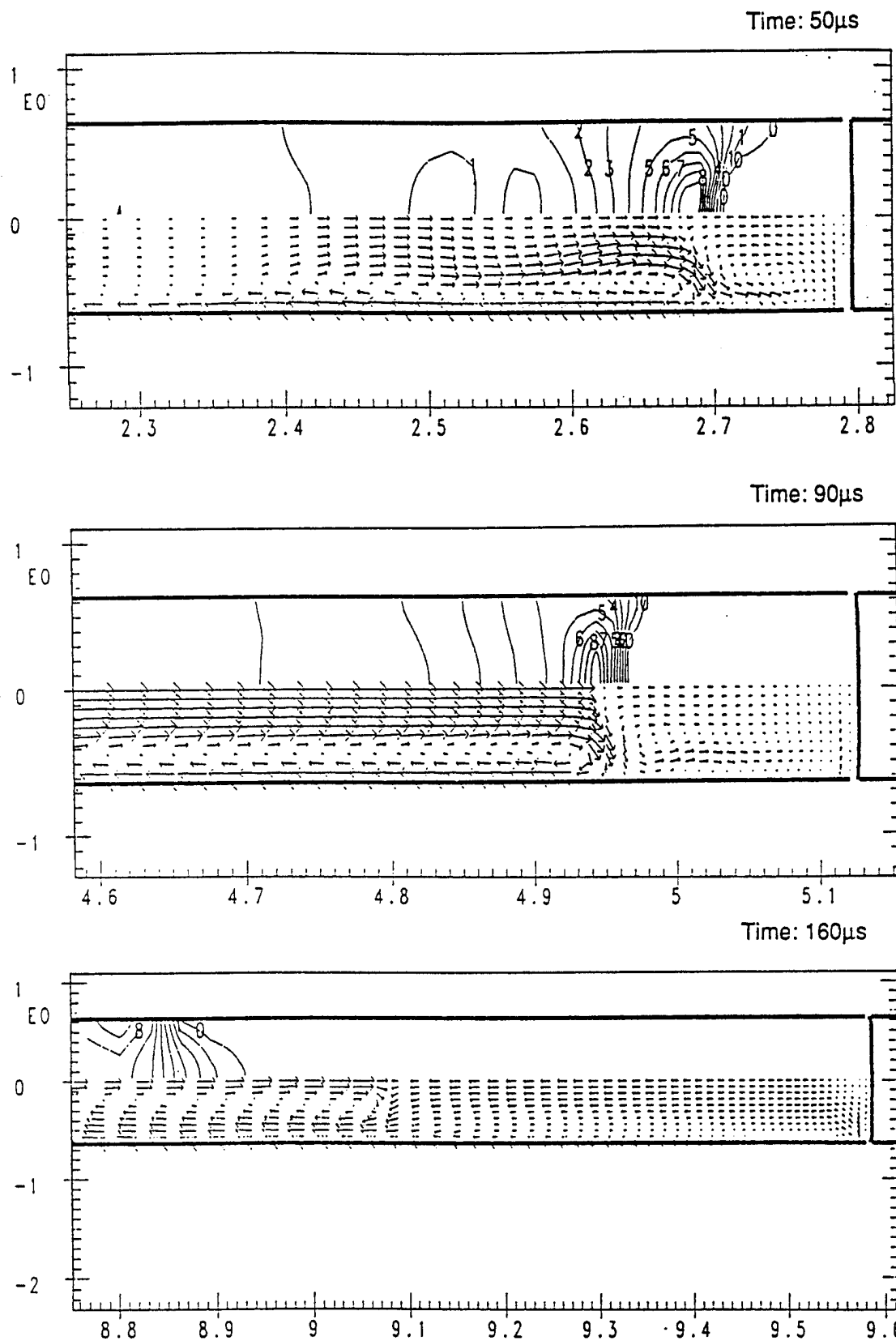
Figure 9. Two-dimensional CALE code simulation of plasma armature showing evolution of a secondary arc. Current density at the axis and near the wall is plotted as a function of distance at 4 different times.

Figure 10. Two-dimensional CALE code simulation of plasma armature showing primary separation from the projectile. Transverse current density contours are shown in the upper half and velocity vectors in the lower half. Axial distance is in units of 10 cm, radial distance in cm.

CG-2044

This figure shows the armature current distribution at four different times as the armature moves down the bore. The secondary initially forms as a peak near the rear of the primary armature which then separates from its parent. It first weakens, but then grows in amplitude as it continues to separate from the primary.

The detailed plasma flow within the armature is shown in Fig. 10. The transverse (rail-to-rail) current density contours are plotted in the upper half of each figure, and the plasma velocity vectors are plotted in the lower half. The strong recirculation produced by ablation drag and acceleration is clearly evident. During the rising part of the current pulse, a nonconducting buffer of compressed gas accumulates at the base of the projectile. This is consistent with the observation that recovered plastic projectiles from plasma railguns rarely show any evidence of base ablation. It is this nonconducting buffer which protects the projectile base from ablation. After passing through current maximum, the electromagnetic pressure decreases and this volume of relatively dense compressed gas begins to expand, moving the projectile away from the primary arc. The primary arc then begins to pump residual bore material forward into the region of decreasing pressure, slowing the primary arc and increasing the separation. The base pressure is now too small to provide significant acceleration to the projectile and its maximum velocity is obtained.

V. Conclusions

The physical models and computer simulations described above provide some insight into the complex MHD flow in plasma armatures, but many questions remain unresolved. The simulations suggested that the buffer region between the projectile and the primary arc was initiated by vapor produced in the sliding interface between the projectile and the bore and introduced into the baseflow region. However, we were unable to postulate a physical mechanism which reliably led to initiation and formation of stable secondary arcs. We speculate that it is the strong three-dimensional components of the flow from the rail to insulator which lead to the isolation of a conducting region of plasma which becomes a secondary arc. Further insight into the complex armature flow will be difficult without the aid of three-dimensional computer simulations of the plasma armature.

In order to achieve higher railgun velocities there must be changes in the structure and operation of railguns and their projectiles. A number of strategies have been suggested to prevent or quench secondary arcs [2]. These include reduction of bore ablation, augmenta-

tion, segmentation of rails and distributed power. Another approach which appears to have promise is the hybrid armature. Experiments have been performed at UTSI using hybrid armatures of various configurations at velocities below 2 km/s to characterize their efficiency and mass ablation rates [7]. Short, hybrid armatures were used on the HELEOS railgun to control the armature configuration and to replenish lost armature material without the associated ablation drag [6]. These armatures have operated without secondary arc formation and provided near ideal theoretical performance up to a velocity of 6.7 km/s and have achieved a maximum velocity of 7.5 km/s. These experiments, together with more sophisticated computer simulations which include hybrid armatures, should provide a sound, rational basis to extend the velocity limit for railguns.

Acknowledgements

References

1. S. C. Rashleigh and R. A. Marshall, "Electromagnetic Acceleration of Macroparticles to High Velocity," J. Appl. Phys., Vol. 49, pp. 2540-2542, 1978.

2. J. V. Parker, "Why Plasma Armature Railguns Don't Work (And What Can be Done About It)," IEEE Trans. on Magn., Vol. 25, pp. 418-424, 1989.

3. D. Keefer and R. Crawford, "Optical Diagnostics of Railgun Plasma Armatures," IEEE Trans on Magn., Vol. 25, pp. 295-299, 1989.

4. D. Keefer, A. Sedghinasab and R. Crawford, "Simultaneous In-Bore Rail and Insulator Spectra From A Railgun Plasma Armature," IEEE Trans. on Magn., Vol. 27, pp. 217-219, 1991.

5. R. S. Hawke, W. J. Nellis, G. H. Newman, J. Rego and A. R. Susoeff, "Summary of EM Launcher Experiments Performed at LLNL," Proc. 3rd Symposium on Electromagnetic Launch Technology, Austin, Texas, April, 1986.

6. R. S. Hawke, A. R. Susoeff, J. R. Asay, J. A. Ang, C. A. Hall, C. H. Konrad, G. W. Wellman, J. L. Sauve and A. R. Vasey, "Railgun Performance With a Two-Stage Light-Gas Gun Injector," IEEE Trans. on Magn., Vol. 27, pp. 28-32, 1991.

7. R. Crawford, D. Keefer and A. Sedghinasab, "Railgun Hybrid Armatures, Experimental Results and Performance Characteristics," IEEE Trans. on Magn., Vol. 27, pp. 240-244, 1991.

Determining Railgun Plasma Current Distribution Using Jansson's Method to Deconvolve B-Dot Probe Signals

Bruno J. Evans, *Member, IEEE*, and L. Montgomery Smith, *Member, IEEE*

Abstract—In this paper we present a method of determining the plasma armature current distribution from B-dot probe signals. This method utilizes the knowledge that the B-dot probe signal can be shown to be a convolution of the plasma armature current distribution with the impulse response function of the B-dot probe. Jansson's relaxation-based nonlinear deconvolution technique is developed for use with recorded B-dot probe data. Results obtained with this technique indicate that significant improvement in estimations can be obtained over previously used linear deconvolution methods.

I. INTRODUCTION

IN order to evaluate the performance of an electromagnetic launcher (railgun), it is essential to understand the plasma armature current density. Over the past decade, current probes (termed B-dot probes) have become a primary diagnostic instrumentation technique used to assess the performance of railguns [1]. A B-dot probe is a small cylindrical coil that produces an output voltage proportional to the time rate of change of the magnetic field component parallel to the axis of the coil. As the plasma armature passes by a B-dot probe located near the barrel of the railgun, it produces a voltage pulse whose functional form is dependent upon the orientation of the probe. With the B-dot probe oriented to sense the armature current, the probe signal is a bimodal pulse consisting of a positive and a negative portion. The B-dot probes on the railgun at the University of Tennessee Space Institute (UTSI) are oriented to sense the rail current, and the probe signal is a unidirectional pulse. Since these signals depend on the shape of the armature current distributions in plasma armature railguns, they are used to infer the current densities in the plasma.

Presently, several methods are used to determine the plasma armature current distributions from recorded B-dot probe signals. Cobb [2] has developed a method for determining current density profiles by least-squares fitting of the B-dot signals. Jamison and Burden [3] have used a similar technique to determine current density profiles. Smith and Keefer [4] have shown the recorded B-dot signal to be a convolution of the B-

dot probe impulse response with the plasma armature current distribution and have retrieved the current density profiles from B-dot signals through deconvolution using a Wiener filter. Bouvier [5] speaks of finding the current distribution by taking the fast Fourier transform of the integral of the B-dot signal and deconvolving it with a geometry-dependent weight function and a Gaussian filter.

All the techniques described for determining the plasma armature current densities give good quantitative information, but they all have drawbacks. The fitting method used by Jamison and Burden assumes a functional form for the armature current distribution. The method used by Cobb assumes a time dependence for the armature current distribution. The deconvolution approach of Bouvier is not optimal since a Wiener filter gives the best least-squares linear estimate. The Wiener filter approach of Smith and Keefer requires an ad hoc parameter in the absence of noise and data statistics. These and other linear methods also suffer since the final estimate can contain nonphysical artifacts (e.g., negative peaks).

Frequently, linear deconvolution produces undesirable artifacts. Nonlinear methods, however, allow the use of constraints based on physical properties, such as nonnegativity, to be enforced during the deconvolution process. Relaxation-based nonlinear iterative methods that use constraints of peak nonnegativity have been successfully used by Crilly [6] to restore severely overlapped and noisy chromatographic and spectroscopic data. For this type of data, Crilly has shown that Jansson's method [7] provides the best results.

In this paper, we present the iterative nonlinear deconvolution method developed by Jansson [7] as a technique for determining the plasma armature current distributions from recorded B-dot probe signals. The results of Smith and Keefer [4] show that the B-dot probe signal is a convolution of the armature current distribution with the B-dot probe impulse response function. Therefore, the current distribution can be recovered from the B-dot probe signal through deconvolution. Based upon the work of Crilly, Jansson's relaxation-based nonlinear iterative deconvolution method, which uses constraints of maximum and minimum peak amplitudes, is developed for use with B-dot probe data. Successive estimates are constrained by upper and lower amplitude bounds that correspond to the physical limits of the data. The constraining operation is done in a gradual fashion without any truncation of information. The procedure makes corrections based on the difference between the recorded B-dot probe signal and the

convolution of the current distribution estimate with the B-dot probe impulse response function. This method requires knowledge only of the B-dot probe impulse response function and the maximum peak amplitude of the armature current distribution.

The derivation of the B-dot probe impulse response function is presented in the following section. In Section III, Jansson's deconvolution method is developed, and its implementation for this application is described. Section IV presents numerical results, both for simulated B-dot probe data and for data from actual railgun firings. Discussion and conclusions are given in Section V.

II. B-DOT PROBE SIGNAL

A typical B-dot probe consists of N multiple turns of wire around a form having a cross-sectional area A. The B-dot probe produces an output voltage proportional to the time rate of change of the magnetic field component parallel to the axis of the coil. The voltage signal induced in a B-dot probe can be found from Faraday's law and is given by

$$V = NA\frac{dB_n}{dt}, \tag{1}$$

where B_n is the component of the magnetic field parallel to the probe normal n.

A magnetic field, B, occupies the space around a current-carrying conductor. The magnetic induction B produced at a point r in space by a distribution of currents is determined by the Biot-Savart law:

$$B(r) = \frac{\mu_0}{4\pi} \int \frac{J(r') \times (r - r')}{|r - r'|^3} d^3r, \tag{2}$$

where $J(r')$ is the current density at the point r'.

Smith and Keefer [4] have shown that, under certain simplifying assumptions, a B-dot probe voltage signal is a convolution of the armature current distribution with an impulse response function which can be derived from the armature velocity and the probe geometry and position. The results of Smith and Keefer considered only the current traveling in the rail nearest the B-dot probe. Evans and Smith [8] have expanded this derivation to include the effects of the current traveling in both rails. A derivation can be found in the cited references. The following derivation follows that of Evans and Smith [8], and is presented for completeness and consistency with the present notation.

The railgun circuit model shown in Fig. 1 consists of a current loop lying in the x–y plane. The rails are oriented in the x direction and are modeled as infinitely thin conductors carrying total gun current I_0. The B-dot probe is oriented to sense the y component of the magnetic field and is at a longitudinal distance x from the origin, at a radial distance r_1 from the nearer rail, and at an angle θ_1 from the z direction. An assumption is made that the breech of the gun barrel lies at a sufficient distance from the probe to approximate $-\infty$.

The armature current distribution (current per unit length) is denoted $I_{arm}(x)$, and is modeled as moving with velocity v in the x direction. As shown in Fig. 1, it lies in the moving ξ coordinate system, with its leading edge at $\xi = 0$. At time
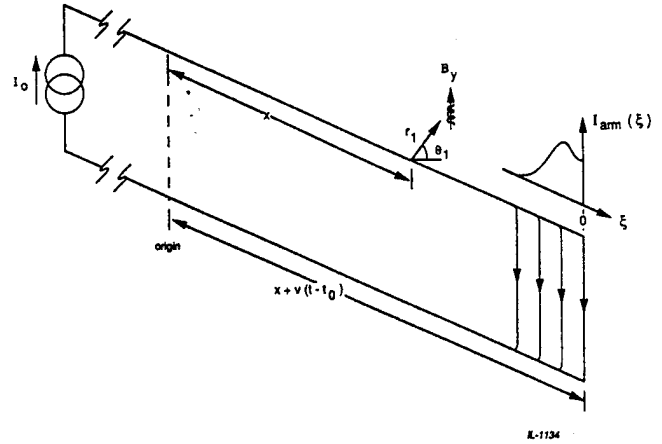
Fig. 1. Circuit model used to derive the expression for the B-dot probe response to a passing armature.

$t = t_0$, the leading edge of the current distribution passes the B-dot probe. Near the time t_0, as the armature passes the probe, a pulse occurs in the signal that deviates from the quiescent value for a short time interval. For typical railgun firings, this interval is on the order of 100 μs. It is assumed that over this time interval, the velocity, v, and total current, I_0, remain constant, and that the shape of the armature current distribution, $I_{arm}(\xi)$, in the moving coordinate system does not change. With these assumptions, the x component of the current in the rails at time t near time t_0 is given by

$$I(x') = I_0 - \int_{-\infty}^{x' - [x + v(t - t_0)]} I_{arm}(\xi) d\xi. \tag{3}$$

From the Biot-Savart law (2), the y component of the magnetic field at the probe location at time t can be expressed explicitly as

$$B_y(t) = \frac{\mu_0}{4\pi} r_1 \cos\theta_1 \int_{-\infty}^{\infty} \frac{I(x')}{[r_1^2 + (x - x')^2]^{3/2}} dx'. \tag{4}$$

This expression can be cast into the form of a convolution integral via a method similar to that described in [8]. Following substitution of (3) into (4), the change of variables $\eta = x' - [x + v(t - t_0)]$ is made. The result is then differentiated with respect to time t. This expression in turn can be evaluated by integration by parts. The B-dot probe response can thereby be shown to be proportional to

$$\frac{dB_y}{dt} = \frac{\mu_0}{4\pi} v r_1 \cos\theta_1 \int_{-\infty}^{\infty} \frac{I_{arm}(\eta)}{\left[r_1^2 + \left(v(t_0 - t) - \eta\right)^2\right]^{3/2}} d\eta. \tag{5}$$

The integral in (5) can be recognized as the one-dimensional convolution of the armature current distribution $I_{arm}(x)$ with an impulse response function $h_1(x)$ with the substitution $x = v(t_0 - t)$ in the result. The impulse response function of the B-dot probe for a single rail is thus given by

$$h_1(x) = \frac{\mu_0}{4\pi} \frac{v r_1 \cos\theta_1}{[r_1^2 + x^2]^{3/2}}, \tag{6}$$

where the convolution is performed with respect to the variable x. Note that the B-dot probe signal is time varying, and that its temporal variation is dependent in form upon the velocity, v.

The impulse response function arising from the current in the farther rail can be found in a similar manner. The probe is located a radial distance r_2 from the farther rail and at an angle θ_2 from the z direction. The current in the farther rail is assumed to be given by (3) but traveling in the opposite direction. This induces a magnetic field in the y direction opposite in sign to that induced by the current in the nearer rail. The expression for the y component of the magnetic field at the probe location caused by the farther rail current is thus given by the negative of (4) with the radial distance and angle for the farther rail. By following the same analysis used in determining the impulse response arising from the current in the nearer rail, the impulse response function of the B-dot probe caused by the current in the farther rail is

$$h_2(x) = -\frac{\mu_0}{4\pi} \frac{vr_2 \cos\theta_2}{\left[r_2^2 + x^2\right]^{3/2}}. \tag{7}$$

By superposition, the impulse response function of the B-dot probe arising from the current in both rails can be expressed as

$$h(x) = \frac{\mu_0}{4\pi} \left[\frac{vr_1 \cos\theta_1}{\left[r_1^2 + x^2\right]^{3/2}} - \frac{vr_2 \cos\theta_2}{\left[r_2^2 + x^2\right]^{3/2}} \right]. \tag{8}$$

It has been shown that the B-dot probe signal is a convolution of the armature current density with the impulse response function of the B-dot probe. Jansson's relaxation-based iterative nonlinear deconvolution method will be developed in the next section. Also, its implementation for this application will be described.

III. Estimation of the Current Distribution

Since it was shown that the B-dot probe signal is a convolution of the plasma armature current distribution with the impulse response function of the B-dot probe, the current distribution can be recovered from the B-dot probe signal using a deconvolution technique. The relaxation-based iterative nonlinear deconvolution method developed by Jansson [7] is presented here as a technique for determining the plasma armature current distributions from recorded B-dot probe signals [9].

Assuming that the leading edge of the armature passes the B-dot probe at time $t_0 = 0$, the B-dot probe signal, denoted $g(t)$, can be written

$$g(t) = \int_{-\infty}^{\infty} I_{\mathrm{arm}}(\eta)h(-vt - \eta)d\eta + \epsilon(t), \tag{9}$$

where $h(x)$ is the B-dot probe impulse response function given in (8), $I_{\mathrm{arm}}(x)$ is the plasma armature current distribution, and $\epsilon(t)$ represents the noise that inevitably corrupts any experimental signal. If the signal is sampled at a uniform sampling interval, Δt, and the result is axis reversed in time, the discrete data sequence can be expressed as

$$g(-n\Delta t) = \int_{-\infty}^{\infty} I_{\mathrm{arm}}(\eta)h(vn\Delta t - \eta)d\eta + \epsilon(-n\Delta t). \tag{10}$$

The convolution integral can be approximated by a rectangular rule integration scheme with interval $v\Delta t$ to yield

$$g(-n\Delta t) = \sum_{m=0}^{M-1} I_{\mathrm{arm}}(mv\Delta t)h\big((n-m)v\Delta t\big)v\Delta t + \epsilon(-n\Delta t), \tag{11}$$

where M is the total number of points in the discrete sequence $I_{\mathrm{arm}}(\eta)$.

For the remainder of this paper, the substitutions $g(n)$ for $g(-n\Delta t)$, $I_{\mathrm{arm}}(n)$ for $I_{\mathrm{arm}}(nv\Delta t)$, $h(n)$ for $h(nv\Delta t)v\Delta t$, and $\epsilon(n)$ for $\epsilon(-n\Delta t)$ will be used. With this obvious abuse in notation, the B-dot probe signal can be written as the convolution of two discrete sequences corrupted by a noise sequence as

$$g(n) = \sum_{m=0}^{M-1} I_{\mathrm{arm}}(m)h(n - m) + \epsilon(n). \tag{12}$$

The sequence $I_{\mathrm{arm}}(n)$ can be recovered from the observed data $g(n)$ by deconvolution. Deconvolution of noisy data is a problem that has been extensively studied, and numerous methods exist for calculating an estimate, $\hat{I}_{\mathrm{arm}}(n)$, from the recorded B-dot probe signal $g(n)$. In general, techniques that take advantage of all *a priori* information will yield better results. Many classes of data have values that are limited by physical constraints such as nonnegativity. Attempts to restore this type of data with linear methods may produce nonphysical results such as negative artifacts.

Jansson's iterative approach is based upon the work of Van Cittert [10]. With Van Cittert's approach, successive estimates are achieved by

$$\hat{I}_{\mathrm{arm}}^{(k+1)}(n) = \hat{I}_{\mathrm{arm}}^{(k)}(n) + b\Big[g(n) - h(n) * \hat{I}_{\mathrm{arm}}^{(k)}(n)\Big], \tag{13}$$

where $\hat{I}_{\mathrm{arm}}^{(k)}(n)$ is the kth estimate of $I_{\mathrm{arm}}(n)$, b is termed the relaxation constant, and the asterisk ($*$) is a shorthand notation for the convolution sum given in (12). Traditionally, the initial estimate is somewhat arbitrarily chosen to be

$$\hat{I}_{\mathrm{arm}}^{(0)}(n) = g(n). \tag{14}$$

Van Cittert's method uses the correction factor $b\Big[g(n) - h(n) * \hat{I}_{\mathrm{arm}}^{(k)}(n)\Big]$ to adjust the kth estimate of $I_{\mathrm{arm}}(n)$ based upon the difference between the actual signal, $g(n)$, and the convolution, $h(x) * \hat{I}_{\mathrm{arm}}^{(k)}(n)$.

If the physical limits of the data are known *a priori*, constraints can be incorporated into Van Cittert's equation to take advantage of the prior knowledge. This can be done by modifying the correction term $\Big[g(n) - h(n) * \hat{I}_{\mathrm{arm}}^{(k)}(n)\Big]$ by a relaxation function that causes corrections to $\hat{I}_{\mathrm{arm}}^{(k)}(n)$ whenever the estimate has nonphysical values.

Jansson's method constrains successive iterations to occur between upper and lower amplitude bounds that correspond to the physical limits of the data. The upper amplitude bound is the maximum peak amplitude of the current distribution estimate, and the lower amplitude bound enforces the non-negativity constraint. The deconvolution algorithm is given
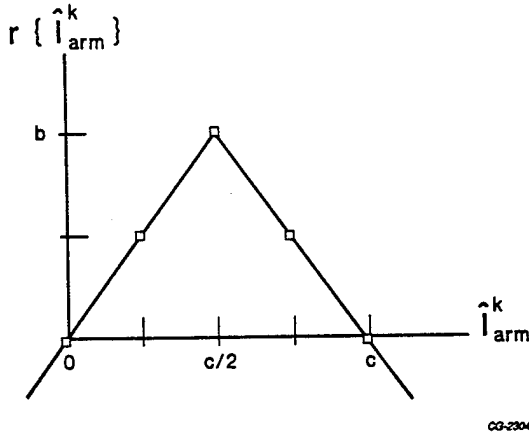
Fig. 2. The relaxation function used in Jansson's deconvolution method.

by

$$\hat{I}_{\text{arm}}^{k+1}(n) = \hat{I}_{\text{arm}}^{(k)}(n) + r\{\hat{I}_{\text{arm}}^{(k)}(n)\}\left[g(n) - h(n) * \hat{I}_{\text{arm}}^{(k)}(n)\right]$$
(15)

where $r\{\hat{I}_{\text{arm}}^{(k)}(n)\}$ is a relaxation function given by

$$r\{\hat{I}_{\text{arm}}^{(k)}(n)\} = b\left[1 - \frac{2}{c}\left|\hat{I}_{\text{arm}}^{(k)}(n) - \frac{c}{2}\right|\right].$$
(16)

In (16), c is the upper amplitude bound, and the first estimate, $\hat{I}_{\text{arm}}^{(0)}(n)$, is given by (14). The relaxation function is plotted in Fig. 2. By examining this figure, it can be seen that $r\{\hat{I}_{\text{arm}}^{(k)}(n)\}$ makes positive corrections if the estimate lies within its physical limits (0 to c) and reverse corrections if the estimate has nonphysical values. The amount of correction is also weighted less as the estimate approaches the physical limits.

The ability of Jansson's method to converge depends on the selection of the relaxation constant, b. If the signal-to-noise ratio of the data is relatively high, b can be large and the solution will quickly converge. However, if the signal-to-noise ratio of the data is small, b must be a small number or else the solution will diverge.

In order to determine whether the solution has converged, the mean square error (MSE) between the recorded B-dot probe signal and the convolution of the current distribution estimate with the B-dot probe impulse response function can be examined. The MSE of the kth estimate is given by

$$\text{MSE} = \frac{1}{M}\sum_{n=0}^{M-1}\left[g(n) - h(n) * \hat{I}_{\text{arm}}^{(k)}(n)\right]^2.$$
(17)

Convergence can be determined by several means. The most obvious is to minimize the MSE, which may require many iterations. To reduce computational time, the number of iterations can be reduced by stopping the algorithm after the MSE or a percent change in the MSE reaches a value specified by the user.

All deconvolution methods are limited in their ability to deconvolve noisy data without introducing any additional spurious components. This limitation is caused by the deconvolution process not only restoring the high-frequency components that constitute the well-defined features in the signal, but also enhancing the high-frequency noise components at an even faster rate. Therefore, it is advantageous to remove as much noise as possible from the signal before starting the deconvolution process [6]. The noise can be removed from the recorded B-dot probe signal using a low-pass filter.

A filtering scheme known as reblurring [6] provides a way of reducing the high-frequency noise in the B-dot probe signal and was found to be necessary for this application. In this method, the signal is prefiltered with the axis-reversed impulse response function to remove high-frequency noise components as follows:

$$g'(n) = h(-n) * g(n).$$
(18)

This requires that, in the deconvolution algorithm, the impulse response $h(n)$ should also be modified in the following manner:

$$h'(n) = h(n) * h(-n)$$
(19)

The new functions, $g'(n)$ and $h'(n)$, replace $g(n)$ and $h(n)$ respectively in (15). (In this particular application, the impulse response is symmetric, so $h(n) = h(-n)$.) This technique can be looked at as forming the cross-correlation between the B-dot probe data, $g(n)$, and the probe impulse response, $h(n)$. It is a low-pass filtering operation that removes signal components that are not common to both $g(n)$ and $h(n)$, specifically, the high-frequency noise.

In addition to removing the high-frequency noise, this filtering technique may also reduce some of the essential high-frequency components contained in the B-dot probe signal which permit well-defined features, thus reducing the resolution of the deconvolved data. This reduction in resolution requires an increase in the number of iterations in order for the deconvolution process to converge to a given goal. Therefore, a trade-off exists between noise reduction and computational time when the B-dot probe signal is filtered in this manner.

In applying the iterative algorithm (14), it was discovered that $h(n)$ needed to be normalized:

$$\sum_{n=0}^{M-1} h(n) = 1.$$
(20)

This ensures that the difference $g(n) - h(n) * \hat{I}_{\text{arm}}^{(k)}(n)$ in the correction term is small. Without this normalization, large differences could result in the correction term causing the solution to diverge rapidly.

The peak amplitude of the plasma armature current distribution is not known *a priori*. This poses a problem since the wrong selection for c will have adverse effects on the solution. Fig. 3 shows the effects of choosing c to be smaller than the actual peak amplitude of the estimate $\hat{I}_{\text{arm}}(n)$. The peak of the armature current density is truncated in response to the reverse corrections made for estimates whose amplitudes are greater than c. Fig. 4 shows the effects if c is chosen to be too large. In this case, c was chosen to be twice the peak amplitude of the B-dot probe signal. The largest corrections are made near
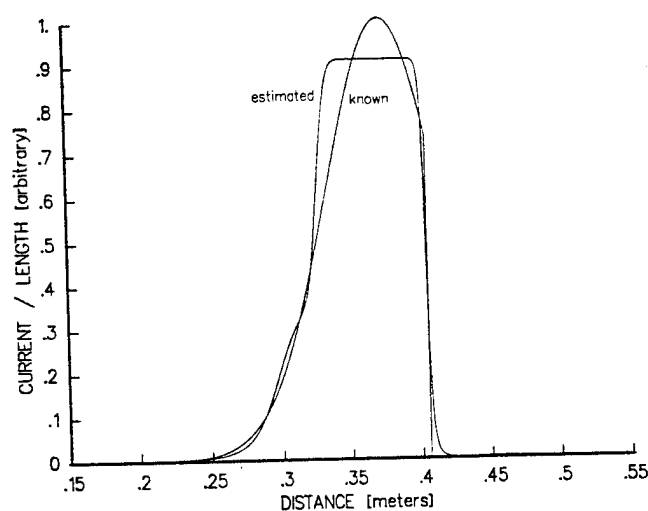
Fig. 3. Typical output resulting from choosing the upper bound c to be smaller than actual peak height.
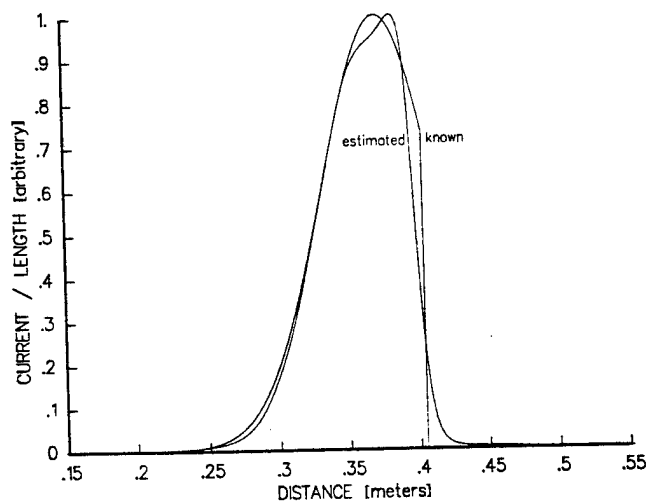

Fig. 4. Typical output resulting from choosing the upper bound c to be much larger than actual peak height.

Fig. 5. Typical output resulting from choosing the upper bound $c^{(k)}$ iteratively based on first estimate from Van Cittert's method.

the peak, resulting in the production of artifacts near the peak not present in the original signal.

A method for determining an approximate peak amplitude for the estimate of the current density $\hat{I}_{arm}(n)$ has been developed based upon updating the value for the upper bound with each iteration. In order to determine the approximate amplitude that will be achieved with Jansson's method, one iteration is performed using Van Cittert's method. The value for $c^{(1)}$ is selected to be 10% greater than the maximum amplitude achieved with this iteration. Jansson's method is then implemented with this selection for $c^{(1)}$. However, after each iteration, the value of $c^{(k)}$ is adjusted to be 10% greater than the maximum amplitude achieved with the previous iteration. This method of selecting $c^{(k)}$ has been tested using simulated B-dot probe signals and works extremely well. Fig. 5 shows the results of deconvolving a simulated B-dot probe signal using this method.
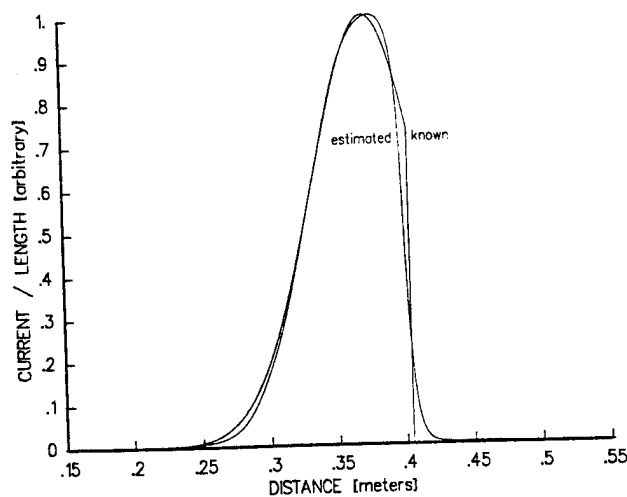
A computer program was written to minimize the MSE between the B-dot probe signal and the estimate convolved with the B-dot probe impulse response function. However, in testing with simulated B-dot probe signals, it required hundreds of iterations for the solution to converge. Upon examining results obtained with the MSE minimization, it was discovered that after the percent change in the MSE was less than 1%, there was no noticeable difference in the successive iterations. To reduce the computational time, the program has been modified to allow the user to specify the cutoff point based on the percentage change in the MSE.

In using Jansson's method to deconvolve B-dot probe data from the UTSI railgun, it was discovered that acceptable results can be achieved by stopping the iterations when the percentage change in the MSE drops below 1%. A value of 1.5 for b was found to work well with recorded B-dot probe signals from the UTSI railgun. With the values for the MSE and b selected as stated above, from 50 to 100 iterations were required for the solution to converge.

IV. RESULTS

To illustrate the effectiveness of this method, numerical simulations were conducted with simulated and experimental B-dot probe signals. The simulated B-dot probe signals were generated in the manner described in [8] and [9]. In order to resemble signals recorded from the UTSI railgun, the simulated signals were corrupted with noise by adding uncorrelated Gaussian random numbers with a standard deviation of 0.129 and quantized to 64 levels.

To examine the effectiveness of using Jansson's method to deconvolve B-dot probe signals, the algorithm was tested on simulated B-dot probe signals. Fig. 6 shows a simulated B-dot probe signal with its known armature current density axis-reversed and scaled to the time sampling interval. In deconvolving the simulated signal, the iterations were stopped when the percentage change in the MSE dropped below 1%. Fig. 7 shows the resulting armature current density estimates obtained using both Jansson's method and the Wiener filter
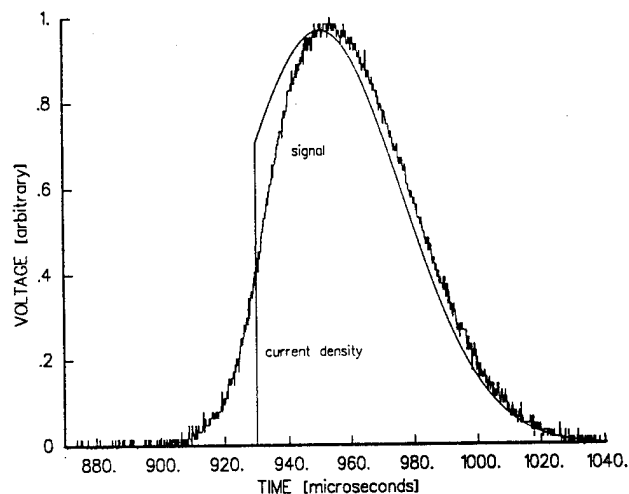
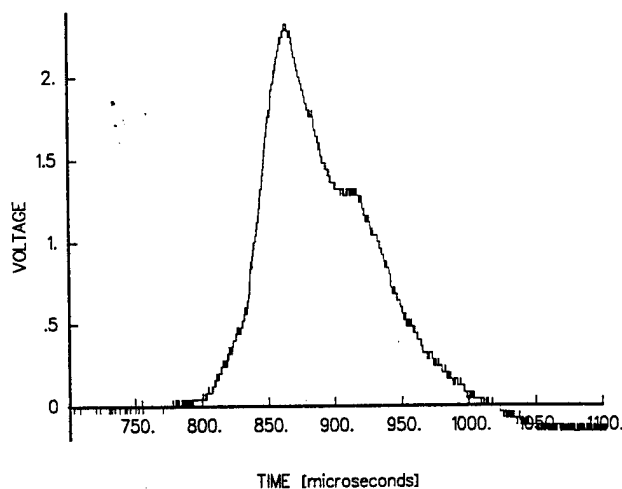Fig. 6. Simulated B-dot signal with known armature current density.

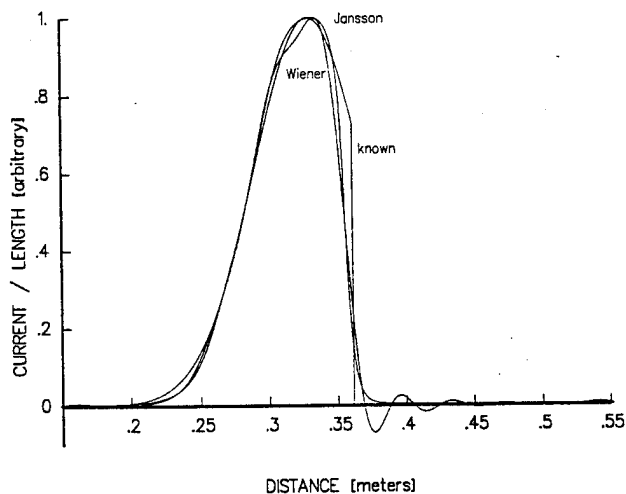Fig. 8. Experimental B-dot probe signal.

Fig. 7. Comparison of results obtained by deconvolving a simulated B-dot probe signal with Jansson's method and with a Wiener filter.
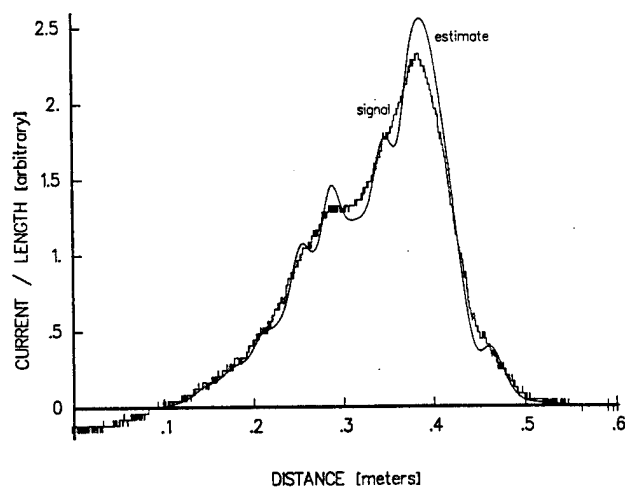

Fig. 9. Deconvolved experimental B-dot probe signal.

approach of [4]. Note that Jansson's method does not produce the "ringing" associated with linear filtering methods. The deconvolution results obtained with Jansson's method using simulated B-dot probe signals are very encouraging. Simulated B-dot probe signals were constructed with different rail current, position, and velocity profiles, with similar results.

Jansson's method has been used on several UTSI railgun firings. Fig. 8 shows one example of a digitized B-dot probe signal. Note that the signal in this figure has negative values, which are a result of the negative dI/dt of the rail current. Fig. 9 shows the resulting armature current distribution after deconvolving the experimental signal using Jansson's method. Also shown in Fig. 9 is the B-dot probe signal plotted in the spatial coordinate x to compare it with the solution. Note that the negative values have been removed owing to the nonnegativity constraint enforced by Jansson's method, corresponding to the a priori knowledge of the physical properties of the armature.

Jansson's deconvolution method for estimating the armature

current density has been adapted for routine use in analyzing B-dot probe signals. The algorithm given in (15) has been implemented with a FORTRAN program written for IBM-compatible computers. It requires approximately 25 min for the program to perform 50 iterations on 2048 samples when running on a system with an 80286 processor and a math coprocessor.

V. CONCLUSIONS

A method for estimating the plasma armature current distribution from recorded B-dot probe signals has been presented. This method utilizes the knowledge that the B-dot probe signal is a convolution of the plasma armature current density with the B-dot probe impulse response function.

The functional form of the armature current distribution is estimated by deconvolving the B-dot probe signal. Jansson's relaxation-based nonlinear iterative deconvolution method has been developed for use with recorded B-dot probe signals. The deconvolution algorithm requires knowledge of only the B-dot probe impulse response and the maximum peak amplitude

of the armature current density. Since the peak amplitude is not known *a priori*, a method was developed to calculate an estimate. Examining methods for determining the peak amplitude is an area of continuing research.

Numerical simulations on simulated B-dot probe signals have been conducted to examine the effectiveness of this method. The current density estimates, determined through deconvolution of the simulated signals, have given much improved results over the linear deconvolution schemes previously used. This method has also been applied to actual railgun firings, and the results obtained show improvements over those from the previously used Wiener filter method.

ACKNOWLEDGMENT

REFERENCES

[1] J. V. Parker, "Magnetic-probe diagnostics for railgun plasma armatures," *IEEE Trans. Plasma Sci.*, vol. 17, pp. 487–500, June 1989.

[2] K. K. Cobb, "Experimental testing of least-square procedure for determining railgun plasma current distribution," *IEEE Trans. Plasma Sci.*, vol. 17, pp. 507–515, June 1989.

[3] K. A. Jamison and H. S. Burden, "Measurements of plasma properties from a large bore, plasma armature railgun," *IEEE Trans. Magn.*, vol. 25, pp. 256–261, Jan. 1989.

[4] L. M. Smith and D. R. Keefer. "Railgun armature plasma-current density from deconvolved B-dot probe signals," *IEEE Trans. Plasma Sci.*, vol. 17, pp. 501–506, June 1989.

[5] B. U. Bouvier, "A deconvolution technique for B-dot signals from a plasma-driven electromagnetic launcher," *IEEE Trans. Plasma Sci.*, vol. 17, pp. 516–519, June 1989.

[6] P. B. Crilly, "A comparative study of relaxation based iterative deconvolution methods," presented at the 22nd Southeastern Symposium on System Theory, Cookeville, TN, Mar. 1990.

[7] P. A. Jansson, *Deconvolution: With Applications in Spectroscopy.* Orlando, FL: Academic Press, 1984, ch. 4.

[8] B. J. Evans and L. M. Smith, "A cross-correlation-based method for determining the position and velocity of a railgun plasma armature from B-dot probe signals," *IEEE Trans. Plasma Sci.*, vol. 19, pp. 926-934, Oct. 1991.

[9] B. J. Evans, "Analysis of railgun magnetic probe signals to determine the plasma armature current distribution," Master's thesis, Dept. Elec. Comp. Eng.. Univ. Tenn., Knoxville, TN, Dec. 1991.

[10] P. H. Van Cittert, "Zum Einfluss der Spaltbreite auf die Intensitätsverteilung in Spektrallinien II," *Z. Phys.*, vol. 69 pp. 298–308, 1931.

Bruno J. Evans (S'88–M'92) received the B.S. degree in electrical engineering from Tennessee Technological University in 1989 and the M.S degree in electrical engineering from the University of Tennessee, Knoxville, in 1991.

During 1990 and 1991 he was a Graduate Research Assistant with the Center for Laser Applications at the University of Tennessee Space Institute, Tullahoma. At UTSI, he conducted an analysis of magnetic probe signals to determine current densities in a plasma armature railgun. He is presently employed by the LTV Aerospace and Defense Company. His current research interests include embedded DSP programs, multidimensional digital signal processing, and thermal imagery analysis.

L. Montgomery Smith (M'87) received the B. S. degree in mathematics and physics from Rhodes College in 1978 and the B.S., M.S., and Ph.D. degrees in electrical engineering from the University of Tennessee, Knoxville, in 1982, 1984, and 1988, respectively.

His work experience includes positions with the Southern Research Institute, Birmingham, AL, and the Tennessee Department of Public Health, Nashville. From 1984 to 1989 he was employed as an Engineer at the Center for Laser Applications at the University of Tennessee Space Institute, Tullahoma, TN. Since 1989 he has been an Assistant Professor in the Department of Electrical and Computer Engineering at the University of Tennessee Space Institute. His current activities include teaching and research in the areas of electro-optics, digital signal and image processing, and data analysis.

A STUDY OF THE UTSI TRANSAUGMENTED AND

CLASSICAL RAILGUN

A Thesis

Presented for the

Master of Science

Degree

The University of Tennessee, Knoxville

Jaime R. Taylor

December 1991

ABSTRACT

In the past few years it has been determined that conventional railguns have nearly reached their velocity limits due to ablation of rail and insulator materials. The UTSI transaugmented railgun was constructed to conduct experiments to investigate the potential of augmentation in increasing the force on the plasma armature without increasing armature current. Preliminary experiments were performed to obtain values for the self and mutual inductances of the UTSI railgun which were needed for performance evaluations. The experiments consisted of generating a current pulse on one of the sets of rails and measuring the voltage and current induced on the other set of rails. From the measurements, the inductances were calculated.

Classical railgun shots were performed to determine an ablation constant, the force on the projectile due to the pressure from the light gas gun and the vaporization of the fuse. Augmented shots in which the operating current on the inner rail was the same as one of the classical shots were performed. Using the parameters obtained from the unaugmented shots, simulations were performed for the augmented shots. The velocity profiles obtained from experimental data were not in agreement with the predicted values. The experimental increase in velocity due to the augmenting field was approximately half the predicted value.

ANALYSIS OF RAILGUN MAGNETIC PROBE SIGNALS TO DETERMINE THE PLASMA ARMATURE CURRENT DISTRIBUTION

A Thesis

Presented for the

Master of Science

Degree

The University of Tennessee, Knoxville

Bruno J. Evans

December 1991

ABSTRACT

Methods were developed for determining the position, velocity, and functional form of a plasma armature from B-dot probe signals. The B-dot probe signal is shown to be a convolution of the armature current density with the B-dot probe impulse response. The methods described here were developed utilizing the knowledge that the probe signal is a convolution.

The method for determining the armature position and velocity utilizes the physical processes governing the plasma armature to model the leading edge of the armature as a unit-step function. The model is convolved with the B-dot probe impulse response to give the probe unit-step response which is a function of the velocity and time of passage of the leading edge of the armature. The unit-step response is compared with the B-dot probe signal using a local-area cross-correlation calculation. Two-parameter iteration determines the time of passage and velocity estimates as the values for which the correlation coefficient is maximized.

The functional form of the plasma armature is estimated by deconvolving the B-dot probe signal to recover the armature current density. Jansson's relaxation based nonlinear iterative method has been developed for use with B-dot probe signals, and it is presented as a method for estimating the armature current density. This approach has advantages over other methods in that only the physical limits of the data need to be known.

Verification of these methods was performed using simulated B-dot probe signals. The simulations indicate that estimates within 10 sampling intervals for the time of passage and 5 percent for the velocity are achievable. Figures are presented of position versus time and velocity versus time for simulated and experimental data. Current density estimates gave improved results over previously used meth-

ods. Plots of deconvolved armature current distributions are shown for simulated and experimental data. Also, Jansson's method estimate is compared to the Wiener filter estimate. Application of these methods to experimental B-dot probe signals has been performed with encouraging results.

Cross-Correlation-Based Method for Determining the Position and Velocity of a Railgun Plasma Armature From B-Dot Probe Signals

Bruno J. Evans, *Student Member, IEEE*, and L. Montgomery Smith, *Member, IEEE*

Abstract—In this paper we present a method of determining the position and velocity of a plasma armature from B-dot probe signals. This method utilizes the physical processes governing the plasma armature current density to model the leading edge of the armature as a unit step function. This model of the current profile is convolved with the impulse response of the probe and compared with B-dot probe data via a local-area cross-correlation (LACC) coefficient. Two-parameter iteration determines the time of passage and velocity of the leading edge of the armature as the values for which the correlation is maximized. Results obtained using this technique indicate that significant improvement in accuracy for time of passage estimates can be obtained over previous *ad hoc* methods. Velocity estimates from individual B-dot probe signals can also be obtained.

I. INTRODUCTION

CURRENT probes, termed B-dot probes, are a useful diagnostic instrumentation technique for the analysis of electromagnetic launcher (railgun) performance. A B-dot probe is a small cylindrical coil that produces an output voltage proportional to the time rate of change of the magnetic field component parallel to the axis of the coil. Passage of the plasma armature by a B-dot probe located near the barrel of a railgun produces a voltage pulse whose functional form is dependent upon the orientation of the probe.

By placing several probes along the length of the railgun barrel, the time at which the armature passes each probe can be measured from the time of occurrence of the voltage pulse. The probe position versus time of passage of the armature is often taken as being indicative of the projectile motion from which position, velocity, and acceleration data are inferred. A fundamental problem exists, however, in determining precisely the location of the projectile from the B-dot probe signal. Even with the obvious assumption that the rear of the projectile coincides with the leading edge of the plasma armature current density, it is difficult to determine unambiguously the location of the leading edge from the B-dot probe signal, since its response is proportional to the magnetic field (i.e., not to the current distribution causing it).

Presently, several methods are used to determine the location of the leading edge of the armature. With the B-dot probe

oriented to sense the armature current, the probe signal is a bimodal pulse consisting of a positive and a negative portion. Jamison and Burden [1] use the first peak as the armature position. Cobb [2] has verified the approach of Jamison and Burden by measuring plasma emission with a photo-diode located at the same position as a B-dot probe, and showed that the leading edge of the armature is approximately adjacent to the probe at the first maximum. With the B-dot probe oriented to sense the rail current, the probe signal consists of a unidirectional pulse. The B-dot probes on the University of Tennessee Space Institute (UTSI) railgun are oriented in this fashion. Previously, the leading edge passage was taken as the time at which the curve reaches one-half of its maximum value. Parker [3] speaks of integrating the probe signal and drawing a straight line coincident with the most steeply rising segment of the curve to give the armature position.

Cobb [2], [4] has developed a method to determine the current distribution in the railgun plasma armature by least-squares fitting the B-dot coil voltage. The fitted parameters provide information on the armature position and velocity, the current distribution, and the dynamic features of the armature. However, this method requires a substantial amount of time to compute the armature parameters. Also, a functional form for the entire armature is assumed.

All of these approaches have limitations and drawbacks due to their *ad hoc* and heuristic natures. Neither the known response of the B-dot probe nor the physical processes governing plasma armature current densities are utilized. Often, the techniques rely upon "eyeball" measurements and human operator judgment, or as in the approach of Cobb, *a priori* assumptions about the armature are made. The effects of noise upon such measurement methods can be significant, but are rarely considered. Thus a great deal of ambiguity as well as the possibility of error is inherent in these previous approaches.

In this paper we present a method based upon a local-area cross-correlation (LACC) calculation to determine unambiguously the location of the leading edge of the plasma armature current density from B-dot probe signals. As with Cobb's method, this technique has the notable added advantage that the velocity of the armature can also be determined from a single B-dot probe signal. Based upon the work of Keefer [5], Sloan [6], and Powell and Batteh [7], who showed that the current density peaks toward the projectile/armature interface, we have modeled the leading edge of the current profile as that of a unit step function. Then using the results of

Smith and Keefer [8], which showed that the B-dot probe signal is a convolution of the armature current profile with a spatially varying impulse response function and that it is dependent in form upon the velocity, a series of unit step B-dot probe responses are calculated. These curves, limited to a finite region, are then used to calculate cross-correlation coefficients with correspondingly limited regions of the B-dot probe data. Two-parameter iteration to determine the peak cross-correlation value yields the optimal values for the time of passage and velocity estimates.

The background equations and notation are presented in the following section. In Section III, the unit step response of a B-dot probe is derived, the local-area cross-correlation coefficient developed, and its implementation for this application is described. Section IV presents numerical results, both for simulated B-dot probe data as well as data from actual railgun firings. Discussion and conclusions are given in Section V.

II. BACKGROUND EQUATIONS

The voltage signal induced in a B-dot probe can be found from Faraday's Law and is given by:

$$V = NA\frac{dB_n}{dt} \qquad (1)$$

where N is the number of turns in the coil, A is the area of one turn, and B_n is the component of the magnetic field parallel to the probe normal n. The magnetic induction B produced at a point r in space by a distribution of currents is determined by the Biot–Savart law,

$$B(r) = \frac{\mu_0}{4\pi}\int \frac{J(r')\times(r-r')}{|r-r'|^3}d^3r \qquad (2)$$

where $J(r')$ is the current density located at the point r'.

In a previous paper [8] these relations were used to show that under certain simplifying assumptions, a B-dot probe voltage signal consists of a convolution of the armature current distribution with an impulse response function. A derivation is found in the cited reference. For completeness and consistency with the present notation, a separate brief derivation is presented here.

The railgun circuit model is shown in Fig. 1 and consists of a current loop lying in the x–y plane. The rails are oriented along the x direction and are modeled as infinitely thin conductors carrying a total gun current I_0. The B-dot probe is oriented to sense the y component of the magnetic field and is located at a longitudinal distance x from the origin, at a radial distance r_1 from the nearer rail and at an angle θ_1 from the z direction. The breech of the gun barrel is assumed to lie at a sufficient distance from the probe to approximate $-\infty$. The effect of the current in the farther rail was neglected in the previous paper.

The armature current distribution (current per unit length) is denoted, $I_{\mathrm{arm}}(x)$, and is modeled as moving with velocity v in the x direction. As shown in Fig. 1, it lies in the moving ξ coordinate system, with its leading edge at $\xi = 0$. At time $t = t_0$, the leading edge of the current distribution passes the B-dot probe. Near the time t_0 as the armature passes the probe, a signal pulse is produced which deviates from the quiescent

value for a short time interval. For typical railgun firings this interval is on the order of 100 μs. It is assumed that over this time interval the velocity v and total current I_0 remain constant, and that the shape of the armature current distribution $I_{\mathrm{arm}}(\xi)$ in the moving coordinate system does not change.

With these assumptions, the x component of the current in the rails at time t near time t_0 is given by:

$$I(x') = I_0 - \int_{-\infty}^{x'-[x+v(t-t_0)]} I_{\mathrm{arm}}(\xi)d\xi. \qquad (3)$$

From the Biot–Savart law (2), the y component of the magnetic field at the probe location at time t can be expressed explicitly as:

$$B_y(t) = \frac{\mu_0}{4\pi}r_1\cos\theta_1\int_{-\infty}^{\infty}\frac{I(x')}{[r_1^2+(x-x')^2]^{3/2}}dx'. \qquad (4)$$

This expression can be cast into the form of a convolution integral via a method similar to that described in [8]. Following substitution of (3) into (4), the change of variables $\eta = x' - [x + v(t - t_0)]$ is made, the resulting expression is differentiated with respect to time t, and integration by parts is carried out. The B-dot probe response can thereby be shown to be proportional to:

$$\frac{dB_y}{dt} = \frac{\mu_0}{4\pi}vr_1\cos\theta_1\int_{-\infty}^{\infty}\frac{I_{\mathrm{arm}}(\eta)}{\left[r_1^2+\left(v(t_0-t)-\eta\right)^2\right]^{3/2}}d\eta. \qquad (5)$$

The integral in (5) can be recognized as the one-dimensional convolution of the armature current distribution $I_{\mathrm{arm}}(x)$ with an impulse response function $h_1(x)$ with the substitution $x = v(t_0 - t)$ in the result. The impulse response function of the B-dot probe for a single rail is thus given by:

$$h_1(x) = \frac{\mu_0}{4\pi}\frac{vr_1\cos\theta_1}{[r_1^2+x^2]^{3/2}} \qquad (6)$$

where the convolution is performed with respect to the variable x. Note that the B-dot probe signal is time varying, and that its temporal variation is dependent in form upon the velocity v.

In the section to follow, this result will be extended to include the effect of the current in the farther rail. That result in turn will be used to develop the local-area cross-correlation method for determining the time of passage and velocity of the leading edge of the armature.

III. DESCRIPTION OF THE METHOD

In the previous section the impulse response function of the B-dot probe for a single rail was determined. For practical purposes, the impulse response due to the current in both rails should be considered. The impulse response function due to the current in the farther rail can be found by the method outlined in Section II. The probe is located a radial distance r_2 from the farther rail, and at an angle θ_2 from the z direction. The current in the farther rail is assumed to be given by (3), but is in the opposite direction from that of the current in the
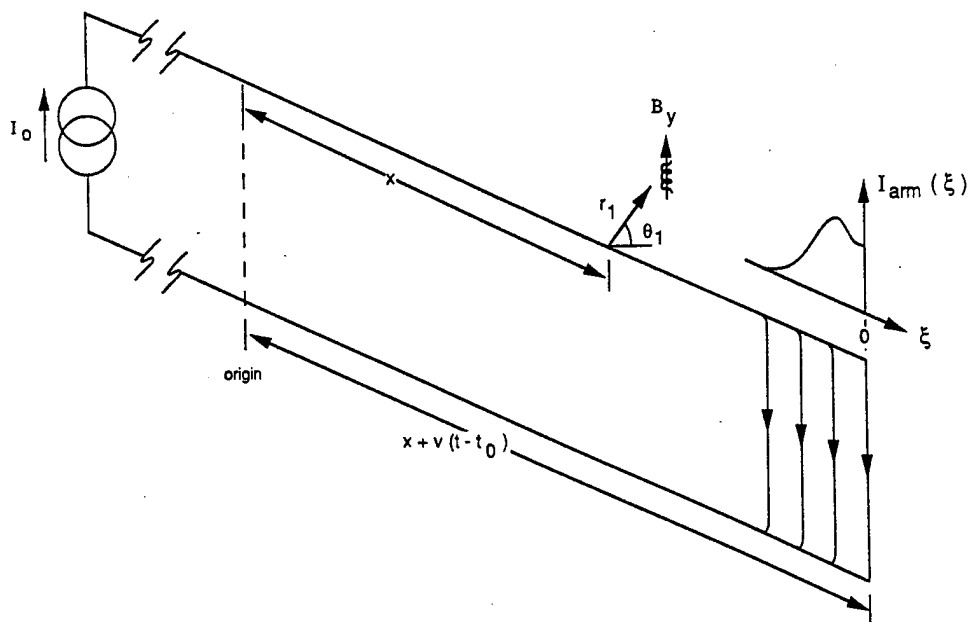
Fig. 1.   Circuit model used to derive the expression for the B-dot probe response to a passing armature.
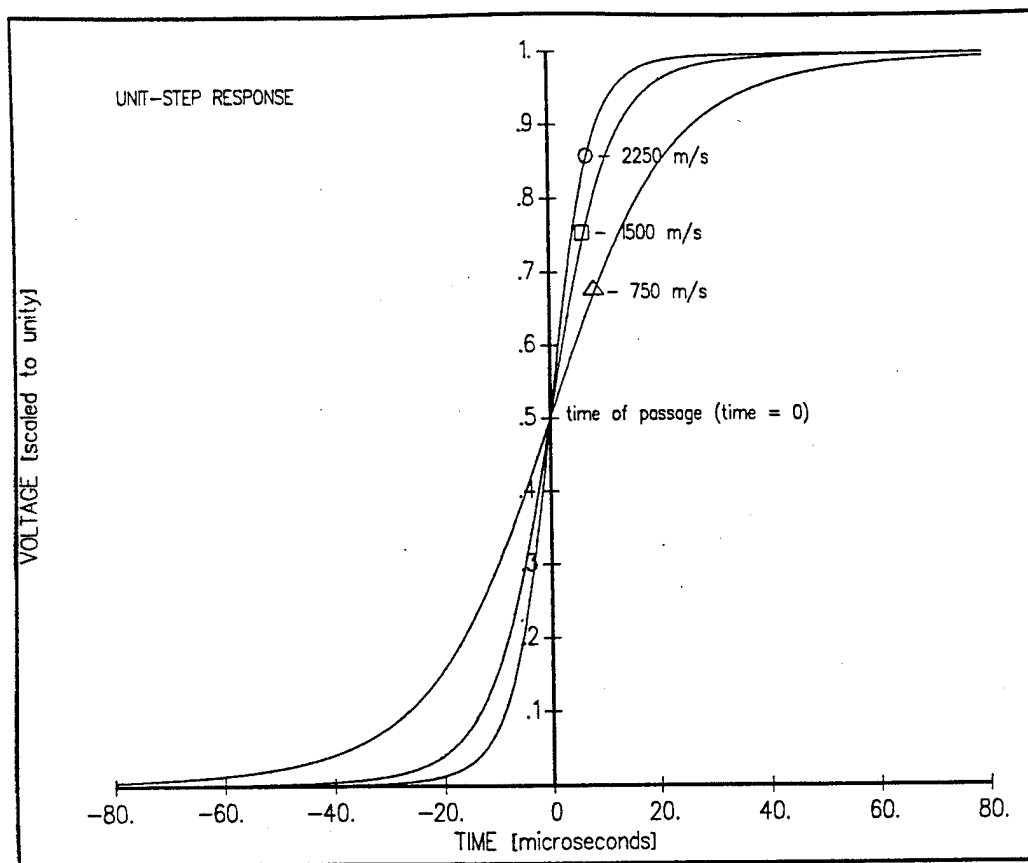

Fig. 2.   The B-dot probe unit step response for velocities of 750, 1500, and 2250 m/s using position parameters from the UTSI railgun.

nearer rail. This induces a magnetic field in the y direction opposite in sign to that induced by the current in the nearer rail. The expression for the y component of the magnetic field at the probe location due to the farther rail current is thus given by the negative of (4) with the radial distance and angle for the farther rail. Therefore the impulse response function of the

B-dot probe due to the current in the farther rail is:

$$h_2(x) = -\frac{\mu_0}{4\pi} \frac{vr_2 \cos\theta_2}{[r_2^2 + x^2]^{3/2}}. \tag{7}$$

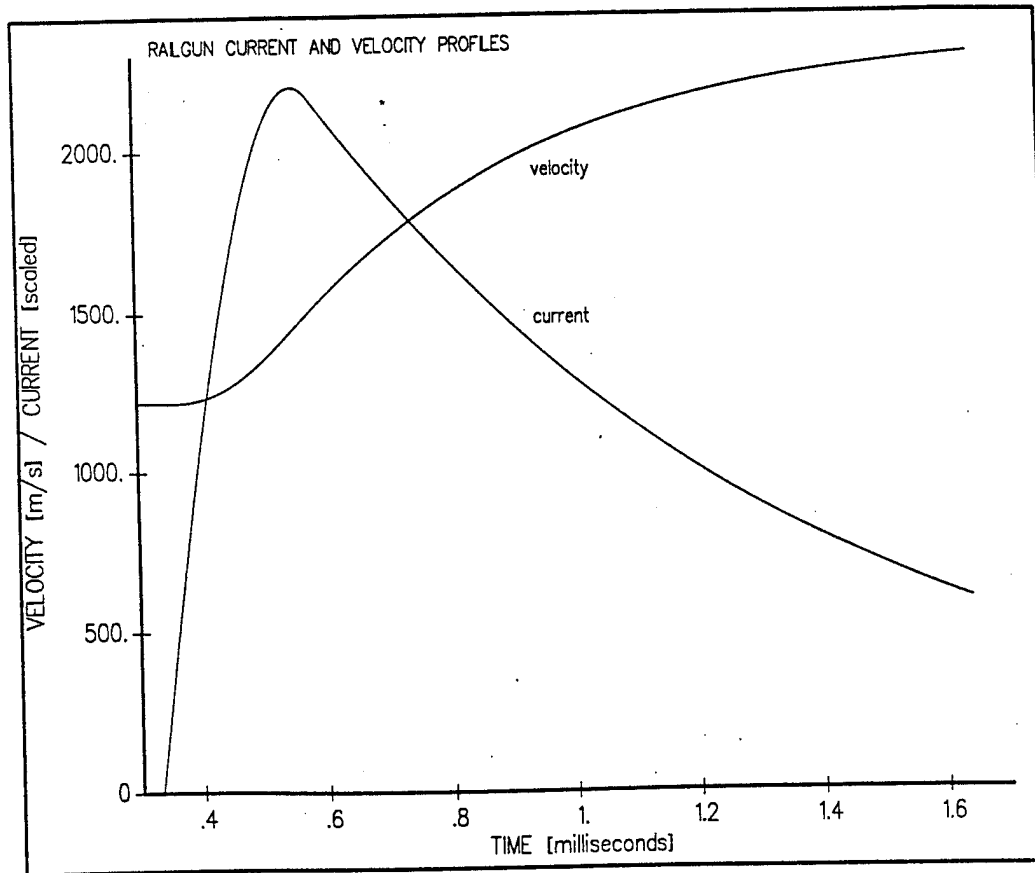By superposition, the impulse response function of the B-dot

Fig. 3. Railgun current and armature velocity profiles used to construct simulated B-dot probe signals.

probe due to the current in both rails can be expressed as:

$$h(x) = \frac{\mu_0}{4\pi} \left[\frac{v r_1 \cos \theta_1}{\left[r_1^2 + x^2\right]^{3/2}} - \frac{v r_2 \cos \theta_2}{\left[r_2^2 + x^2\right]^{3/2}} \right]. \tag{8}$$

Keefer [5], Sloan [6], and Powell and Batteh [7] have shown that the current in the railgun plasma armature peaks near the base of the projectile. Keefer states that for a railgun plasma armature, there are thermal mechanisms which do not exist for solid armatures that tend to move the peak of the current density forward toward the base of the projectile, thereby mitigating the tendency of the velocity skin effect to concentrate the current density toward the rear. Sloan states that armature resistance varies as a function of both temperature and pressure, and such dependence leads to a forward peaking of current toward the projectile/armature interface. Powell and Batteh have shown that the pressure, mass density, and electron density are maximum near the projectile surface, while temperature and current density peak near the projectile surface. An assumption is therefore made that the functional form of the leading edge of the plasma armature current density can be modeled as a unit step function:

$$I_{\mathrm{arm}}(x) = u(x) = \begin{cases} 1, & \text{if } x \geq 0 \\ 0, & \text{if } x < 0. \end{cases} \tag{9}$$

The amplitude of the current profile is irrelevant in the correlation coefficient calculation, and so it is set equal to unity for simplicity of notation.

Since the B-dot probe signal has been shown to be a

convolution of the armature current density with the probe impulse response function, the impulse response function (8) can be convolved with the unit step function (9) to give the probe unit step response:

$$h(x) * u(x) = \frac{\mu_0}{4\pi} \int_{-\infty}^{x} \left[\frac{v r_1 \cos \theta_1}{\left[r_1^2 + \eta^2\right]^{3/2}} - \frac{v r_2 \cos \theta_2}{\left[r_2^2 + \eta^2\right]^{3/2}} \right] d\eta. \tag{10}$$

The probe unit step response, $f\big(v(t_0 - t)\big) = h(x) * u(x)\big|_{x=v(t_0-t)}$, can be found by solving the integral in (10), which yields:

$$f\big(v(t_0 - t)\big) = \frac{\mu_0 v}{4\pi} \left[\frac{v(t_0 - t)\cos\theta_1}{r_1\sqrt{r_1^2 + v^2(t_0 - t)^2}} + \frac{\cos\theta_1}{r_1} \right.$$
$$\left. - \frac{v(t_0 - t)\cos\theta_2}{r_2\sqrt{r_2^2 + v^2(t_0 - t)^2}} - \frac{\cos\theta_2}{r_2} \right]. \tag{11}$$

The B-dot probe unit step response shown in (11) is used as a model of the B-dot probe signal for the leading edge of the armature. The probe unit step response is thus dependent on two parameters, velocity v and time of passage of the leading edge of the armature t_0, with time t as its independent variable. Fig. 2 shows the resulting curves for velocities of 750, 1500, and 2250 m/s calculated at a 0.2 μs sampling interval using position parameters from UTSI B-dot probes. The time of passage of the armature in these curves is found at time zero. Note that as the velocity increases, the slope of the curve at the time of passage ($t_0 = 0$) also increases. By comparing the curves to actual B-dot probe signals, the time of passage of
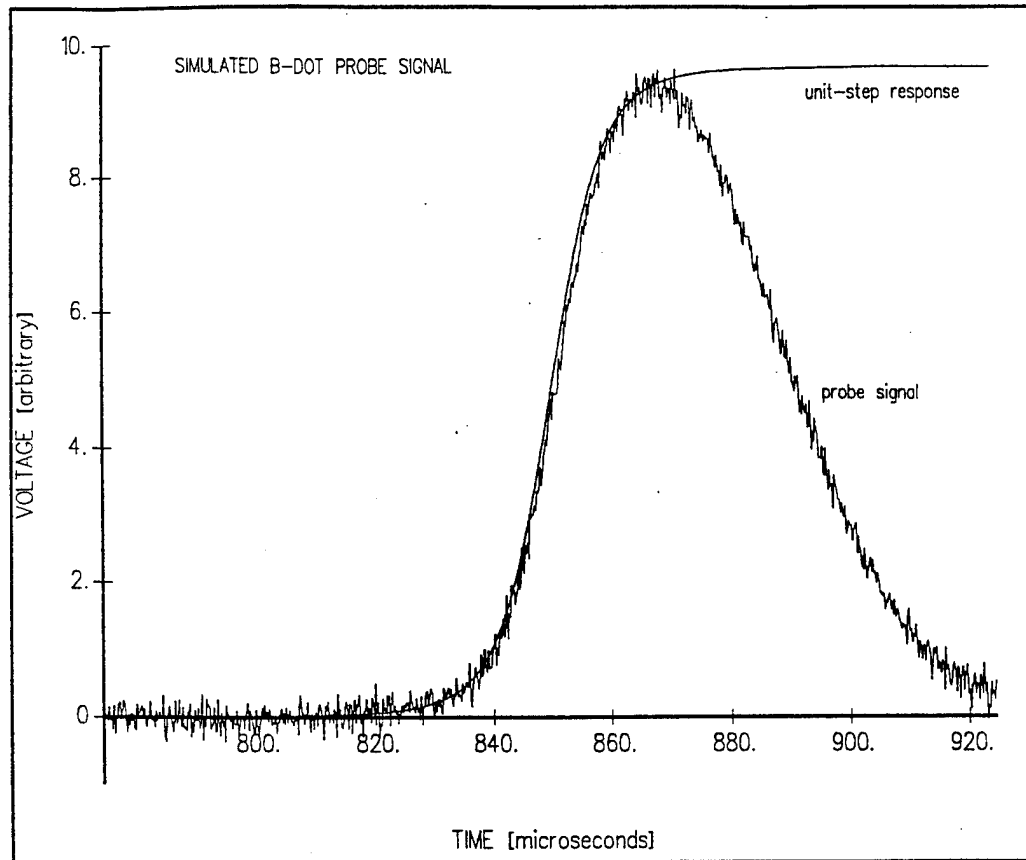
Fig. 4.   Simulated B-dot probe signal as a function of time. Also shown is the probe unit step response at the known time of passage (0.8498 ms) and armature velocity (1920 m/s).

the armature can be determined and its velocity estimated.

The cross-correlation coefficient of two signals is often used to measure the similarity between them [9]. Ideally, the correlation coefficient is unity, but because the relationship between the two signals may be nonlinear and/or there is noise in the measurements, the value is often less than unity. However, the closer the calculated correlation coefficient is to unity, the more similar the signals are in functional form. In comparing a B-dot probe signal to the probe unit step response (11), a standard method of determining the correlation coefficient cannot be used. The correlation is to be examined over the entire signal, but only for a selected fixed-length interval. The unit step response is thus calculated for $t_0 = 0$, over a selected range of time t, and compared with different intervals of the shifted B-dot probe signal. Modifying the standard equation for determining the correlation coefficient, we define the LACC coefficient in the following manner:

$$\rho(t_0, v) = \frac{\int_{t_1}^{t_2} b(t + t_0)f(-vt)dt}{\sqrt{\int_{t_1}^{t_2} b^2(t + t_0)dt \int_{t_1}^{t_2} f^2(-vt)dt}} \tag{12}$$

where $b(t + t_0)$ is the shifted B-dot probe signal, $f(-vt)$ is the probe unit step response (11), and t_0 is the estimated time of passage at which the correlation between the B-dot probe signal and probe unit step response is being examined. The limits t_1 and t_2 give the time interval over which the unit step response model is taken to be valid. The correlation makes a

comparison over the stated interval, and it is dependent on both velocity and time. Although the comparison is made only over the defined interval, the B-dot probe signal is shifted when the next interval of the probe signal is to be examined. After the entire probe signal has been examined, the shift value yielding the maximum correlation coefficient is then taken to be the time of passage of the armature, and the velocity at this point is taken to be the estimated armature velocity.

From the definition of the LACC coefficient (12) and the B-dot probe unit step response (11), the point of maximum correlation between the B-dot probe signal and probe unit step response is taken to be the time of passage of the armature. The velocity of the probe unit step response at this point is the estimated armature velocity. The time of maximum correlation thus gives the time at which the B-dot signal is most similar to the unit step response of the probe at the location of the leading edge of the armature.

Approximation of the integral in (12) by rectangular rule integration yields the LACC coefficient for discretized data:

$$\rho(k\Delta t, v) = \frac{\sum_{i=m}^{n} b\big((k + i)\Delta t\big)f(-iv\Delta t)}{\sqrt{\sum_{i=m}^{n} b^2\big((k + i)\Delta t\big) \sum_{i=m}^{n} f^2(-iv\Delta t)}}. \tag{13}$$

Using a two variable iterative approach, the time of passage, given by $k\Delta t$, and the estimated velocity of the armature are found.
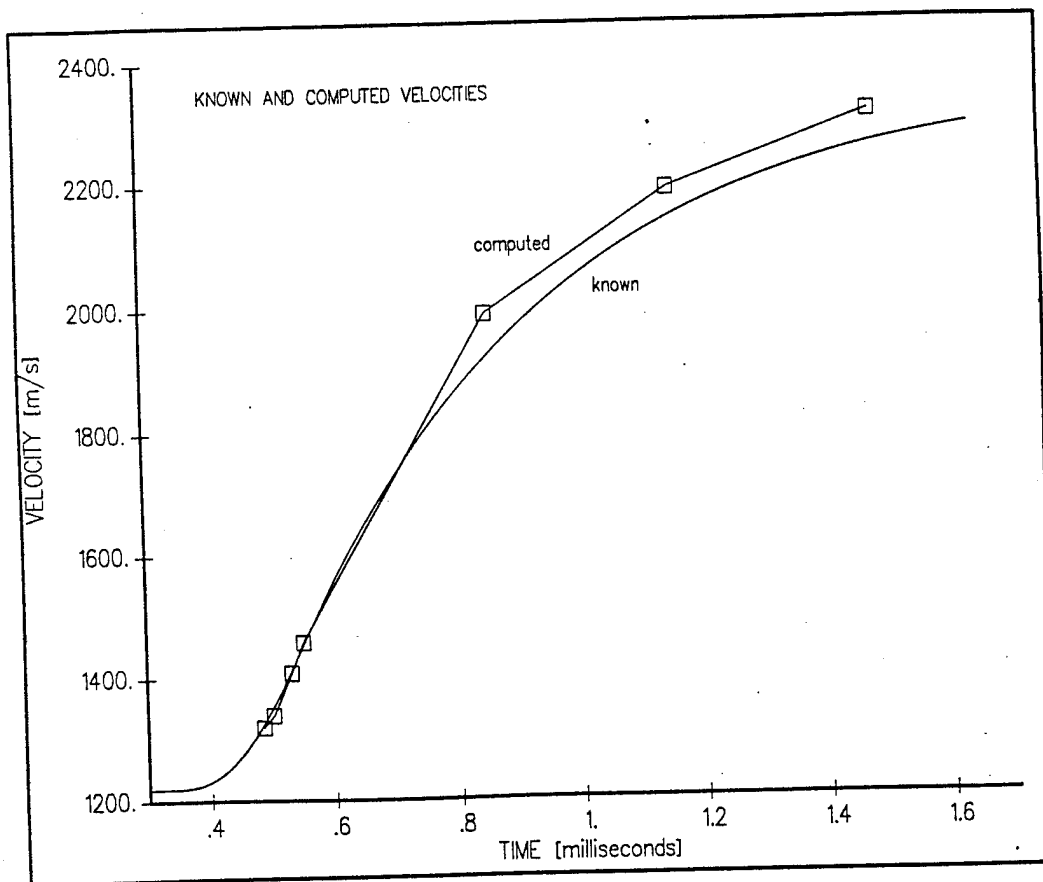
Fig. 5. Comparison of computed and known velocities for the simulated B-dot probe signals.
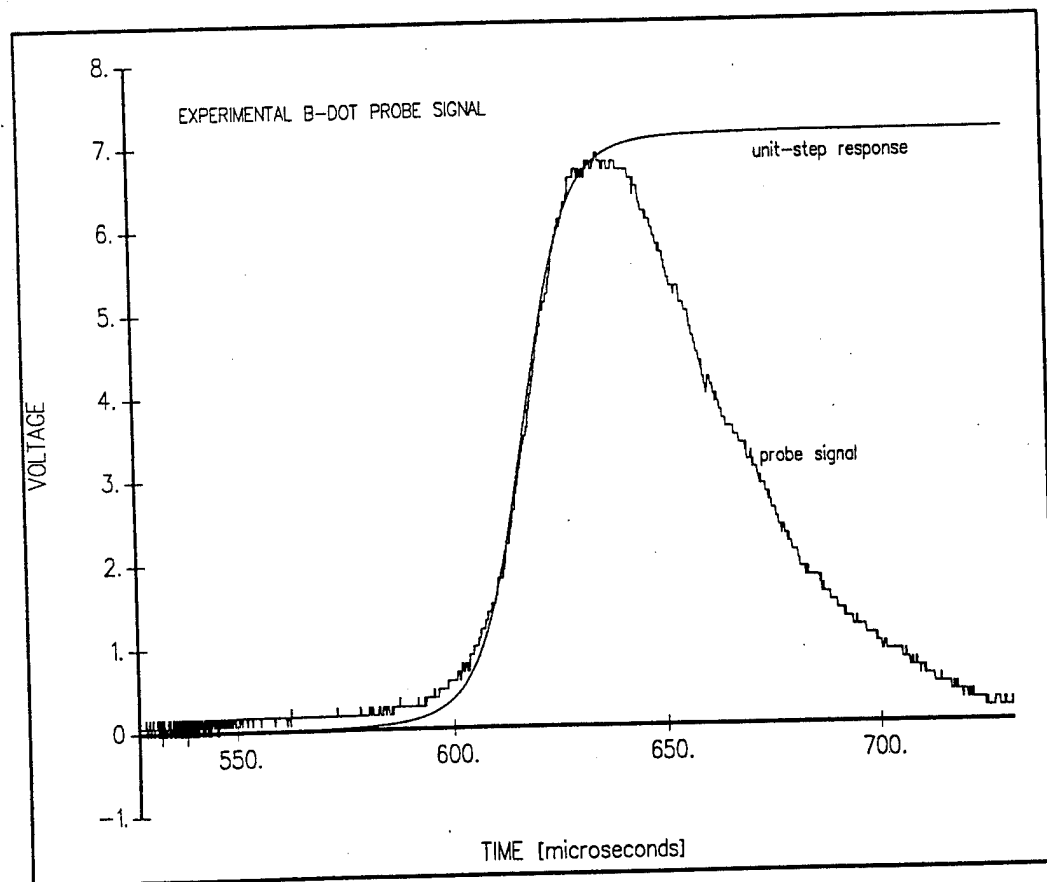

Fig. 6. Experimentally acquired B-dot probe signal. Also shown is the probe unit step response at the computed time of passage (0.6174 ms) and armature velocity (1600 m/s).
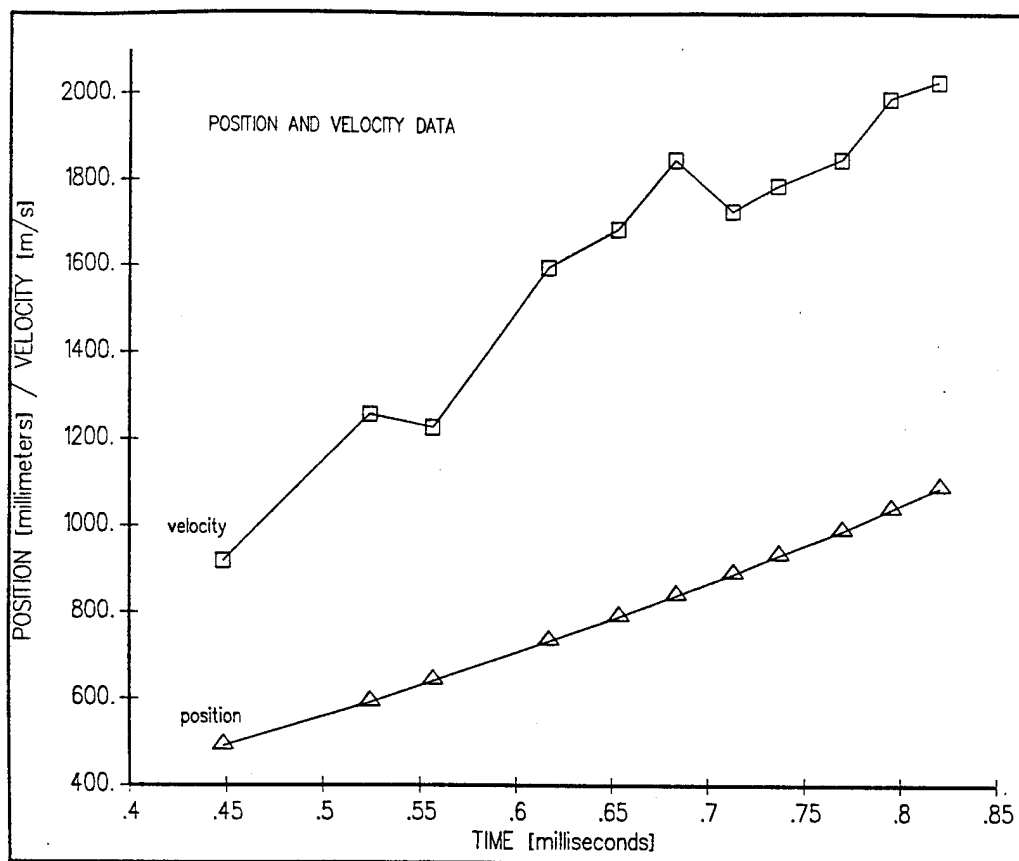
Fig. 7. Armature position and velocity data for a complete UTSI railgun firing. The values shown were obtained from the B-dot probe unit step response.

The iterative procedure involves checking the leading edge of the unidirectional B-dot probe signal at the times between 25 and 75% of the signal maximum. A FORTRAN program is used to determine the point of maximum correlation over this portion of the signal. With a given initial velocity estimate input by the user, the program finds the point of maximum correlation. This point is held fixed while the velocity is varied between 500 m/s below to 500 m/s above the initial velocity, until the velocity that gives the largest correlation coefficient is determined. Using the new velocity, the leading edge of the B-dot probe signal is re-examined until the point of maximum correlation is found. This procedure is repeated until the time-of-passage estimate converges to within one sample interval and the velocity estimate converges to within 10 m/s. More precision in these values could be attained with additional computation. This procedure requires approximately 3 min of computer time on an IBM compatible with an 80286/287 processor running at 16 MHz.

The time interval over which the unit step response is taken to be valid was determined through numerical trials using simulated B-dot probe signals. Since Jamison and Burden [1], Sloan [6], and others have assumed the functional form of the armature current density to be a truncated Gaussian curve, a known armature current density was produced by truncating a Gaussian curve on one side to simulate a current distribution with a discontinuous rise in current. The equation for this current profile is given

by:

$$I_{\text{arm}}(x) = \begin{cases} \exp\left[-\frac{(x-0.12)^2}{0.0032}\right], & \text{if } x \le 0.152 \\ 0, & \text{otherwise} \end{cases} \quad (14)$$

where x is in meters. This distribution simulates an armature approximately 15 cm in length. This current density was convolved with the B-dot probe impulse response function (8) for different velocity values using parameters from the UTSI railgun, and corrupted with noise by adding uncorrelated Gaussian random numbers, giving simulated B-dot probe signals. Using these signals, the time of passage and the estimated velocity were determined using the iterative procedure described previously. The time interval over which the unit step response can be assumed to be valid was determined by examining several known current densities using different time intervals. The interval was varied until the velocity estimates were within 5% and the time of passage estimates were within 1.6 μs of the known values. The interval, as defined by the variables m and n, was selected to start and stop at the times where the unit step response reached 1.5 and 98.5% of its maximum value, respectively. Note that this interval will vary in length with the value of velocity. These limits provide a range over which a sharply rising leading edge in armature current produces a probe signal which approximates the unit step response of the B-dot probe.

IV. RESULTS

To illustrate the effectiveness of the cross-correlation-based method for determining the position and velocity of the armature from B-dot probe signals, a numerical simulation with a known armature current density was conducted. In order to generate B-dot signals which resemble B-dot signals recorded from railguns, the armature velocity and rail current must vary with time. The armature current distribution was chosen to be the product of the time-varying total gun current $I(t)$ with a spatially varying pulse form $\rho(x)$, and the velocity was assumed to be a time-varying quantity $V(t)$. Note that the three-dimensional characteristics of the railgun and armature or the possibility of the armature changing its form were not considered in the following analysis. The x component of the current in the rails at time t is given by:

$$I(x',t) = I(t)\left[1 - \int_{-\infty}^{x'-[x+V(t)(t-t_0)]} \rho(\xi)d\xi\right] \quad (15)$$

where

$$\int_{-\infty}^{\infty} \rho(\xi)d\xi = 1. \quad (16)$$

Using the Biot–Savart law (2), an expression for $B_y(t)$ can be obtained. The B-dot probe response due to the current in one rail can then be determined and is proportional to:

$$\frac{dB_y}{dt} = \frac{\mu_0}{4\pi}\left[\frac{dI}{dt}\int_{-\infty}^{\infty}\frac{1 - \int_{-\infty}^{\eta}\rho(\xi)d\xi}{\left[r^2 + \left(V(t)(t_0 - t) - \eta\right)^2\right]^{3/2}}d\eta\right.$$
$$+ I(t)[V(t) - (t_0 - t)\frac{dV}{dt}]$$
$$\left.\cdot\int_{-\infty}^{\infty}\frac{\rho(\eta)}{\left[r^2 + \left(V(t)(t_0 - t) - \eta\right)^2\right]^{3/2}}d\eta\right]. \quad (17)$$

Applying (17) for both rails, simulated B-dot probe signals can be generated.

The validity of the LACC approach to determining the position and velocity of the armature was examined using simulated B-dot probe data produced in the manner described above. Fig. 3 gives the railgun current and armature velocity profiles used in generating one set of B-dot probe data. The simulated B-dot signals were corrupted with noise by adding uncorrelated Gaussian random numbers. The conductor to probe distances and angles correspond to probe locations in the UTSI railgun ($r_1 = 0.023659$ m; $r_2 = 0.029028$ m; $\theta_1 = 22.74°$; $\theta_2 = 41.26°$). The data was acquired at a 0.2 μs sampling interval. Shown in Fig. 4 is a simulated B-dot probe signal, where the known time of passage and velocity of the armature are 0.8498 ms and 1920 m/s, respectively. Also shown in Fig. 4 is the scaled unit step response (11) evaluated at the known time of the passage and velocity of the armature, where it has been extended beyond the interval over which it is taken to be valid for presentation purposes. Using the iterative process described in the previous section, the estimated time of passage was determined to be 0.8502 ms, and the velocity, 1990 m/s. The computed time of passage is only two sampling intervals from the known value, while the velocity estimate is within 5% of the known value.

TABLE I
RESULTS FOR SIMULATED B-DOT PROBE SIGNALS. KNOWN AND COMPUTED TIMES OF PASSAGE AND VELOCITIES GIVEN

Known Velocity (m/s)	Estimated Velocity (m/s)	Known Time of Passage (ms)	Time of Maximum Correlation (ms)
1325	1320	0.4838	0.4856
1354	1340	0.4998	0.5016
1413	1410	0.5298	0.5318
1455	1460	0.5498	0.5516
1920	1990	0.8498	0.8502
2143	2190	1.1498	1.1502
2258	2310	1.4798	1.4800

Simulated B-dot probe signals for this armature current density, rail current profile, and velocity profile were constructed at several different known times of passage. The iterative procedure described in the previous section was used to determine the time of passage and estimated velocity for these known current densities. Table I gives a comparison of the known times of passage and velocities with the estimated times of passage and velocities. The computed velocities are plotted in Fig. 5, along with the known velocity profile for ease of comparison. The estimated velocity results are very encouraging. By examining Table I, it can be seen that the estimated velocities are very similar to the known velocities (within 5%). These results show that for known armature current densities, constructed in the manner described above, this method works extremely well in determining the time of passage and velocity of the armature. Simulated B-dot signals were constructed with different railgun current and velocity profiles, and similar results were obtained.

The cross-correlation-based method has been used on several UTSI railgun firings. Fig. 6 shows one example of a digitized B-dot probe signal acquired at a 0.2 μs sampling interval. In determining the time of passage of the armature, the velocity was estimated to be 1600 m/s. Also shown in Fig. 6 is the scaled unit step response (11) evaluated at 1600 m/s and located at the computed time of passage, where it has been extended beyond the interval over which it is taken to be valid for presentation purposes. An analysis of a typical UTSI railgun firing follows.

Table II gives the B-dot probe position, armature velocity, time of passage of the armature, and the maximum correlation for all the B-dot probes on one UTSI railgun firing. The time

TABLE II
RESULTS FOR UTSI RAILGUN FIRING. B-DOT PROBE POSITION GIVEN
ALONG WITH VELOCITY, TIME OF PASSAGE, AND MAXIMUM CORRELATION
AS COMPUTED FROM THE LACC COEFFICIENT

B-Dot Probe Number	Probe Position (mm)	Estimated Velocity (m/s)	Armature Time of Passage (ms)	Maximum Correlation
7	490.00	920	0.4484	0.9995774
9	590.00	1260	0.5244	0.9997101
10	640.00	1230	0.5568	0.9996501
11	732.71	1600	0.6174	0.9992909
12	790.00	1690	0.6540	0.9990039
13	840.00	1850	0.6840	0.9992103
14	890.00	1730	0.7132	0.9988849
15	932.80	1790	0.7368	0.9991789
16	990.04	1850	0.7696	0.9994166
17	1040.04	1990	0.7956	0.9990333
18	1090.04	2030	0.8214	0.9992125

of passage, armature velocity, and maximum correlation were computed using the iterative process described in the previous section. The computed time of passage and velocity of the armature are plotted in Fig. 7 for visual interpretation. Note the nonmonatonic variations in the estimated velocities. This is currently under investigation, and it is believed to be due to misaligned B-dot probes.

V. CONCLUSIONS

A method for determining the time of passage of a plasma armature and estimating its velocity from B-dot probe signals, where the probe is oriented to sense the rail current, has been presented. This method is based on calculating a local-area cross-correlation coefficient between the B-dot probe signal and B-dot probe unit step response using a two-parameter iterative approach. The unit step response is used, since it was assumed that the leading edge of the armature current density could be modeled as a unit step function. Numerical simulations on simulated B-dot probe data indicate that accuracies within 2.0 μs for the time of passage estimate

and 5% for the velocity estimate are achievable with this method. Application to actual railgun firing data has been performed with encouraging results.

REFERENCES

[1] K. A. Jamison and H. S. Burden, "Measurements of plasma properties from a large bore, plasma armature railgun," *IEEE Trans. Magn.*, vol. 25, pp. 256–261, Jan. 1989.
[2] K. K. Cobb, "Experimental testing of least-square procedure for determining railgun plasma current distribution," *IEEE Trans. Plasma Sci.*, vol. 17, pp. 507–515, June 1989.
[3] J. V. Parker, "Magnetic-probe diagnostics for railgun plasma armatures," *IEEE Trans. Plasma Sci.*, vol. 17, pp. 487–500, June 1989.
[4] K. K. Cobb, "Determination of current distribution in EM gun armature by least squares fitting of B coil voltage," *IEEE Trans. Plasma Sci.*, vol. 16, pp. 352–359, June 1988.
[5] D. R. Keefer, "Arc motion in railgun plasma armatures," *IEEE Trans. Plasma Sci.*, vol. 17, pp. 446–449, June 1989.
[6] M. L. Sloan, "The role of convective flow processes in determining plasma armature characteristics," *IEEE Trans. Magn.*, vol. 25, pp. 525–528, Jan. 1989.
[7] J. D. Powell and J. H. Batteh, "Plasma dynamics of an arc-driven, electromagnetic, projectile accelerator," *J. Appl. Phys.*, vol. 52, no. 4, pp. 2717–2730, Apr. 1981.
[8] L. M. Smith and D. R. Keefer, "Railgun armature plasma-current density from deconvolved B-dot probe signals," *IEEE Plasma Sci.*, vol. 17, pp. 501–506, June 1989.
[9] J. S. Bendat and A. G. Piersol, *Engineering Applications of Correlation and Spectral Analysis*. New York, Wiley, 1980, chaps. 3, 4, 7.

Bruno J. Evans (S'88) received the B.S. degree in electrical engineering from Tennessee Technological University in 1989. He is currently working on the M.S. degree in electrical engineering at the University of Tennessee Space Institute, Tullahoma.

Since 1990 he has been a Graduate Research Assistant with the Center for Laser Applications at the University of Tennessee Space Institute, Tullahoma. His current research interests include multidimensional digital signal processing and the analysis of electromagnetic probe signals.
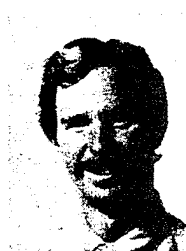
L. Montgomery Smith (M'87) received the B.S. degree from Rhodes College in mathematics and physics in 1978, and the B.S., M.S., and Ph.D. degrees from the University of Tennessee, Knoxville, in electrical engineering in 1982, 1984, and 1988, respectively.

He has previously worked for the Southern Research Institute, Birmingham, AL, and for the Tennessee Department of Public Health, Nashville. From 1984 to 1989 he was employed as an Engineer for the Center for Laser Applications at the University of Tennessee Space Institute, Tullahoma. Since 1989 he has been an Assistant Professor with the Department of Electrical and Computer Engineering at the University of Tennessee Space Institute. His current activities include teaching and research in the areas of electro-optics, digital signal and image processing, and data analysis.

SIMULTANEOUS IN-BORE RAIL AND INSULATOR SPECTRA
FROM A RAILGUN PLASMA ARMATURE

Dennis Keefer, Ahad Sedghinasab, and Roger Crawford

University of Tennessee Space Institute
Tullahoma, Tennessee 37388
(615) 455-0631

ABSTRACT

Absolute spectral radiance measurements have been obtained simultaneously at the rail and insulator surfaces of the UTSI 1 cm square-bore railgun. The emission spectra were obtained through the use of quartz optical fibers which penetrated both the rail and the insulator walls. The spectral characteristics of the rail and insulator emission are quite similar but differ significantly in magnitude. A detailed plasma radiation model was used to analyze these spectra. In order to obtain reasonable agreement between the model predictions and the experimental spectra, it was necessary to assume that there existed a broadband absorbing layer at the insulator surface. This result suggests a new physical model of the plasma armature in which insulator ablation leads to significant 3-dimensional flow and affects the shape of the current emission pattern on the rail surfaces.

INTRODUCTION

Previous attempts at understanding the radiation and flow characteristics of the railgun plasma armatures using emission spectroscopy have been restricted to data taken through optical ports on the insulator walls [1]. These studies used the time averaged emission spectra taken at the insulator surface, and have provided invaluable information on some of the main plasma parameters such as the plasma armature centerline temperature, the temperature profile, and the plasma composition.

Due to the inherent complexity of the flow in railgun plasma armatures, measured radiation at the rail surface is not expected to be similar to that on the insulator surface. In order to investigate the differences in the boundary layer characteristics on the rail and the insulator surfaces, time resolved simultaneous emission spectra have been recorded at near peak current using quartz fiber optics and two optical systems consisting of spectrometers and optical multichannel analyzers (OMA).

A detailed plasma radiation model developed previously [1], has been used to predict the temperature profile and the average plasma composition based on the experimentally obtained spectra. In this paper, we report on the measured simultaneous radiation spectra and their spectral features, and utilize the plasma radiation model predictions to formulate a physical model of plasma armatures which results from ablation and ablation product removal through the boundary layers and is consistent with the observed spectra.

EXPERIMENT

The UTSI railgun has a 1 cm square bore and is 2.2 m in length, consisting of a 1.1 m light gas gun and a 1.1 m railgun. The single stage light gas gun accelerates a polycarbonate projectile into the railgun with a velocity of approximately 1 km/s. The railgun is powered by a 240 kJ capacitor discharge power supply. Projectile position and velocity in the railgun is determined by signals obtained from an array of 20 magnetic pick-up coils (rail B-dot probes) positioned along the length of the gun. A fast- response piezoelectric pressure transducer is located near the midpoint of the barrel to provide an independent measurement of the plasma pressure.

Quartz optical fibers were used to measure spectral radiance at the rail and insulator surfaces. The two optical systems were calibrated for absolute spectral radiance using both a tungsten strip filament standard lamp and a standard deuterium lamp. The spectral calibration was accomplished using spectral emission lines from mercury and neon low pressure discharge lamps. The optical fibers were placed at the bore centerline approximately 57 mm downstream of the pressure transducer. Knowledge of the plasma velocity in the railgun enabled us to use the pressure transducer signal to estimate the plasma pressure at the position of the optical ports. The OMAs were triggered simultaneously to obtain a 1 microsecond exposure at a time which corresponded to the peak current density in the plasma armature. The barrel was fitted with Glidcop AL60 rails and G-9 insulators. The peak gun current for this experiment was approximately 140 kA and, using a 1.5 gram projectile, the muzzle velocity was approximately 2 km/s. Details of the UTSI railgun facilities and data acquisition techniques have been described elsewhere [2].

RADIATION MODEL

The plasma radiation model developed at UTSI [1] calculates the plasma emission spectra for a given pressure, centerline temperature, temperature profile, and plasma constituents. The model assumes LTE which has been shown to be valid for these plasmas [1]. The model further assumes that the transverse temperature profile of the plasma has the simple analytic form proposed by Tidman et al. [3] which is given by

$$T = T_0 \left(1 - \frac{x}{D}\right)^{1/N} \qquad (1)$$

where T_0 is the centerline temperature, D is the channel halfwidth, and N is a parameter adopted from turbulent fluid mechanics theory for fully developed pipe flows. Due to the abundance of hydrogen in the projectile and the insulator material, the only elements considered in the model were hydrogen, copper (rails), and aluminum (fuse).

The calculation of the emission and absorption coefficients for hydrogen was based on the formulae by Griem [4,5]. The Gaunt factors used in the continuum relation were taken from Karzas and Latter [6]. Stark broadening of the spectral lines

in the plasma core and other broadening mechanisms, such as resonance and van der Waals broadening in the cooler regions near the boundary, have been taken into account. The radiation emitted by the plasma is calculated using the radiation transfer equation given by [7]

$$I_\nu(x) = I_{\nu b} \int_0^x \frac{\epsilon(x')}{I_{\nu b}(T)} dx'$$
$$+ \int_0^x \epsilon(x') \exp\left[-\int_{x'}^x \frac{\epsilon(x'')}{I_{\nu b}(T)} dx''\right] dx' \qquad (2)$$

where I_ν is the spectral radiance, $I_{\nu b}(T)$ is the blackbody spectral radiance, and ϵ is the emission coefficient. This equation is numerically integrated from the centerline out to the edge of the channel for each wavelength within the spectral region of interest.

DISCUSSION OF RESULTS

The spectra obtained in the wavelength interval from 300 to 440 nm are shown in Figure 1. The spectral characteristics of the rail and insulator emission are quite similar, but the amplitude of the rail signal is significantly larger than that of the insulator. The spectrum consists of continuum radiation from the high temperature plasma originating in the interior of plasma armature and resonant absorption lines from the cooler material near the surface of the bore. The strong absorption lines have been identified as those belonging to copper and aluminum. Other lines have been identified as calcium (from insulator material), and iron, which was a contaminant that remained on the bore surfaces after bore honing and cleaning.
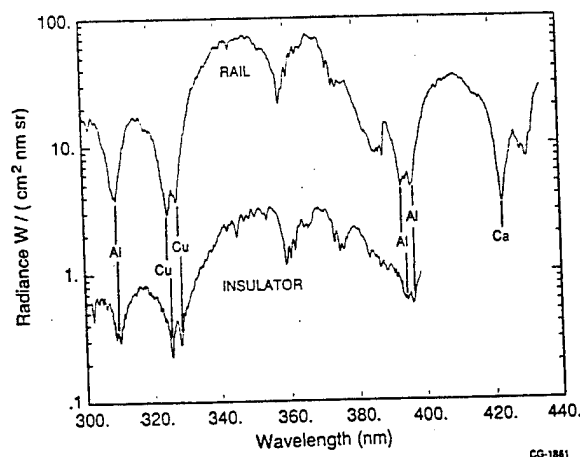

Figure 1. Experimentally obtained spectra through rail and insulator.

The radiation transfer model, used to analyze the spectra, assumes that the plasma is composed of three components, hydrogen, copper, and aluminum. Neglect of the other elements found in the insulator material should have little impact on the radiation transfer calculations, since the insulator products have no strong absorption lines in this spectral region. The depth and broadening of the copper and aluminum lines are determined, primarily, by the concentration of these species in the viscous boundary layer. The spectral features are similar for both the rail and insulator emission. The model indicated that the concentration of aluminum is approximately 15% and copper is approximately 15% in either the rail or the insulator boundary layer. Since the centerline temperature which enters

the model must be the same for both the rail and the insulator, we found that it was impossible to predict the 30-fold difference in absolute intensity by adjusting the shape of the temperature distribution. In order to obtain reasonable agreement, it was necessary to assume that there was a broadband absorbing layer at the surface of the insulator. This layer could consist of a dense liquid layer of insulator decomposition products and/or particulate matter. The comparison between the model predictions and the observed spectra is shown in Figure 2.
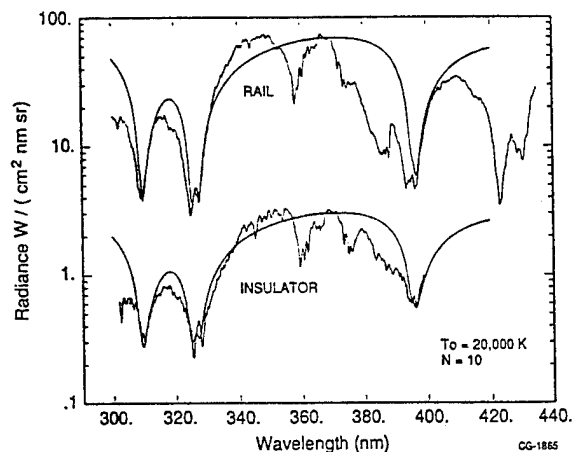

Figure 2. Comparison of the radiation model predictions to the observed spectra.

The final set of parameters used in the model to obtain reasonable agreement with the observed spectra was $T_0 = 20,000$ K and $N = 10$ for both rail and insulator spectra, although a thin layer of broadband absorbing media with an adjustable absorption coefficient was added to the insulator surface. The absorption coefficient of this layer was adjusted to obtain agreement with the experimental data.

These spectral data, together with our earlier comparisons of the time dependent emission from rail and insulator fiberoptic probes [2], suggest important differences in the character of the boundary layers formed on the rails and insulators. Figure 3 shows a schematic representation of these boundary layers. At the rail surface, the current density is continuous and the JxB force extends to the rail surface, resulting in normal velocity and temperature boundary layer profiles. However, on the insulator surface the cooling produced by ablation and the absorption of radiation in the ablation products result in a thicker temperature boundary layer. The lower electrical conductivity in this cooler layer results in reduced current density near the insulator surface. Since the current density is reduced near the insulator surface, the JxB force can no longer balance the hydrostatic pressure in the plasma, and material from the armature is lost through the insulator boundary layer. This produces a strong cross flow which can rapidly transfer material from the rail surface to the insulator surface, therefore explaining the similarity in the observed absorption spectra. Much of the material ablated from the surface of the insulator is also lost through this boundary layer, since there is no

strong JxB force to accelerate the ablation products into the moving armature. On the other hand, the products from rail ablation can be accelerated into the moving armature since the JxB force extends all the way to the rail surface.
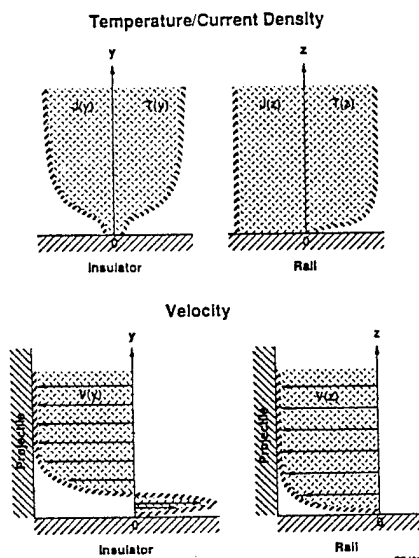

Figure 3. Illustration of the various boundary layer profiles at the rail and the insulator.

Based on these qualitative conclusions concerning the boundary layers, we have constructed a physical model of the resulting flows in the plasma armature. A strong 3-dimensional flow develops in the armature with material being added from the rails and lost through the insulator boundary layer. This flow of material from the armature into the insulator boundary layer would explain why the concentrations of copper and aluminum are similar in both the rail and insulator spectra. Since large volumes of material are ablated from the insulator wall, it is likely that when these products expand in the lower pressure region near the rear of the armature, the thickness of the nonconducting boundary layer will increase, resulting in a current "footprint" on the rail that resembles an airfoil shape. This model of the plasma armature flow is illustrated
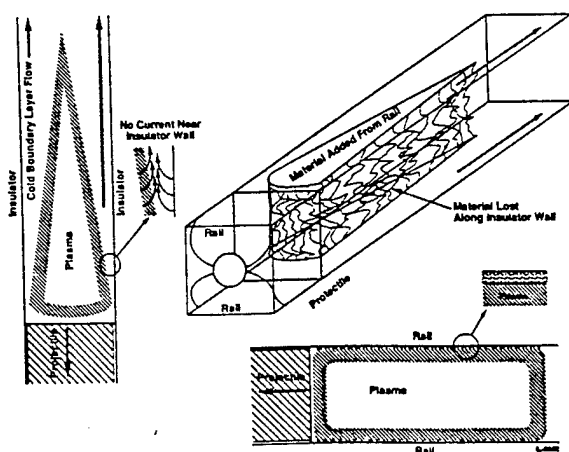
in Figure 4. Crawford et al. [8] have observed flow patterns on the surfaces of recovered hybrid armatures which are entirely consistent with this physical model.

CONCLUSION

In-bore, simultaneous, time-resolved spectral emission from plasma armatures has now been observed in the UTSI railgun using both rail and insulator fiberoptic probes. Analysis of these data has led us to propose a new physical model of the plasma armature in which insulator ablation leads to significant 3-dimensional flow and affects the shape of the current emission pattern on the rail surfaces.

ACKNOWLEDGEMENT

REFERENCES

1. A. Sedghinasab, D. Keefer and H. L. Crowder, "In-Bore Spectral Measurements in a Plasma-Armature Railgun," IEEE Trans. on Plasma Sci., Vol. 17, No. 3, pp. 360-364, June, 1989.

2. D. Keefer and R. Crawford, "Optical Diagnostics of Railgun Plasma Armatures," IEEE Trans. on Magnetics, Vol. 25, No. 1, pp. 295-299, Jan. 1989.

3. D. A. Tidman, S. A. Goldstein, and N. K. Winsor. GT Devices, Inc., Alexandria, VA, Tech. Note GTD 86-3, Mar. 1986.

4. H. U. Griem, Plasma Spectroscopy. New York: McGraw-Hill, 1964.

5. H. U. Griem, Spectral Line Broadening by Plasmas. New York: Academic, 1974.

6. W. J. Karzas and R. Latter, Astrophys. J. Suppl. VI, no. 55, p.167, 1961.

7. M. N. Özisik, Radiative Transfer, New York: Wiley, 1973.

8. R. Crawford, D. Keefer and A. Sedghinasab, "Railgun Hybrid Armatures, Experimental Results and Performance Characteristics," submitted for this conference.

Figure 4. Schematic of the physical model describing the flow characteristics of railgun plasma armatures.

RAILGUN HYBRID ARMATURES, EXPERIMENTAL RESULTS
AND
PERFORMANCE CHARACTERISTICS

Roger Crawford
Dennis Keefer
Ahad Sedghinasab

Center for Laser Applications
University of Tennessee Space Institute
Tullahoma, TN 37388

ABSTRACT

A current research effort at the University of Tennessee Space Institute (UTSI) is devoted to the development of diagnostic methods for the study of railgun armatures. Recent investigations suggest that hybrid armatures having a solid conducting core and plasma brushes in contact with the rails may offer substantial advantages during a major portion of the acceleration in a hyper-velocity railgun. In this investigation six hybrid armature designs were evaluated in the UTSI one centimeter square bore railgun. Advanced diagnostic instrumentation was used to determine the characteristics of hybrid armatures which include a compound armature (current in plasma brushes to the metal armature followed by a plasma armature). The hybrid armatures were compact with shorter current distributions than plasma armatures as measured with both optical and electromagnetic probes. Although the results are preliminary, due to the limited geometries investigated, the results are very encouraging. The short (less than one-bore diameter) hybrids demonstrated efficiencies equal to or greater than plasma armatures and good armature stability.

I. INTRODUCTION

A continuing research program at the University of Tennessee Space Institute has been focused on the development of diagnostic instrumentation and analytic models for the investigation of railgun armatures [1,2,3].* Because of the recognized velocity limitations of solid armatures to a maximum of 2-3 kilometers/second, and the plasma armature difficulties in obtaining velocities greater than 5-6 kilometers/second, UTSI conducted an experimental investigation of hybrid armatures utilizing proven advanced instrumentation and diagnostic capabilities. This paper summarizes the objectives and results of the hybrid armature investigation.

Thornhill, Batteh and Brown [4] provided a definition of a hybrid armature, which consists of a metal armature with thin plasma brushes between the rail and the armature. The metal armature is attached to a non-conducting bore rider and gas seal. It has been assumed that a solid armature would transition at a contact limit velocity to a hybrid armature [5]. Until this investigation the hybrid armature current distribution has been assumed to be confined to the metal armature and plasma brushes.

II. OBJECTIVES

The investigation of the operating characteristics of hybrid armatures for railgun projectiles is complicated by the large number of design variables for the hybrid armature. A systematic investigation of the following armature design variables would be required to fully characterize and optimize a hybrid armature for a specific railgun system.

- Metal armature length to bore diameter ratio
- Initial plasma brush gap thickness
- Insulator wall gap, if not zero
- Axial shape of metal, i.e. cylinder, cone, spike
- Armature material, Al, Li, Mg, Cu, W ...
- Fuse design, fusing technique

To limit the scope of the UTSI investigation, the following research objectives and associated design variations were defined.

a. Determine the current distribution in the hybrid armature (including the trailing plasma if present)

b. Evaluate muzzle voltage and current distribution for level and stability

c. Evaluate metal armature length and plasma brush gap effects on a. and b. above

d. Compare and evaluate performance and efficiency of the hybrid designs tested

Current distribution and muzzle voltage were selected for detailed investigation because of the insight into the armature physics provided by these measurements. UTSI has developed techniques for resolving current distribution in plasma armatures using optical emission data and B-dot deconvolution [1,3].

III. HYBRID ARMATURE DESIGN

The hybrid projectiles were designed with an armature length of one-bore diameter or less. The aluminum armatures were securely attached to a polycarbonate nose piece which served as a bore rider and gas seal. The initial plasma brush gap was machined into the hybrid armature along with a small fuse tab to initiate the plasma brushes. Figure 1 illustrates the six armature designs which were evaluated in this investigation. The logic behind the selected designs is explained as follows. The baseline armature is the 10 mm (0.40") long, 0.5-1.0 mm (0.02" − 0.04") narrow gap design. The 10 mm (0.40") long, medium gap design represents the recovered configuration of the narrow gap design after firing in the 1-meter railgun. And likewise the wide gap design reflects the recovered configuration
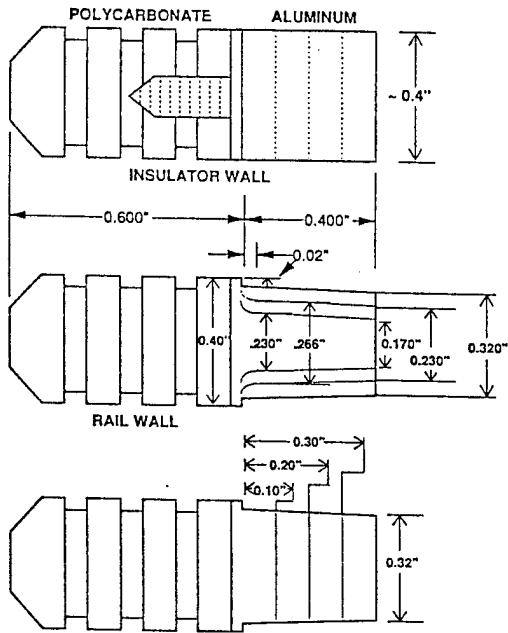
Figure 1. Hybrid Armature Designs

TABLE 1. HYBRID ARMATURE EXPERIMENTAL RESULTS

ARMATURE	INIT. MASS (m_1) gm	FIN. MASS (m_2) gm	INIT. VEL. (v_1) m/s	FIN. VEL. (v_2) m/s
PLASMA	1.53	1.53	909	1857
10 mm NG	4.25	2.92	629	1249
10 mm NG	4.24	2.92	612	1259
10 mm MG	3.68	2.65	645	1251
10 mm MG	3.74	2.68	654	1374
10 mm MG	3.79	2.67	639	1335
10 mm WG	3.24	2.38	704	1391
10 mm WG	3.25	2.34	694	1419
10 mm NG	4.23	2.81	637	1365
PLASMA	1.50	1.50	971	1800
2.5 mm NG	2.54	2.03	858	1644
5.0 mm NG	3.12	2.51	760	1482
7.5 mm NG	3.57	2.87	733	1362
2.5 mm NG	2.51	2.01	763	1608
2.5 mm NG	2.53	2.02	800	1573
5.0 mm NG	3.17	2.42	741	1538
7.5 mm NG	3.74	2.71	697	1365

NG - Narrow Gap, MG - Medium Gap, WG - Wide Gap

of the medium gap design. The choice of armature shape for the 10 mm (0.40″) long, medium gap and wide gap designs should yield performance characteristics similar to the narrow gap design fired in a longer gun, and provide insight into the influence of plasma gap on armature characteristics.

The baseline design was then shortened to 75, 50 and 25 percent of the original length for the investigation of hybrid length influence. This investigation did not evaluate configurations with combinations of variable armature gap and length. The shorter armatures contain less parasitic mass to accelerate and should lose less molten material due to plasma fluid flow.

These projectiles were designed to prevent armature blow-by and precursor arcs. The armatures were also bonded to the nose piece and attached with a stud to improve projectile/armature integrity. The machined plasma brush gaps limited the transitioning armature mode to the fusing transient. Any test shot in which the metal armature separated from the nose piece was not evaluated as a hybrid armature shot.

IV. EXPERIMENTAL INVESTIGATION

The six hybrid armature configurations were fired in the UTSI railgun which has a one centimeter square bore and a one meter length [1]. A single stage, one meter long, light gas injector was used to pre-accelerate the projectiles into the railgun. Injection velocity ranges from 600 meters/second to 900 meters/second for projectile masses of 4.25 to 1.50 grams. The railgun power supply was operated at 7000 volts capacitor charge, which corresponds to approximately 120 kilojoules stored energy. Peak current delivered to the railgun through the pulse shaping inductor was nominally 140 kilo-amperes.

A total of 15 hybrid projectiles were successfully tested during this investigation, and the results presented in Table 1 summarize the 15 shots. The first 8 firings, which investigated the influence of plasma gap thickness on the 10 mm armatures,

were conducted with G-9 insulators in the railgun. High quality optical data was obtained through both rail and insulator fiber optics. The final 7 firings, which investigated armature length, were conducted with Torlon insulators. Both railgun barrels were identical (Glidcop rails) except for the insulator wall material. Poor quality optical data was obtained with the Torlon insulators. The rail fibers observed the initial portion of the plasma passage, however the insulator wall fiber optics were completely obscured by insulator ablation products. This was an unexpected result due to the improved thermal properties of Torlon. Thus the value of in-bore optical diagnostics can be strongly influenced by insulator materials. Good armature current distribution was obtained from the 20 B-dot probes which respond to rail current. Deconvolution of the rail B-dots in combination with the rail fiber optic probes provided good definition of the armature current distribution. In the following section the six armatures will be evaluated based on current distribution, breech and muzzle voltage, performance efficiency, and armature stability.

V. HYBRID ARMATURE RESULTS

Current Distribution

The first significant experimental observation was that the hybrid armature is really a compound armature. Part of the current is carried by plasma brushes to the metal armature, and the remaining current is carried by a plasma armature attached to the rear of the metal armature. The division of current between the hybrid armature and the trailing plasma is determined by the length and plasma gap size of the metal armature. Figure 2 shows a comparison of the current distributions in a plasma armature and the 10 mm narrow gap hybrid armature. Both the deconvolved B-dot signals and rail optical emission profiles are presented in Figure 2. The deconvolved B-dot data from the UTSI railgun has a resolution of one-centimeter. The baseline hybrid armature operates with

a nearly equal current split between the 1 cm hybrid and the 1 cm trailing plasma. This results in a compound armature which is about one-fourth the length of the pure plasma armature. All six hybrid armature designs tested operated in the compound armature mode with differences in the current split and overall armature stability. Figure 3 presents typical B-dot signatures for the hybrid armatures compared with a plasma armature. The data presented in Figure 3 has not been de-
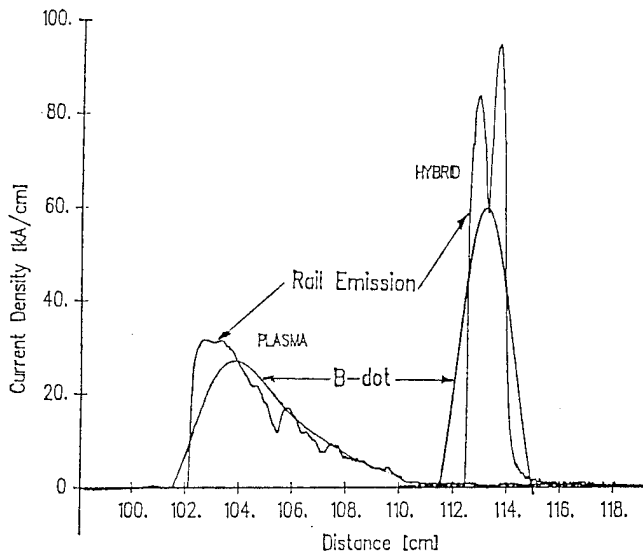

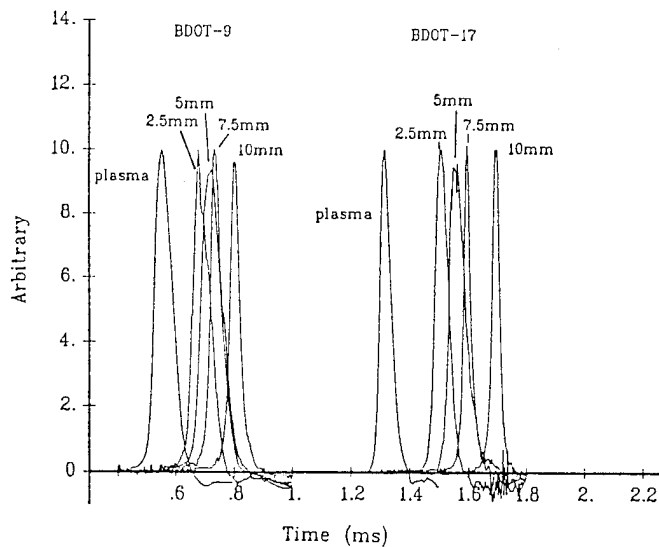Figure 2. Current Distribution Plasma vs Hybrid

Figure 3. Typical B-Dot Signatures Plasma vs Hybrid

convolved and is plotted as a function of time. To accurately evaluate and compare current distribution the deconvolved B-dot data must be plotted as a function of bore position. In Figure 3 the faster plasma armature appears narrower than it would on a bore position plot. The 2.5 and 5.0 mm hybrid armatures have current distributions only slightly shorter than the plasma. The 7.5 and 10 mm hybrid armatures, however, have current distributions of one-half and one-quarter the plasma length.

Hybrid Plasma Flow Field

The second significant experimental result was unexpected and provided additional insight into the complex three-dimensional flow field in the plasma armature. The hybrid armatures were soft recovered after firing, and the metal surfaces retained the ablated metal flow patterns driven by the three-dimensional plasma flows. Figure 4 clearly shows that the rail facing-surface ablated products flows toward the insulator facing portion of the metal armature. All six hybrid armature designs fit tight to the insulator wall, however after launch significant material has been removed from the insulator facing sides of the armature. A stagnation line is clearly visible along the insulator sides of the armature. These flow patterns confirmed results from the plasma armature investigation which suggested that the non-conducting ablated insulator wall material is driven rearward along the insulator wall by unbalanced pressure forces. The stagnation pattern on the back of the metal armature is consistent with high forward velocities in the center of the trailing plasma armature. It is important to recognize that the plasma brushes contain very high pressure gradients, and the hybrid armature must be securely attached to the bore rider/gas seal to prevent mechanical failure or plasma blow-by.
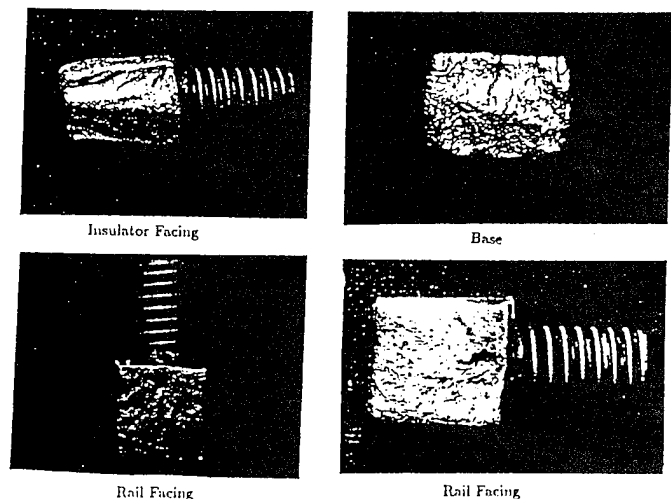

Insulator Facing   Base

Rail Facing   Rail Facing

Figure 4. Post Fire Armature Flow Patterns

Breech and Muzzle Voltage

The breech and muzzle voltage data were utilized along with gun current to calculate total electrical work input at the breech, armature electromagnetic work and impulse. Figure 5 presents the breech and muzzle voltage for the baseline, 10 mm, narrow gap hybrid and a plasma armature at the same current level. The baseline hybrid armature had about 100 volts reduction in breech and muzzle voltage compared to the plasma armature. As the plasma brush gap is increased the breech and muzzle voltage increase significantly. Figure 6 shows the influence of plasma gap on muzzle voltage in comparison to plasma muzzle voltage. Note that the wide gap, 10 mm, armature muzzle voltage actually exceeds plasma muzzle voltage over part of the shot.
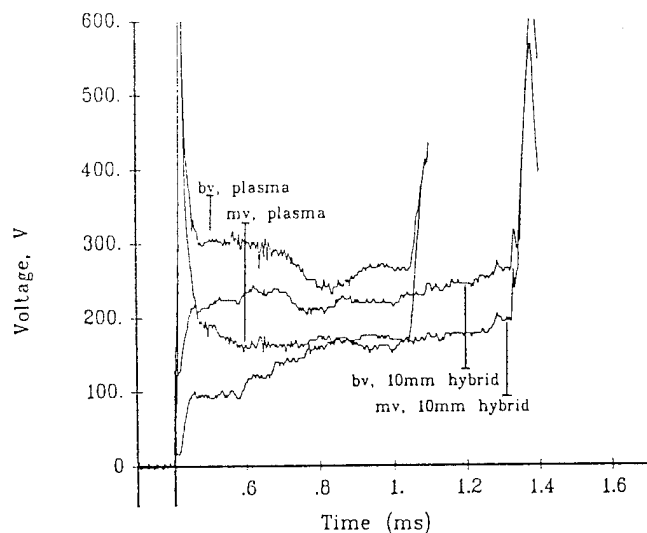
Figure 5. Breech and Muzzle Voltage, Baseline Hybrid vs Plasma Armature
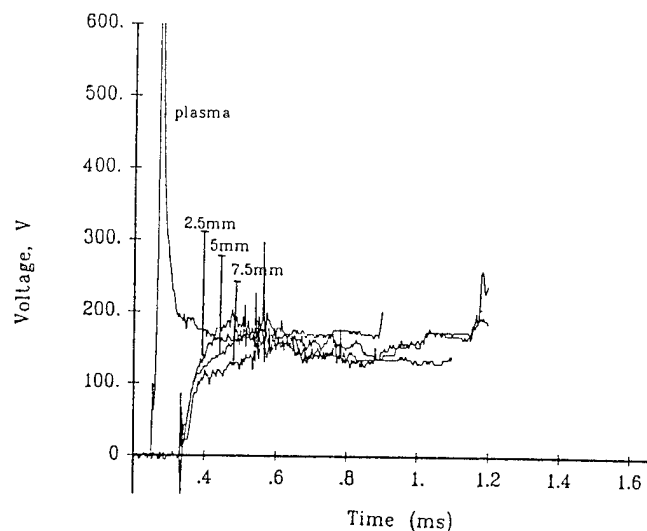

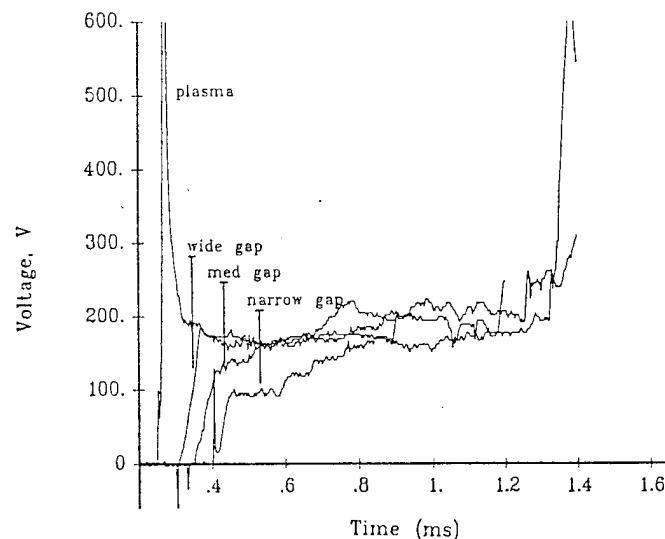Figure 7. Muzzle Voltage, Hybrid Length Influence

Figure 6. Muzzle Voltage, Plasma Gap Influence

Comparison of muzzle voltages for the three shortened armatures with the plasma armature shows that even the 2.5 mm hybrid has a significant influence on armature characteristics (Figure 7). The shorter the metal length in the hybrid armature the closer the breech and muzzle voltages approach plasma armature voltage levels. In all test cases the metal hybrid participated in current sharing with the accompanying plasma armature and influenced muzzle voltage.

Armature Efficiency and Performance

The evaluation of hybrid armature performance requires a careful definition of efficiency due to the changing mass of the projectile. Four different efficiencies were applied to the hybrid armature experimental data in an attempt to evaluate performance improvements.

Kinetic energy efficiency is defined as the increase in projectile kinetic energy divided by the electromagnetic work of the armature.

$$\eta_{KE} = \frac{\frac{1}{2}(m_2 v_2^2 - m_1 v_1^2)}{\int_{x_1}^{x_2} \frac{1}{2} L' I^2 dx}$$

Momentum efficiency is defined as the increase in projectile momentum divided by the electromagnetic impulse of the armature.

$$\eta_{MOM} = \frac{m_2 v_2 - m_1 v_1}{\frac{1}{2} L' \int_{t_1}^{t_2} I^2 dt}$$

Armature efficiency defined by Thornhill [6] ratios the projectile kinetic energy increase to total energy applied to the armature.

$$\eta_{ARM} = \frac{\frac{1}{2}(m_2 v_2^2 - m_1 v_1^2)}{\int_{t_1}^{t_2} (IV_{MUZ} + \frac{1}{2} L' I^2 v) dt}$$

Total gun efficiency is defined as the increase in projectile kinetic energy divided by total electrical energy input to the gun breech.

$$\eta_{GUN} = \frac{\frac{1}{2}(m_2 v_2^2 - m_1 v_1^2)}{\int_{t_1}^{t_2} IV_{BR} dt}$$

The six hybrid armature designs and a plasma armature were evaluated using the four efficiency definitions above. Figure 8 shows that kinetic energy efficiency increases with hybrid armature length to 5.0 mm then decreases with the 10 mm NG armature having nearly the same kinetic energy efficiency as the plasma armature. However the momentum efficiency is highest for the plasma armature and decreases with hybrid armature length. Armature and gun efficiency show that the plasma and 2.5 mm hybrid armatures have nearly the same efficiency. The longer hybrid armatures have lower overall efficiency which may be due in part to molten armature material being blown off by the plasma flow. The data symbols in Figure 8 represent the average value of efficiency for each armature design. The "error bars" indicate the range of the experimental data including measurement error. The three symbols on the 10 mm armature efficiencies represent the narrow, medium and wide plasma gap designs. In all cases the narrow gap had the highest efficiency of the three 10 mm armatures, and the wide gap had the lowest efficiencies.
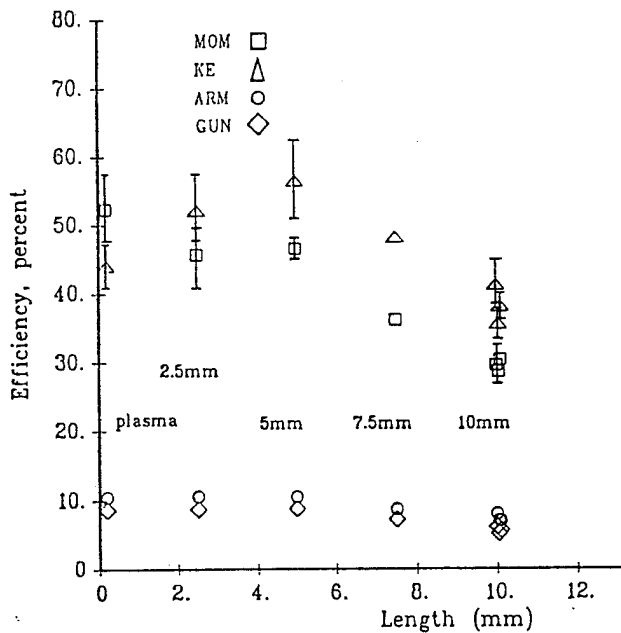
Figure 8. Armature Efficiency Comparison

REFERENCES

1. D. Keefer and R. Crawford, "Optical Diagnostics of Rail-gun Plasma Armatures," IEEE Trans. on Magnetics, Vol. 25, No. 1, Jan. 1989, pp. 295-299.

2. A. Sedghinasab, D. Keefer, and H. Crowder, "In-bore Spectral Measurements in a Plasma Armature Railgun," IEEE Trans. on Plasma Science, Vol. 17, No. 3, June 1989, pp. 360-364.

3. L. M. Smith and D. Keefer, "Railgun Armature Plasma-Current Density From Deconvolved B-Dot Probe Signals," IEEE Trans. on Plasma Science, Vol. 17, No. 3, June 1989, pp. 501-506.

4. L. Thornhill, J. Batteh, and J. Brown, "Armature Options for Hypervelocity Railguns," IEEE Trans. on Magnetics, Vol. 25, No. 1, Jan. 1989, pp. 552-557.

5. D. Kuhlmann-Wilsdorf, J. Cuardos, and M. Skidmore, "Insights Gained From Tests of Solid Armatures With and Without Payload in a 15 mm EML," IEEE Trans. on Magnetics, Vol. 25, No. 1, Jan. 1989, pp. 316-322.

6. L. Thornhill, J. Batteh, and D. Littrell, "Scaling Study for the Performance of Railgun Armatures," IEEE Trans. on Plasma Science, Vol. 17, No. 3, June 1989, pp. 409- 421.

Armature Stability

Secondary armature formation in plasma armatures has been recognized as a significant phenomenon limiting maximum projectile velocity. Although the UTSI hybrid armature experiments were conducted at velocities below expected secondary armature formation, the hybrid armatures remained compact and demonstrated stable characteristics. The wide-gap hybrid armatures produced some irregular current distributions in mid-bore, but stabilized to single smooth current distributions before muzzle exit. The 2.5 and 5.0 mm hybrid armatures also demonstrate occasional mid-bore current distribution irregularities, which damped out before muzzle exit. High velocity hybrid experiments will be required to evaluate and confirm the potential stabilizing influence of the metal vapor seeding from hybrid armatures.

VI. CONCLUSIONS

Although this investigation was conducted in a one meter long, one centimeter square bore railgun the results indicate that short hybrid armatures offer improved armature characteristics. The shorter hybrid armature current distribution has the potential for reducing bore erosion and improving armature stability. The reduced muzzle voltage of the hybrid armatures improves armature efficiency through reduced heating losses. The 2.5 and 5.0 mm hybrid armatures had performance efficiencies as good or better than the plasma armature.

Additional research is required to determine hybrid armature performance at high velocity and in larger railguns. The metal vapor seeding provided by the hybrid armature may improve stability of armature current distribution and prevent armature bifurcation and loss of acceleration. The hybrid armature may offer the best solution to the present plasma armature velocity limits.